Tensor Polarization of the Deuteron at High Momentum Transfer in Elastic (e, d) Scattering

by

Wenxia Zhao

B.Sc., Tsinghua University, China (1991)

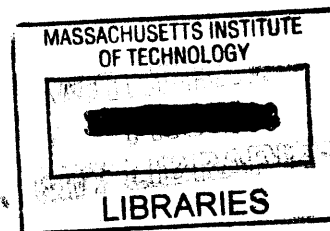M.Sc., Institute of High Energy Physics, China (1994)

Submitted to the Department of Physics
in partial fulfillment of the requirements for the degree of

Doctor of Philosophy

at the

MASSACHUSETTS INSTITUTE OF TECHNOLOGY

September 1999

Signature of Author . . . .
Department of Physics
June 30, 1999

Certified by . . . .
Dr. Claude F. Williamson
Thesis Supervisor

Accepted by . . . .
Professor Thomas J. Greytak
Associate Department Head for Education

Tensor Polarization of the Deuteron at High Momentum Transfer in Elastic (e, d) Scattering

by

Wenxia Zhao

Abstract

The measurement of deuteron tensor polarization using (e, d) elastic scattering was performed in Hall C, Jefferson Lab by the t_{20} collaboration at four-momentum transfers of 4.10, 4.46, 5.08, 5.48, 6.23 and 6.65 fm^{-1}. The scattered electrons were detected by the High Momentum Spectrometer, and a specially designed magnetic channel was used to detect deuterons in coincidence. The polarization of the recoil deuterons was measured in the polarimeter POLDER, using $^1\text{H}(\vec{d},2\text{p})\text{n}$ reaction. A 12 cm liquid deuterium target was used for (e, d) elastic scattering, and the second scattering took place in a 20 cm liquid hydrogen target in POLDER. The deuteron arm was fixed at $60.5°$ while the electron arm angle θ_e was changed with different beam energies to obtain different momentum transfers. The extracted values of $t_{20}(G_C, G_Q, G_M, \theta_e)$, combined with the structure functions $A(G_C, G_Q, G_M)$ measured in this experiment and the world data of $B(G_M)$, were used to separate the charge monopole form factor G_C and charge quadrupole form factor G_Q of the deuteron.

The extracted values of t_{20} were compared to predictions of different theoretical models of the electromagnetic form factors of the deuteron. The present data favor the calculations of the "nucleon-only" models with the inclusion of the relativistic effects and the meson exchange currents. The position of the node in the G_C form factor from the present experiment is somewhat lower in four-momentum transfer than in a previous Bates measurement. This tends to give a more consistent position of the node in G_C for the two-nucleon and the three-nucleon systems. The need for more precise polarization data in the four-momentum transfer range of the node in G_C is discussed.

Thesis Supervisor: Dr. Claude F. Williamson
Title: Senior Research Scientist, Department of Physics and Laboratory for Nuclear Science

Contents

List of Tables

List of Figures

12

Chapter 1

Introduction

The deuteron, consisting of a proton and a neutron, is the simplest nuclear system in nature. It provides one of the best testing grounds for the nucleon-nucleon (NN) interaction. The deuteron is a bound state of a proton and a neutron coupled in a spin-one and isospin-zero state. It can be described as a $^3S_1$ state mostly, mixed with a $^3D_1$ state (between 4% and 7.5%) due to the tensor component of the NN interaction.

The basic components of the NN interaction are a long-range attraction well described by a one-pion exchange potential, an intermediate-range attraction, and a short-range repulsion. At moderate and short distances, where the NN interaction is more complicated, a wide variety of interaction models has been proposed, ranging from one-boson-exchange (OBE) models to models with explicit two-meson exchanges to purely phenomenological parametrizations. Typical models are Paris [1], Bonn [2], Argonne v_{14} [3], and Argonne v_{18} [4]. The parameters of these potential models, such as coupling constants and cutoff mass for the form factors are adjusted to fit the deuteron properties and NN scattering data. While these models produce a qualitatively similar description of the NN interaction, such as the deuteron static properties and NN phase shifts, they have different short-range behavior and different off-shell

T matrix elements.

Elastic electron scattering provides further tests of our understanding in investigating the ground state electromagnetic structure of the deuteron with high precision. For several decades, many experiments have been performed to study the electromagnetic form factors of the deuteron. They contribute significantly to the description of the NN interaction, especially its off-shell properties, its behavior at short distances, and the role of non-nucleonic degrees of freedom.

The cross section for elastic e-d scattering is proportional to $A(Q)+B(Q)\tan^2(\theta/2)$, where $A(Q)$ and $B(Q)$, the electric and magnetic structure functions respectively, are functions of the electromagnetic form factors of the deuteron: charge monopole G_C, charge quadrupole G_Q, and magnetic dipole G_M. The structure functions $A(Q)$ and $B(Q)$ can be separated with the Rosenbluth method by measuring the cross sections at different electron angle θ for the same four-momentum transfer Q. The structure function $B(Q)$ depends only on G_M, thus G_M can be obtained directly from the $B(Q)$ result. The charge form factors G_C and G_Q, contained in the structure function $A(Q)$, cannot be separated from the inclusive cross section measurements.

The determination of the structure of the deuteron is one of the most fundamental task in nuclear physics. The separation of the charge monopole and charge quadrupole form factors of the deuteron is a necessary input for understanding the deuteron structure. A third observable is needed to separate G_C and G_Q. The tensor polarization of the deuteron can accomplish this goal. With an unpolarized electron beam, one may use a tensor polarized target to extract the analyzing powers from the asymmetry of the yields for the scattering. Alternatively, one may measure the polarization of the recoil deuteron with an unpolarized target, and extract the three tensor components t_{20}, t_{21}, and t_{22} simultaneously. The tensor polarization t_{20} depends on an interference term of G_C and G_Q and a small term from G_M, while t_{21} is proportional to $G_Q G_M$. Both t_{20} and t_{21} can be used to separate G_C and G_Q. In

this experiment, we used t_{20} in the separation because it is larger than t_{21} and almost independent of the nucleon form factors up to about Q = 6-7 fm^{-1}. The result of t_{21} was used to resolve the ambiguity of G_C which will be explained in detail in the data analysis in Chapter 6. Finally, t_{22} is proportional to G_M^2 and was used as cross check for the tensor polarization measurement since G_M is obtained from a more precise measurement of $B(Q)$.

Many models of the deuteron electromagnetic form factors have been proposed. In the conventional impulse approximation (IA) description of *e-d* scattering, the electron interacts with each nucleon in the deuteron via a virtual photon and the electromagnetic form factors of the interacting nucleons are taken to be the same as those for a free nucleon. At large four-momentum transfers, various corrections to the IA model become important. These include isoscalar meson-exchange currents (MEC), isobar components, relativistic effects, and perhaps quark degrees of freedom. Relativistic models have been developed both in the light front formalism [5] and by solving the Bethe-Salpeter equation [6]. Most do not include contributions from MEC such as the $\rho\pi\gamma$ process and therefore are referred to as relativistic impulse approximation (RIA). Some nonrelativistic models used coupled-channel formalism of nucleons and isobar (Δ and N^*) and included contributions from MEC. At high four-momentum transfer (Q > 5 fm^{-1}), the deuteron is probed at smaller internucleon distances, and the quark substructure may manifest itself in the deuteron observables. Quark configurations are incorporated in several hybrid quark-hadron models. with a quark confinement radius taken as a free parameter. Some of them give predictions similar to those of IA model while others have completely different results for the high four-momentum transfer region. A Skyrme model, which is equivalent to a low energy version of QCD in the limit of a large number of colors, determines the form of the one-body and two-body exchange current operators from the Lagrangian fields and predicts results for the deuteron form factors similar to those obtained

from conventional nucleon-meson dynamics. Finally, at sufficiently large momentum transfer, PQCD, which predicts simple relations between the form factors of the deuteron, is expected to become applicable.

Previous measurements of the tensor polarization t_{20} [7, 8, 9, 10, 11, 12] have been carried out up to a four momentum transfer of Q $= 4.6$ fm^{-1}. Most experiments were performed at relatively low momentum transfer (Q < 3 fm^{-1}) where t_{20} is well determined by the non-relativistic impulse approximation with small theoretical uncertainties. One recent experiment [12] performed at MIT-Bates extended the measurement to high four momentum transfer region (up to 4.6 fm^{-1}) and measured all three tensor moments of the recoil deuteron tensor polarization (t_{20}, t_{21}, and t_{22}). In this four momentum transfer region, the predictions from various models differ significantly, although G_C is expected in most models to pass through zero. In the same experiment, the node of G_C was determined to be at Q $= 4.39 \pm 0.16$ fm^{-1}. This value for the node for G_C presents a serious problem for the potential model calculations as was pointed out by Henning *et al.* [13]. These authors have calculated the isoscalar charge monopole (G_C) form factors to order $(v/c)^2$ for the deuteron and for the three-nucleon ^{3}He/^{3}H systems using several potential models. If one plots the predicted position of the node for the G_C form factors for the three-nucleon systems vs. the same quantity for the deuteron, one obtains a rather good linear relationship. The positions of these nodes for the deuteron [12] and the three-nucleon systems [14] have been measured experimentally. When plotted on the same graph as above, the box representing the measurements with their associated errors fails very significantly to intersect the straight line defined by the calculations (see Figure 8-1).

This failure represents something of a "crisis" in the theory of these few-nucleon systems. It appeared from the data that existed prior to the present experiment that standard potential theories with corrections to order $(v/c)^2$ could not simultaneously account for the nodes in the G_C form factors for the deuteron and the three-nucleon

systems.

One of the principal motivations of the present experiment, performed in Hall C at the Thomas Jefferson National Accelerator Facility (Jefferson Lab) was to obtain polarization data with better precision in the region of momentum transfer, Q, expected to contain the node in the G_C form factor. Precise measurements of the structure function $A(Q)$ were performed in the same time in the present experiment [32] and in another experiment [33] in Hall A at Jefferson Lab. The present experiment obtained data for six values of Q in the range 4.1 fm^{-1} $< Q <$ 6.7 fm^{-1}. The lowest four values of Q span the region of the node in the G_C form factor, and the present thesis concentrates on the physics to be learned from these data. The higher momentum data may bear on the PQCD formulation of the two-nucleon system and will be the subject of a separate thesis [38]. This experiment was carried out by an international collaboration whose members and affiliated institutions are given in Appendix A. The groups most heavily involved in the data analysis and the kinematics analyzed by each group is shown in Table 6.1.

In Chapter 2, the theoretical background is presented, including the deuteron properties, the description of e-d elastic scattering, the definition of the tensor polarization and various theoretical models for the deuteron form factors. A survey of previous experiments is presented in Chapter 3. The experimental setup for this experiment is introduced in Chapter 4. A separate calibration experiment is described in Chapter 5. The detailed data analysis and results are described in Chapter 6. The comparison with predictions from different theories is in Chapter 7. Finally, the conclusions are presented in Chapter 8.

Chapter 2

Theoretical Background

2.1   Deuteron Properties

The deuteron is the simplest nucleus in nature, consisting of a proton and a neutron loosely bound by nuclear force. The binding energy E_B is 2.22 MeV, much less than the average value between a pair of nucleons in all the other stable nuclei. The static properties of the deuteron are listed in Table 2.1. The scale of the separation between the neutron and the proton is given by the size parameter R,

$$R = \gamma_d^{-1} = (2m_R E_B)^{-\frac{1}{2}} = 4.31770(2) \text{ fm}, \tag{2.1}$$

where m_R is the reduced mass of the nucleons in the deuteron. It is more than twice the average distance between nucleons in heavy nuclei ($\sim$2 fm), indicating the loosely bound nature of the two nucleons as well.

Spin-parity (J^P), isospin (I)	1^+, 0	[15]
Mass (M_d)	1875.61339(57) MeV/c^2	[16]
Binding energy (E_B)	2.224575(9) MeV	[17]
Quadrupole moment (Q_d)	0.28590(30) fm^2	[18]
Magnetic moment (μ_d)	0.857406(1) μ_N	[19]
Asymptotic S-wave amplitude (A_S)	0.8846(8)	[20]
Asymptotic D/S-wave ratio (η)	0.0256(4)	[21]
RMS radius (r_d)	1.9627(38) fm	[22]

Table 2.1: Static properties of the deuteron. Table taken from Ref. [12].

The existence of electric quadrupole moment and the departure of the measured magnetic dipole moment from the value expected from a pure $^3S_1$ state for the deuteron indicates the ground state of the deuteron is an admixture of $^3S_1$ and $^3D_1$ state. The D-state component is coupled to the S-state component by the tensor force. The wave function of the deuteron [20] is:

$$\Psi_{J=1,M} = \frac{1}{\sqrt{4\pi}} \left[\frac{u(r)}{r} + \frac{1}{\sqrt{8}} \frac{\omega(r)}{r} S_{12}(\hat{\mathbf{r}}) \right] \chi_{1M} \tag{2.2}$$

$$S_{12}(\hat{r}) = 3(\sigma_1 \cdot \hat{\mathbf{r}})(\sigma_2 \cdot \hat{\mathbf{r}}) - \sigma_1 \cdot \sigma_2 \tag{2.3}$$

$$\hat{\mathbf{r}} \equiv \mathbf{r}/r, \tag{2.4}$$

where $u(r)$, $w(r)$, and χ_{1M} are the radial S-state, D-state, and triplet spin wave functions respectively, $\sigma_{1,2}$ are the Pauli matrices, and $\mathbf{r}$ is the relative position vector of the nucleons in the deuteron. The S-state and D-state wave functions are normalized as

$$\int_0^\infty [u^2 + w^2] dr = 1 \tag{2.5}$$

Figure 2-1 displays the S-state and D-state wave functions in configuration space for a particular nucleon-nucleon potential and Figure 2-2 shows the same functions in

momentum space. For large r, the S-state and
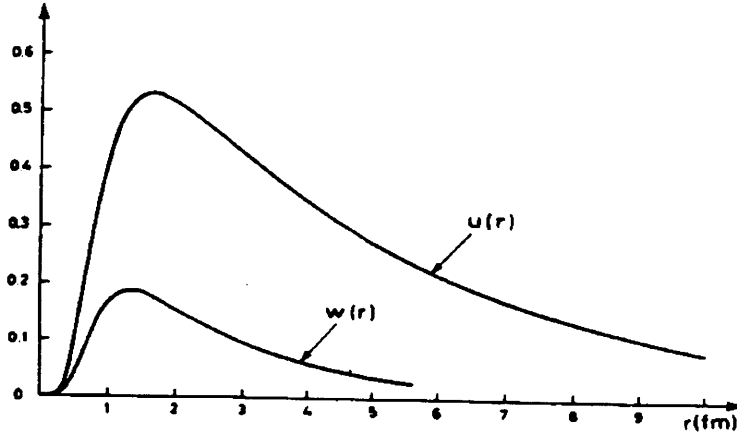
Figure 2-1: S- and D-state wave functions, $u(r)$ and $w(r)$, calculated using the Reid soft core potential [23]. Figure taken from Ref. [24].
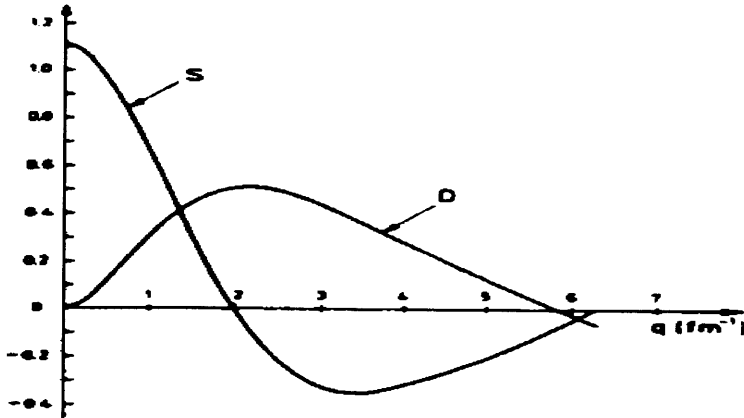
Figure 2-2: The same S- and D-state wave functions as in Figure 2-1 in momentum space. Figure taken from Ref. [24].

D-state wave functions are approximated by

$$u(r) \xrightarrow{r \to \infty} A_S \exp^{-\gamma_d r}, \tag{2.6}$$

$$w(r) \xrightarrow{r \to \infty} A_D \left(1 + \frac{3}{\gamma_d r} + \frac{3}{(\gamma_d r)^2}\right) \exp^{-\gamma_d r}, \tag{2.7}$$

where γ_d is defined in Eq. 2.1, A_S (see Table 2.1 and A_D are the asymptotic amplitudes for S-state and D-state respectively. The asymptotic D/S ratio η is given by

$$\eta \equiv \frac{A_D}{A_S} = \lim_{r \to \infty} \frac{w(r)}{u(r)}. \tag{2.8}$$

2.2 Elastic Electron-Deuteron Scattering

In elastic scattering of an ultra-relativistic electron from a deuteron, the scattered electron energy $E_{e'}$ is given by

$$E_{e'} = f E_e, \tag{2.9}$$

where E_e is the incident electron energy, and f is the recoil factor

$$f = \frac{1}{1 + (2E_e/M_d)\sin^2(\frac{\theta_e}{2})}. \tag{2.10}$$

Here θ_e is the electron scattering angle in the lab frame. The square of the four-momentum transfer, q^2, carried by a virtual photon exchanged between the electron and the deuteron is space-like

$$Q^2 = -q^2 = 4f E_e^2 \sin^2(\theta_e/2). \tag{2.11}$$

The electron scattering angle θ_e and the kinetic energy T_d of the recoil deuteron are

given below

$$T_d = E_e - E_{e'} = \frac{Q^2}{2M_d},$$ (2.12)

$$\sin^2(\theta_e/2) = \frac{\cos^2(\theta_d)}{1 + (2 + E_e/M_d)(E_e/M_d)\sin^2(\theta_d)}.$$ (2.13)

Many authors[25, 26, 27, 28] have investigated elastic e-d scattering in the literature. By using the first Born approximation (one-photon exchange approximation) and imposing relativistic Lorentz and gauge invariance, the differential cross section can be written as:

$$d\sigma/d\Omega_e = (d\sigma/d\Omega_e)_{\text{Mott}}[A(Q) + B(Q)\tan^2(\theta_e/2)]$$ (2.14)

where the Mott cross section describes the scattering of an electron off a pointlike spinless particle and is given by

$$(d\sigma/d\Omega_e)_{\text{Mott}} = \frac{(\alpha\hbar c)^2\cos^2(\theta_e/2)}{4E_i^2\sin^4(\theta_e/2)} \cdot f$$ (2.15)

for the deuteron. Here α is the fine structure constant.

Due to angular momentum conservation, parity invariance and time-reversal invariance, the electromagnetic structure functions, $A(Q)$ and $B(Q)$, are given in terms of the three Sachs form factors of the deuteron in elastic e-d scattering : charge monopole (G_C), charge quadrupole (G_Q), and magnetic dipole (G_M). In this formalism, $A(Q)$ and $B(Q)$ can be expressed as

$$A(Q) = G_C^2(Q) + \frac{8}{9}\eta^2 G_Q^2(Q) + \frac{2}{3}\eta G_M^2(Q),$$ (2.16)

$$B(Q) = \frac{4}{3}\eta(1 + \eta)G_M^2(Q),$$ (2.17)

$$\eta = Q^2/4M_d^2.$$ (2.18)

The normalization of the form factors G_C, G_Q and G_M at $Q = 0$ are chosen so that

$$G_C(0) \;\; = \;\; 1, \tag{2.19}$$

$$G_Q(0) \;\; = \;\; M_d^2 Q_d = 25.830, \tag{2.20}$$

$$G_M(0) \;\; = \;\; (M_d/M_p)\mu_d = 1.714, \tag{2.21}$$

where M_p is the proton mass.

Using the Rosenbluth separation, the structure functions $A(Q)$ and $B(Q)$ have been obtained up to 10 fm^{-1} and 8.4 fm^{-1} respectively [29, 30, 31, 32, 33].

2.3 Tensor Polarization of the Deuteron

Polarization describes the state of spin orientation of an assembly of particles. The notations and coordinate systems for describing polarization here are those of the Madison convention [34]. For spin-one particles, either spherical tensor moments (t_{kq}) or Cartesian tensor moments (p_{ij} and p_i) are used to describe the polarization of the particles. The effect of initial polarization of beam or target on the differential cross section for a nuclear reaction is described by analyzing powers A_i and A_{ij} (Cartesian) or T_{kq} (spherical). The two sets of operators are given below in terms of the spin-one

angular momentum operators and the unit matrix:

$$t_{00} = 1 \tag{2.22}$$

$$t_{10} = \sqrt{\frac{3}{2}} < S_Z > \tag{2.23}$$

$$t_{1\pm1} = \mp(\sqrt{3}/2) < S_x \pm iS_y > \tag{2.24}$$

$$t_{20} = (\frac{1}{\sqrt{2}}) < 3S_z^2 - 2 > \tag{2.25}$$

$$t_{2\pm1} = \mp(\sqrt{3}/2) < (S_x \pm iS_y)S_z + S_z(S_x \pm iS_y) > \tag{2.26}$$

$$t_{2\pm2} = (\sqrt{3}/2) < (S_x \pm iS_y)^2 > \tag{2.27}$$

$$p_i = < S_i > \tag{2.28}$$

$$p_{ij} = < S_{ij} >= \frac{3}{2} < S_iS_j + S_jS_i > -2\delta_{ij} \tag{2.29}$$

$$i, j = x, y, z \tag{2.30}$$

The polarization of particles is referred to a right-handed coordinate system with z-axis along the direction of the outgoing particle momentum, $\vec{k}_f$, and y-axis along $\vec{k}_i \times \vec{k}_f$ as shown in Figure 2-3. Here $\vec{k}_i$ is the momentum vector of the incident beam. For the analyzing power, the coordinate system (Figure 2-4) is one in which the z-axis is along the $\vec{k}_i$, and the y-axis is along $\vec{k}_i \times \vec{k}_f$, for the reaction in question.
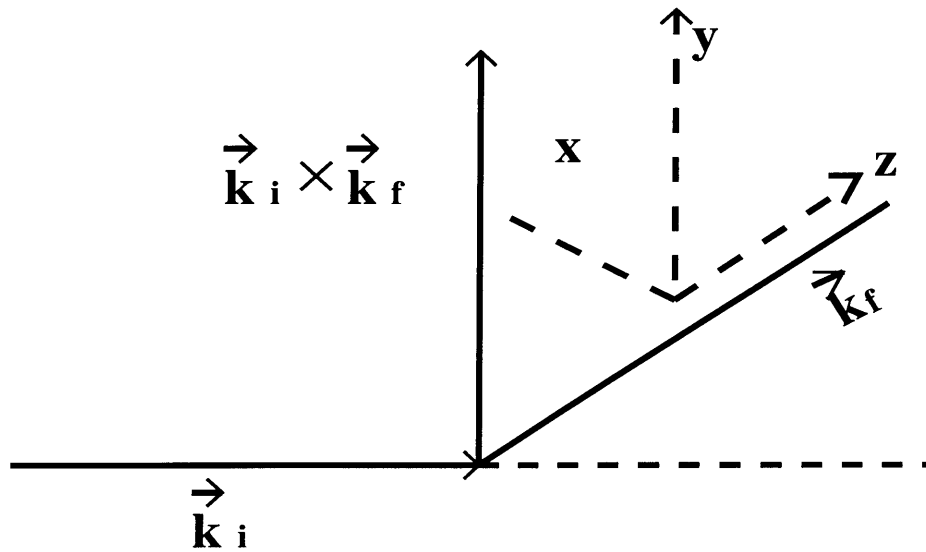
Figure 2-3: Right-handed coordinate system for polarization components t_{kq} or p_i, p_{ij}. Figure taken from Ref. [34].
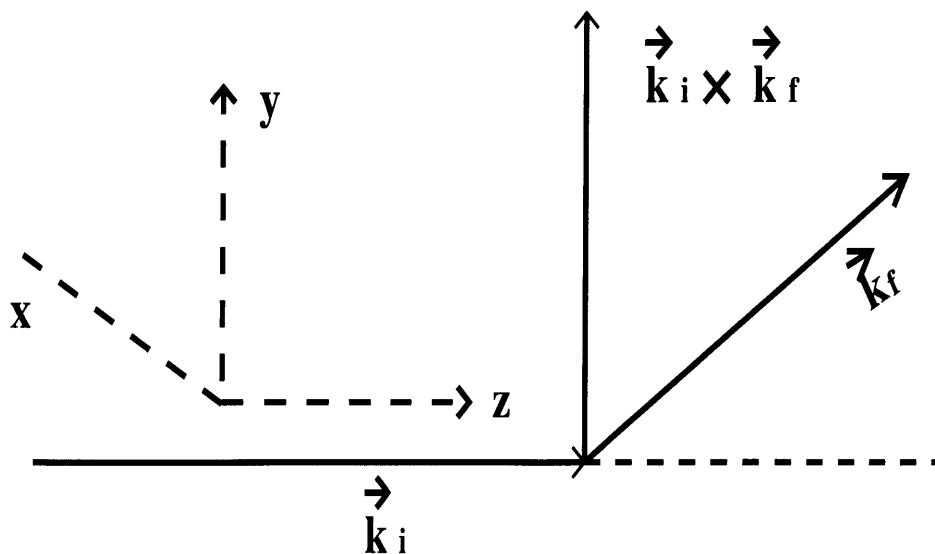
Figure 2-4: Right-handed coordinate system for analyzing powers T_{kq} or A_i, A_{ij}. Figure taken from Ref. [34].

The experiment to measure the deuteron tensor polarization described in this thesis was a double-scattering experiment. Unpolarized electrons were scattered elastically from unpolarized deuterons. The recoil deuterons were tensor polarized with components t_{20}, t_{21} and t_{22} and were transported to a liquid hydrogen target to undergo a second scattering, the ^{1}H($\vec{d}$,2p)n reaction, in which the tensor polarization of the recoil deuterons was measured.

The general relations between the tensor polarization variables and the deuteron form factors have been studied by Schildknecht [35, 36] and by Arnold, Carlson and Gross [37]. In terms of G_C, G_Q and G_M, the tensor polarization t_{kq} of the deuteron are given as

$$t_{20} = -\frac{1}{\sqrt{2}I_0}[\frac{8}{3}\eta G_c G_Q + \frac{8}{9}\eta^2 G_Q^2 + \frac{1}{3}\eta(1+2(1+\eta)\tan^2\frac{\theta}{2})G_M^2], \quad (2.31)$$

$$t_{21} = \frac{2}{\sqrt{3}I_0}\eta[\eta+\eta^2\sin^2\frac{\theta}{2}]^{1/2}G_M G_Q \sec\frac{\theta}{2}, \quad (2.32)$$

$$t_{22} = -\frac{1}{2\sqrt{3}I_0}\eta G_M^2, \quad (2.33)$$

$$I_0 = A(Q) + B(Q)\tan^2\frac{\theta}{2}. \quad (2.34)$$

2.4 Theoretical Models of the Deuteron

To understand the structure of the deuteron, many models have been proposed to describe the elastic e-d scattering. The different models are summarized in six groups: non-relativistic impulse approximation; relativistic impulse approximation; coupled-channel models of the nucleons and Δ isobars; hybrid quark-hadron models; Skyrmion model; and perturbative quantum chromodynamics (PQCD) model. The first three groups of models, which are "nucleon-only" models, are described in this chapter. The last three groups of models involve higher momentum transfer and even the quark degrees of freedom. The description of these "non-nucleonic" models and the comparison of their predictions with the experimental data can be found in Ref.

[38]. In this thesis, the predictions of the various "nucleon-only" models for the $A(Q)$ and $B(Q)$ structure function are discussed in the subsequent sections. The predictions for G_C, G_Q and t_{20} from representative calculations based on these models will be shown and compared to the data in Chapter 7.

As mentioned in Chapter 1, the NN interaction can be described by the exchange of mesons. The effects of the meson exchange currents (MEC) have been found to be important to explain experimental data [39, 40]. Because the deuteron is in a isospin-zero state, only isoscalar MEC's can contribute in elastic e-d scattering. The contributions of MEC's to the deuteron form factors are generally calculated perturbatively by evaluating various Feynman diagrams in increasing powers of p/M_n, where M_n is the mass of nucleon and p is some characteristic nuclear momentum. A detailed discussion of different isoscalar MEC's can be found in Ref. [41].

2.4.1   Non-Relativistic Impulse Approximation (NRIA)

The conventional approach to study the deuteron electromagnetic form factors (DEFF) is the non-relativistic impulse approximation. In the impulse approximation (IA) description of e-d elastic scattering, the electron interacts with each nucleon in the deuteron via a virtual photon and the electromagnetic form factors of the interacting nucleon are taken to be the same as those for a free nucleon. The deuteron form factors G_i are given in terms of a product of the isoscalar nucleon form factors and the integral of the S- and D-state wave functions [1]:

$$G_C(Q) \;=\; 2G_E^S(Q)C_E(Q), \tag{2.35}$$

$$G_Q(Q) \;=\; 2G_E^S(Q)C_Q(Q), \tag{2.36}$$

$$G_M(Q) \;=\; (M_d/M_p)(2G_M^S(Q)C_S(Q) + G_E^S(Q)C_L(Q)), \tag{2.37}$$

where G_E^S and G_M^S are the isoscalar electric and magnetic nucleon form factors respectively. In terms of the proton electric and the magnetic form factors (G_E^p and

G_M^p) and the neutron electric and the magnetic form factors (G_E^n and G_M^n), G_E^S and G_M^S are given by:

$$G_E^S(Q) = \frac{1}{2}(G_E^p(Q) + G_E^n(Q)), \tag{2.38}$$

$$G_M^S(Q) = \frac{1}{2}(G_M^p(Q) + G_M^n(Q)). \tag{2.39}$$

The structure functions $C_i(Q)$ are expressed by integrals of the deuteron S-state and D-state radial wave functions $u(r)$ and $\omega(r)$ respectively, which describe the distribution of the neutron and proton point currents:

$$C_E = \int_0^\infty [u^2(r) + w^2(r)]j_0(k)dr, \tag{2.40}$$

$$C_Q = \frac{3}{\sqrt{2}\eta}\int_0^\infty w(r)\left[u(r) - \frac{1}{\sqrt{8}}w(r)\right]j_2(k)dr, \tag{2.41}$$

$$C_S = \int_0^\infty \{[u^2(r) - \frac{1}{2}w^2(r)]j_0(k) + \frac{1}{2}w(r)[\sqrt{2}u(r) + w(r)]j_2(k)\}dr, \tag{2.42}$$

$$C_L = \frac{3}{2}\int_0^\infty w^2(r)[j_0(k) + j_2(k)]dr, \tag{2.43}$$

$$k = \frac{1}{2}Qr, \tag{2.44}$$

where $j_0(k)$ and $j_2(k)$ are the spherical Bessel functions.

Many calculations of the DEFF within the NRIA framework using different NN potentials and various parametrizations of the nucleon form factors have been published. Several recent and typical NRIA calculations will be described in this section. The authors used "realistic" modern potentials in their calculations: Paris in Ref. [1], Argonne v_{14} in Ref. [42], Argonne v_{18} in Ref. [4], Paris and various versions of Bonn potential in Ref. [43]. In addition, various relativistic corrections, MEC contributions and the effects of different parametrizations for the nucleon electromagnetic form factors were included in the calculations of the DEFF to study their importance at high momentum transfers.

1. Mosconi and Ricci Calculation

Mosconi and Ricci [1] performed the DEFF calculation using the Paris potential [44] with relativistic nucleonic and mesonic corrections. They used four different parametrizations of nucleon electromagnetic form factors G_E^n: Iachello, Jackson and Lande (IJL) [45]; IJL with the G_E^n taken from that of Galster *et al.*. (IJLG) [46]; Höhler (H) *et al.* [47]; Gari and Krümpelmann (GK) [48, 49]. The relativistic corrections (RC) in their calculations include:

1. One-body relativistic corrections due to the Darwin-Foldy and spin-orbit contributions, to the order of $O(1/M^2)$ for the charge operator and to the order of $O(1/M^3)$ for the current operator.

2. One-body corrections from the relativistic modifications of the wave functions due to the nuclear motion (NM).

3. Pionic contributions to the charge density operator to the order of $O(1/M^3)$.

4. Two-body corrections due to the ρ-exchange processes to the order of $O(1/M^3)$ for the charge operator, and to the oder of $O(1/M^2)$ for the current operator.

5. Two-body corrections due to $\rho\pi\gamma$ MEC.

The hadronic form factors in the conventional monopole form were inserted at the meson-nucleon vertices

$$F_{\alpha N} = \frac{\Lambda_\alpha^2 - m_\alpha^2}{\Lambda_\alpha^2 + k^2}, \tag{2.45}$$

where $\alpha = \pi, \rho$. They used the cutoff masses: $\Lambda_\pi = 1$ GeV and $\Lambda_\rho = 1.5$ GeV. The coupling constants for the ρ and $\rho\pi\gamma$ MEC's they used were: $k_\rho = 6.6$, $g_{\rho N}^2/4\pi = 0.55$, and $g_{\rho\pi\gamma} = 0.4$.

Among the four parametrizations, the results for $A(Q)$ calculated by Mosconi and Ricci using the H parametrization give the best agreement with the $A(Q)$ data. Both the full calculations (IA+RC+MEC) and those without ρ and $\rho\pi\gamma$ MEC's using the H parametrization overestimate the experimental $A(q)$ for 5 fm^{-2} < Q^2 < 15 fm^{-2}.

2. Schiavilla and Riska Calculation

Schiavilla and Riska [42] calculated the DEFF using the Argonne v_{14} potential [3]. The parametrizations for the nucleon form factors they used are: the IJL, the H, the GK and a dipole form D with G_E^n given by

$$G_E^n(Q) = -\mu_n \frac{Q^2}{4m_N^2} \frac{1}{1 + Q^2/m_N^2} G_E^p(Q), \tag{2.46}$$

where $\mu_n = -1.913$, and m_N is the mass of nucleon.

In this calculation, the exchange-current operator was separated into a "model-independent" term and a purely transverse "model-dependent" term. The "model-independent" term corresponds to the spin-orbit, quadratic spin-orbit and L^2 components of the potential. The "model-dependent" term is unconstrained by the NN interaction and included the pion-exchange-current, ρ-meson-exchange-current, the $\rho\pi\gamma$ and the $\omega\pi\gamma$ exchange-current operators. The authors investigated the sensitivity to the cutoff parameters. The cutoff masses in the monopole form factor inserted at the meson-nucleon vertices are $\Lambda_\pi = 1.2$ GeV, and $\Lambda_\rho = \Lambda_\omega = 2$ GeV. The $\rho\pi\gamma$ and $\omega\pi\gamma$ coupling constants used are $g_{\rho\pi\gamma} = 0.56$, and $g_{\omega\pi\gamma} = 0.63$.

The most important charge-exchange operators are model dependent and are viewed as relativistic corrections. Charge-exchange operators due to π, ρ, ω MEC's and due to the charge component of the $\rho\pi\gamma$ process, were taken into account. The value 14.6 was used for g_ω, the ωNN coupling constant. The Darwin-Foldy and the spin-orbit relativistic corrections to the nucleon charge operator were also included in the calculations.

At the meson-nucleon vertices for the $\rho\pi\gamma$ and ω-meson exchange-charge operators, a hadronic monopole form factor was inserted with $\Lambda_\pi = 1.2$ GeV and $\Lambda_\rho = \Lambda_\omega = 2$ GeV to take into account the structure of the nucleon. For the pion and ρ-meson charge-exchange operators, their propagators were not multiplied by hadronic vertex form factors. Instead, to reduce the model dependence of those charge-exchange

operators, their bare propagators were replaced by generalized meson propagators constructed from the Fourier transforms of the isospin dependent spin-spin and tensor components of the NN potential.

For $A(Q)$, their full calculation (IA+MEC) gives better agreement than the IA calculation. The difference of the results of $A(Q)$ using various nucleon form factor parametrizations is large for $Q^2 > 20$ fm^{-2}. For $B(Q)$, both IA and the full calculation describe the data well up to $Q^2 = 40$ fm^{-2}. Above $Q^2 = 40$ fm^{-2}, the full calculation overestimates the data while the IA result underestimates them. The calculations using the H, IJL, GK, and D form factor parametrizations give similar results for $B(Q)$. The sensitivity of the $B(Q)$ results to different cutoff masses was also studied and it was found that the cutoff masses $\Lambda_\pi = 0.9$ GeV and $\Lambda_\rho = 1.5$ GeV give a reasonably good fit to the data.

3. Wiringa, Stoks and Schiavilla Calculation

Wiringa, Stoks and Schiavilla [4] calculated the DEFF using the Argonne v_{18} potential, which is an updated version of the Argonne v_{14} potential. The Argonne v_{18} potential was obtained by writing the strong interaction potential in an operator that depends on the values of S, T and T_z of the NN pair. Then the potential was projected into a charge-independent part with 14 operator components (as in the older Argonne v_{14} potential) and a charge-independent breaking part with three charge-dependent and one charge-asymmetric operators. A complete electromagnetic potential, containing Coulomb, Darwin- Foldy, vacuum polarization, and magnetic moment terms with finite-size effects, was also included in this potential. This potential gives an excellent fit to pp, np, low-energy nn scattering data and the deuteron binding energy. The authors used the isoscalar electromagnetic current operators in Schiavilla and Riska Calculation [42]. In addition, they considered the two-body charge and current operators associated with the $\rho\pi\gamma$ mechanism. The H parametrization was used for the nucleon form factor and an ω-pole term form factor was included at the

$\rho\pi\gamma$ electromagnetic vertex. The predicted results for $A(Q)$ including the relativistic corrections and MEC's are in good agreement with the experimental data. For $B(q)$, their results overestimate the experimental data in the momentum transfer range 10-45 fm^{-2}. They indicated that the contributions due to the spin-orbit and quadratic spin-orbit components of the interaction are of opposite sign and the cancellation between them is not enough to describe the data. The contribution from the $\rho\pi\gamma$ current is small for the momentum transfer range considered in their calculation.

4. **Pauschenwein, Plessas and Mathelitsch Calculation**

Calculations of the DEFF have also been performed by Pauschenwein, Plessas and Mathelitsch [43] using the Paris potential, various versions of the Bonn potential: Bonn OBEPR, Bonn OBEPQ and full Bonn in Ref. [2] and folded-diagram full Bonn in Ref. [50]. Bonn OBEPR and Bonn OBEPQ potentials are energy independent while full Bonn potential contains an explicit energy dependence. The energy dependence is removed by folded-diagram technique in the folded-diagram full Bonn potential. The authors included relativistic corrections (Darwin-Foldy, spin orbit and nuclear motion) as well as MEC's (π pair, π retardation and $\rho\pi\gamma$ with $g_{\rho\pi\gamma} = 0.578$) in their calculations. For the DEFF calculations using the Bonn potentials, the hadronic vertices for the MEC's were treated consistently with the underlying potentials. They used the Dirac form factors and the H parametrization of the nucleon form factors.

The results of $A(Q)$ and $B(Q)$ in their calculation agree with each other and with the data for $Q < 4$ fm^{-1}. For $Q > 5$ fm^{-1}, the prediction of $A(Q)$ using the full Bonn potential give the best agreement to the data while the predictions for $B(Q)$ disagree with the data for $Q > 5$ fm^{-1}.

2.4.2   Relativistic Models

At high momentum transfer, the usual non-relativistic description of the nucleus is no longer reliable, and it is necessary to develop relativistically covariant models of

the nuclear system in the DEFF calculation. According to the choice of the kinematic four-momentum variable, relativistic models can be summarized in two approaches: instant form and front form [5]. The instant form relativistic calculations are based on the relativistic Bethe-Salpeter equation (BSE). The front form approach, light-front quantum mechanics (LFQM), is a form of relativistic Hamiltonian quantum dynamics applied to systems with a fixed number of particles.

1. **Instant Form Calculations**

Several authors have developed DEFF calculations in the instant form type. Gross [6] originated the relativistic-impulse approximation (RIA) formalism. Starting from relativistic BSE, he assumed that the spectator nucleon is on the mass shell and the interacting nucleon is off shell. In his calculation, relativistic corrections were calculated perturbatively. The nucleon current was expanded to order $O(1/M^2)$ and the effect of the deuteron motion on the deuteron wave function was calculated relativistically to order $O(1/M^2)$ (where M is the nucleon mass). Friar [51] performed the DEFF calcultaion relativistically with a different method and obtained the Darwin-Foldy, the spin-orbit terms, together with the terms due to nucleon motion. The correction terms due to the NN interaction were not included in his derivation as they were in the Gross calculation. Coester and Ostebee [52] derived the relativistic corrections based on the Lorentz covariance of the four vector charge-current density operators. In their calculation, the potential is local and the correction due to the NN potential is the largest correction. Their results are close to those of Gross. In the DEFF calculations, some relativistic effects were already included in MEC corrections as illustrated by Gross [53]. The relativistic correction due to the NN potential was interpreted in his calculation as a sum of the contributions from the pair and retardation currents.

Arnold, Carlson, and Gross [54, 55] extended the original RIA formalism without making non-relativistic approximations or Q^2/M^2 expansion. They retained terms

to all orders in $(v/c)^2$ or Q^2/M^2. They assumed that at least one nucleon is off the mass shell while the spectator nucleon is on shell. To describe the deuteron-nucleon-nucleon vertex function, four invariants or scalar functions were rewritten to have the character of wave functions and corresponded to the $S-$, $D-$, $^1P-$, and $^3P-$ state wave functions. The authors used the relativistic wave functions from a relativistic one boson exchange model with π, σ, ρ, and ω exchanges [6]. The π-NN vertex is a mixture of γ^5 and $\gamma^5\gamma_\mu$ couplings, with the mixing parameter λ defined such that the coupling is independent of λ when both nucleons are on shell, and is pure γ^5 when $\lambda = 1$ and pure $\gamma^5\gamma^\mu$ when $\lambda = 0$. The P-state wave function turned out to increase nearly linearly with λ.

The $A(Q)$ and $B(Q)$ structure functions from Arnold, Carlson, and Gross's calculations using the Reid soft core (RSC) potential [23] and the dipole nucleon form factors for different values of λ were compared with the experimental data. The results for $A(Q)$ are below the experimental results and are reduced by a factor of 2 to 5 at Q^2 of $100\,\mathrm{fm}^{-2}$ over those for the nonrelativistic approximation. The predictions of $B(Q)$ shift the position of the minimum to lower four-momentum transfers. The authors indicated that the discrepancy between their predictions and the data could be removed by adding $\rho\pi\gamma$ MEC and isobar effects which were not included in the calculation. The G_E^n, not well known, is another factor that could cause a discrepancy between the prediction and the data.

Zuilhof and Tjon [56, 57, 58] demonstrated the importance of treating relativistic effects and MEC's within a consistent framework. They used the Bethe-Salpeter equation in the ladder approximation using one-boson-exchange (OBE) model to generate the NN interaction. Their results for $A(Q)$ and $B(Q)$ are similar to those obtained by Arnold, Carlson, and Gross [55].

Hummel and Tjon [59, 60] performed the calculation of $\rho\pi\gamma$ and $\omega\sigma\gamma$ MEC contributions to the deuteron form factors in a relativistic quasipotential OBE model.

Their calculation is consistent with the NN dynamics. It was shown that the recoil correction could not be neglected at high momentum transfer. In the analysis of the $\rho\pi\gamma$ and $\omega\sigma\gamma$ MEC's, they used a relativistic OBE model with the six mesons: π, ρ, ω, σ, η , and δ. The matrix elements of the MEC operators were calculated in a quasipotential approximation using the prescription of Blankenbecler and Sugar [61] and Logunov and Tavkhelidze [62]. Boost effects and contributions from negative energy states were studied and were found to be small. The $\rho\pi\gamma$ calculation included the negative energy state contributions and the boost effects while the $\omega\sigma\gamma$ graph was evaluated without them (or called in a static approximation).

The hadronic form factors of the monopole form were used at the meson-nucleon vertices:

$$F_\alpha(k) = \frac{\Lambda^2}{\Lambda^2 - k^2}, \qquad (2.47)$$

where α represents one of the six mesons mentioned above and k is the momentum of the meson. The cutoff mass, $\Lambda^2 = 1.5M_N^2$, was used, where M_N is the nucleon mass. The coupling constant, $g_{\rho\pi\gamma} = 0.56$, and electromagnetic form factors derived from vector-meson dominance model were used for the $\rho\pi\gamma$ vertex. The authors used $g_{\omega\pi\gamma} = -g_{\rho\pi\gamma} = -0.56$ for the calculation of the $\omega\pi\gamma$ process.

Hummel and Tjon used H and GK parametrizations of the nucleon form factors in their DEFF calculation. For $A(Q)$, the $\rho\pi\gamma$ MEC is the largest contribution which is partially cancelled by the contribution from the $\omega\sigma\gamma$ MEC. For $B(Q)$, the effect of the $\rho\pi\gamma$ is negligible up to $Q^2 = 40$ fm^{-2}. The contribution from the $\omega\sigma\gamma$ MEC shifts the minimum of $B(Q)$ to higher momentum transfer. The predictions are insensible to the H and GK parametrizations up to $Q^2 = 45$ fm^{-2}, but the prediction for $B(Q)$ using the H parametrization falls below that using the GK parametrization for $Q^2 > 45$ fm^{-2}. The authors also indicated that their calculations are sensitive to the $\omega\sigma\gamma$ coupling constant.

2. Light Front Calculations

The light-front quantum mechanics (LFQM, or also called light-cone quantum mechanics), as mentioned before, is another approach to perform a relativistically covariant calculation of the DEFF. Several authors have calculated the DEFF with the LFQM formalism.

Chung, Coester, Keister, and Polyzou [5] have calculated the DEFF using the light-front dynamics. They used six different potential models for the deuteron wave function: Reid soft core; Argonne v_{14}; Paris; and three Bonn potentials: Bonn OBEPR, Bonn OBEPQ, and full Bonn. They used four different parametrizations of the nucleon form factors: GK, H, Lomon [28], and Dipole. The prediction of $A(Q)$ exhibits significant difference for different potential models and different parametrizations for $Q^2 > 2$ GeV^2. The calculated $A(Q)$ with the Paris or the Argonne v_{14} potential and the GK parametrization is in good agreement with the data. The calculation for $B(Q)$ using the Argonne v_{14} and the GK parametrization gives the closest agreement with the data.

Carbonell, Desplanques, Karmanov, and Mathiot [65] also performed the DEFF calculation using light-front dynamics with the following light-front equation:

$$[4(q^2 + m^2) - M^2]\Psi(\vec{q}, \hat{n}) = -\frac{m^2}{2\pi^3} \int \frac{d^3q'}{\epsilon(q')} \hat{V}(\vec{q'}, \vec{q}, \hat{n}, M^2)\Psi(\vec{q'}, \hat{n}) \qquad (2.48)$$

where $\hat{V}$ is the interaction kernel. They solved the light-front equation perturbatively with the Bonn OBEP potential. The deuteron wave function in their calculation was written as:

$$\begin{aligned}
\Psi(\vec{q}, \vec{n}) &= \frac{1}{\sqrt{2}} f_1\vec{\sigma} + \frac{1}{2}f_2[3\hat{q}(\hat{q}.\vec{\sigma}) - \vec{\sigma}] + \frac{1}{2}f_3[3\vec{n}(\vec{n}.\vec{\sigma}) - \vec{\sigma}] \\
&\quad + \frac{1}{2}f_4[3\hat{q}(\vec{n}.\vec{\sigma}) + 3\vec{n}(\hat{q}.\vec{\sigma}) - 2(\hat{q}.\vec{n})\vec{\sigma}] \\
&\quad + i\sqrt{\frac{3}{2}} f_5(\hat{q} \times \vec{n}) + \frac{\sqrt{3}}{2} f_6[(\hat{q} \times \vec{n}) \times \vec{\sigma}],
\end{aligned} \qquad (2.49)$$

where f_{1-6} are scalar functions, $\vec{n}$ is the unit vector for the spatial direction of the light front, $\vec{q}$ is the relative momentum, and $\vec{\sigma}$ is the Pauli matrix. At the non-relativistic limit, where $f_1 \rightarrow +u_S$, $f_2 \rightarrow -u_D$, and $f_{3-6} \rightarrow 0$, the wave function becomes:

$$\Psi(\vec{q}) \rightarrow \frac{u_S}{\sqrt{2}}\vec{\sigma} - \frac{u_D}{2}[3\hat{q}(\hat{q}.\vec{\sigma}) - \vec{\sigma}] \tag{2.50}$$

They took into account the sum over the six mesons that contribute to the Bonn potential for the contact interaction NNM_γ, where $M = \pi$, ρ, ω, σ, η, and δ. To study the influence of relativistic effects on the structure of the deuteron, the authors first calculated the DEFF in the non-relativistic impulse approximation with the S- and D-waves of the Bonn-QA wave function [2]. In the light-front formalism, they performed the calculations in three approximations: one with the relativistic deuteron components f_1 and f_2 only, one with the addition of component f_5, and one including a contact term together with the above three components. Their prediction for $B(Q^2)$ is more sensitive to the different approximations and contributions than that for $A(Q^2)$. The relativistic deuteron component f_5 has important influence in the DEFF calculations. The minimum of $B(Q^2)$ in their calculation is the consequence of the f_5 component.

3. Relativistic One Boson Exchange Model

Van Orden, Devine, and Gross [66] presented a third approach to the relativistically covariant calculation of the DEFF based on field theory. They calculated the DEFF in the context of a one-boson-exchange model using the Gross or spectator equation [67]. The formalism is manifestly covariant and gauge invariant. Some effects of the underlying quark-gluon structure of nucleons and mesons were included through the introduction of phenomenological form factors. The form factors were simplified in a factorable form [68, 69]

$$F(p'^2, p^2, l^2) = h(p'^2)h(p^2)f(l^2) \tag{2.51}$$

where p and p' are the initial and final nucleon four-momenta, $l = p - p'$ is the meson four-momentum, and the $f(l^2)$ and $h(p^2)$ are meson and nucleon form factors, respectively. The interaction model they used was a one-boson-exchange kernel containing six mesons: π, η, σ, σ_1, ω, and ρ. Four wave functions were used for the deuteron: the usual S and D wave functions and the singlet and triplet P wave functions of relativistic origin.

The Feynman diagrams for the Gross current matrix element the authors used in their calculation are displayed in Figure 1 in Ref. [66]. Diagrams (a)-(c) are related to relativistic impulse approximation. The combination of them represents a complete gauge invariant description of the Gross one-body current matrix elements. This description is called the complete impulse approximation (CIA). They included the contribution of the $\rho\pi\gamma$ MEC in the calculation of the DEFF using three different form factors: the VMD (vector dominance model) form factors, the quark model form factors by Gross and Ito [70] and by Mitchell and Tandy [71]. The $\rho\pi\gamma$ MEC increases $A(Q^2)$ and moves the minimum of $B(Q^2)$. For both $A(Q^2)$ and $B(Q^2)$, the VMD form factors give large effects, while the softer quark model form factors give smaller effects.

2.4.3 Coupled-Channel Models

In addition to MEC's and relativistic corrections, non-nucleonic degrees of freedom, such as isobar components or even possibly quark effects, are expected to become important at high Q^2. The approach which includes isobar components in the deuteron wave functions is called coupled-channel (CC) model.

Sitarski, Blunden and Lomon [72] calculated the DEFF using coupled-channel formalism of nucleons and isobar components. In addition to the $NN(^3S_1,^3D_1)$ components, the $\Delta\Delta(^3S_1,^3D_1,^7D_1)$ and the $NN^*(^3S_1)$ components were included in their calculation. For the NN interaction, the Feshbach-Lomon (FL) potential [73], which

includes exchanges of π, 2π, η, ρ and ω mesons, was used. The parameters for the FL potential were fitted to the NN scattering data for $T_{lab} \leq 1$ GeV. They imposed a homogeneous condition at r_0, within which the hadronic components of the deuteron wave function vanish. Two boundary condition radii, $r_0^{FL} = 0.74$ fm and $r_o^{CBM} = 1.05$ fm, were obtained by fitting the NN scattering data using FL potential and a cloudy bag model (CBM) separately. They presented six different models:A, B, C, D, E, and F. Each model is characterized with a combination of the boundary condition radius (r_0^{FL} or r_0^{CBM}), isobar channels coupling to the NN channel and the distributions of probabilities among the isobar components. The contributions of the NN and the isobar channels to the DEFF were calculated in the impulse approximation (IA). Three sets of nucleon form factor parametrizations were used, the H parametrization, the GK parametrization and a third one which is a mixture of different parametrizations: IJL for G_E^p and G_M^p, Bartel parametrization [74] for G_M^n, and Galster parametrization [46] for G_E^n. The form factors for the Δ and N^* were assumed to have the same form as those for nucleons with a scaling factor. The MEC contributions from the pair currents (π, ρ and ω) and $\rho\pi\gamma$ were added to the IA results. Hadronic form factors with the monopole form as shown in Eq. 2.47, were inserted at the meson-nucleon vertices with $\Lambda_\pi = 1.0$ GeV and $\Lambda_\rho = \Lambda_\omega = 1.44$ GeV. They used coupling constants, $g_{\rho\pi\gamma} = 0.406$ and 0.56 separately in the calculations to study the contribution of $\rho\pi\gamma$.

Model C and D give a reasonably good description of the data for the $A(Q)$ and $B(Q)$ structure functions. The channels in these two models are $NN({}^3S_1, {}^3D_1)$ and $\Delta\Delta({}^3S_1, {}^3D_1, {}^7D_1)$ with the $\Delta\Delta$ probabilities of 1.76% and 7.20% for model C and model D respectively. The H parametrization gives the best agreement with the data for $A(Q)$, while the GK parametrization provides the best agreement with the data for $B(Q)$.

2.4.4 Other Models for High Momentum Transfers

For electron scattering at high momentum transfers, it may be necessary to take into account the quark-gluon degrees of freedom in the calculation of the DEFF. One approach is the quark-hadron hybrid model. The quark configurations were considered in a quark cluster model or a quark compound bag model. Another approach to calculate the DEFF is the Skyrme model, which describes baryons as topological solitons of a self-interacting meson field. Finally, Perturbative QCD (PQCD) predicts the DEFF at sufficiently high momentum transfers and obtained the simple relation between G_C and G_Q and the value of the t_{20}:

$$\lim_{Q^2 \to \infty} G_C = \frac{2}{3}\eta G_Q, \tag{2.52}$$

$$\lim_{Q^2 \to \infty} t_{20} = -\sqrt{2}. \tag{2.53}$$

Detailed descriptions of these models involving high momentum transfer can be found in Ref. [38].

Chapter 3

Survey of Previous Experiments

As mentioned before, deuteron structure functions $A(Q)$ and $B(Q)$ obtained from the Rosenbluth separation of the elastic e-d cross section can not separate the charge form factor G_C and the quadrupole form factor G_Q of the deuteron. A third obervable is necessary to separate G_C and G_Q. To achieve this goal, tensor polarization observables were measured in several previous experiments mainly using two different techniques: one method was to extract the analyzing power T_{2j} from asymmetries in elastic scattering of unpolarized electrons from a polarized deuteron target; the other was to measure the tensor polarization t_{2j} of recoil deuterons from e-d elastic scattering with unpolarized electron beams. The analyzing power T_{20} has been measured for the four-momentum transfer Q up to 3.6 fm^{-1} in experiments at Novosibirsk [7, 8] and NIKHEF [9, 10]. The tensor polarization t_{20} was measured up to 4.6 fm^{-1} for the four-momentum transfer at Bates [11, 12] Three recent experiments will be described briefly in this chapter.

3.1   Experiments at Novosibirsk

An internal-target technique was first used to measure the tensor analyzing power T_{20} in electron-deuteron elastic scattering in the experiment [8] performed at the 2-

GeV electron storage ring VEPP-3 in Novosibirsk. Electron bunches were circulated in the ring to form a 0.1–0.2 A current. The internal target was an aluminum tube (called a storage cell) with polarized deuterium atoms injected into it. The storage cell was coaxial with the electron beam in the ring and was installed in a straight section of the ring. The polarized deuterium atoms were provided from an atomic-beam source with tensor polarization p_{zz} close to unity. The total thickness of atoms in the cell was approximately 3×10^{12} cm^{-2} which was 15 times larger than the thickness of the atomic beam. The polarization of the atoms was aligned along one of the two directions which were perpendicular to the electron beam axis. The scattered electrons and recoil deuterons were detected in coincidence in four almost identical detector systems placed symmetrically around the electron-beam axis. The scattered electrons were detected with the scattering angle θ from 10° to 22° and azimuthal angle of a 40° range, while the deuterons were detected from 68° to 80° for the scattering angle. A six plane drift chamber in each system was used for the tracking information of the particles. Behind the electron drift chamber was a Pb converter followed by a 10 mm thick plastic scintillator. Three thin plastic scintillators were installed behind the deuteron drift chambers and were followed by thick plastic scintillator or a NaI counter. During the data taking, the sign of p_{zz} was reversed every 200 s.

The tensor analyzing power T_{20} was extracted from the asymmetries formed with four systems, two polarization directions, and two values of p_{zz} (see Ref. [8] for details). The target polarization p_{zz} was not measured absolutely. It was determined by normalizing the datum at the lowest value of Q to the theoretical value of T_{20} given by the Paris potential, thus inducing additional systematic error for the results. The value of p_{zz} was found to be 0.572 ± 0.053. The terms involving T_{21} and T_{22} were corrected by integrating the predictions of the Paris potential over the acceptance of the apparatus. The results of T_{20} in the four-momentum transfer range of 2–3 fm^{-1} were consistent with theoretical predictions. However, these predictions do not differ

significantly in this range of Q. To distinguish between theories, data with Q values larger than 3 fm^{-1} are necessaray.

3.2   Experiments at NIKHEF

The experiments on the absolute measurement of the tensor analyzing power T_{20} in elastic e-d scattering with four-momentum transfer from 1.8 to 3.2 fm^{-1} were performed at the Amsterdam Pulse Stretcher Ring at NIKHEF [10]. Unpolarized electrons of 704 Mev were scattered from a polarized deuterium internal target. The scattered electrons were detected in an electromagnetic calorimeter with 6 layers of CsI(Tl) crystals. The electron trigger was provided by two plastic scintillators. A pair of chambers was used to determine the trajectories of the scattered electrons. The central angle of the calorimeter was set at 45°. The recoil deuterons were detected in coincidence in a 16 layer plastic scintillator range telescope positioned at a central angle of 62.3°. The tracking information of the recoil deuterons was provided by two wire chambers.

The polarized deuterium was provided by an atomic beam source. The deuterium atoms with spin up electrons were focused by two sextupole magnets. Transitions between the hyperfine states were induced by RF units and resulted in a tensor polarization $P_{zz}^-(P_{zz}^+)$ with zero vector polarization. The atomic beam was fed into a T-shaped dwell cell with a temperature of 150 K. The integrated target density was 2×10^{13} atoms/cm^2. Two polarimeters, a Breit-Rabi polarimeter and an ion-extraction system, were used to measure the polarization of the deuterium atoms. The effective target polarization was found to be $\Delta P_{zz} = P_{zz}^+ - P_{zz}^- = 1.175 \pm 0.057$.

To extract the tensor analyzing power, an asymmetry A_d^T was formed using the expression

$$A_d^T = \sqrt{2}\frac{N^+ - N^-}{P_{zz}^+ N^- - P_{zz}^- N^+}, \qquad (3.1)$$

where N^+ (N^-) is the number of the events when the target polarization was positive (negative) (see Ref. [10] for details).

It was claimed in Ref. [10] that the non-relativistic calculation of Ref. [4] gave the best description of their results and the meson exchange currents was important to describe the data.

3.3 Experiments at Bates

Two experiments [11, 12] using the polarimeter technique were carried out at MIT-Bates to measure the tensor polarization t_{20} of the recoil deuterons in elastic e-d scattering. The recent one [12] is described in this section. It was the first experiment to measure the tensor polarization of deuteron at a high momentum transfer range of 3 fm^{-1} < Q < 6 fm^{-1}, where the theoretical predictions vary significantly and the charge form factor G_C of the deuteron was expected to pass zero. The short-distance structure of the deuteron and non-nucleonic degrees of freedom are expected to be significant at this Q range.

The electron beam, provided by the MIT-Bates Linear Accelerator Center with energies of 653, 755, and 853 MeV, was incident on a 7 cm long liquid deuterium target. The scattered electrons were detected in the OHIPS spectrometer. The recoil deuterons were selected in coincidence in a specially designed magnetic channel, fixed at an angle of 41°. The deuteron channel consists of a QQD section, an intermediate focus detector (IFD) used for tuning, and a QQQD section. The polarimeter AHEAD, based on d-p elastic scattering [82], was installed at the end of the channel. The trajectories of the deuterons were determined by two MWPC's. Two scintillators provided the trigger information. The deuterons were incident on a 27 cm long liquid hydrogen (LH$_2$) target where the elastic d-p scattering took place. The asymmetry of the scattered particles from the second scattering was measured with two cylindrical wire chambers (CWC's), which were installed concentrically around the LH$_2$ target.

An array of six ΔE and eighteen E plastic scintillators were placed outside of the CWC's to identify the particles through their energy loss.

The polarimeter AHEAD was calibrated at the Laboratoire National Saturne with a deuteron beam of known polarization. The analyzing powers and the yield for the scattering of unpolarized deuterons was measured for the deuteron energies of 120, 145, and 170 MeV. The calibration results were interpolated for the deuteron energies used in the tensor polarization measurement at Bates. With the interpolated unpolarized yield and the analyzing powers, the tensor polarization components t_{20}, t_{21}, and t_{22} were extracted from the asymmetry in θ and ϕ of the d-p elastic scattering. The deuteron charge form factor G_C and quadrupole form factor G_Q were separated with their measurements of t_{20} and the world data for the A and B structure functions. The results were compared with various theoretical predictions. The data unambiguously showed a sharp rise of t_{20} from a minimum towards less negative values. The first node of G_C was determined to be at $Q = 4.39 \pm 0.16$ fm^{-1}.

Chapter 4

CEBAF Experiment

4.1 Introduction

The present experiment to measure the tensor polarization of the deuteron in elastic electron deuteron scattering was performed in Hall C at the Thomas Jefferson National Accelerator Facility (TJNAF, previously named CEBAF) from April to September in 1997. During the running of this experiment, CEBAF provided high current, continous wave (CW) unpolarized electron beams with the energies up to 4 GeV and currents up to 120 μA. The high energy and high current beam made it possible to extend the tensor polarization measurement of the deuteron to higher four-momentum transfer regions with good precision.

The experimental arrangement is illustrated in Figure 4-1. The apparatus mainly consists of the following pieces: High Momentum Spectrometer (HMS), high power liquid deuterium (LD2) target, deuteron transport channel, and polarimeter (POLDER).

This experiment was a coincidence, double scattering experiment. The electron beam was incident on the deuterium scattering target. The scattered electrons were detected by the High Momentum Spectrometer (HMS) between the angles of 20.3° and 35.8°. A specially designed magnetic channel was used to detect the recoil deuterons
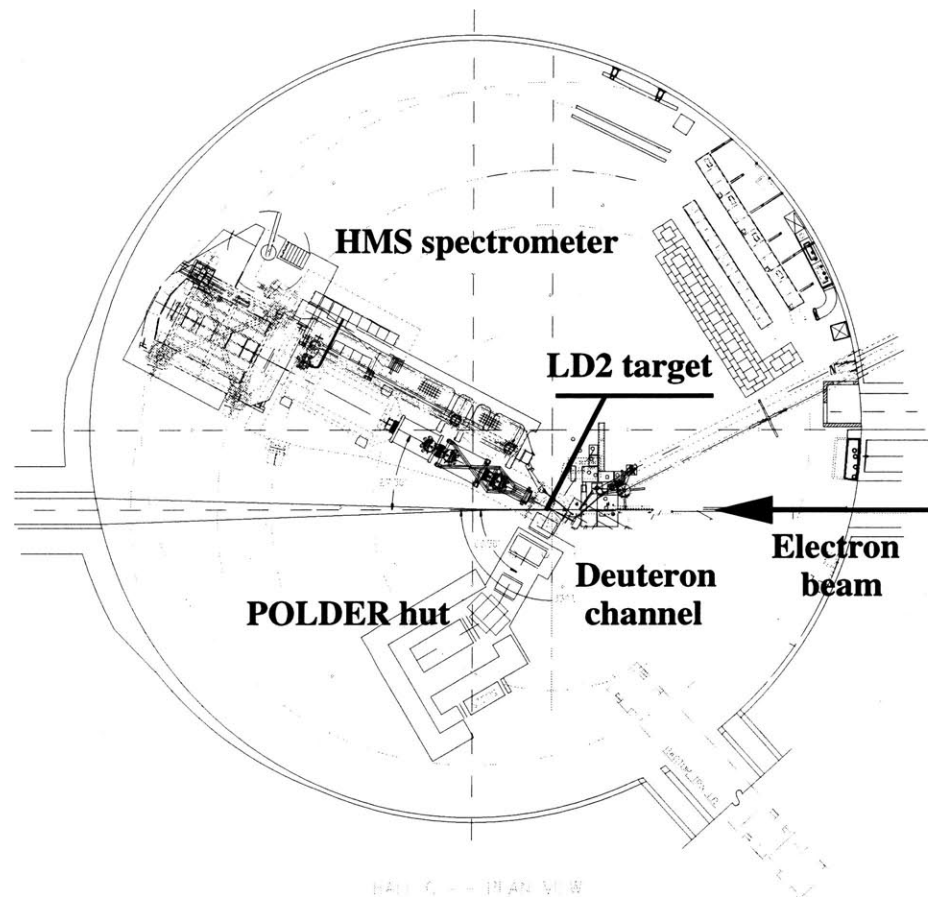
Figure 4-1: The plan view of the experimental setup in Hall C. Figure taken from Ref. [89].

in coincidence with the electrons and was fixed at 60°. The angle of the HMS varied with different beam energies to achieve six four-momentum transfers. The kinematics for the six points measured in this experiment are shown in Table 4.1. The polarization of the recoil deuterons was measured in the polarimeter POLDER, using the ^{1}H($\vec{d}$,2p)n reaction. The angular distribution of the protons coming from this reaction was measured in POLDER and compared to the angular distribution when unpolarized deuterons were used for the second scattering. The tensor polarization of the recoil deuterons was extracted from this comparison. In the following sections,

the accelerator and beamline, the liquid deuterium target, the deuteron channel and the spectrometers used in this experiment will be explained separately.

Kinematics	E_{beam} (GeV)	θ_e (degree)	Q (fm^{-1})	$\overline{T_d}$ (MeV)
1	1.412	35.83	4.10	174.5
2	1.646	33.60	4.46	206.5
3	2.098	29.93	5.08	268.1
4	2.447	27.62	5.48	311.7
5	3.251	23.36	6.23	402.9
6	4.046	20.33	6.65	459.0

Table 4.1: Kinematics of the six points measured in this experiment. The quantities displayed are: electron beam energy E_{beam}, electron scattering angle θ_e, four-momentum transfer Q, and mean value of the energy of the recoil deuterons $\overline{T_d}$.

4.2   Accelerator
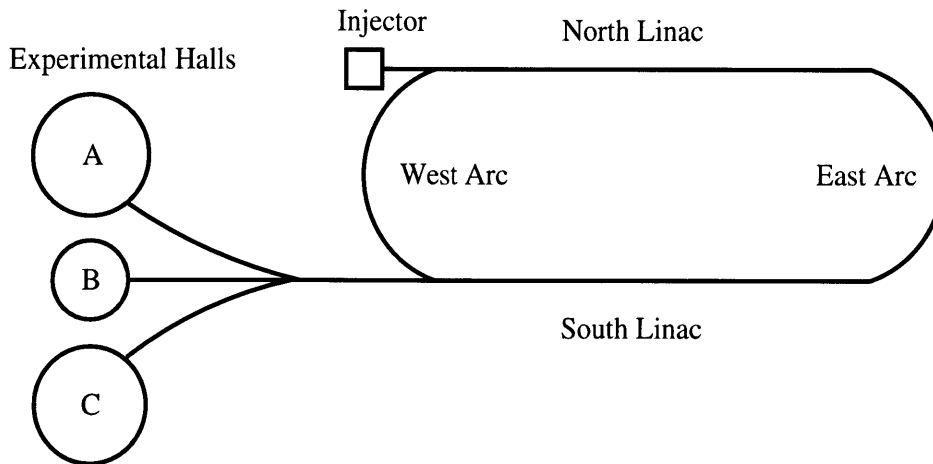
Figure 4-2: Schematic of CEBAF accelerator

A schematic of the accelerator at CEBAF is shown in Figure 4-2. The electron beam is first accelerated by an injector to an energy of 45 MeV, then sent to the

superconducting linacs (South Linac and North Linac) and arcs (East Arc and West Arc) for circulations. The beam is accelerated an additional energy of 400 MeV by superconducting radio frequency cavities in each linac and is deflected 180° in each arc. In one complete circuit, the beam gains an energy of 845 MeV. After the beam passes through the South Linac, it can be extracted to the three experimental halls, or it can be sent through the west arc for additional acceleration in the linacs. The electron beam can be recirculated through the system up to 5 times and delivered to the three experimental halls (hall A, B and C) independently and simultaneously after each pass. The available beam energies were 0.845, 1.645, 2.445, 3.245 and 4.045 GeV. In addition, the linacs can be set to provide energies less than 800 MeV to provide different beam energies than the above values. The characteristics of the beam at CEBAF at the time of this experiment is illustrated in Table 4.2.

Maximum energy	4.045 GeV
Duty cycle	100%, CW
Emittance	2×10^{-9} m
Energy spread (4σ)	10^{-4}
Maximum intensity	200 μA
Vertical size (4σ)	100 μm
Horizontal size (4σ)	500 μm

Table 4.2: Characteristics of the beam at CEBAF at the time of this experiment.

In this experiment, data were taken at six beam energies of 1.411, 1.646, 2.098, 2.447, 3.251 and 4.046 GeV, corresponding to six values of four-momentum transfer of 4.10, 4.46, 5.08, 5.48, 6.23 and 6.65 fm^{-1}.

4.3 Hall C Beamline

The control and measurement equipment used in the Hall C beamline execute these

functions:

- 1. Determination of the beam energy

- 2. Control of beam position, emittance and energy stability

- 3. Determination of the beam current, total charge and luminosity
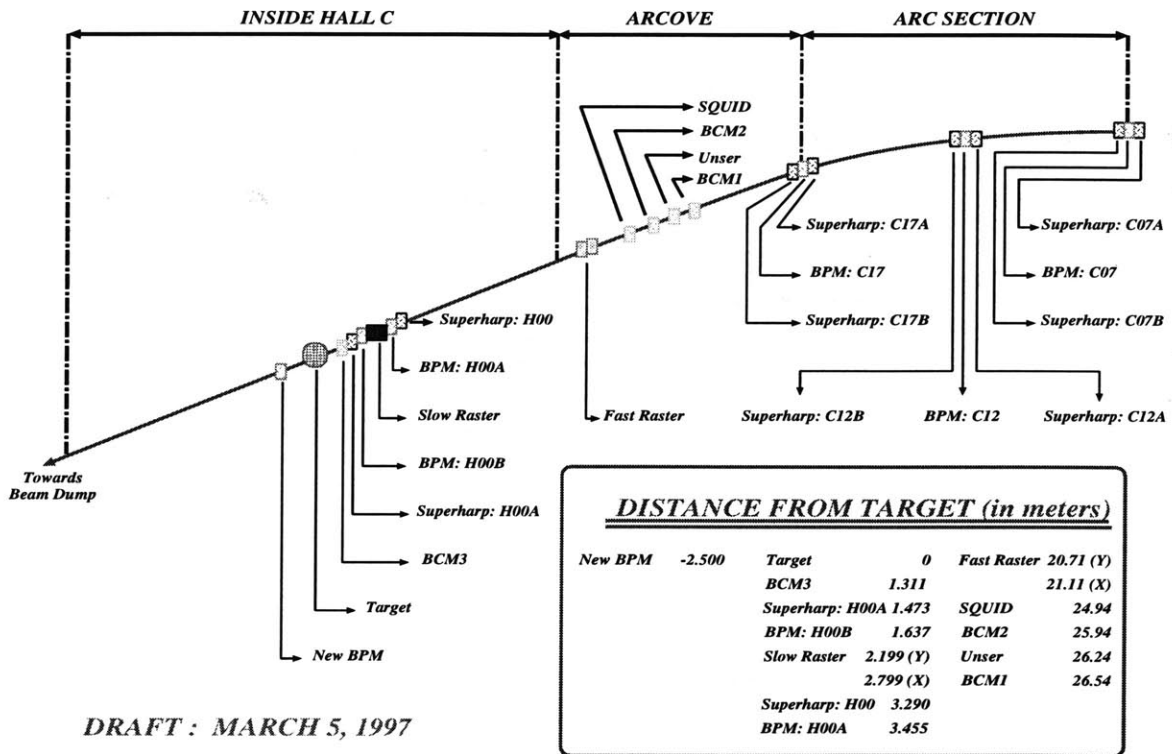
Figure 4-3: Instrumentation in the Hall C beam line

The equipment in the beamline include various magnets (dipoles, quadrupoles, sextupoles, beam corrector) to focus and steer the beam, and beam diagnostic devices (BPM, harp, BCM) to measure the energy, position and profile of the beam. Figure 4-3 illustrates the instrumentation in the Hall C beam line, which is described in the next sections.

4.3.1 Beam Position Measurement

The position of the beam in Hall C was monitored with five beam position monitors (BPM). Before the target, two BPMs (H00A and H00B) were used to measure the position and the direction of the beam incident on the target. The beam position on the target in the horizontal and vertical directions was stable within ± 1.25 mm, and the angles stable with ± 0.5 mrad. Detailed descriptions of the BPMs can be found in Ref. [83].

4.3.2 Beam Current Measurement

The beam current to Hall C was measured by three RF cavity beam current monitors BCM1, BCM2 and BCM3. They provided very good relative measurement of currents by measuring the power of the RF radiation coupled in the cavity. An Unser current monitor was also used to measure the absolute current. The three BCMs were periodically calibrated absolutely using an Unser current monitor. Detailed description of these devices are in Ref. [84].

4.3.3 Superharp System

The superharp system was used as the standard beam profile monitor and as a reference for BPM calibration. The schematic of the superharp system is shown in Figure 4-4. A superharp consists of a fork with three wires, two vertical wires that measure the horizontal beam profile and one horizontal wire that measures the vertical beam profile. When a stepper motor connected to the fork moves, the wires pass through the beam and the ADC signals were generated. A position encoder measures the position of the fork. The position information from the encoder and the ADC signal were used to extract the position and the profile of the beam. As shown in Figure 4-3, three pairs of superharps are located at the beginning, the mid-point and the end of the Hall C arc. Separate superharps in combination with BPM's are

located in the Hall C beamline segment close to the Hall C target.
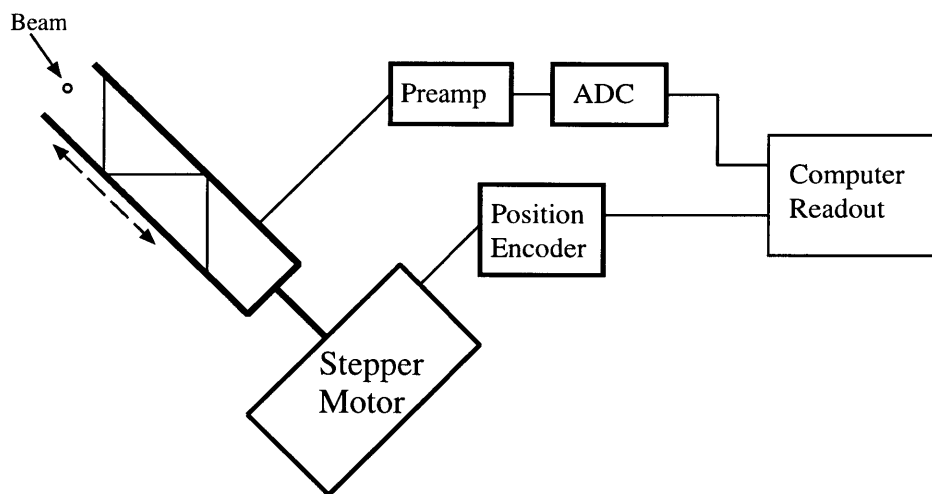
Figure 4-4: Schematic of the superharp system

The superharps in the Hall C arc were mainly used for beam energy measurement. The three pairs of superharps were successively operated to obtain the positions and orientations of the incident and outgoing beam, which renders also the central trajectory. The combination of beam positions and beam profile as given by the three superharp pairs, together with the known field integral of the arc bend magnets, can be used to derive the beam energy and also the beam emittance and dispersion. Details of the beam energy measurement will be described in Section 4.3.6.

4.3.4   Raster System

Due to the high current and the small size (FWHM $\cong$ 300 μm) of the beam, local heating in the target would cause boiling of the liquid deuterium if measures were not taken to reduce the power density. To minimize the reduction of the target liquid density and to prevent possible damage of material by overheating, vertical and horizontal air-core magnets were used to impart a rastering pattern to the beam on

the Hall C target (Fast Raster or FR) and Hall C beam dump (Slow Raster or SR).
During this experiment, the raster size of the beam before the target was ±2 mm.

4.3.5 Scattering Chamber

The scattering chamber in Hall C was a cylinder. The cutouts on the cylinder
for the High Momentum Spectrometer (HMS) and the deuteron channel were large
enough to cover angular acceptances of HMS and the deuteron channel . In addition,
there were entrance and exit openings for the beam as well as a pumping port and
several viewing ports. The HMS window was 20.32 cm tall and covered with a 0.04064
cm thick Aluminum window. The beam exit window consisted of a Titanium foil,
approximately 60 mg/cm^2, 136.5 cm high. There was a 24m long beamline between
the target and the beam dump.

4.3.6 Beam Energy Measurement

The Hall C arc transport beamline was used as a spectrometer to measure the beam
energy and energy spread. During the beam energy measurement, the arc optics were
set from the normal achromatic mode to dispersive mode by setting all non-dipole
elements (quadrupoles, sextupoles) to a zero of $\int$Bdl value. The beam correctors
were used to compensate the terrestrial field. The absolute transverse beam position
and orientation at the entrance, the mid-point, and at the end of Hall C arc line were
measured by a set of two pairs of superharps (see Figure 4-3) equipped with absolute
position encoders with an accuracy of 10 μ. The current in the calibrated bending
magnets was varied to set the position of the beam to be along the central ray of the
dipoles in the arc. The current was then transferred into a $\int Bdl$ value for the dipoles
through precalibrated $\int Bdl - I$ data. Thus the beam energy E_0 is determined. The
dispersion of the arc is 12.5 cm/% with all the quadrupoles, sextupoles, and beam
correctors switched off. The effective length of the arc is 300 cm.
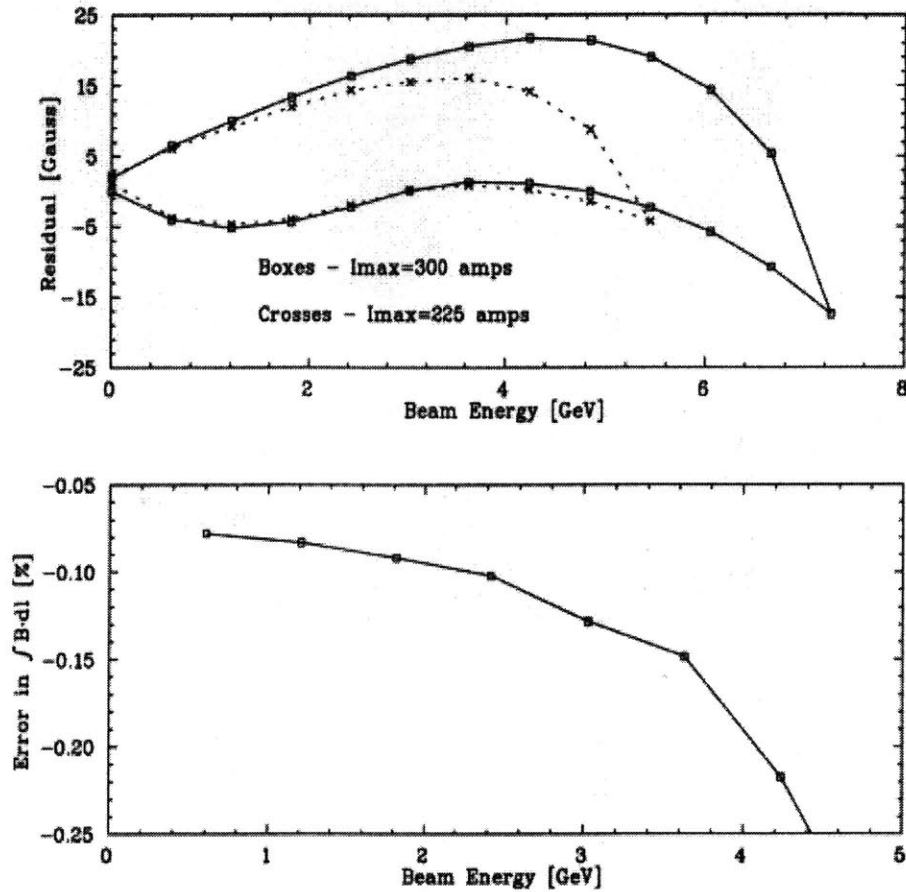
Figure 4-5: Residual field for both Arc dipole degaussing procedures and the errors induced in the beam energy measurement. The top figure shows the residual field for the two different degaussing procedures. The bottom figures shows the correction to the beam energy caused by using the two different degaussing procedures as described in the text. Figure taken from Ref. [85].

With the precise knowledge of the field, and the absolute beam positions measured with the superharps, the field integral can be calculated with high precision. The beam energy can then be determined with an uncertainty of $\delta p/p \sim 2 \times 10^{-4}$. However, it was discovered that the degaussing procedure used for the arc dipoles during the energy measurements was not the same as was used when the dipole fields were

initially mapped. In the mapping of the dipole fields, the dipoles were first ramped up to 300 Amps, then reduced to the desired current values. During data taking, the dipoles were only ramped to 225 Amps. This caused a difference in residual field which led to overestimated beam energies. Figure 4-5 shows the residual field versus beam energy for the degaussing procedure and the errors of the Hall C arc measurement of the beam energy due to this effect. An additional uncertainty was introduced due to this correction: 0.01% for energies below 3 GeV, 0.02% for higher energies. The energies used in this experiment were corrected for this effect and are listed in Table 4.3.

Kinematics	beam energies from arc measurement	corrected beam energies
1	1.413 GeV	1.412 GeV
2	1.647 GeV	1.646 GeV
3	2.100 GeV	2.098 GeV
4	2.449 GeV	2.447 GeV
5	3.255 GeV	3.251 GeV
6	4.054 GeV	4.046 GeV

Table 4.3: Results of beam energy measurement using Hall C arc method and their values after the correction of the different residual field effect.

Another method used to determine the beam energy kinematically was to calculate the beam energy from the scattered electron momentum and the scattering angle reconstructed in the HMS. Due to the limited precision of this method, it was only used to study the stability of the beam energies during the experiment, instead of the absolute beam energy determination.

When the electron beam is incident on the deuteron target, it loses energy (E_{loss1}) in the liquid deuterium before scattering. The energy of the electron at the vertex of

the scattering ($E_{beamcor}$) is

$$E_{beamcor} = E_{beam} - E_{loss1} \qquad (4.1)$$

The energy of the scattered electron at the vertex (E_{hmscor}) is obtained after adding the energy loss of the scattered electron in the target (E_{loss2}) to the scattered electron energy (E_{hms}) measured in the HMS.

$$E_{hmscor} = E_{hms} + E_{loss2} \qquad (4.2)$$

At the vertex of the scattering, $E_{beamcor}$ and E_{hmscor} are related by

$$E_{hmscor} = \frac{E_{beamcor}}{1 + \frac{2E_{beamcor}\sin^2\frac{\theta_e}{2}}{M_D}} \qquad (4.3)$$

where θ_e is the scattering angle of the electron, M_D is the deuteron mass. So the beam energy can be calculated as follows:

$$E_{beam} = \frac{E_{hms} + E_{loss2}}{1 - \frac{2(E_{beamcor}+E_{loss2})\sin^2\frac{\theta_e}{2}}{M_D}} + E_{loss1} \qquad (4.4)$$

A typical spectrum for the reconstructed beam energy using this method for Kinematics 1 is shown in Figure 4-6. Events in the shaded area, representing the e-d elastic scattering events, were obtained after applying cuts on the scattered electron energy E_{hms} and the scattering angle θ_e. It was then fitted with a Gaussian function. The peak value from the fit was used as a measure of the beam energy. The reconstructed beam energy for each run for different kinematics is shown in Figure 4-7. The beam energies were stable within the level of 10^{-3}.
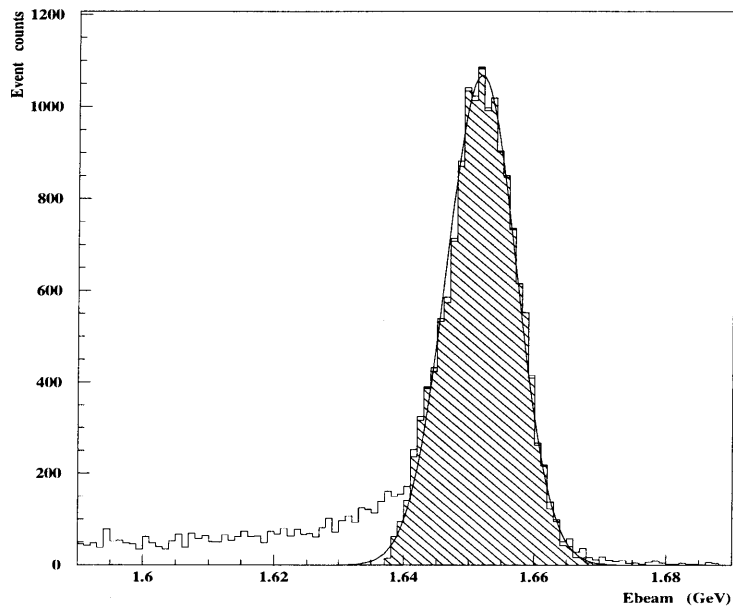
Figure 4-6: Spectrum of reconstructed beam energy for Kinematics 2

4.4 Liquid Deuterium Target

The Hall C scattering chamber contained two target ladders, one for cryogenic targets as shown in Figure 4-8 and one was for solid targets. When the solid target was in use, a target lifting mechanism and a rotating mechanism were used to lift the cryogenic target out of the beam and rotate it out of the way so that the solid targets could be inserted. In this experiment, the cryogenic target was used. The solid target was used only in the optics study of the HMS spectrometer.
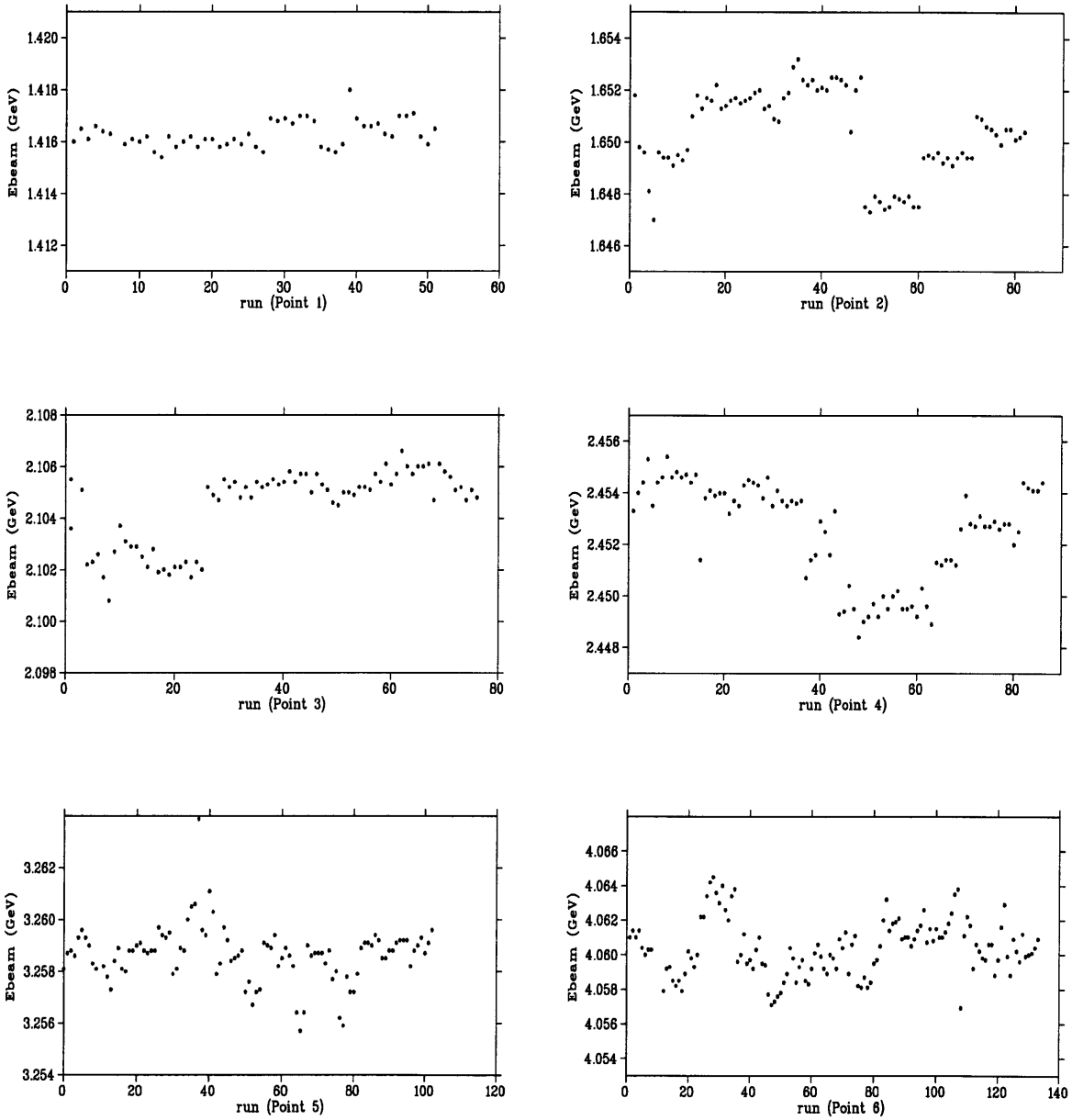
Figure 4-7: Stability of reconstructed beam energy for the six kinematics.
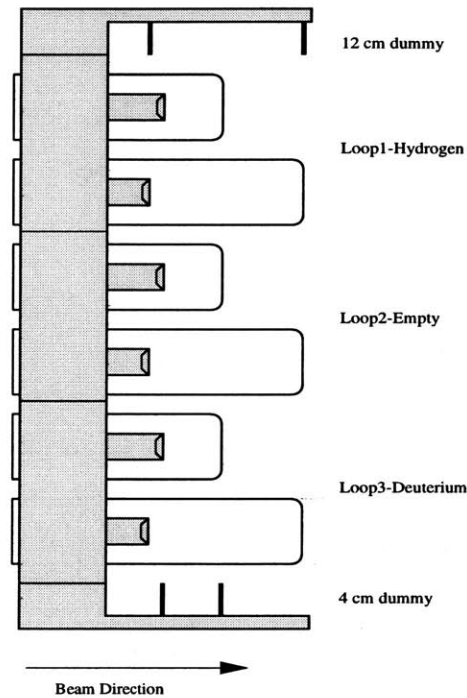
Figure 4-8: Side view of the full cryotarget ladder

The cryogenic system had three separate loops for Hydrogen, Deuterium and Helium targets (see Figure 4-8). The Helium targets in loop 2 were empty during this experiment. The side view of an individual target loop is shown in Figure 4-9. Two target cells, 4 cm and 12 cm long separately, were attached to an aluminum cell block for each target loop. The desired target cell could be moved into the path of the electron beam with the target lifting mechanism. The cells were thin aluminum cylinders made from beer can stock, 6.731 cm in diameter, with 0.0178 cm walls. Inside of the large cells were smaller aluminum flasks. The entrance and exit endcaps were both curved slightly, which gave a thickness variation with beam position.
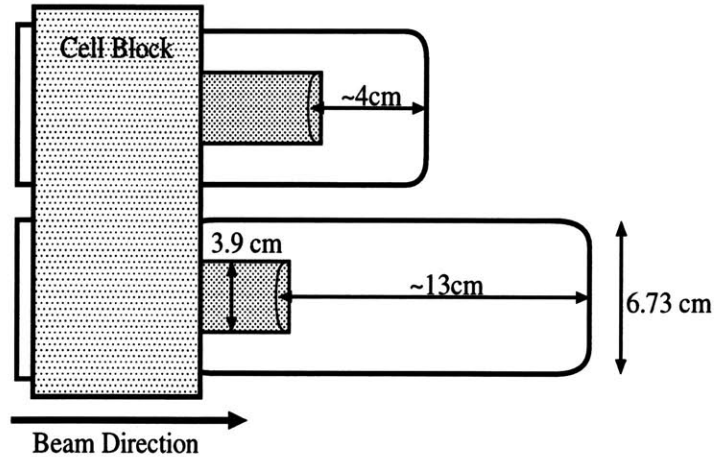
Figure 4-9: Side view of a cryotarget loop. Figure taken frim Ref. [89].

Each loop consisted of a circulation fan, two target cells, heat exchangers and high and low power heaters. The heat exchangers were used to remove the heat deposited by the beam by bringing the target fluid into thermal contact with 4 K cold helium provided by the CEBAF End Station refrigerator. In the loops, an axial fan inside a heat exchanger forced the target liquid to flow through the cell as shown in Figure 4-10. High power heaters were used to maintain a constant heat load for the system, so that the cooling power stayed constant as the beam current changed. Low power heaters maintained the cryotargets at their operating temperatures, and corrected for small fluctuations in the beam current.

Each target loop had its own intelligent temperature controller, Oxford ITC-502, which could monitor three independent sensors. Two channels of each ITC-502 were dedicated to reading the temperature of the target fluid from a pair of Cernox resistors which were mounted at either end of the low power heater carrier board. These resistors provided sensitive measurements of the temperature with an accuracy of $\sim$100 mK.
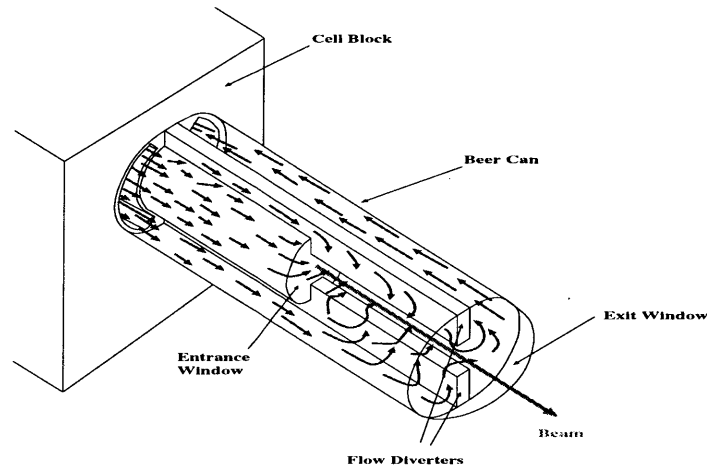
Figure 4-10: Inside structure of a cryotarget cell. Figure taken from Ref. [89].

The cryogenic system was controlled using the Experimental Physics and Industrial Control System (EPICS). It consisted of operator Interfaces (OPI's - typically X terms) and Input Output Controllers (IOC's - typically single board computers). The communication between the OPI's and the IOC is via Ethernet. To operate the cryogenic system safely, it was important to monitor the state of the target constantly. For this purpose, software for user interface was developed by the author to record continuously various parameters, such as the temperature, the pressure, and the power readings of the power heaters.

For the experiment, the 12 cm deuterium target was used with an operating temperature of 22K. The targets were run at a maximum beam intensity of 110 μA with a ± 2 mm beam raster. The beam deposited about 500 W of power in the 12 cm deuterium target cell when running at 110 μA. The total cooling power of the cryogenic target system was about 600 W, which was adequate for this experiment.

4.5 High Momentum Spectrometer (HMS)

The High Momentum Spectrometer in Hall C was used to detect the scattered electrons in the experiment. The HMS was composed of three quadrupole magnets, Q1, Q2, and Q3, and one superconducting dipole magnet D. The three quadrupoles were cold iron superconducting magnets. The basic parameters for the quadrupoles are contained in Table 4.4. The HMS dipole was a warm iron superconducting, cryostable magnet. Its basic parameters were an effective length of 5.26 meter, a bend radius of 12.06 meter, and a gap width of 42 cm. Its actual size was 5.99 meter long, 2.75 meter wide, and 4.46 meter high. The bending angle of the dipole was 25°. Figure 4-11 shows a side view of the HMS spectrometer and the detector hut.
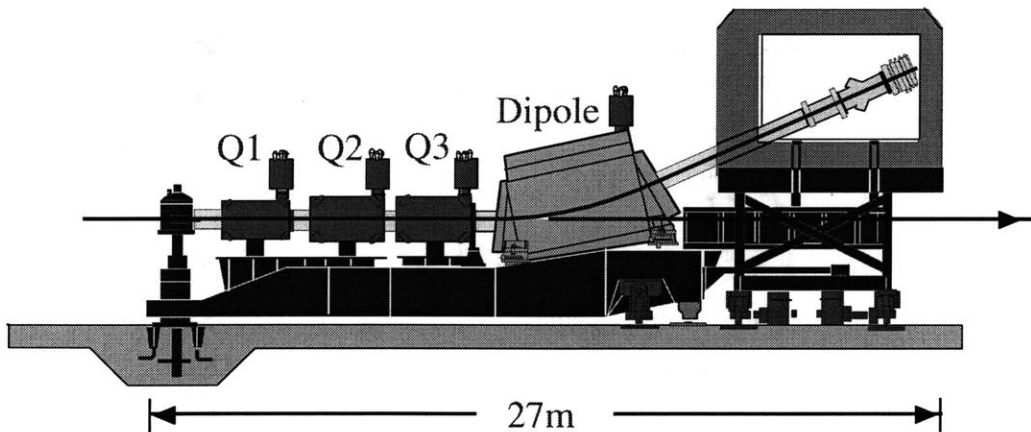
Figure 4-11: Side view of the HMS

The magnets were operated in a point-to-point focus tune in both the dispersive direction and nondispersive direction. In this tune, Q1 and Q3 focused in the dispersive direction and Q2 focused in the transverse direction. The HMS had a large acceptance, fairly large solid angle, and extended target acceptance. The design goals [86] and final performance of the HMS are listed in Table 4.5.

magnet	effective length	inner pole radius	I^*_{max}
Q1	1.89 m	25.0 m	580 A
Q2	2.155 m	35.0 m	440 A
Q3	2.186 m	35.0 m	220 A

Table 4.4: Operating parameters of the HMS quadrupoles

The magnetic fields were set remotely from the counting room. The field of the dipole was regulated using an NMR probe located in a region of uniform field. The quadrupoles were regulated by current. The fields of dipole and quadrupoles were stable at the 10^{-4} level.

	Design Goal	Final Performance
Maximum central momentum	6.0 GeV/c	7.4 GeV/c
Momentum bite $[(p_{max} - p_{min})/p_0]$	20%	20%
Momentum resolution $[\delta p/p]$	0.1%	0.02%
Solid angle (no collimator)	10 msr	8.1 msr
Angular acceptance - scattering angle		± 32mr
Angular acceptance - out-of-plane		± 85mr
Scattering angle reconstruction	0.1 mr	0.5 mr
out-of-plane angle reconstruction	1.0 mr	0.8 mr
Vertex reconstruction accuracy	1 mm	2 mm

Table 4.5: HMS design goals and final performance

A slit system before Q1 was used to insert various collimators. Three collimators and one blank space were in the slit box. Two collimators were octagonal apertures designed to limit the solid angle acceptance of the HMS. They were not used in this experiment. The third collimator was a 3.175 cm thick sieve slit used for optics study, shown in Figure 4-12. It was an array of small holes, each with 0.508 cm diameter.

Each hole allowed particles with a certain polar and azimuthal angle to pass through. The vertical hole spacing corresponds to 19.90 mr steps, and the horizontal spacing corresponds to 11.93 mr steps. Thus the optics of the spectrometer could be studied by comparing focal plane distributions to data with known angular distributions. Two holes were missing in the sieve slit in order to verify proper left-right and top-bottom reconstruction. The central hole was smaller than the others in order to obtain the resolution of the angular reconstruction. Figure 4-13 shows the scatter plot of the reconstructed events at the front of the sieve slit.
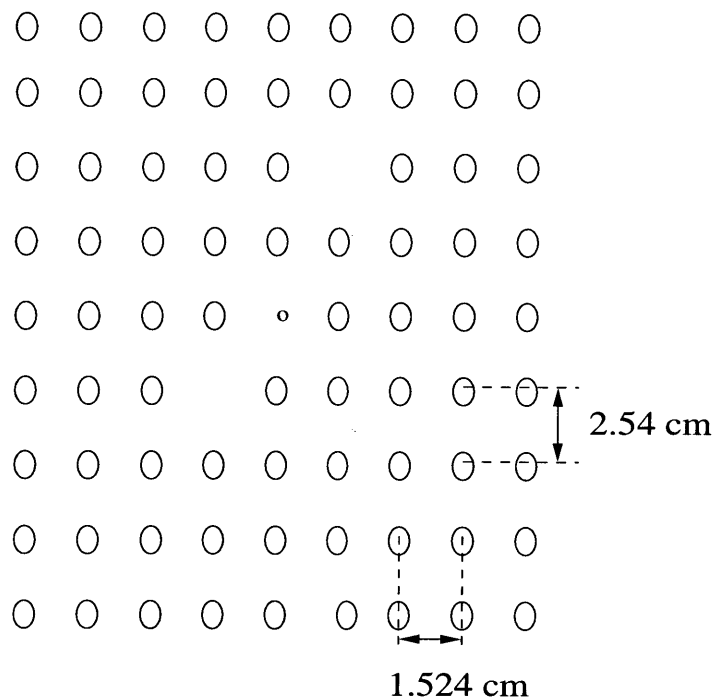
Figure 4-12: Schematic of the HMS sieve slit. Two holes are missing for left-right and top-bottom reconstruction. The central hole is smaller than the others to measure the angular resolution.
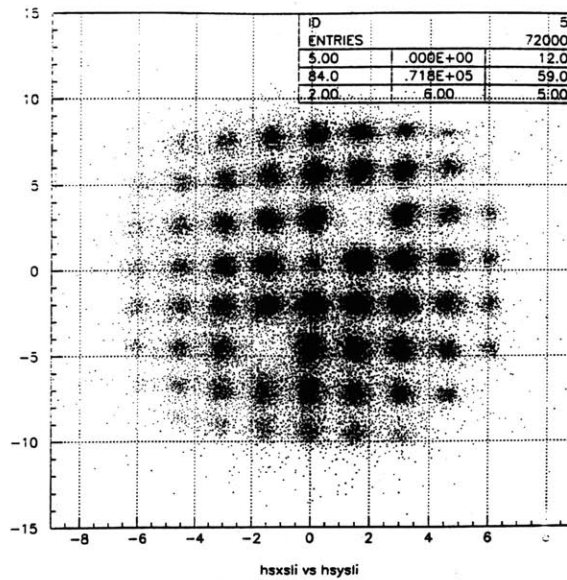
Figure 4-13: Scatter plot of the events at the front of the sieve slit. One can see that two holes were missing and the central hole was smaller than the others. Figure taken from Ref. [87]

The HMS detector package consisted of two drift chambers, two sets of scintillator hodoscopes, a gas Čerenkov detector and a lead glass shower counter calorimeter. A schematic of the HMS detector package is shown in Figure 4-14.
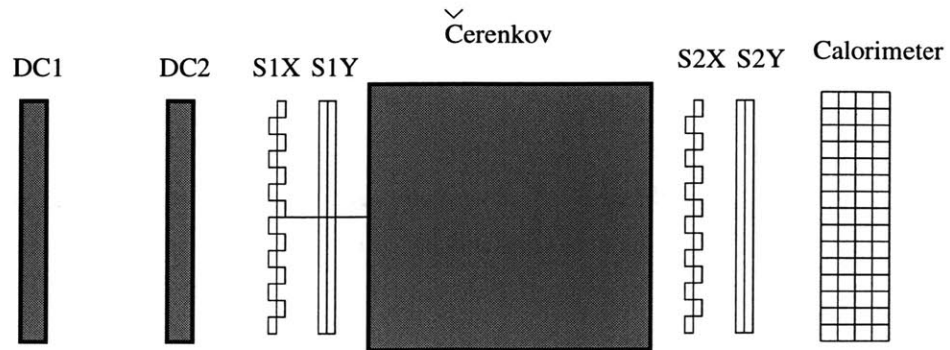
Figure 4-14: Schematic diagram of the HMS detector hut

4.5.1 Drift Chambers

The two Drift Chambers provided the position and angle information of the scattered electrons. This information was combined with the optics of the spectrometer to infer the trajectory of electrons at the target. Each chamber consisted of six planes, X, Y, U, V, Y' and X' as shown in Figure 4-15. X and X' wires measured position along the dispersive direction. Y and Y' wires measured in the transverse direction while the U and V planes were inclined 15 degree with respect to the X planes to provide the stereo measurements. The active area of the chambers was about 113 cm (x) by 52 cm (y) with 1 cm spacing wires. Each plane was separated by 1.8 cm and the two drift chambers were separated by 81.2 cm. The chambers were filled with a mixture of Ar(49.5%), Ethane(49.5%) and Isopropyl Alcohol(1%). The resolution of the chambers was 140 μm. The efficiency was greater than 98%.
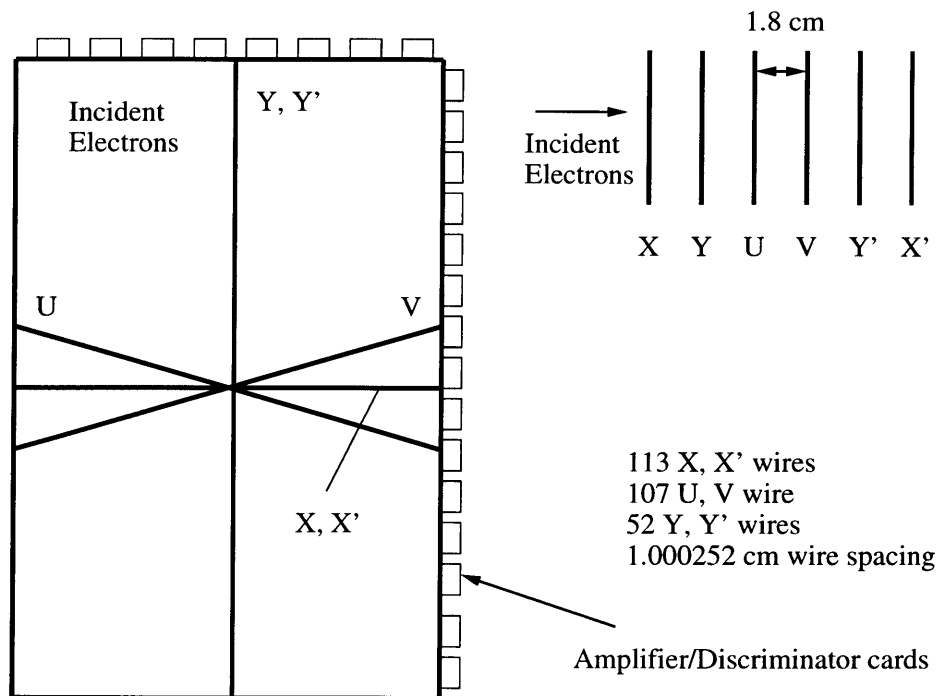
Figure 4-15: Front view of the HMS drift chambers

4.5.2 Scintillator Hodoscopes

The scintillator hodoscopes provided a fast, clean trigger and particle identification by time of flight (TOF). These detectors consisted of two pairs of spatially separated scintillator layers: a pair comprising of S1X and S1Y, and approximately 2 meters away a pair comprising of S2X and S2Y. Each hodoscope plane was constructed of 9 to 16 elements. The hodoscope elements were long narrow strips of scintillator with light guides and phototubes on both ends. Each scintillator was read out by two photomultiplier tubes (PMT's). The specific dimensions for the scintillator elements in the HMS can be found in Table 4.6.

	thickness	width	length	number
X	1 cm	8.0 cm	75.5 cm	32 units
Y	1 cm	8.0 cm	120.5 cm	20 units

Table 4.6: Dimensions of the scintillators of HMS

4.5.3 Gas Čerenkov Detector

The gas Čerenkov detector in the HMS consisted of a large cylindrical tank with a diameter of 59 inches and a length of 60 inches. Two mirrors were contained in the tank to focus light onto two 5 inch PMT's. The tank was filled with N2 at the desired operating pressure, about 1 Atm. A Čerenkov counter is used to discriminate between particles of different masses which have the same momentum. A charged particle travelling faster than the speed of light in the medium will emit Čerenkov radiation which is distributed about the trajectory of the particle, with an angle θ_c given by $\cos\theta_c = 1/(\beta n)$, where the index of refraction n=c/u and β = v/c, with c the speed of light in vacuum, u the speed of light in the medium, and v the speed of the particle. The index of refraction allows one to control the threshold

particle velocity $V_T = u = c/n$, below which there is no Čerenkov light produced, and above which there is Čerenkov light produced. For a gas, the quantity n-1 is proportional to the pressure, so adjusting the pressure of the gas allows one to select the threshold velocity. Given the same momentum, two particles of different mass will have different velocity. Therefore, a Čerenkov detector can be tuned to distinguish particles of different masses. For this experiment, the HMS was operated to detect only scattered electrons from the e-d elastic scattering with no other particles (such as pions) being detected; therefore although the Čerenkov detector was active in this experiment, it actually had no significant effect on the results.

4.5.4 Lead Glass Shower Calorimeter

The lead glass shower calorimeter was used to provide additional triggering and particle identification. It consisted of four stacks of TF1 leaded glass. Each stack contained thirteen blocks lying lengthwise along the dispersive direction. The blocks were 10 cm by 10 cm by 70 cm and were read out at one end by a PMT. High energy particles emit Čerenkov radiation when passing through the glass, and a signal is collected that is proportional to the sum of the path lengths traveled by all the shower particles which are above the threshold for Cerenkov emission. Very light particles, such as electrons, shower heavily and deposit much of their energy in the first one or two layers. Heavier articles, on the other hand, do not shower heavily and tend to deposit about the same amount of energy in all layers. Thus it is possible to distinguish electrons from other heavier particles by comparing the energy deposited in the first layers of lead glass. During this experiment. the calorimeter was not used to perform particle identification since very clean elastic e-d events were selected by the kinematics setup of the spectrometers and applying cuts on the momentum detected in the HMS. These cuts are described in Section 6.2.2.

4.6 Deuteron Transport Channel
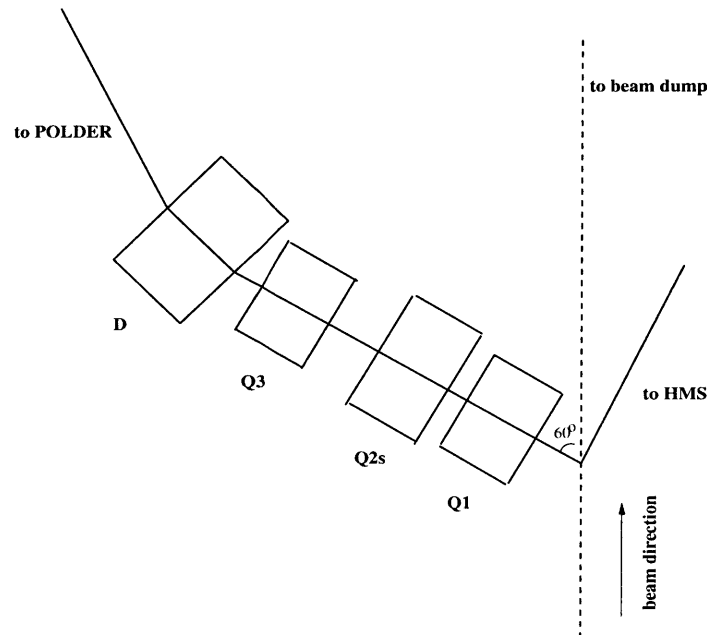
Figure 4-16: Top view of deuteron transport channel.

The deuteron arm was fixed at 60° for the experiment, as shown in Figure 4-16. It was a specially designed magnetic channel to focus the maximum number of deuterons onto the polarimeter target and to protect the polarimeter from a direct view of the primary target of deuterium. This channel was in a QQ_SQD configuration, where the S subscript means additional coils for sextupole corrections which were built into the quadrupole. The dipole was used to bend the trajectories of the deuterons horizontally through 30°. This unit was supplied and field mapped by the MIT group. The first quadrupole Q1 and the third quadrupole Q3 focused vertically. These units were supplied and mapped by CEBAF and the Indiana Univeristy group. The second quadrupole Q2 focused horizontally. This was a specially designed quadrupole with sextupole components to minimize the size of the deuteron distribution on the

polarimeter. This unit was designed, built, and field mapped by the Saclay group. For the deuteron channel, the following coordinate system was used: z coordinate was the optical axis, x and θ were the coordinate and angle in the dispersive (horizontal) plane, and y and ϕ referred to the vertical plane. The first order tune of the dipole and the quadrupoles were given with the conditions (y|ϕ)=0 and (x|θ)+ k(x|δ)=0. Details of the deuteron channel can be found in Ref. [88]. For the deuteron channel, the acceptance of the vertical angle ϕ was ±130 mrad, while the theta and momentum acceptance overlapped completely with the HMS acceptance.

For each kinematics, the magnets were tuned during the commissioning of the experiment using a test detector supplied by the Rutgers group, which consists of straw chambers and scintillator detectors. The method used was to adjust the fields of the magnets so that the deuteron beam spot size on POLDER was minimized and compatible with the size of the POLDER detectors.

Most of the charged-particle background was rejected in the deuteron channel. Only the protons which came from the inelastic *e-d* scattering and had similar momentum of the deuterons, were left. After the deuteron channel, the deuterons arrived at the polarimeter POLDER, where the second scattering took place and the angular distribution of the protons from ^{1}H($\vec{d}$,2p)n reaction was measured.

4.7 Polarimeter (POLDER)

4.7.1 Introduction

A polarimeter is usually based on a nuclear reaction and designed to measure the asymmetries of the particles out of this reaction corresponding to the incident particle polarizations. The cross section for this reaction is as follows:

$$
\begin{aligned}
\sigma(\theta, \phi) \;=\; & \sigma_0(\theta)[1 + 2it_{11}iT_{11}(\theta) + t_{20}T_{20}(\theta) \\
& + 2t_{21}T_{21}(\theta)\cos\phi + 2t_{22}T_{22}(\theta)\cos 2\phi]
\end{aligned}
\tag{4.5}
$$

where t_{kq} are the polarization coefficients of the beam and T_{kq} the analyzing powers. σ_0 is the cross section for unpolarized beam and ϕ is the angle between the normal to the reaction plane and the spin axis of the incident particles. An important character of polarimeters is called figures of merit given by :

$$(F_{kq})^2 = \int (T_{kq})^2 \epsilon(\Omega) d\Omega \tag{4.6}$$

where ϵ, called the efficiency, is the ratio of the number of detected reactions to the number of incident particles. The integration is over the phase space covered by the polarimeter. F_{kq} is a function of the cross section, target thickness and all detector efficiencies. It is related to the statistical error through

$$\Delta t_{kq} \approx \frac{1}{F_{kq}\sqrt{N_{inc}}} \tag{4.7}$$

with N_{inc} the number of incident particles.

The analyzing powers T_{kq} and the unpolarized cross section σ_0 for a polarimeter are obtained first in a calibration experiment using beams with known intensity and polarization. Then with the calibrated polarimeter, the polarization coefficients of incident particles can be determined through an asymmetry measurement in a separate experiment.

POLDER [89] was designed and built by the Grenoble and Saclay group. It was based on the ^{1}H($\vec{d}$,2p)n reaction proposed by Bugg and Wilkin[90]. In this reaction as shown in Figure 4-17, the neutron in the deuteron exchanges charge with the proton in the hydrogen target so that two protons come out after the reaction with the same velocity. According to Pauli principle, two protons with the same momentum (or velocity) must be in different spin states so that the neutron flips its spin in the charge exchange reaction. The spin-flip increases the analyzing powers of the charge-exchange reaction significantly. At 200 MeV the measured figures of merit (F_{20} and F_{22}) in the ^{1}H($\vec{d}$,2p)n reaction [91] were found to be comparable to those

of the ^{1}H($\vec{d}$,p)X reaction used in the AHEAD polarimeter [92]. However the crucial feature of the ^{1}H($\vec{d}$,2p)n reaction is that its figures of merit remain large up to at least 500 MeV [91] whereas those of the ^{1}H($\vec{d}$,2p)X reaction fall quickly above 200 MeV [82]. The figure of merit F_{11} for the vector analyzing power
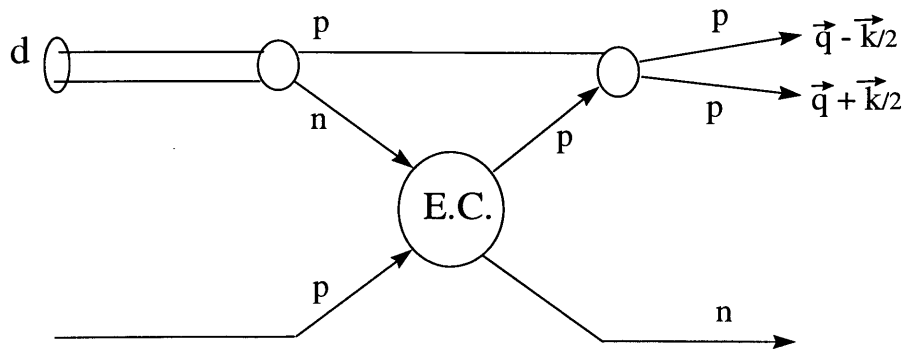
Figure 4-17: Diagram for ^{1}H($\vec{d}$,2p)n (charge-exchange) reaction.

is zero for this reaction. Further the ^{1}H($\vec{d}$,2p)n reaction is well understood in terms of the impulse approximation [93].

The detectors of POLDER are shown in Figure 4-18. There were three parts with specific tasks: the target in which the reaction ^{1}H($\vec{d}$,2p)n took place; the detectors before the target used for beam monitoring (direction and intensity); the detectors after the target used to measure the outgoing protons from this reaction.

4.7.2 Detection of the Incident Deuterons

1. The start detectors S1 and S2

The number of deuterons incident on the target was determined by a coincidence between two start detectors S1 and S2 which were placed before the target. These detectors were composed of thin fast plastic scintillators (1 mm thick for S1 and 2 mm thick for S2) optically coupled to two phototubes. The coincidence signal from

S1 and S2 was part of the hardware trigger and was used as the start signal for the time-of-flight measurement of the protons produced in the reaction. The coincidence between the signal from the scintillators
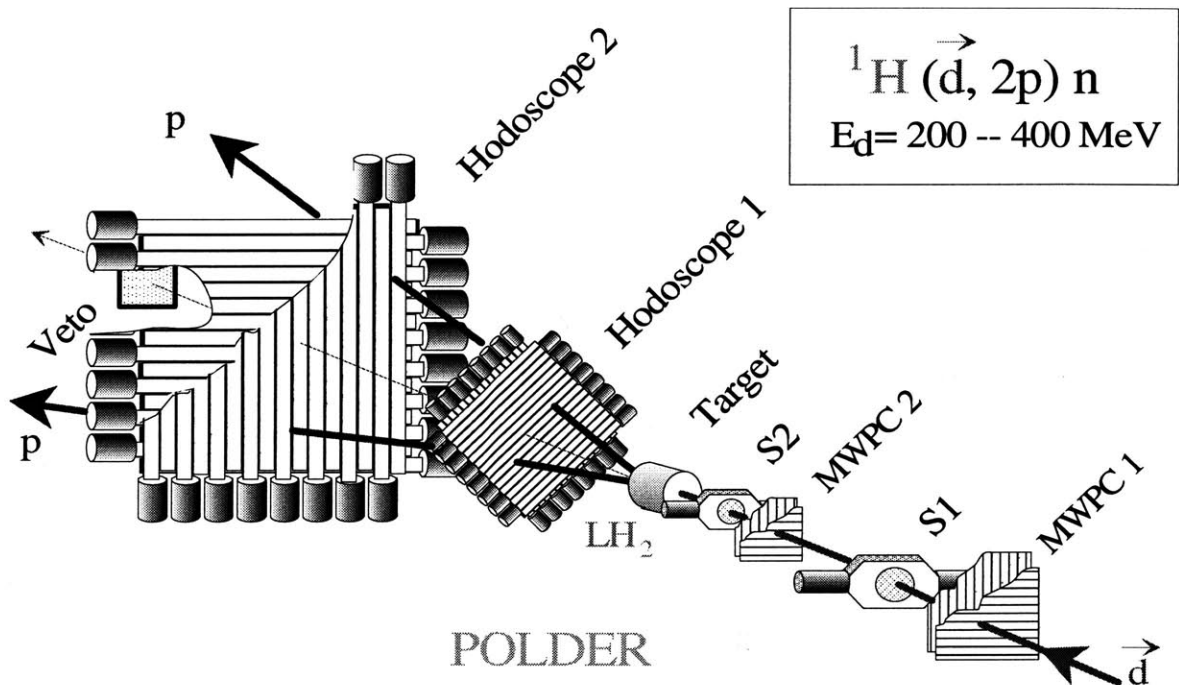
Figure 4-18: Sketch view of the POLDER polarimeter.

in HMS and the coincidence signal from S1 and S2 rejected the background particles reaching POLDER. The analog signals of the start detectors were also recorded to permit additional discrimination between deuterons and background protons of the same momentum.

2. MultiWire Proportional Chambers

The measurement of the precise direction and impact points of the deuterons incident on the target was performed by two multiwire proportional chambers (MWPC1/2) placed at 92.75 cm and 44.35 cm upstream of the target respectively. Each chamber was composed of three planes tilted at 120° to one another as shown in Fig-

ure 4-19. The plane spacing was 4 mm. Each plane consisted of 158 wires 1 mm apart. The chambers were operated with a gas mixture of Ar(70%), Ethane(30%) and Freon(0.5%) and provided 100% efficiency separately. These detectors were also capable of detecting multi-hit events with good precision, thus rejecting events with two charged incident particles (the proton background). A third chamber (not shown in Figure 4-18) was identical with the first two and was 191.8 cm behind the hydrogen target used for the alignment of the detectors in POLDER. The alignment parameters used in the data analysis were from the Saclay group.
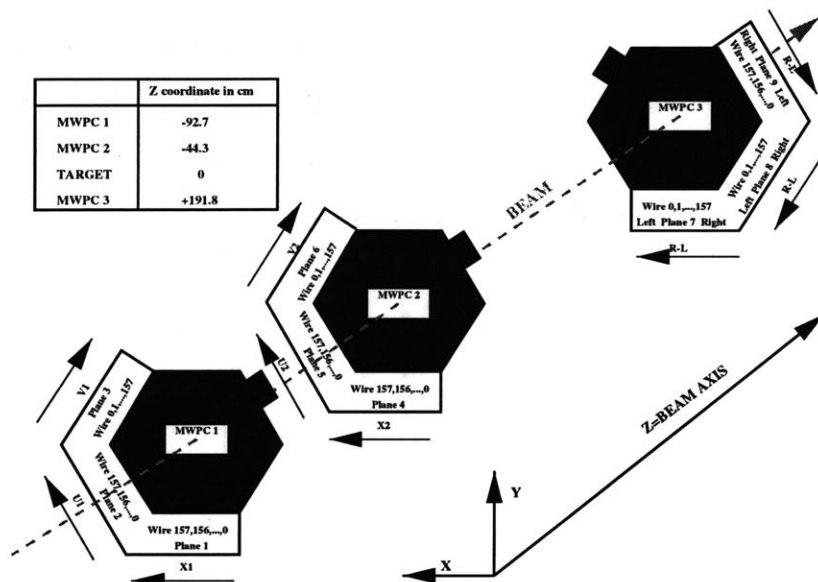
Figure 4-19: Layout of MWPC.

4.7.3 The Liquid Hydrogen Target

The $^1H(\vec{d},2p)n$ reaction took place in a liquid hydrogen (LH$_2$) target developed at the Laboratoire National Saturne [94]. This target was of cylindrical shape, 20.6 cm long and 14 cm in diameter with the total volume of 3.08 l (see Figure 4-20). The target cell was made of 170 μm thick mylar fixed onto a ring of aluminum located at

the entrance side and of an entrance window of 120 μm thick kapton. The cell was mounted in a vacuum chamber whose entrance and exit windows were made of 0.05 mm and 0.10 mm thick titanium respectively, backed by kevlar.
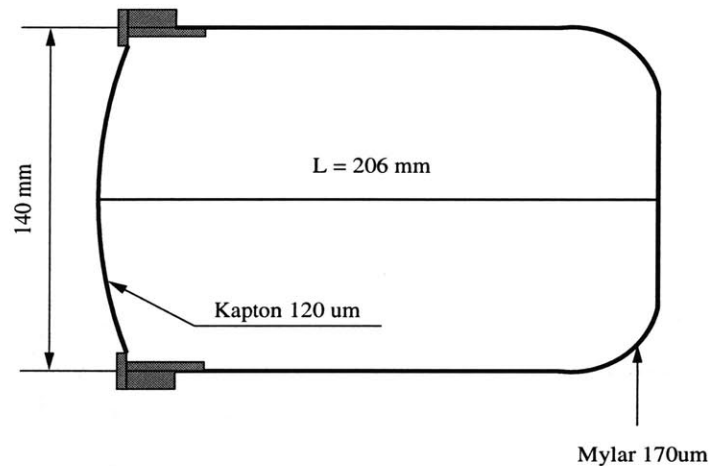
Figure 4-20: Sketch view of the liquid hydrogen target cell.

The target was operated at a temperature of 23.5 K with a 20 W cryogenic system. The working pressure of the target was 1075 mbar. The temperature and pressure were controlled by a monitoring system (called AUTOMATION) which was run on a PC. The precise measurement of the target shape was sufficient to control corrections for the incident deuterons hitting the target on its border. These corrections will be described in detail in Section 6.4.

4.7.4 Detection of the Protons

The protons produced in the ^{1}H($\vec{d}$,2p)n reaction were detected in two hodoscopes placed after the target, as shown in Figure 4-18. The one closer to the target was the small hodoscope (called H1), the other was the large hodoscope (called H2). The solid angles covered by H1 and H2 were matched. Their distances to the target varied with incident deuteron energies. Three sets of distances for H1 and H2 were used during

the experiment and were referred to position 1, position 2 and position 3. The values of the distances for the three positions, together with the corresponding deuteron energies, are shown in Table 5.1. Each position was optimal for a given energy range considering the requirements of large solid angle and good angular resolution. These features permitted the detection of protons from the ^{1}H($\vec{d}$,2p)n reaction in the range of momentum transfer to the neutron $q = 0 - 300\text{MeV}/c$ with good efficiency, almost independent of beam energy. In fact, most of the cross section of the ^{1}H($\vec{d}$,2p)n reaction with low pp excitation energy is located in this momentum transfer region (corresponding to a cone of 15° opening angle at 400 MeV and 20° at 200 MeV), and here the analyzing powers are large [91].

The small and large hodoscopes were put in three groups of positions for the various deuteron energies. The positions of the hodoscopes for each position set are listed in Table 5.1. Each position was optimal for a given energy range considering the requirements of large solid angle and good angular resolution.

Each hodoscope consisted of a X plane and a Y plane. Each plane consisted of 30 bars of plastic scintillators for H1 and 24 bars for H2. The scintillator bars in H1 were 37.5 cm long, 1.12 cm wide, 2 mm thick with a 1.15 cm spacing. In H2, the scintillator bars were 84.5 cm long, 3.38 cm wide, 1cm thick with a spacing of 3.4 cm. Each plastic bar was optically coupled to a phototube at only one end. From the positions of the bars fired in H1 and H2, the directions of the protons were determined and thus the angular distribution of the protons were obtained. To remove ambiguities in the determination of the directions of the protons, H1 was rotated by 45°.

In this experiment, the characteristics and kinematics of the ^{1}H($\vec{d}$,2p)n reaction allow one to discriminate charge exchange events from other parasitic reactions by imposing the condition that two charged particles are detected at forward angles and at velocities close to those of the incident deuteron. The thin plastic scintillators making up POLDER were mostly sensitive to charged particles. Thus the coincidence of

signals in several bars of the hodoscope was a reliable signature of the detection of a charged particle, and no particle identification was necessary. The velocity of the detected particles (protons) was obtained by measuring the time of flight between the start detector placed before the target and the second hodoscope. Energy measurements and particle identification for the protons were therefore not necessary and the selection of charge exchange events relied on quantities which were not sensitive to changes in experimental conditions. This feature reduced the problems of cuts and event selections in the data analysis.

Finally, a veto detector was placed on the beam axis to reject background events associated with the detection of at least one incident deuteron. An energy degrader was used to stop the protons of the ^{1}H($\vec{d}$,2p)n reaction while deuterons of same velocity, which had different energy loss from the protons, were detected in a plastic scintillator placed after the degrader.

4.8   Trigger and Data Acquisition

4.8.1   Trigger

The trigger electronics in Hall C provided single triggers and coincidence triggers. The trigger Supervisor (TS) was programmed to accept, reject, or prescale each of the different trigger types. The trigger electronics in the HMS and POLDER, shown in Figure 4-21, generate single electron events (HMS event), single POLDER events, coincidence e-d events and Charge Exchange (CE) events.

1. HMS event

The single arm trigger event in the HMS was an HMS event. The electronics for HMS trigger is shown in Figure 4-22. The hodoscopes in the HMS provided the trigger information. Each hodoscope plane consisted of 9-16 individual elements. The signals, read out from both ends of the tubes (positive and negative ends), were

amplitude discriminated. The tubes from the positive and negative ends were OR'ed to generate the signals S1X+, S1X-, etc. A hit in a given plane was defined as a coincidence of a hit in one of the positive tubes and a hit in one of the negative tubes. Both tubes did not have to be on the same scintillator. The trigger 'STOF' required the coincidence of one of the planes in the front hodoscope and one of the planes in the back hodoscope. This trigger was the minimum requirement for a good time of flight measurement in the scintillators. The trigger 'SCIN' required 3 of the 4 planes fired, and provided a tighter scintillator trigger. Obviously, the 'SCIN' trigger was included the 'STOF' trigger. For this experiment, 'SCIN' was used as the electron trigger.

2. *e-d* **event**

The start detectors S1 and S2 in POLDER were used to provide the deuteron trigger. The deuteron candidate was found when there was a coincidence between S1 and S2. The *e-d* events were defined as the coincidence of an electron from HMS and a deuteron from POLDER.
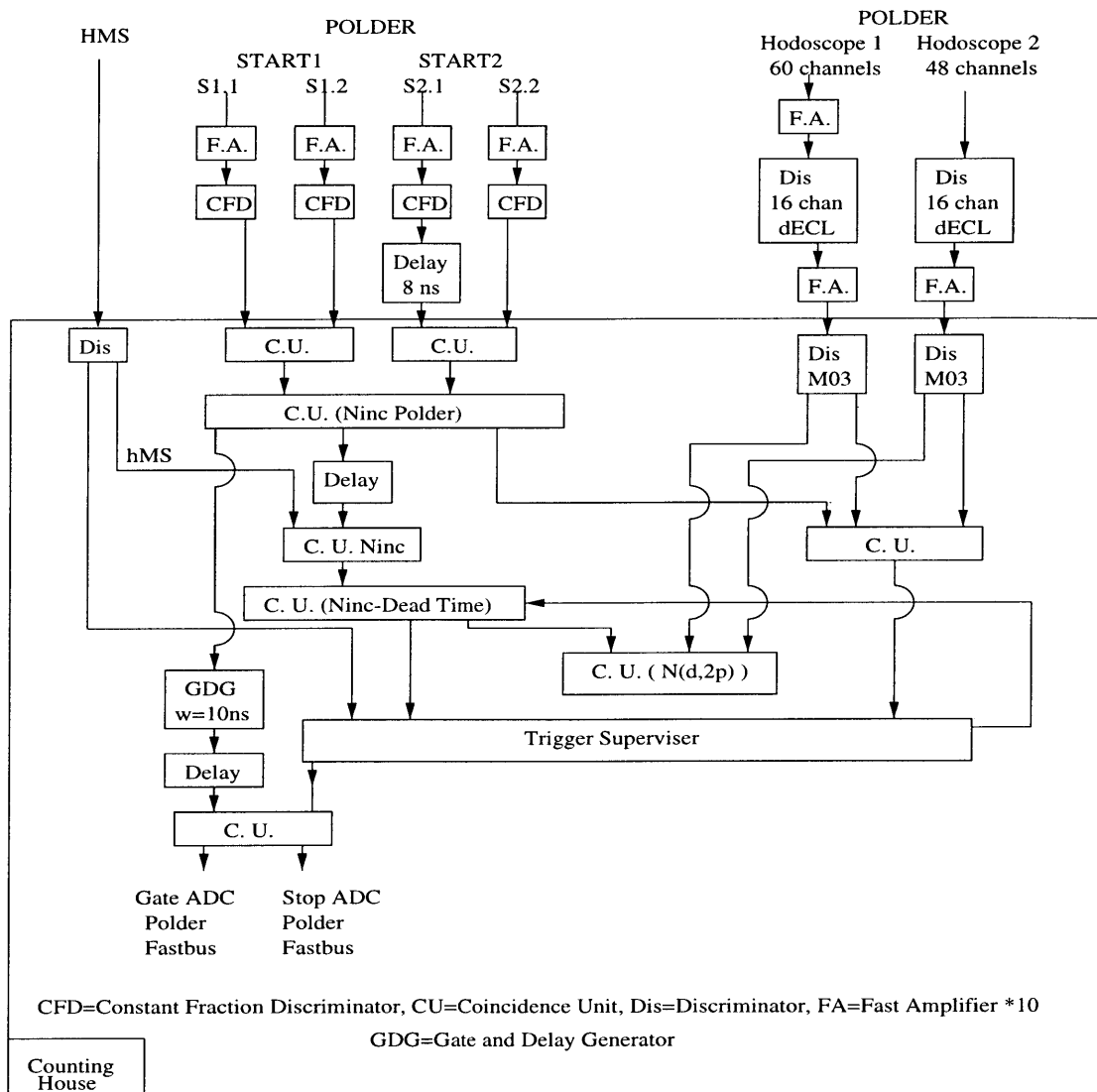
Figure 4-21: Electronics diagram for t20 experiment. Figure taken from Ref. [89].
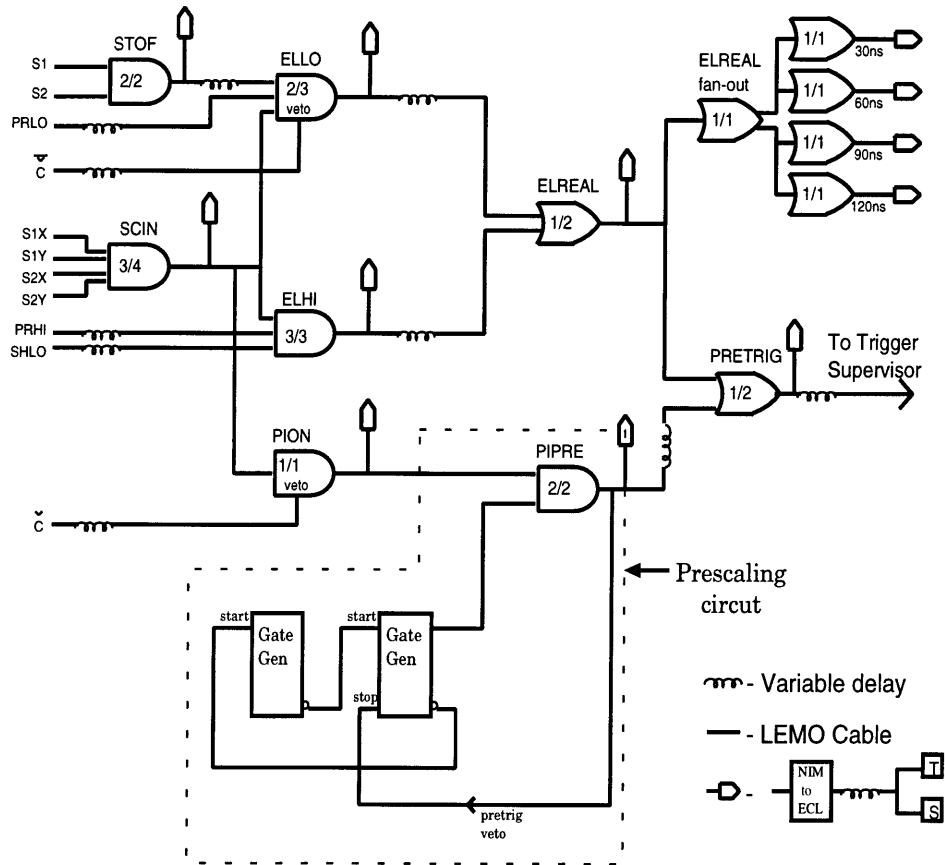
Figure 4-22: Diagram of electron trigger in the HMS

3. POLDER event

The POLDER event was the single arm trigger event in POLDER. The hodoscopes in POLDER provided the trigger information for protons. The coincidence between the signals from the start detectors S1 and S2 and the signal from the hodoscopes generated a POLDER event.

4. CE event

The coincidence of the electron from the HMS, the deuteron from the start detectors, and the protons from the hodoscopes generated the CE (Charge Exchange) event.

4.8.2   Data Acquisition
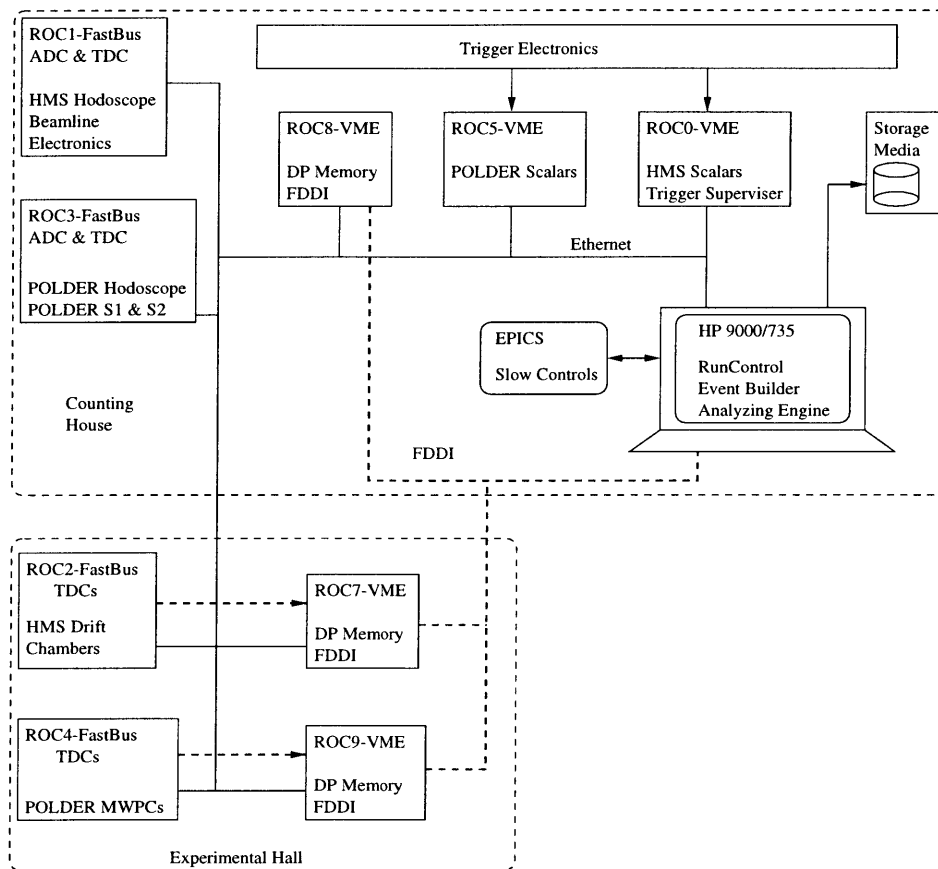
Figure 4-23: Schematic of the Data Acquisition System in Hall C

CODA (the CEBAF Online DATA Acquisition system) [95] was the data acqui-
sition system at CEBAF. The system for Hall C is shown in Figure 4-23. The data
were read from Read-Out controllers (ROC's). The ROC's were CPU's in Fastbus
and VME crates in Hall C and in the electronics rooms. These crates contained the
ADC's, TDC's, and scalers that recorded the event information. The Trigger Super-
visor (TS) controlled the state of the run, and generated the triggers that caused the
ROC's to be read out. The Event Builder subsystem (EB) read the data fragments

from the ROC's and collected the data together into an event. After the event was built by the EB, it was placed into a buffer, after which it could be tested and analyzed (online data analysis), or sent to disk or tape and analyzed later (offline data analysis). A graphical user interface (RunControl) in CODA allowed the user to start and stop runs, as well as define run parameters.

The data files for the runs contain both event information and slow controls readout. There were three main types of events: status events that had information about the run, physics events that contained data read out from events in the spectrometer, and EPICS (Experimental Physics Industrial Control System [96]) events which had readout from slow controls.

The status events were the first events in the log file for each run. When the state of the run changed, the prestart, start, pause or end events were generated. At the beginning of the run, the user could enter information about the run (kinematics, magnetic settings, comments) in a Tk/Tcl window. This information was stored in the beginning of the run event. In addition, at the beginning of the run, there were status events that recorded the ADC threshold values that were programmed in at the beginning of the run. This allowed the analysis software to compare the set thresholds to the desired values, as determined by the pedestal events.

The physics events contained data for single events from the HMS or POLDER, as well as coincidence events from them. Both TDC's and ADC's were read out in sparsified mode. The LeCroy 1881M ADC's had programmable thresholds for each channel. The thresholds at 15 channels were set above the pedestal. To measure the centroids and widths of the pedestals, 1000 random triggers were generated at the beginning of each run. Some beam related quantities, such as beam position monitors, beam loss monitors, and beam raster readback values were also recorded in each event.

In addition to the physics events, other user event types could be defined in CODA,

allowing readout of hardware scalers or execution of user scripts. The hardware HMS and POLDER scalers were read out every two seconds. The detector and beamline controls and readouts were triggered every 30 seconds. These readouts were put in the EPICS database. Values such as spectrometer magnet settings, accelerator settings, and target status variables were accessed this way.

Chapter 5

Saturne Calibration Experiment

As mentioned before, a polarimeter must first be calibrated to measure the analyzing powers and the unpolarized cross section. The calibration experiment [89] for the polarimeter POLDER was performed at the Laboratoire National Saturne in 1996. Polarized deuteron beams were delivered by the Saturne synchrotron. The axially symmetric source HYPERION provided deuterons of known polarization in eight different spin states. Four of them (5,6,7,8) were used during the calibration experiment. The four spin states had vector and tensor polarizations (ρ_{10}, ρ_{20}) of $(1/\sqrt{6}, 1/\sqrt{2})$, (-$1/\sqrt{6}, 1/\sqrt{2})$, $(1/\sqrt{6}, -1/\sqrt{2})$ and $(-1/\sqrt{6}, -1/\sqrt{2})$ respectively. The deuteron beams were delivered in bursts every second with the four spin states in sequence as illustrated in Figure 5-1. The polarizations of the deuteron beam was measured by a low-energy polarimeter during the calibration experiment.
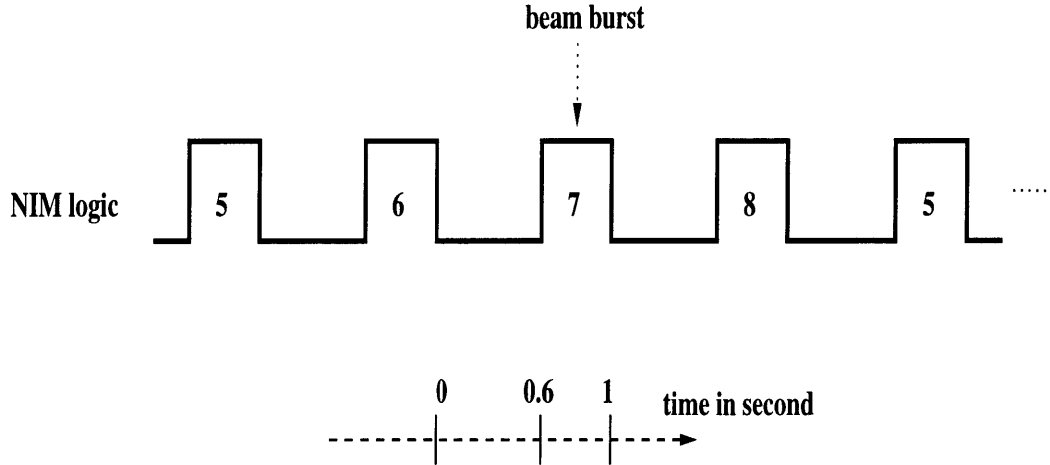
Figure 5-1: Logic signal of the deuteron beam bursts in four spin states delivered by HYPERION.

The polarimeter POLDER was installed in the focal plane of the spectrometer SPES1, which was placed at 0° with respect to the incident deuteron beam. The beam as delivered had no longitudinal component of polarization. A superconducting solenoid was used to rotate the spin axis of the beam by 90° from the vertical to the horizontal plane. The spin of the beam was precessed in the SPES1 spectrometer through an angle α given by:

$$\alpha = \gamma \theta_s G_d \tag{5.1}$$

where γ is the Lorentz factor, $G_d = g_d - 1 = -0.143$, and θ_s is the bend angle in SPES1 (97°).

The efficiency ϵ for the ^{1}H($\vec{d}$,2p)n reaction, as defined in Section 4.7.1, is the ratio of the number of detected reactions and the number of incident deuterons. In the Saturne calibration experiment, the efficiency was grouped in bins of θ and ϕ and

expressed in the helicity frame as:

$$\epsilon(\theta, \phi) = \epsilon_0(\theta)(1 + \sqrt{2}\rho_{10}\sin(\beta)\cos(\phi)iT_{11}(\theta) + \rho_{20}[\frac{1}{2}(3\cos^2(\beta) - 1)T_{20}(\theta)$$

$$\sqrt{6}\sin(\beta)\cos(\beta)\sin(\phi)T_{21}(\theta) - \sqrt{\frac{3}{2}}\sin^2(\beta)\cos(2\phi)T_{22}(\theta)]) \qquad (5.2)$$

where θ the scattering angle for the center of mass of the two protons, ϕ, T_{kq} were defined in Section 4.7.1, ϵ_0 is the unpolarized efficiency, β is the angle between the beam momentum and its spin axis and given by:

$$\beta = \pi/2 + \alpha \qquad (5.3)$$

where α was defined in Eq. 5.1.

With the known beam polarizations ρ_{10} and ρ_{20}, the analyzing powers and the unpolarized efficiency were extracted from Eq. 5.2 by constructing vector R_V and tensor R_T asymmetries

$$R_V(\theta, \phi) = \frac{\epsilon_5(\theta, \phi) + \epsilon_7(\theta, \phi) - \epsilon_6(\theta, \phi) - \epsilon_8(\theta, \phi)}{\epsilon_5(\theta, \phi) + \epsilon_7(\theta, \phi) + \epsilon_6(\theta, \phi) + \epsilon_8(\theta, \phi)} \qquad (5.4)$$

$$R_T(\theta, \phi) = \frac{\epsilon_5(\theta, \phi) + \epsilon_6(\theta, \phi) - \epsilon_7(\theta, \phi) - \epsilon_8(\theta, \phi)}{\epsilon_5(\theta, \phi) + \epsilon_7(\theta, \phi) + \epsilon_6(\theta, \phi) + \epsilon_8(\theta, \phi)} \qquad (5.5)$$

where ϵ_i are efficiencies measured for beam state 'i'. These efficiencies were normalized to the same number of incident deuterons in the four beam spin states. So the sum of the normalized efficiencies provided the efficiency for unpolarized beam. The asymmetries are related to the analyzing powers by:

$$R_V(\theta, \phi) = \sqrt{2}\rho_{10}(iT_{11}(q))\sin(\beta)\cos(\phi) \qquad (5.6)$$

$$R_T(\theta, \phi) = \rho_{20}[\frac{1}{2}(3\cos^2(\beta) - 1)T_{20}(q) + \sqrt{6}\sin(\beta)\cos(\beta)\sin(\phi)T_{21}(q)$$

$$-\sqrt{\frac{3}{2}}\sin^2(\beta)\cos(2\phi)T_{22}(q)] \tag{5.7}$$

POLDER was calibrated for incident deuteron energies from 140 MeV to 520 MeV with a step of 10 to 20 MeV. The small and large hodoscopes were put in three groups of positions for the various deuteron energies. The positions of the hodoscopes and the corresponding energies for each position set are listed in Table 5.1. For a given hodoscope position, the data were taken at several energies. This allowed interpolation for a given incident deuteron energy in the CEBAF experiment when POLDER was run as a polarimeter. The analyzing powers and unpolarized efficiencies were deduced from Eqs. 5.4-5.7 with a χ^2 minimization procedure (MINUIT).

Setup	H1 position in cm	H2 position in cm	Deuteron energies in MeV
position 1	32	110	140,160,170,180,200,210,220
position 2	40	135	240,250,260,280,300,320,340
position 3	49	165	360,375,390,420,450,485,520

Table 5.1: Distances of the hodoscopes to the center of the target for the three different setups of POLDER and the corresponding energies measured in the calibration runs

Chapter 6

Data Analysis and Results

6.1 Overview

The standard HALL C event reconstruction software ENGINE was used for the data analysis. ENGINE was developed at CEBAF to analyze the raw data from the standard detector packages, the HMS and the SOS (Short Orbit Spectrometer). For this experiment, the parts for SOS were substituted by the software package for the polarimeter POLDER, which was developed at Saclay and Grenoble in France. The whole software including the codes for the HMS and POLDER was written to run under HP unix system. The MIT group converted the software to a new version that can be run under Linux system. In ENGINE, the event reconstruction code read the raw events, decode the detector hits, generated tracks and particle identification information for each event, and performed physics calculations. In addition, it kept track of the hardware scalers and generated software scalers for the run. Four forms of output files were generated from ENGINE:

- Report files containing hardware software scalers and calculated detector efficiencies.

- HBOOK files containing the histograms to check detector performance and mon-

itor the hardware during a run.

- Ntuple files containing the event by event information for the physics analysis.

- Text files containing necessary information for the extraction of the tensor po-
  larization of the deuteron.

The input parameters, software scalers, histograms and tests were handled by
the CEBAF Test Package (CTP) [97]. In this chapter, the methods and procedure to
analyze the data from the CEBAF experiment and the Saturne calibration experiment
will be explained in detail. The dataflow chart in the data analysis is given in Figure
6-1. For the CEBAF data, after the coincidence trigger between the HMS and the
POLDER, cuts on the quantities measured in the HMS were applied to the e-d events
and charge-exchange (CE) events (as defined in Section 4.8.1). Therefore the events
left were mostly elastic e-d scattering events. Then cuts on the coincidence time
of flight (TOF) between HMS and POLDER was applied to these events to remove
most of the proton background. Next, the same data analysis procedure in POLDER
was applied to the e-d and CE events in both the CEBAF experiment data and
the calibration data. Various cuts (software constraint) to identify good deuterons
and good CE events are displayed in the dataflow chart. The e-d events surviving
the cuts on the ADC signals from the start detectors, the deuteron tracking in the
chambers, and the external cone of the deuteron were good deuteron events. The CE
events, which passed the above three cuts, the cuts on the time of flight (TOF) of
the hodoscopes, proton trajectories in the hodoscopes, and the internal and external
cones of the protons were good CE events. These various cuts will be explained in
detail in the following sections. Finally, with the number of good deuterons and good
CE events, the efficiencies related to the angular distribution of the two protons were
calculated.

The data analysis in the HMS is first described in Section 6.2, followed by Section
6.3 for the data analysis in POLDER. The efficiencies are discussed in Section 6.4. The

interpolation of the calibration results and the extraction of the tensor moments are explained in Section 6.5 and 6.6 respectively. The Instrumental asymmetries in ϕ are discussed in Section 6.7. The correction of the tensor moments due to the precession of the deuteron in the Dipole is described in Section 6.8. The systematic uncertainties are discussed in Section 6.9. The separation of the monopole and quadrupole form factors of the deuteron is described in Section 6.10. A comparison of the extracted and calculated t_{21} and t_{22} is discussed in Section 6.11.
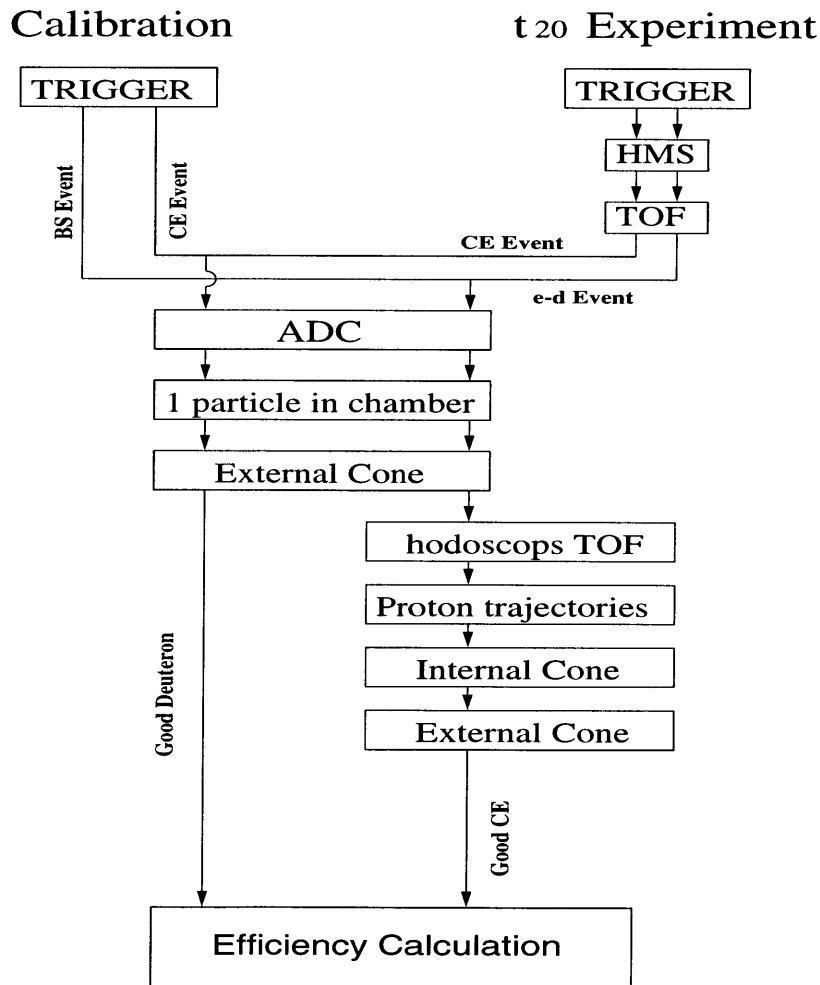
Figure 6-1: Dataflow Chart for the Saturne Calibration and the CEBAF Experiment.

The analysis of the six kinematics was carried out simultaneously and independently by four different groups. Each kinematic point was analyzed by at least two groups, and good agreement was obtained except for kinematics number 2. There is presently a significant discrepancy between the Saclay and MIT results. The MIT results are presented in this thesis. Table 6.1 shows the four groups involved in the data analysis and the kinematics analyzed by each group. The MIT group has analyzed kinematics 1-4, and numerical results are given below only for these points. Numerical results by other groups are given in Refs. [101, 38]. All six kinematics are shown in the graphs in Chapter 7 for the comparison with theories.

Kinematics	Grenoble	Saclay	Maryland	MIT
1	×	×		×
2	×	×		×
3		×		×
4		×	×	×
5		×	×	
6		×	×	

Table 6.1: Four groups involved in the data analysis and the kinematics analyzed by each group.

6.2 Data Analysis for the High Momentum Spectrometer (HMS)

6.2.1 Tracking in the HMS

The scattered electrons from e-d scattering were detected by the HMS. The trajectory of the electron was measured with two drift chambers. As described in Section 4.5.1, there are four x-like planes (x,x',u,v) and two y-like planes (y,y') in each chamber. In order to obtain both x and y information for the event reconstruction, it was required that 4 out of the 6 planes were fired and at least one y plane was fired for

each chamber. After the number of hits in each chamber was identified, the following main steps were done to find the track.

For each group of hits within a chamber, all the intersections of each pair of non-parallel wires were formed. The distance between all combinations of these intersections was calculated and tested to see if it were less than the space point criterion (typically 1.2 cm). Hits which satisfied this condition were grouped to form space points in each drift chamber.

To resolve the left-right ambiguity for each wire in the space point, short tracks in a given chamber (also called stubs) were fit to all possible left right combinations and the stub with the smallest χ^2 was chosen.

Finally, tracks were fit for each pair of stubs in the two chambers. The track with the least χ^2 was chosen and its position in the detection plane was recorded.
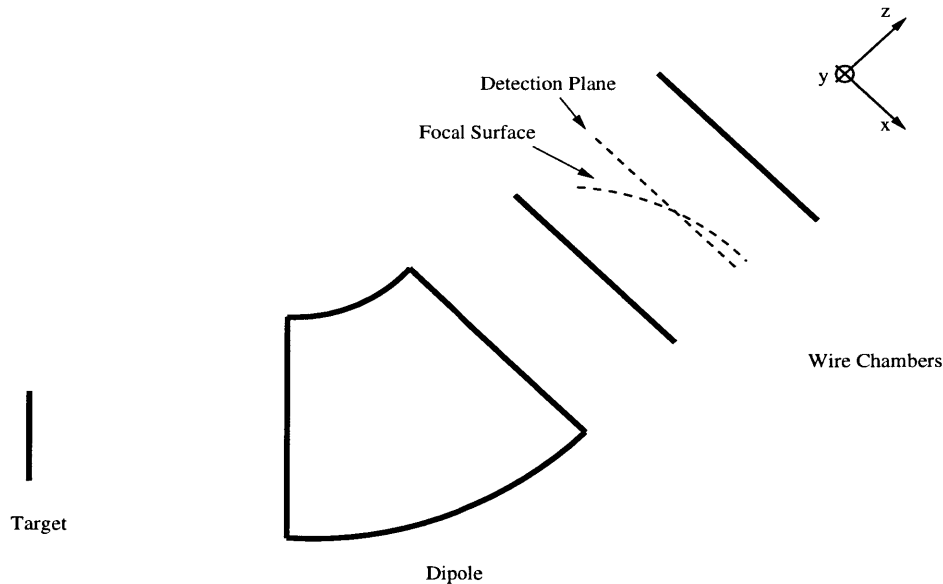
Figure 6-2: The HMS focal plane and its coordinate system.

The detection plane (also called the focal plane) was defined as the mid plane between the two drift chambers. the true focal plane of the spectrometer is actually

a surface tilted about 85° from the detector focal plane. At the focal plane, a given x corresponds to a certain value of momentum for a track. The right-handed coordinate system at the focal plane was defined as follows: x is the coordinate in the dispersive plane and $\hat{x}$ points downwards; y is the coordinate in the non-dispersive plane with $\hat{y}$ points to the left when looking at the spectrometer from the target; $\hat{z}$ is along the central ray with $z=0$ at the focal plane. The trajectory of the particle in the focal plane was described in terms of two positions (x_{fp} and y_{fp}) and two angles (x'_{fp} and y'_{fp}). The focal plane and the coordinates at the focal plane are shown in Figure 6-2. In terms of the quantities in the focal plane, the position and momentum of the particle at the target were reconstructed via Taylor expansion. The quantities reconstructed at the target were the relative momentum $\Delta p/p$ (also called δ), the position and angle in the scattering plane (y_{tar}, y'_{tar}) and the angle in the dispersive plane (x'_{tar}) of the event, with respect to the central ray in the spectrometer. The position in the dispersive direction (x_{tar}) was assumed to be known (usually $x_{tar}=0$) in the momentum reconstruction and was not reconstructed. Usually, the angles x'_{fp}, y'_{fp}, x'_{tar} and y'_{tar} were small enough that they were defined as the slopes of dx/dz and dy/dz at the focal plane and at the target separately. The target quantities can be expressed in terms of the quantities at the focal plane and the coefficients of the Taylor expansion, the transfer matrix elements.

$$X_i \;=\; \sum R_{ij} X_j \tag{6.1}$$

X_i stands for the target quantities and i refers to y_{tar}, x'$_{tar}$, y'$_{tar}$, and δ. X_j stands for the focal plane quantities and j refers to x_{fp}, y_{fp}, x'_{fp}, and y'_{fp}. R_{ij} is the transfer matrix element.

6.2.2   Cuts in the HMS

The deuterium target used in this experiment was an extended target with a to-
tal length of 12.4 cm. In the data analysis in the HMS, cuts on the reconstructed
quantities at the target (y_{tar}, y'_{tar} and x'_{tar}) were applied to the data to make sure the
scattering took place in the target. Figure 6-3, Figure 6-4, and Figure 6-5 show the
distribution of y_{tar}, y'_{tar} and x'_{tar} before (total) and after (shaded) the cuts respec-
tively. Most of the events in these spectra were selected except some events in the tail
of each spectrum. The coordinate z_v for the vertex position in the target was given
by $z_v = y_{tar}/\sin\theta_e$ (here θ_e is the electron scattering angle). The spectrum of y_{tar}
reflects the length (12.4 cm) of the deuterium target. z_v was used in the calculation
of the energy loss for the incident electrons, the scattered electrons, and the recoil
deuterons. The spectrum of x'$_{tar}$ and y'$_{tar}$ exhibit the acceptance of the spectrometer
HMS in θ (± 30 mr) and the azimuthal angle ϕ (± 70 mr).
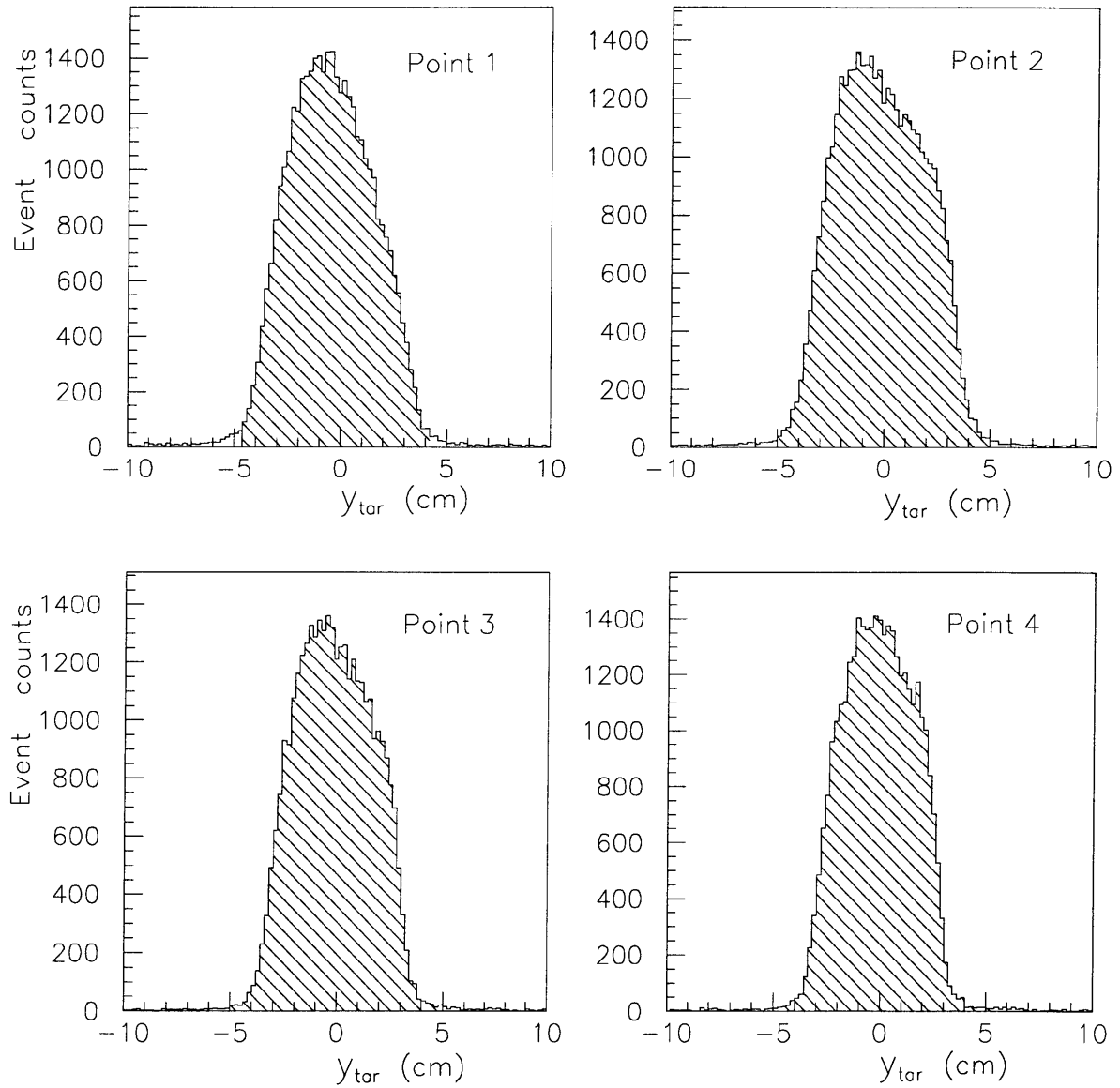
Figure 6-3: Spectra of y_{tar} for the four kinematics points. y_{tar} is related to the vertex position z_{beam} along beam direction via $y_{tar} = z_{beam}\sin\theta$, where θ is the electron scattering angle. The spectra reflect the length (12 cm) of the extended target.
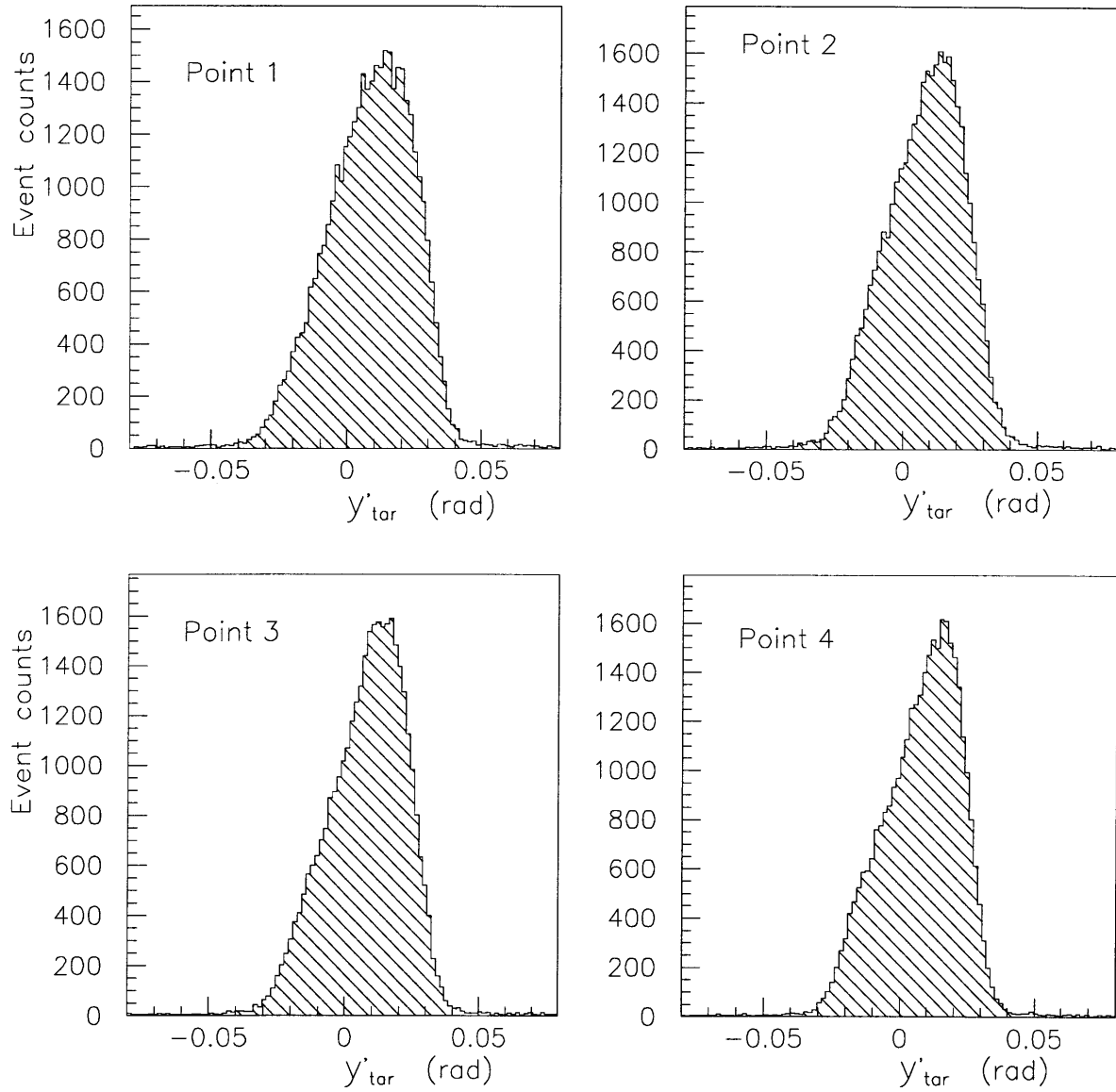
Figure 6-4: Spectra of y'_{tar} for the four kinematics points. y'_{tar} is defined as $dy_{tar}/$ dz. It shows the acceptance of the HMS in the scattering angle θ: ± 30 mr.
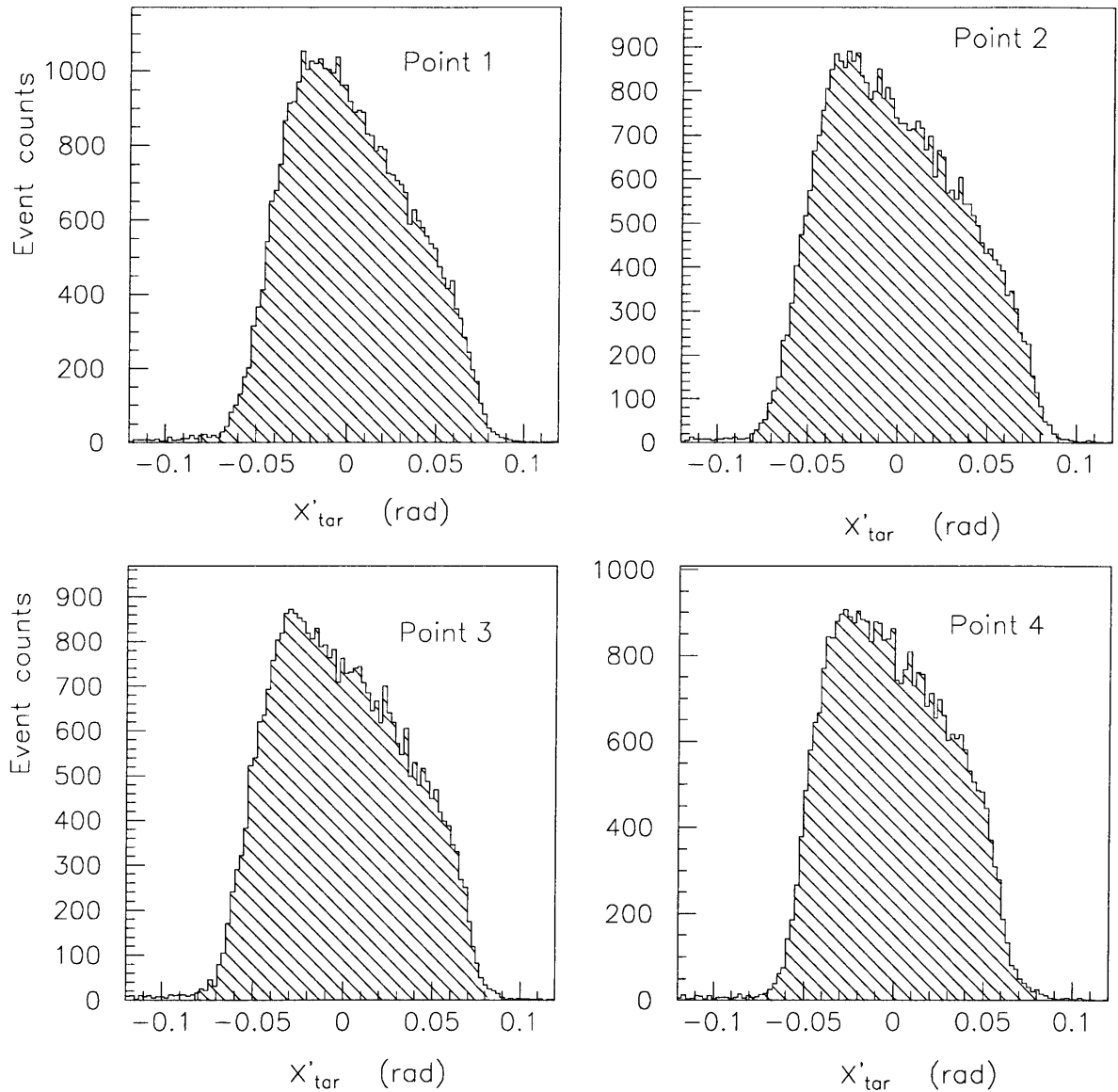
Figure 6-5: Spectra of x'_{tar} for the four kinematics points. x'_{tar} is defined as dx_{tar}/dz. It shows the acceptance of the HMS in the scattering angle θ: ± 70 mr.

In addition, a radiative cut was applied to the data on quantity δ_{cor}, which is the relative momentum (δ) after correcting for kinematic broadening. Thus the width of the spectrum of δ_{cor} is only due to the resolution of the spectrometer. Typical spectra

of the relative momentum δ and the relative momentum δ_{cor} after the kinematic correction are shown in Figure 6-6. The right peak in each spectrum consists of e-d elastic scattering events, while the inelastic events are in the right bump in the spectrum. Obviously, because of the kinematic correction, the elastic peak in the δ_{cor} spectrum was much sharper than in the uncorrected spectrum. Thus a cut on δ_{cor} is more efficient and reasonable to choose the elastic events than a cut on δ. The spectra of δ_{cor} for the four kinematics points before (total) and after (shaded) the radiative cut are shown in Figure 6-7. By requiring δ_{cor} to be in the range of the elastic peak, most of the elastic e-d scattering events were selected and were analyzed later for the good deuteron and CE event identification.
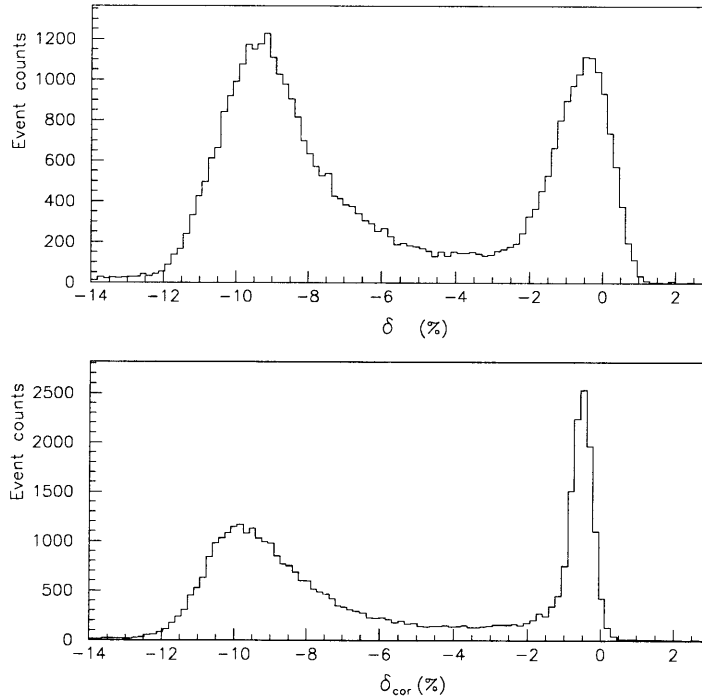
Figure 6-6: Spectrum of relative momentum δ (top) and δ_{cor} (bottom). δ, the relative momentum, is defined as $\delta = (p - p_0)/p_0$ where p_0 is the central momentum of the spectrometer. δ_{cor} is the relative momentum after the kinematic correction.
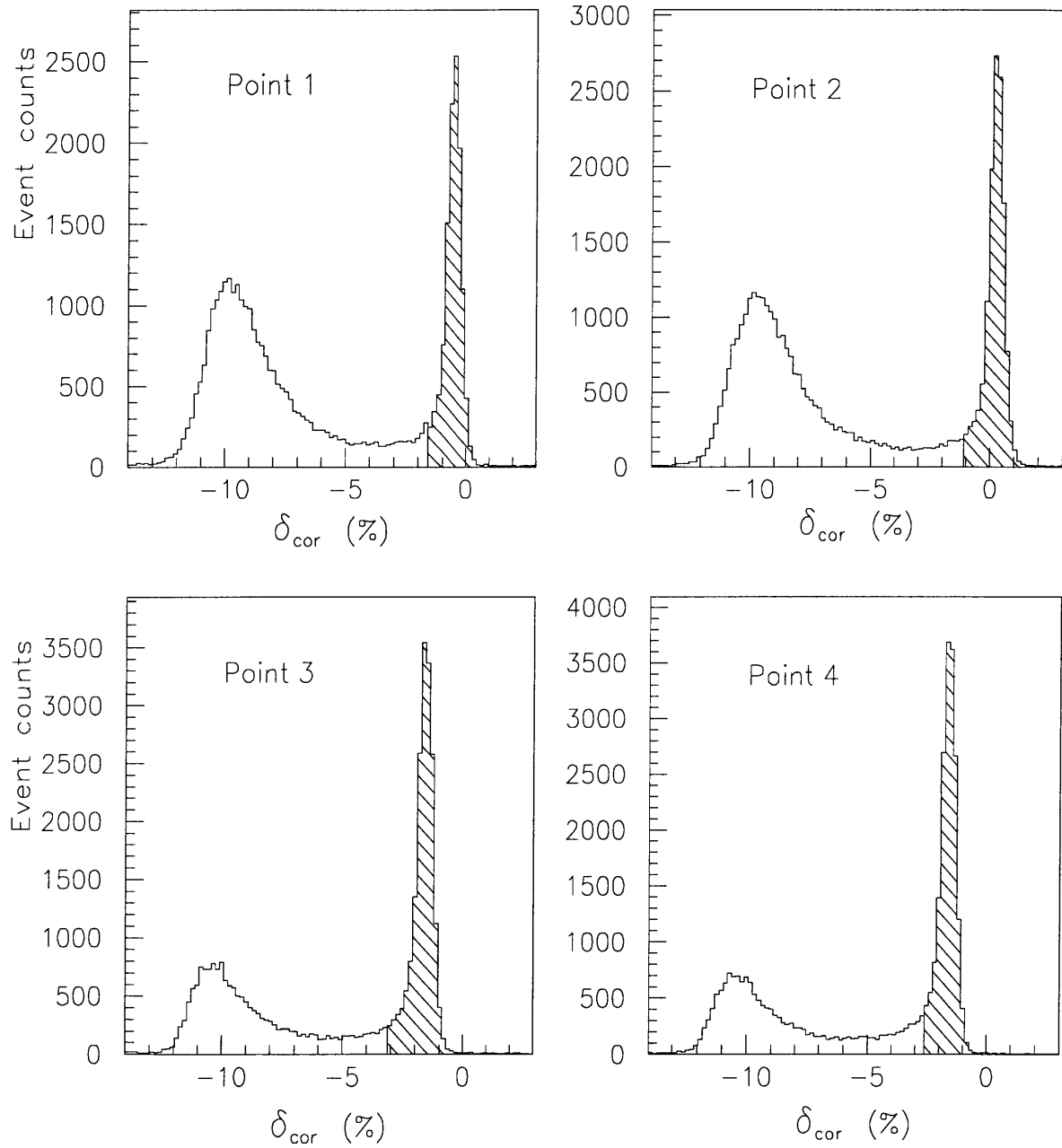
Figure 6-7: Spectrum of δ_{cor} before (total) and after (shaded) the radiative cut for the four kinematics points. δ_{cor} is the relative momentum after the kinematics correction.

6.3   Data Analysis in POLDER

The recoil deuterons from e-d elastic scattering were transported by the deuteron channel and were incident on the liquid hydrogen target (LH$_2$) where the charge exchange reaction ^{1}H($\vec{d}$,2p)n took place. As described in Section 4.7.2, the deuterons triggered two thin scintillator detectors S1 and S2. The tracking information of the deuteron was provided by the two multiple proportional chambers. The angular distribution of the protons from the ^{1}H($\vec{d}$,2p)n reaction was measured with two hodoscopes. In POLDER, the coordinate system (see for Figure 6-8) to describe the tensor polarization is right-handed with y axis downward, z is along the central axis of the detectors in POLDER, and as a result x pointing to the left when one looks in the direction of the incident deuteron. θ is the angle between incident deuterons and the center of mass of the two protons from the charge exchange reaction, ϕ is the angle between the e-d scattering plane and the ^{1}H($\vec{d}$,2p)n reaction plane.
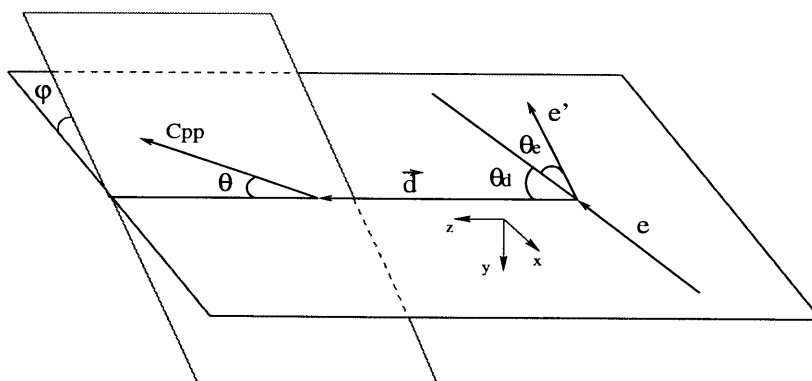
Elastic e-d Scattering   D(e,e $\vec{d}$)

Charge Exchange Reaction   H($\vec{d}$,2p)n

Figure 6-8: The coordinate system for t_{20} in POLDER: z is along the central axis of the detectors, y is downward, and x points to the left when one looks in the direction of the incident deuteron.

6.3.1 Deuteron tracking

The trajectory of the incident deuteron was reconstructed in the two wire chambers. Each chamber consisted of three planes. These wire chambers were able to detect multiple hits. For this experiment, the recoil deuteron was incident on the liquid hydrogen target, passing through the chambers. If more than one particles were found in the chambers, the event was classified as a background event. Therefore it was required that only one track be found in the chambers.

In each plane of a chamber, the TDC signal for each wire that fired was recorded and was tested to see if the TDC were smaller than a predetermined constant t_{max} and bigger than another predetermined constant t_{min} based on the TDC spectra. The hits which met these conditions were used to reconstruct the track of the deuteron. Hits close to one other within a criterion formed a cluster. A wire began a new cluster when its adjacent wire was not fired or the TDC difference with the adjacent wire was bigger than a predetermined criterion t_{diff}. Otherwise, this wire was in the same cluster with the adjacent wire and was added to the cluster. The coordinate of a cluster was the average coordinate for the hits in that cluster. The TDC of a cluster was the average value of the TDC's for the hits in that cluster. In each chamber, at least two planes with only one cluster were required for the clean track of the deuteron. The x and y coordinates of the deuteron at each chamber were calculated with the positions of the track in each plane. The directions dx/dz and dy/dz were calculated with the x and y information in the two chambers and the distance between them. The track of the deuteron was projected onto the midplane of the target and the planes of the two hodoscopes H1 and H2.

6.3.2 Proton tracking

The trajectories of the protons from the $^1H(\vec{d},2p)n$ reaction were reconstructed in the small hodoscope (H1) and large hodoscope (H2). The scattering angle θ and the

azimuthal angle ϕ were calculated from the tracking information of the two protons. The distributions of protons in θ and ϕ were recorded and were used to extract the tensor polarization.

Each of the two hodoscopes had two planes, with bars along x and y direction separately. All TDC's of the hits in each plane were first checked to see if they were in a range between limits $t_{hodomin}$ and $t_{hodomax}$ determined from the TDC spectra. Hits that satisfied this condition were accepted as good hits and were used for the tracking of protons. A quantity multiplicity μ was defined as the number of bars hit in each hodoscope. To reconstruct the tracks for the two protons, μ was required to be greater than 2 for both H1 and H2. In each hodoscope, a hit in a x-plane bar and a hit in a y-plane bar determine the position of a proton at this hodoscope. A pair of such positions at the two hodoscopes forms a possible track of a proton. All possible tracks were examined by looping over all hit bars in the four planes to form various combinations of proton trajectories. Three points for each combination, the hit positions P_1 and P_2 at the two hodoscopes and the point V_0 where the deuteron was incident on the hydrogen target at z=0 plane, were checked to see if they were in an almost straight line for a track. The angle α, which is $P_1\hat{V_0}P_2$, was calculated and required to be smaller than a criterion α_{max} (see Figure 6-9). In case several combinations satisfied this condition, the combination with the smallest α was accepted as the track of one proton, and the combination with the second smallest α was accepted as the track of the other proton. A typical α spectrum for Kinematics 4 is shown in Figure 6-10.
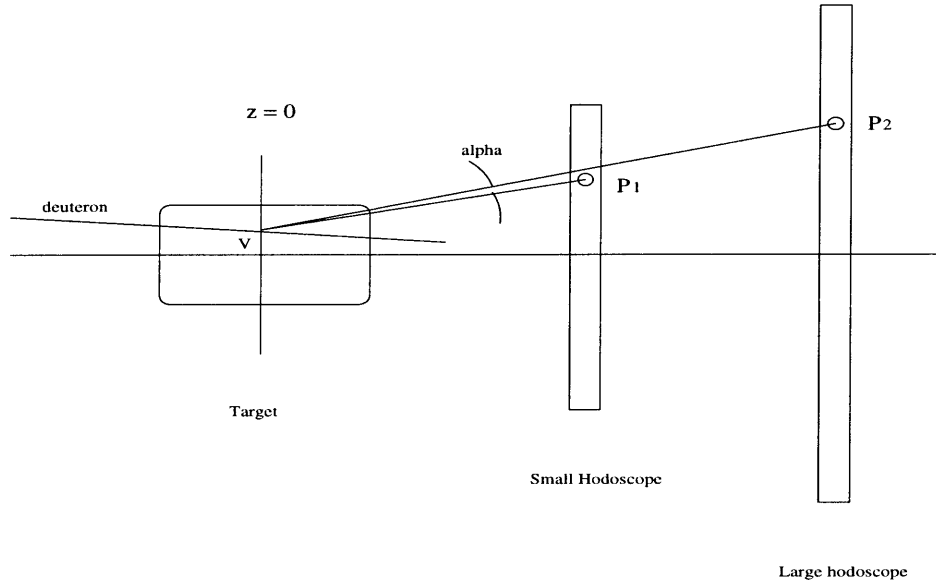
Figure 6-9: Schematic for α angle in geometry. α was defined as the angle $P_1\hat{V_0}P_2$, where V_0 is the intersection of the deuteron track with the z=0 plane. P_1 and P_2 are the positions for the bars fired in H1 and H2 respectively.

The coordinates x and y for the impact position of a proton in each hodoscope were calculated from the bars fired in the hodoscope. A randomization over the width of a fired bar was performed to fix a position for the proton. The resolution of x or y obtained in this way is the width of the bar. Although the randomization implies a degrading of the vertex and angle resolution, it is necessary to obtain smooth angle distribution for the extraction of the tensor polarizations from the MINUIT fit, which is explained in Section 6.6.
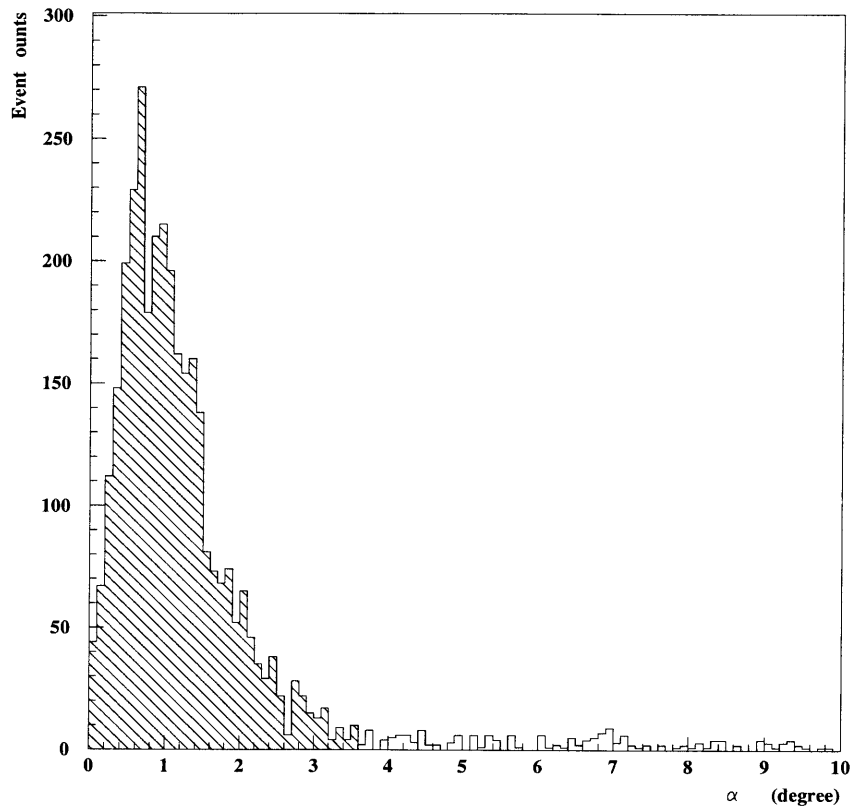
Figure 6-10: Spectrum of α angle in degree for Kinematics 4. A cut of $\alpha < 3.5°$ was applied to the data of Kinematics 4 for good proton tracks.

The vertex for the Change Exchange reaction was reconstructed from the trajectories of the incident deuteron and the two protons from this reaction. A vertex was calculated as the point that minimizes χ_v^2, the sum of distances to the three tracks. Because the deuteron track was defined with mm precision and the proton tracks with about 1 cm precision, the weights 100, 1, and 1 were applied to the deuteron track and to the proton tracks respectively in the sum of distances. Figure 6-11 is the spectrum for the vertex in the target. The resolution is about ± 10 cm.
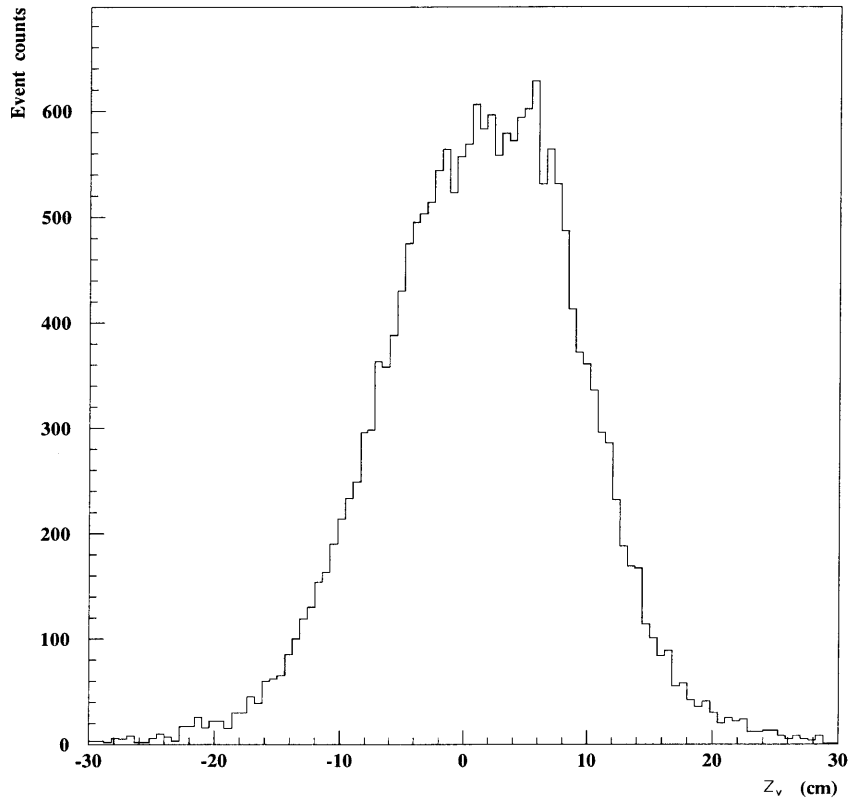
Figure 6-11: Spectrum of the z coordinate of the vertex in the hydrogen target.

In the Charge Exchange reaction, the two protons with similar momentum come out of the hydrogen target. The scattering angle (polar angle) θ for this reaction was calculated as the angle between the direction of the incident deuteron and the direction of the center of mass of the two protons. The azimuthal angle ϕ was calculated as the angle between the e-d scattering plane and charge exchange reaction plane as shown in Figure 6-8. The direction of the center of mass of the two protons was determined using the vertex and the mid point between the two proton positions at H2.

6.3.3 Cuts for good deuterons

Within the HMS momentum acceptance, many protons coming from the inelastic e-d scattering were detected in coincidence with the scattered electrons. These protons, with similar momenta to those of the recoil deuterons, had different velocities from that of the deuterons. In this experiment, most of these protons were removed from the raw data using the electronics by adjusting the coincidence timing between the deuteron channel and the HMS. The remaining background of random protons were almost completely removed with ADC and TDC cuts in the data analysis. The time spectra were measured with three methods for the coincidence timing between the deuteron channel and the HMS:

- TOF1, e-d coincidence time with the coincidence of S1 and S2 as the start signal and a resolution of 0.5 ns per channel;

- TOF2, the same definition as TOF1, but with a higher resolution of 0.1 ns per channel;

- TOF3, the coincidence time with the HMS trigger as the start signal and a resolution of 0.1 ns per channel.

Cuts were made on all three TDC spectra to identify the deuterons from the protons in the data analysis. TOF1, TOF2, and TOF3 are shown in the left spectra of Figure 6-12. The peaks for the deuterons are on top of the random proton background in each spectrum. The extra sharp peak in the right of the TOF3 spectrum was generated by the stop signal in the electronics.

The ADC from the start detectors S1 and S2 were also used to distinguish the deuterons from the background protons. After the deuteron triggered S1 and S2, the ADC signals were collected from the phototube at each end of S1 and S2. The sum of the ADC from S1 and S2 are shown at the top two spectra of Figure 6-13. Each ADC spectrum has two peaks. The peak with higher amplitude is for deuterons and

the other peak is for protons.

In order to have clean cuts on the TDC's, strict cuts on ADC from S1 and S2 were applied to the data such that only events in the second peak for the deuterons were chosen, as shown in the bottom of Figure 6-13. Then the three TDC spectra for these deuterons are plotted, as shown in the right of Figure 6-12. The cuts on TOF1, TOF2, and TOF3 were obtained from these clean spectra. A Gaussian fit was applied to the ADC spectrum after the strict cuts and the ADC cuts were obtained from the fit. After the ADC and TDC cuts, the proton background was only about 0.1%.

In the data analysis, the incident deuterons were tuned to ensure that the two protons hit the effective area of the two hodoscopes with no ϕ asymmetry bias. This was done by requiring the trajectories of the incident deuterons be in a cone. This cut, called the external cone cut, is equivalent to the requirement that the projections of the incident deuterons on H1 and H2 be within small circles. Typical spectra of the distance between the deuteron projection point and the center at H1 and H2 are shown in Figure 6-14. The two dimensional scatter plot of the deuterons at the target and the two hodoscopes are also shown in Figure 6-15 to give a clearer picture of this external cone cut. The radius r_d of the circle at each hodoscopes was optimized from the experimental data. Deuteron candidates which passed the HMS cuts, the ADC and TOF cuts, the timing cuts for the wires in the chambers (mentioned in Section 6.3.1, and the external cone cut were accepted as good deuterons.
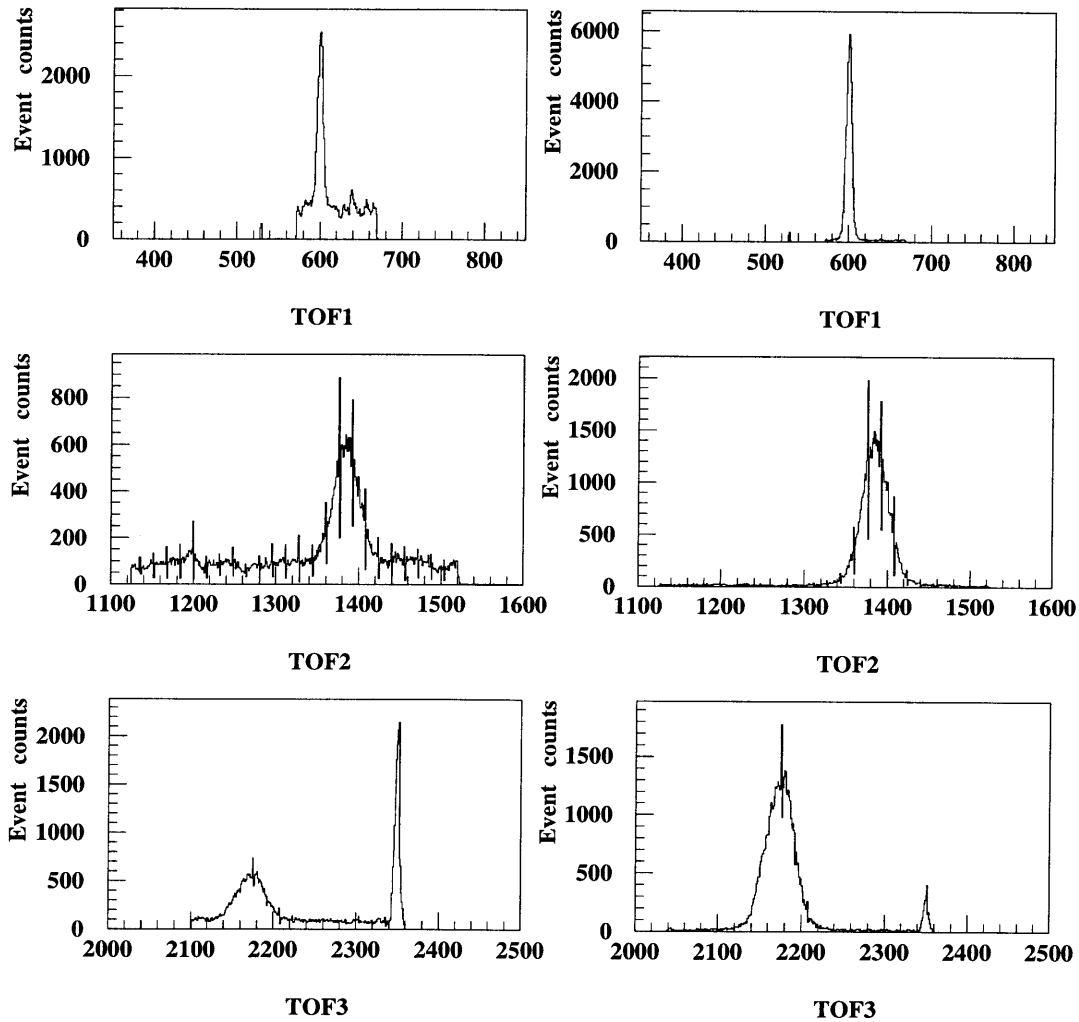
Figure 6-12: ed coincidence time spectra before (left) and after (right) the ADC cuts. The widths per TDC channel are 0.5 ns for TOF1 and 0.1 ns for TOF2 and TOF3.
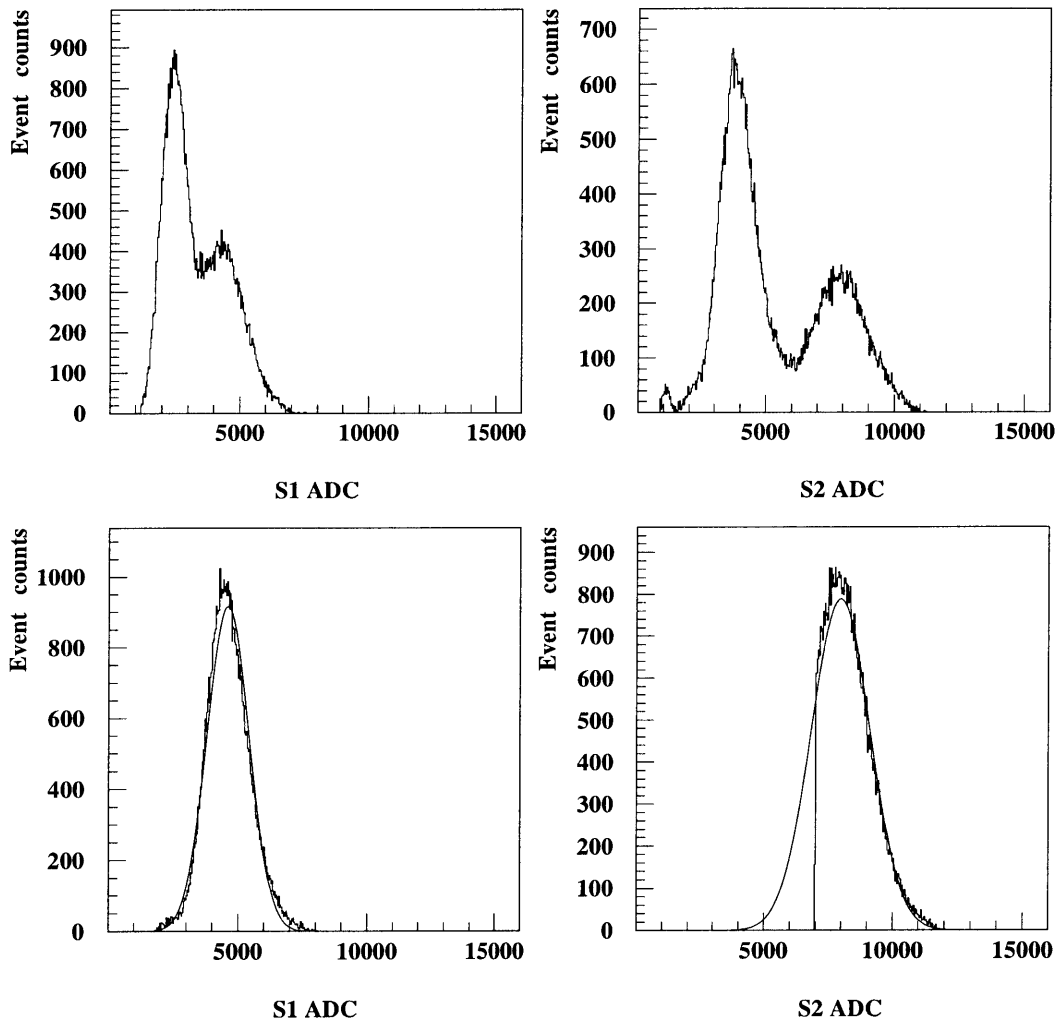
Figure 6-13: Spectrum of ADC from S1 and S2 before (top) and after (bottom) ADC cuts.
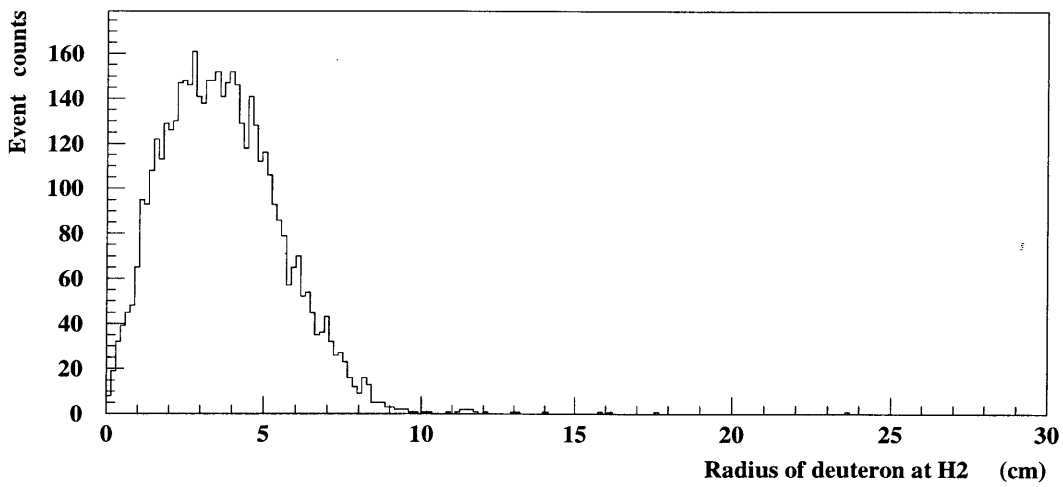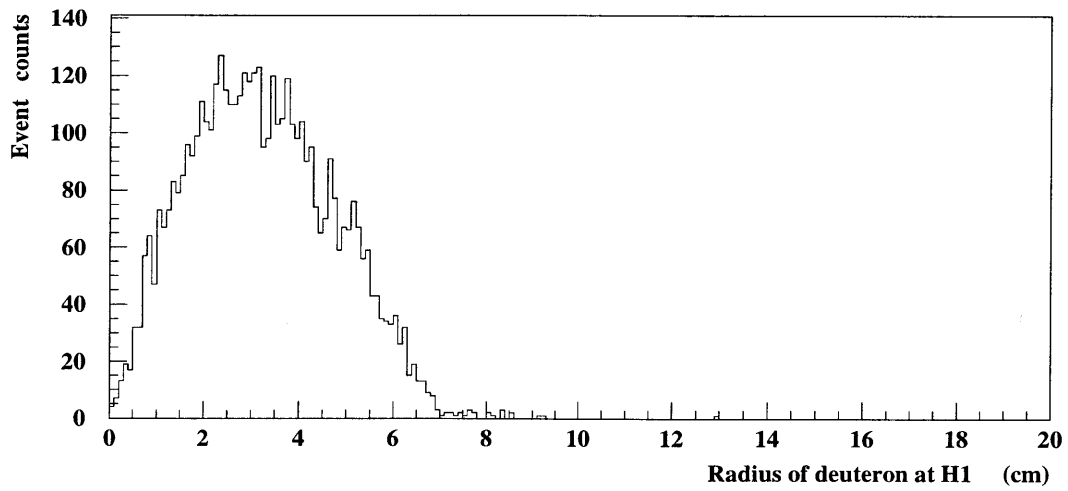
Figure 6-14: Radius of deuteron hits at H1 and H2.
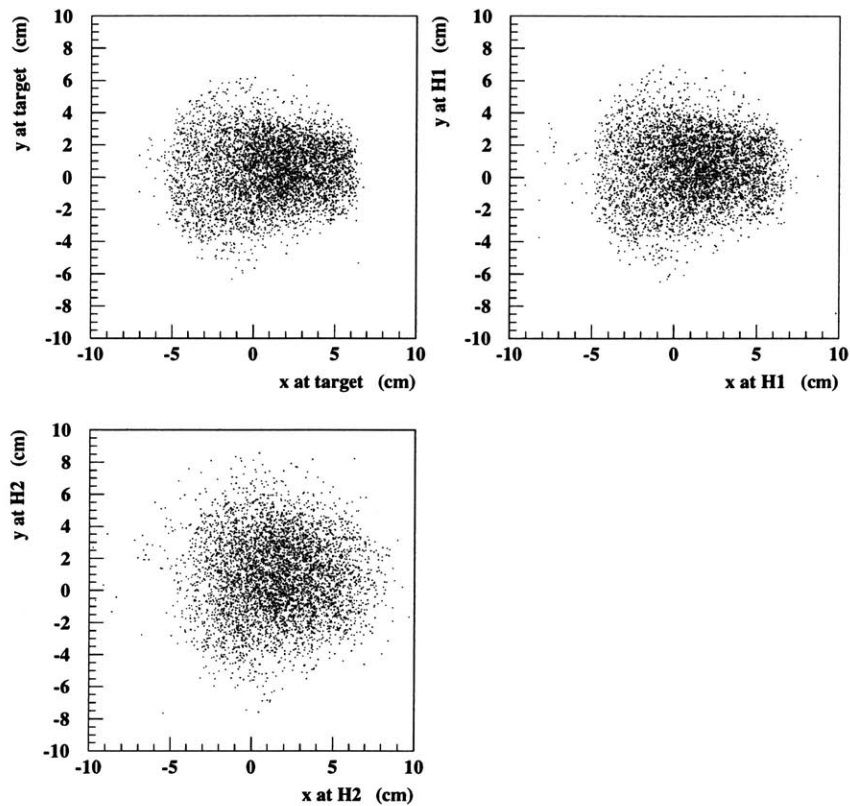
Figure 6-15: Scatter plot for the deuterons at the hydrogen target, H1 and H2.

6.3.4 Cuts for good protons

An external cone cut was applied to the protons as well. The protons were required to hit the effective area of each hodoscope within a ring centered at the deuteron projection point. The purpose for this cut is the same as for the deuteron external cone cut, i.e., there should be no ϕ asymmetry in geometry brought into the distribution of protons. The inner radius of the ring was the same as r_d used in the deuteron external cone cut. The outer radius of the ring was the radius of the effective area

for each hodoscope.

In addition, an internal cone cut was the requirement that the distance between the deuteron and a proton at the each hodoscope be bigger than a minimum value r_{min}. This cut eliminated events with protons too close to the deuteron track. It was originally introduced to get rid of accidental double deuterons at the SATURNE calibration run. In the end, the CE events surviving the HMS cuts, the TOF and ADC cuts, the proton trajectory cuts as described in Section 6.3.2, and the external cone and internal cone cuts were accepted as good CE events.

6.3.5 Special Proton Tracking Algorithm for Kinematics 1

The preliminary calibration results of the polarimeter POLDER showed that the unpolarized efficiencies decreased rapidly below 180 MeV [98]. The strong dependence of the unpolarized efficiency on the deuteron energy at these lower energies was due to the stopping effect of the low-energy protons from the charge exchange reaction. In Ref. [98], the percentage of events with more than 2 particles detected in the two planes of H2 was studied. This percentage decreased from 85% at 210 MeV to 30% at 140 MeV at the second plane, while it was roughly constant at 90% at the first plane for all the energies in the calibration experiment. This fact indicated that at least one proton from the charge exchange reaction stopped in the first plane of H2 for low-energy incident deuterons. As a result of the stopping effect, some CE events lost the multiplicity required at H2 and were not identified as good CE events. Thus the efficiency decreased rapidly with decreasing energy, leading to a larger systematic error for a given uncertainty of the deuteron energy. Losing protons could also cause a bad trajectory reconstruction since the angles θ and ϕ were calculated with the information at H2, as described in Section 6.3.2.

The mean deuteron energy for Kinematics 1 in the CEBAF experiment was about 170 MeV. It was in this energy range that the unpolarized efficiency was very sensitive

to the deuteron energy. A different algorithm [99][100] from the standard one (described in Section 6.3.2) was developed for the tracking of protons at this kinematics.

In the new algorithm, the requirement of the multiplicity at H2 (μ_2) was changed from $\mu_2 > 2$ to $\mu_2 \geq 2$. After a randomization at the bars of H1 and H2 for the proton positions, the vertex was reconstructed and was checked to see if it lay within the geometrical bound of the hydrogen target cell. The reconstructed vertex was used to calculate the α angle which was used to select the tracks for the two protons. Due to the stopping effect at H2, the trajectory of the second proton was reconstructed using H1 instead of H2.

In addition to the new algorithm, a special external cone cut was applied to the data for Kinematics 1. A small value of 5 cm and a large value of 8 cm were used for the radius of the cone at H1 and H2 respectively. Therefore, most protons were cut at H1 where the proton coordinates were determined more accurately.

With the new algorithm, the statistics of calibration data was increased by 10% at 170 MeV deuteron energy [100]. The spectrum of θ, ϕ, and $\theta_{relative}$ (the angle between the two protons) with the standard and the new algorithm are almost the same as shown in Ref. [100]. This implies that the new algorithm does not change the angular distribution of the charge exchange events, and the tensor moments extracted should be the same as those with the standard algorithm. Detailed description of this new algorithm can be found in Ref. [101].

6.4 Efficiency

In the data analysis, the efficiency ϵ is defined as:

$$\epsilon = \frac{N_{CE}}{N_d \overline{L}},$$

(6.2)

where N_d is the number of good deuterons, N_{CE} is the number of good CE events,

and $\overline{L}$ is the average length of the deuteron trajectory in the hydrogen target for the CE events. L was calculated as the distance between the two intersection points of the deuteron track with the upstream and end window of the hydrogen target. The profile of the upstream window of the target was fit with an analytical function given by

$$z_{uw} = Ar^2 + Br^4, \qquad (6.3)$$

where z_{uw} is the coordinate in mm in the beam direction, r is the radius in mm on the window, and A and B are the coefficients of the fit. The coordinates of the intersection point of the trajectory with the upstream window are the solutions of the two functions: the above fit function for the upstream window and the one for the trajectory of the deuteron. An iteration was used to get the solutions instead of a complicated analytical solution. The end window of the target consisted of two spherical parts and an annular part. The intersection point with the annular part of the end window was determined through an iteration while the cross point with the spherical part was calculated analytically, as shown in Figure 6-16.
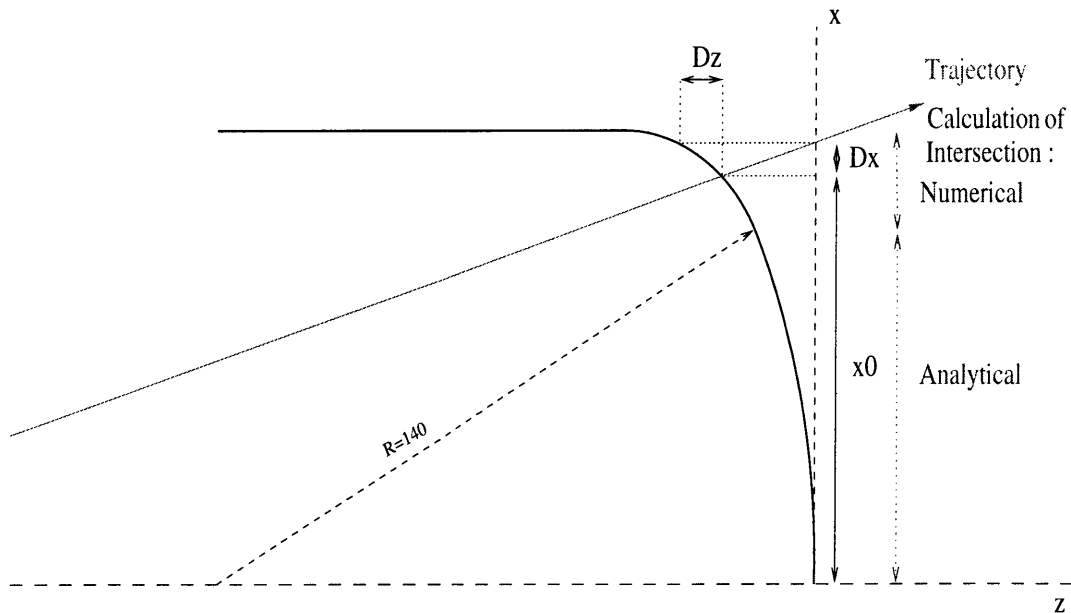
Figure 6-16: Geometry for the end window of the hydrogen target for the calculation of the inter-sections with the deuteron track. Figure taken from Ref. [102].

In Figure 6-17 and Figure 6-18, the efficiencies with the statistical error for each run for the four kinematics are displayed. Two dotted lines in the figure indicate ±1% of the average efficiency for all the runs. Two solid lines denote the statistical error of the average efficiency. From the figure, one can conclude that the efficiency was stable at 1% level during the experiment.
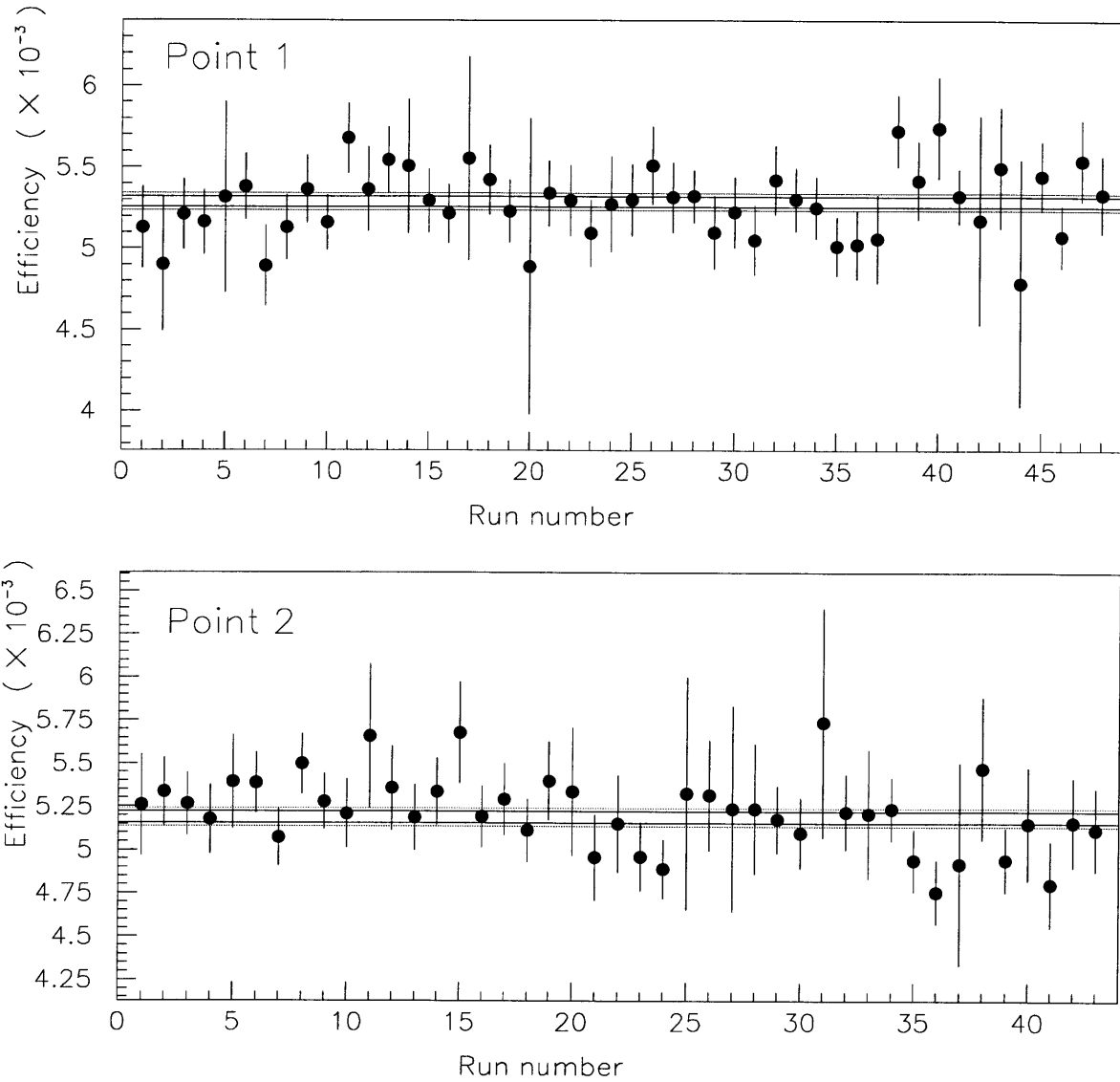
Figure 6-17: The efficiency with statistical error versus the run number for points 1 and 2. Two dotted lines indicate ±1% of the average efficiency. Two solid lines denote the statistical error of the average efficiency. The results for Point 1 were obtained using the special (Saclay) proton tracking algorithm. The results for Point 2 were obtained using the standard proton tracking algorithm.
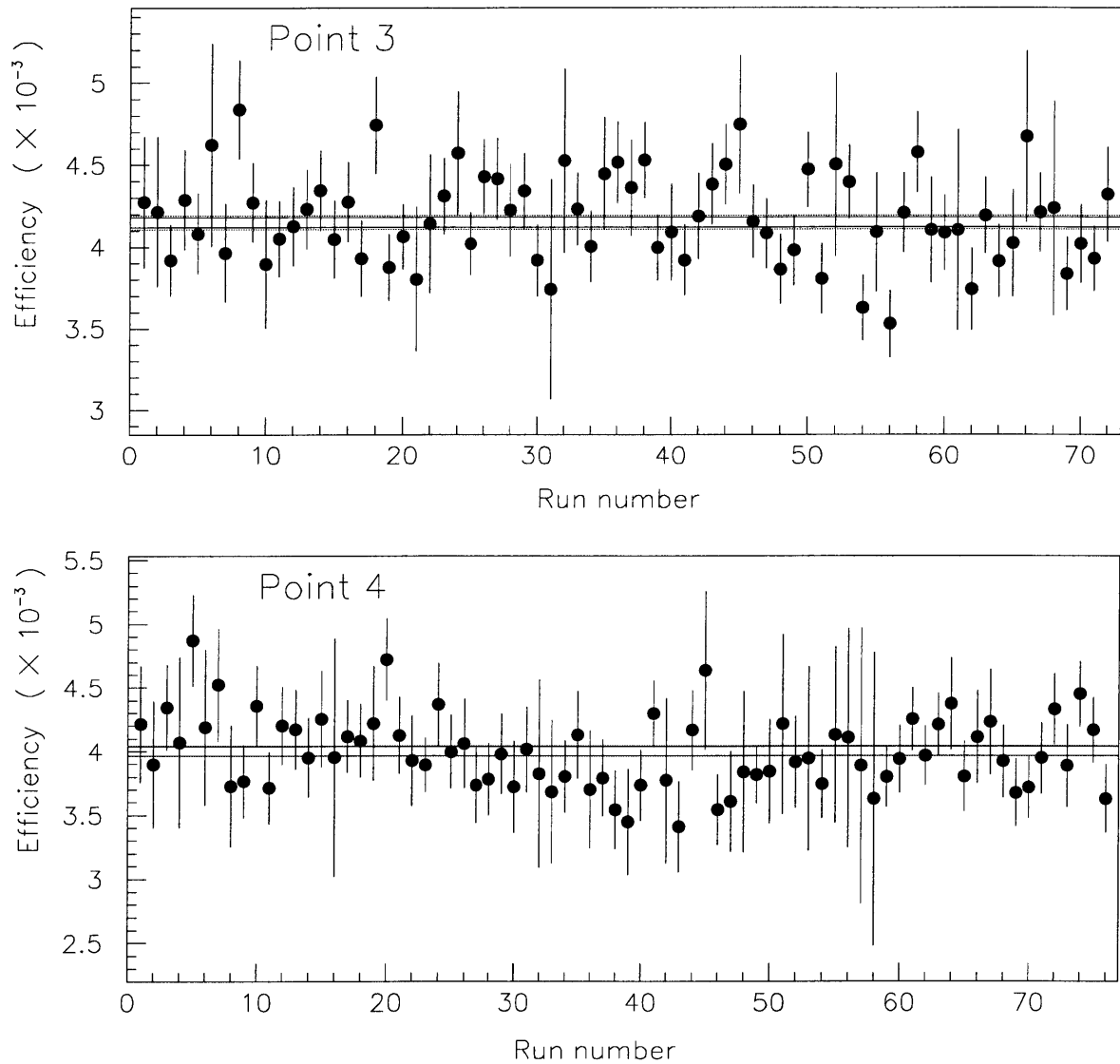
Figure 6-18: The efficiency with statistical error versus the run number for points 3 and 4. Two dotted lines indicate ±1% of the average efficiency. Two solid lines denote the statistical error of the average efficiency. The results for points 3 and 4 were obtained using the standard proton tracking algorithm.

6.5 Interpolation of Calibration Results

The analyzing powers and unpolarized efficiencies for the ^{1}H($\vec{d}$,2p)n reaction were measured for the deuteron energies from 140 MeV to 520 MeV with 10 to 20 MeV in steps in the calibration experiment. In the CEBAF experiment to measure the tensor polarization, the energies of the recoil deuterons did not necessarily match the energies of the deuteron beams in the calibration experiment. An energy interpolation was applied to get the analyzing powers and unpolarized efficiencies for the recoil deuterons at energies of interest. The uncertainty of the deuteron energy affects the accuracy of the interpolated analyzing powers and unpolarized efficiency. As a result, it affects the accuracy of the tensor moments extracted. In this section, the method of calculating the deuteron energy and the procedure to do the energy interpolation are explained.

6.5.1 Determination of Deuteron Energy

The energy T_d of the recoil deuteron from the e-d elastic scattering is related to the electron beam energy E_{beam}, the scattering angle θ_e and the momentum of the scattered electron. E_{beam} was measured using the Hall C arc beamline as described in Section 4.3.6. The angle θ_e and the momentum of the scattered electron were reconstructed in the HMS. A combination of any two among these three quantities can determine the energy of the recoil deuteron. Other methods, such as the kinematic shift in elastic and inelastic electron scattering from different mass target, were considered. The method using E_{beam} and θ_e was determined to have the best accuracy and was used to calculate the deuteron energy in the data analysis:

$$T_d = E_{beam} - \frac{E_{beam}}{1 + \frac{2E_{beam}\sin^2(\frac{\theta_e}{2})}{M_D}}. \tag{6.4}$$

The average energy loss of both incident and scattered electrons in the deuterium

target and of the deuterons up to the first chamber of POLDER were taken into account. As described in Section 6.2.2, the coordinate z_v of the e-d scattering vertex was calculated using the coordinate y_{tar} of the scattered electron in the target. z_v was used in the determination of the path length of the particles in the target for the energy loss calculation. The spectra of the deuteron energy for the six kinematics points are shown in Figure 6-19. The deuteron energies had large spreads of 20-60 MeV (FWHM). The shapes of the deuteron energy spectra were not symmetric. Due to this effect, the tensor polarization components were extracted at the weighted mean value $\overline{T_d}$ [103]. The errors due to this method are listed in Table 6.6 in Section 6.9 for the systematic error analysis for t_{20}. The four momentum transfer Q was calculated from the mean value of the deuteron energies at the vertex of the e-d scattering using Eq. 2.12.

Another method to determine the deuteron energy was used from the optics of the deuteron channel. This work was done by the Saclay group. It was found that the difference between the deuteron energy using this method and the values calculated kinematicaly was roughly 2 MeV for all the six kinematics. This difference of the deuteron energy was taken into account in the uncertainty of the deuteron energy determination.
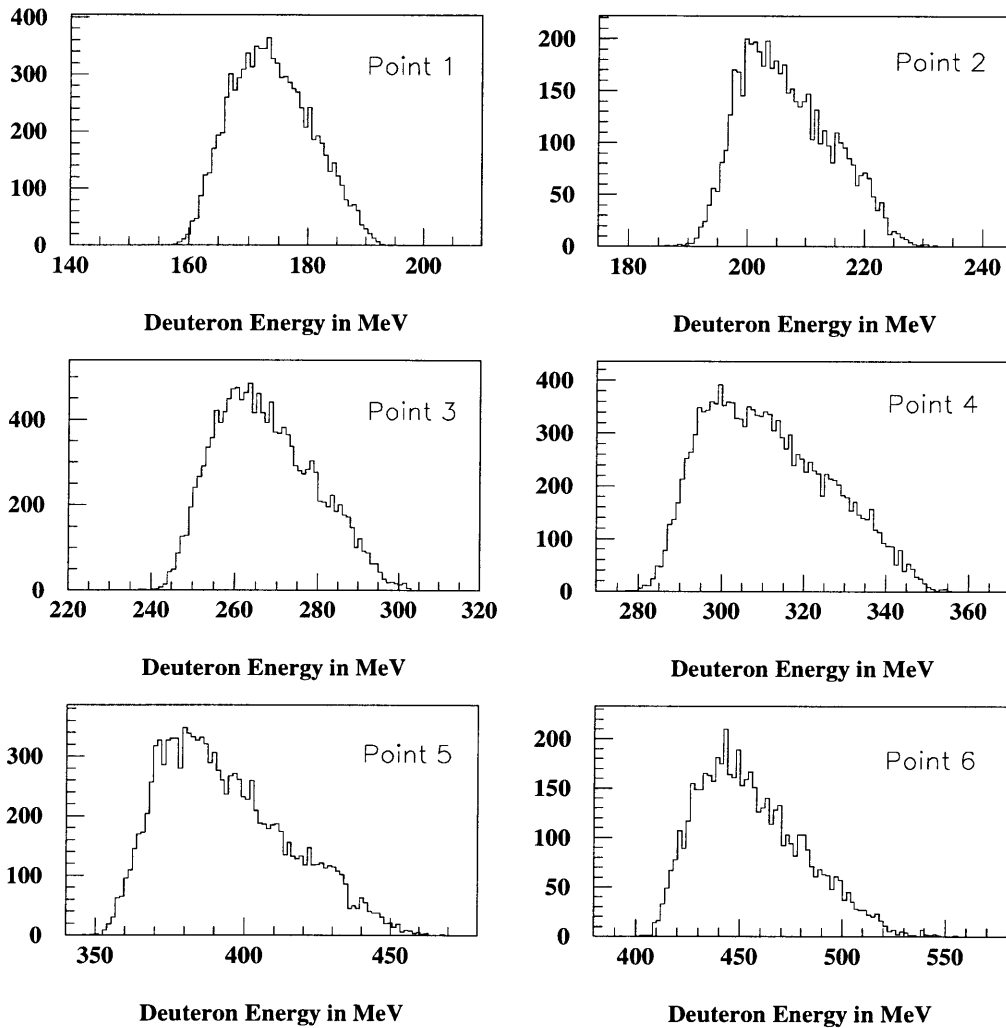
Figure 6-19: Deuteron energies for the six kinematics using the beam energy and the scattering angle of the electron.

6.5.2 Interpolation

The calibration data were taken at several incident deuteron energies for each of

the three positions of the two hodoscopes. During the CEBAF experiment, the hodoscopes were set at position 1 for Kinematics 1 and 2, at position 2 for Kinematics 3 and 4, and at position 3 for Kinematics 5 and 6 according to the deuteron energies. The interpolation of the unpolarized efficiency and the analyzing powers was done for each position separately. The results from the calibration were fit with a parametrization of the form

$$y = a + \frac{b}{T_d} + \frac{c}{T_d^2} \tag{6.5}$$

where y is either the efficiency ϵ_0 or one of the three analyzing powers T_{2q} at a given angle θ of the pp pair from the ^{1}H($\vec{d}$,2p)n reaction. a, b, and c are the coefficients from the fit.

The results for the analyzing powers and unpolarized efficiencies are shown in Figure 6-20, 6-21, 6-22, and 6-23 for the beam energies of 170, 200, 260, and 300 MeV which correspond approximately to the mean values of the deuteron energy in the four kinematics respectively. In the actual data analysis, the interpolation were made for the mean value of the deuteron energy distribution. The data exhibited a very smooth dependence on the four momentum transfer q. As shown in the figures, T_{20} and T_{21} are large for θ-bin number 1-9, while The T_{21} is small. T_{11} is consistent with zero. The effective unpolarized cross section, shown in the figures, were not corrected for geometrical detection efficiencies in the hodoscope and the rapid fall above 250 MeV/c was due to a decreasing detection efficiency in POLDER at large angles. The unpolarized efficiency is stable at 1% level as indicated by two dotted lines. Two solid lines stand for statistical error of the efficiency.

The unpolarized efficiency ϵ_0, the figure of merit F_{20}, and the analyzing power T_{20} as functions of the deuteron energy T_d for hodoscope position 1 and 2 are shown in Figure 6-24. The points in circle and square stand for the results for position 1 and 2 respectively. The points in filled and blank circle stand for the results using the new

(Saclay) and the standard proton tracking algorithm respectively. The unpolarized efficiency ϵ_0 is roughly constant for position 2, but it decreases with decreasing energy at the low deuteron energies for position 1. So the t_{20} extracted is very sensitive to the deuteron energy. F_{20} and T_{20} don't change too much with the deuteron energy T_d.
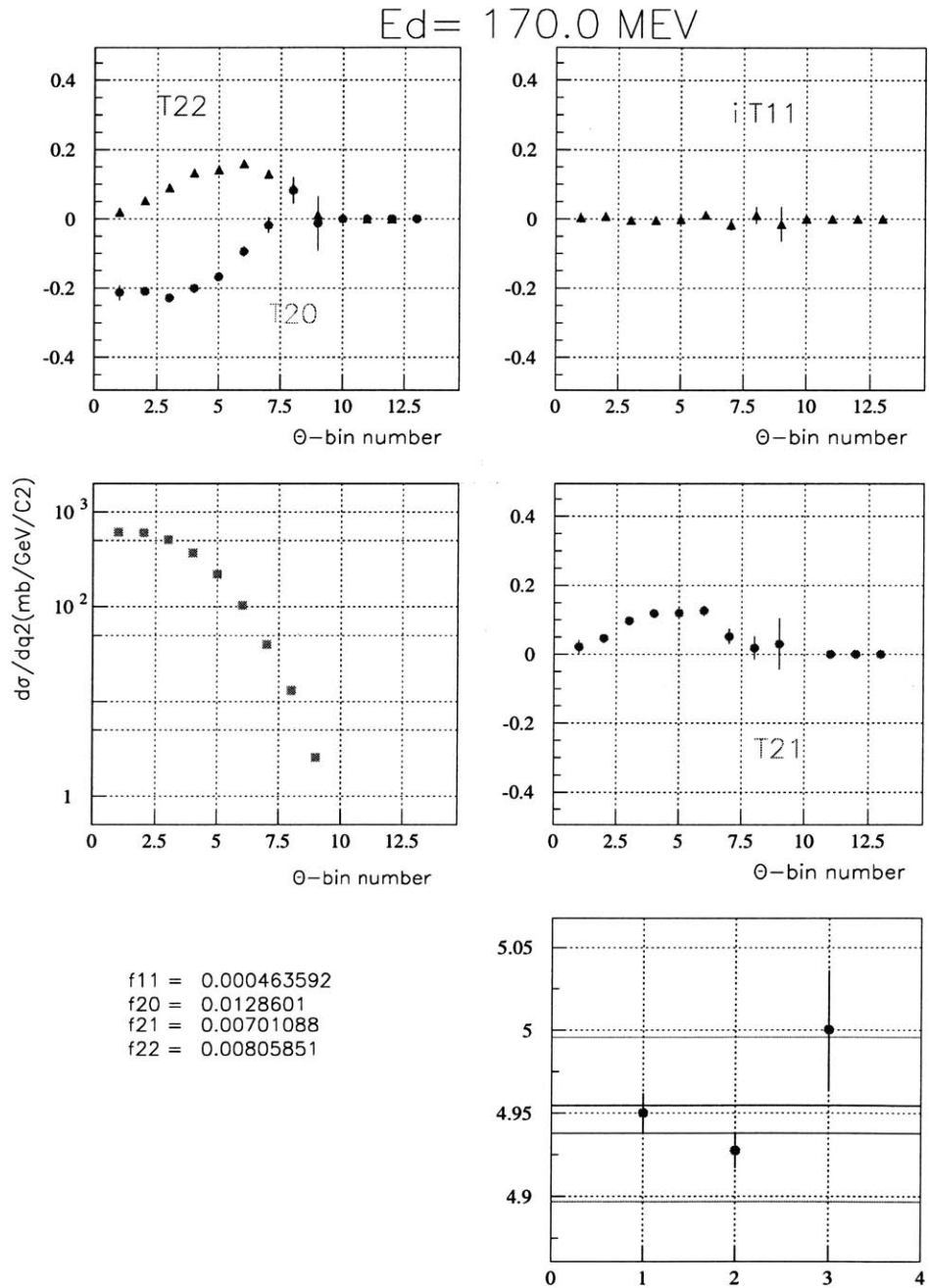
Figure 6-20: Analyzing powers, effective unpolarized cross section, and unpolarized efficiencies measured with the polarimeter POLDER for 170 MeV deuterons. The width of the θ bin is 2°. The results were obtained using the new (Saclay) proton tracking algorithm.
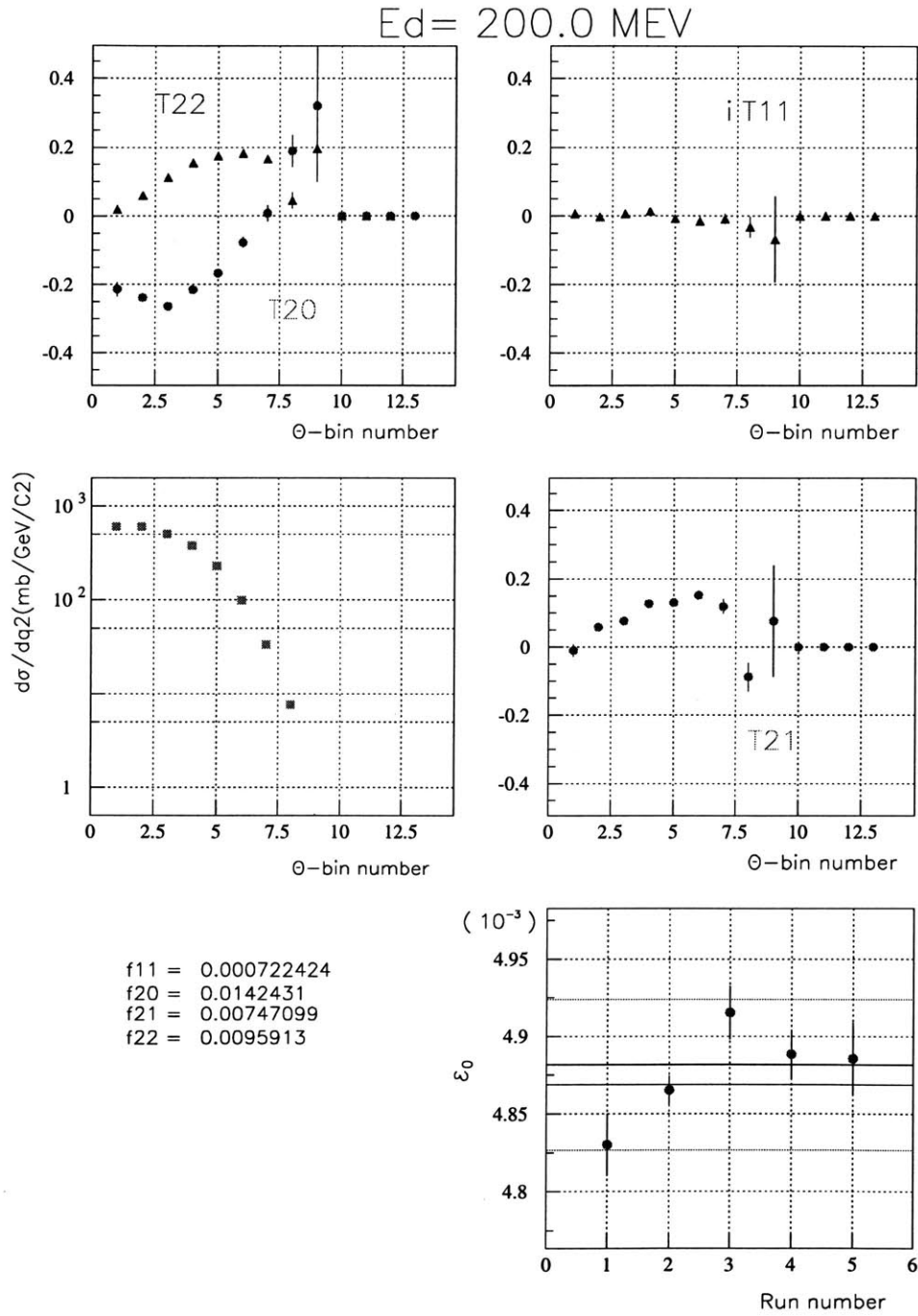
Figure 6-21: Analyzing powers, effective unpolarized cross section, and unpolarized efficiencies measured with the polarimeter POLDER for 200 MeV deuterons. The width of the θ bin is 2°. The results were obtained using the standard proton tracking algorithm.

Ed= 260.0 MEV

$$f11 = 0.000450134$$
$$f20 = 0.013882$$
$$f21 = 0.00748175$$
$$f22 = 0.0107316$$
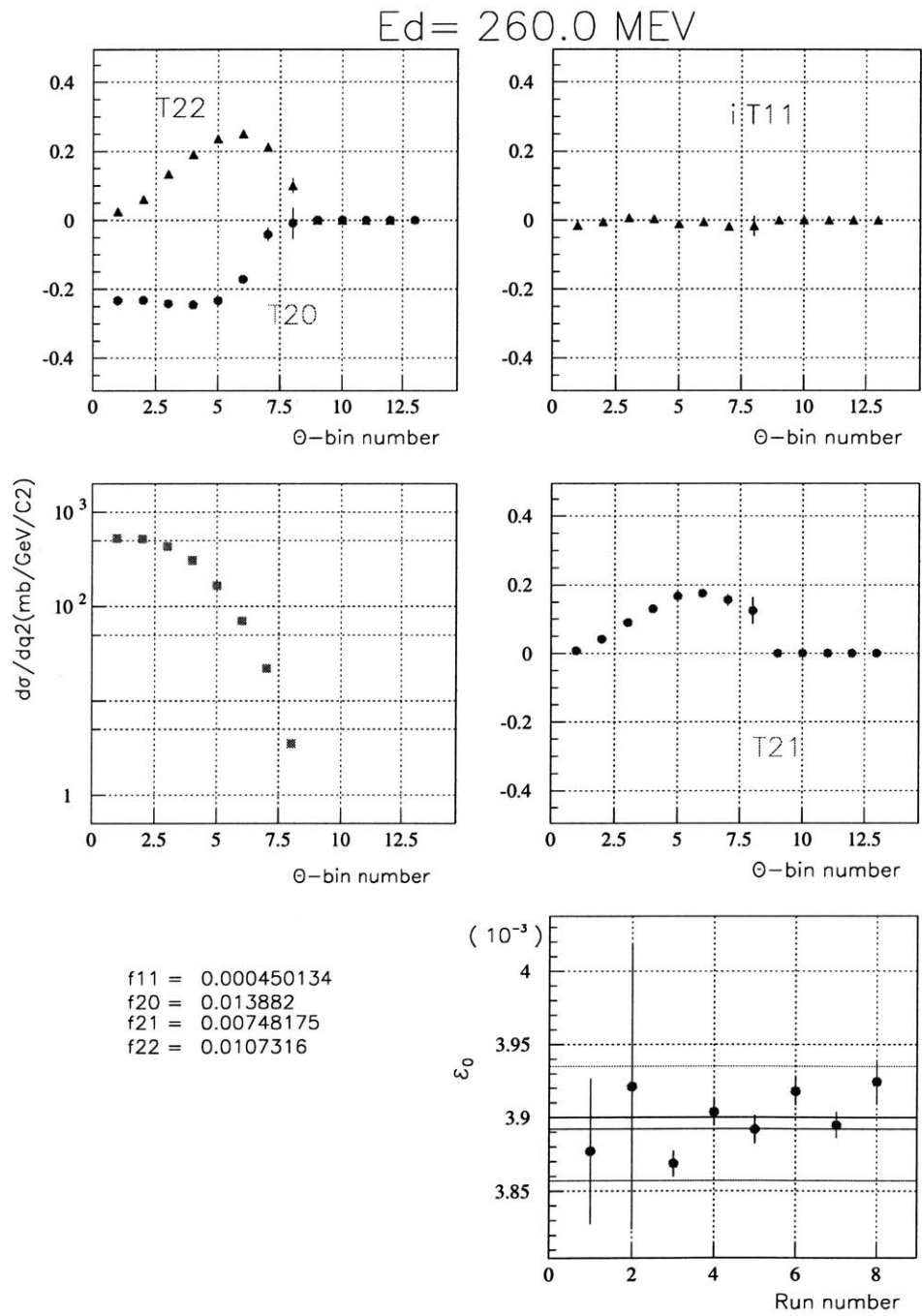
Figure 6-22: Analyzing powers, effective unpolarized cross section, and unpolarized efficiencies measured with the polarimeter POLDER for 260 MeV deuterons. The width of the θ bin is 1.67°. The results were obtained using the standard proton tracking algorithm.
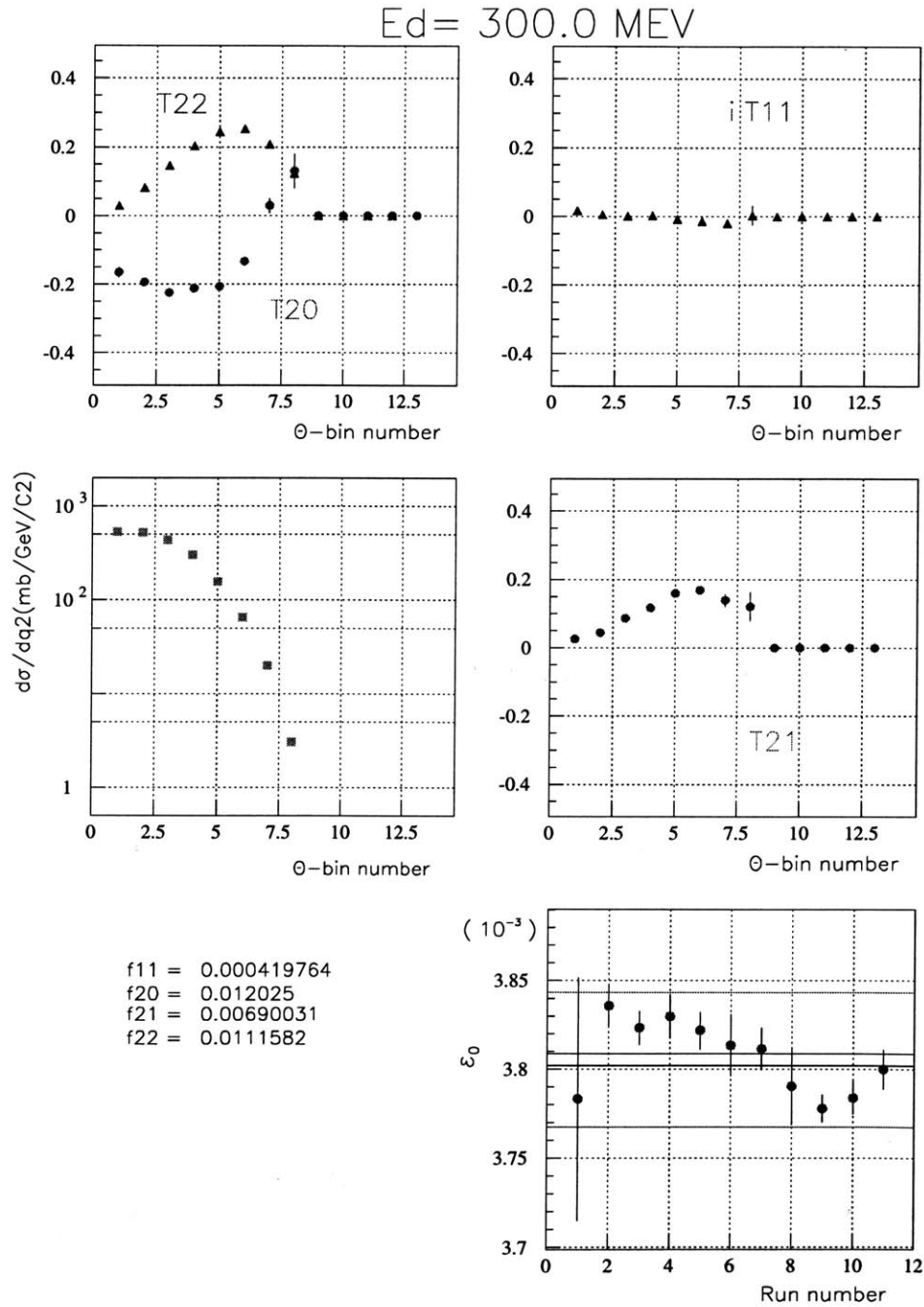
Figure 6-23: Analyzing powers, effective unpolarized cross section, and unpolarized efficiencies measured with the polarimeter POLDER for 300 MeV deuterons. The width of the θ bin is 1.67°. The results were obtained using the standard proton tracking algorithm.
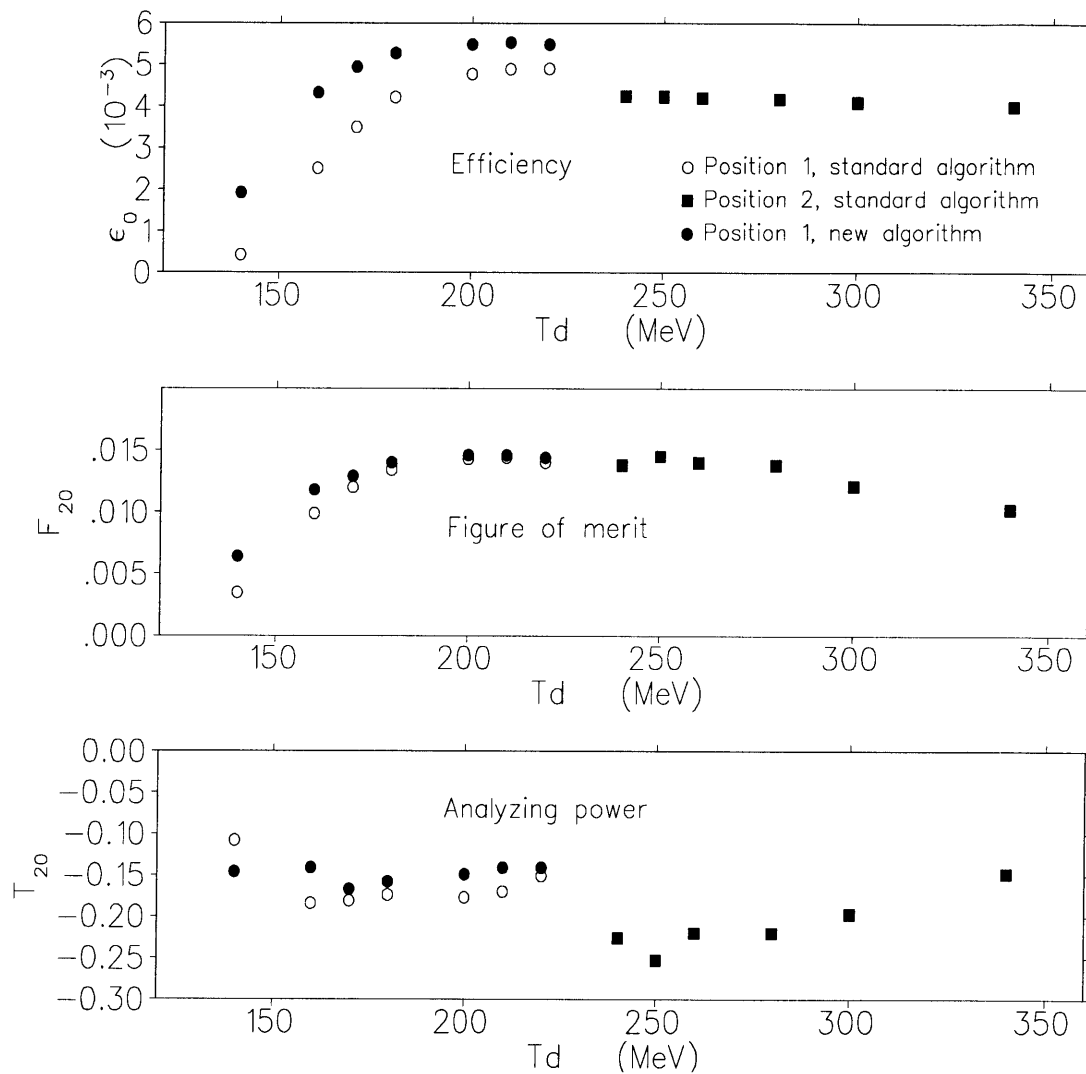
Figure 6-24: Unpolarized efficiency ϵ_0, figure of merit F_{20}, and analyzing power T_{20} as functions of the deuteron energy for the hodoscope position 1 and 2. The points in circle and square stand for the results for position 1 and 2 respectively. The points in filled and blank circle stand for the results using the new (Saclay) and the standard proton tracking algorithm respectively.

6.6 Extraction of Tensor Moments

The efficiency for the scattering of polarized deuteron beam in the CEBAF experiment is given by

$$\epsilon(\theta, \phi) = k\epsilon_0(\theta, \phi)[1 + t_{20}T_{20}(\theta) + 2t_{21}T_{21}(\theta)cos\phi + 2t_{22}T_{22}(\theta)cos(2\phi)] \qquad (6.6)$$

where ϵ_0 is the efficiency for the scattering of unpolarized deuterons, k is a normalization factor, t_{kq} are the tensor moments of the deuteron, T_{kq} are the analyzing powers for the polarimeter POLDER, θ and ϕ are defined in Section 6.3 as shown in Figure 6-8. The tensor moment t_{20} depends only on the θ distribution, while t_{21} and t_{22} depend also on the ϕ distribution.

The efficiency (or angular distribution) for the scattering of tensor polarized deuterons measured in this experiment was grouped in 12 bins in θ and 12 bins in ϕ. Then the angular distribution was integrated over ϕ from 0° to 360° and Eq. 6.6 becomes

$$\epsilon(\theta) = k\epsilon_0(\theta)[1 + t_{t20}T_{20}(\theta)] \qquad (6.7)$$

To extract the values of t_{20}, the data in the CEBAF experiment were fit using Eq. 6.7 first, with k and t_{20} as free parameters. In this fit, the normalization factor k was introduced as a free parameter. The polarimeter POLDER was operated in the same condition in the CEBAF measurement experiment as in the SATURNE calibration experiment, thus k should be close to 1. In the data analysis, once k was determined close to one, the data were fit again using Eq. 6.7 with k fixed to 1. The error of the extracted value of t_{20} with fixed k is smaller than that for free k. The fitting results with fixed k were chosen. The tensor moments t_{21} and t_{22} were extracted together with tensor moment t_{20} by fitting the data using Eq. 6.6, again with k free and k fixed to 1. The results with k fixed to 1 were chosen as the extracted values of t_{21} and t_{22}.

The χ^2 minimization technique was applied in the fit. The data were assumed to be sample from a Gaussian parent distribution and were grouped into 12 θ-bins and 12 ϕ-bins, covering the angular ranges $0 < \theta < 24°$ and $0 < \phi < 360°$. Some of the bins in the CEBAF data contain very few counts for the kinematics with high four momentum transfer. In these cases, it was assumed that the data were a sample from a Poisson parent distribution.

The method of maximum likelihood was used to derive the condition for the best fit. For Poisson statistics, the probability of observing $N_B(i)$ counts in bin i is given by

$$P_P(N_B(i), N_C(i)) = \frac{N_C(i)^{N_B(i)}}{N_B(i)!} e^{-N_C(i)} \tag{6.8}$$

where $N_C(i)$ is the mean value for the number of counts in bin i. If the number of counts in each bin is independent of each other, the probability of obtaining a given distribution is the product of the probabilities for each bin

$$P_T(N_B(i), N_C(i)) = \prod_i P_P(N_B(i), N_C(i)) \tag{6.9}$$

The most probable parameters are obtained by maximizing P_T, which is equivalent to minimizing the following quantity [104, 41]

$$\xi^2 = \sum_i \left[N_C(i) - N_B(i) + N_B(i)\ln\frac{N_B(i)}{N_C(i)} \right]. \tag{6.10}$$

To extract the tensor moment t_{kq} and k, $N_C(i)$ was replaced with the expression in Eq. 6.7 and $N_B(i)$ with the efficiency of the CEBAF data. The minimization code MINUIT [105] was used to minimize the quantity ξ^2. The results of the fit for the tensor moments t_{20}, t_{21}, and t_{22} are listed in Table 6.2. The uncertainties of t_{kq} are statistical uncertainties which represent one standard deviation uncertainty in the fit.

The results of the fit for t_{20} for the four kinematics using Eq. 6.7 are shown in

Figure 6-25 to 6-28. The cross points with a thin line joining them are the CEBAF data for the efficiency as a function of θ-bin number. The thick line stands for the unpolarized efficiency from the Saturne calibration experiment. The fitting results are listed in the bottom of the figure. the results for k were from the fit with k free. the results for t_{20} were from the fit with k fixed to 1. Two numbers following the value of k or t_{20} are the statistical errors from the calibration data and the CEBAF experimental data respectively. The χ^2 per degree of freedom in the figures were calculated using the standard χ^2 formula,

$$\chi^2 = \frac{1}{10} \sum_i \frac{[N_B(\theta_i) - N_C(\theta_i)]^2}{N_B(\theta_i)} \tag{6.11}$$

where $N_B(\theta_i)$ is the number of counts in bin θ_i from the CEBAF data, $N_C(\theta_i)$ is the counts in bin θ_i from Eqn. 6.7, and the factor 1/10 reflects 10 degrees of freedom in the data analysis for this experiment. The number of degrees of freedom was obtained by subtracting the number of parameters used (k and t_{20}) from the number of bins (12 θ bins).

An example of the ϕ distributions for the various θ-bins is shown in Figure 6-29. This figure shows the ϕ distributions and the fitting results for t_{20}, t_{21}, and t_{22} for Kinematics 4. The ϕ distributions for the other data points are qualitatively similar.

Asymmetry Fit for Kinematics 1

$k = 1.017 \quad 0.006 \quad 0.018$

$t_{20} = -0.675 \quad 0.012 \quad 0.038$

$\chi^2 = 0.8 \quad 0.2$
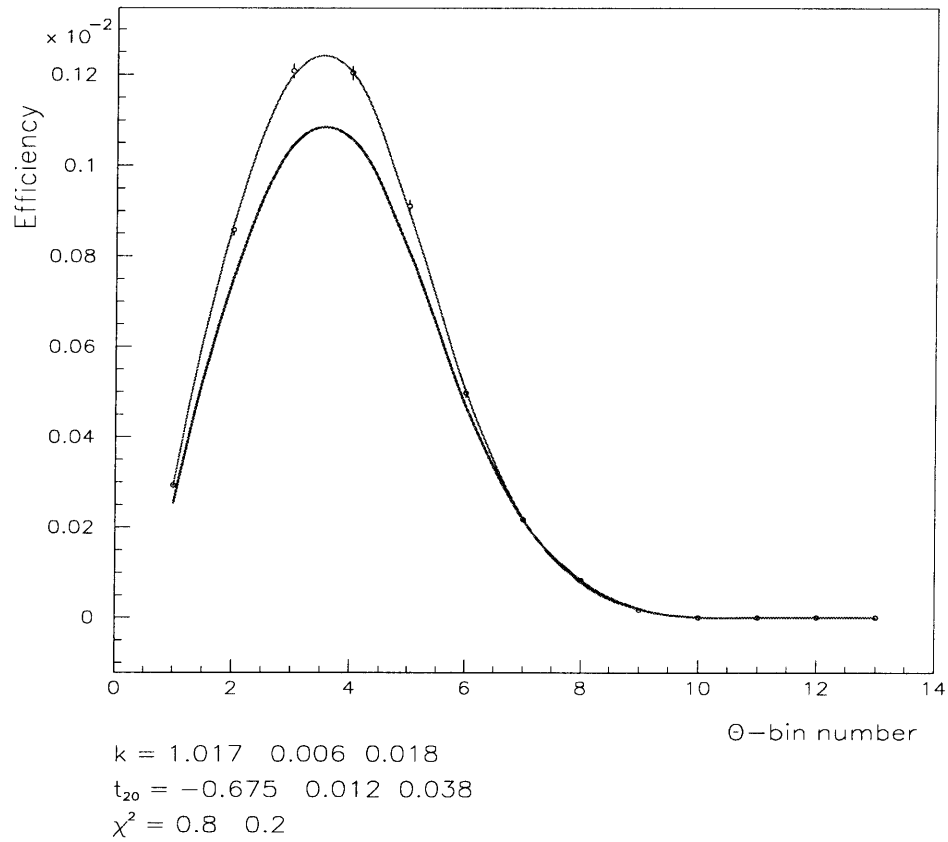
Figure 6-25: Fitting results for t_{20} for Kinematics 1. The cross points with the thin line joining them are the CEBAF data for the efficiency as a function of θ-bin number. The thick line stands for the unpolarized efficiency from the Saturne calibration experiment. For both k and t_{20}, the fitting results (first number) together with the statistical errors from the calibration data (second number) and the CEBAF experimental data (third number) are listed in the bottom of the figure. For χ^2, the result is shown with its statistical error.

Asymmetry Fit for Kinematics 2

$k = 0.991 \quad 0.003 \quad 0.021$

$t_{20} = -0.281 \quad 0.005 \quad 0.034$

$\chi^2 = 1.0 \quad 0.0$
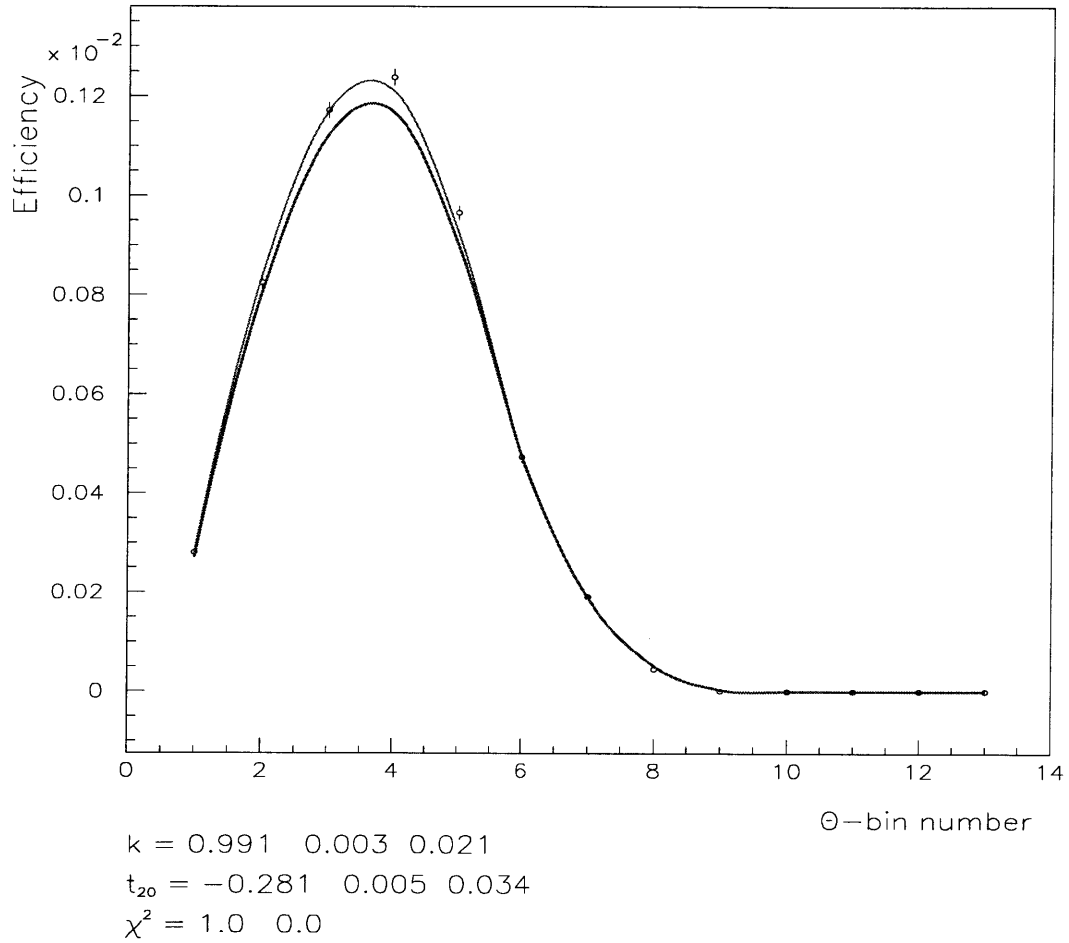
Figure 6-26: Fitting results for t_{20} for Kinematics 2. The same notation as in Figure 6-25.

Asymmetry Fit for Kinematics 3

$k = 0.991 \quad 0.004 \quad 0.028$

$t_{20} = 0.154 \quad 0.003 \quad 0.033$

$\chi^2 = 1.2 \quad 0.1$
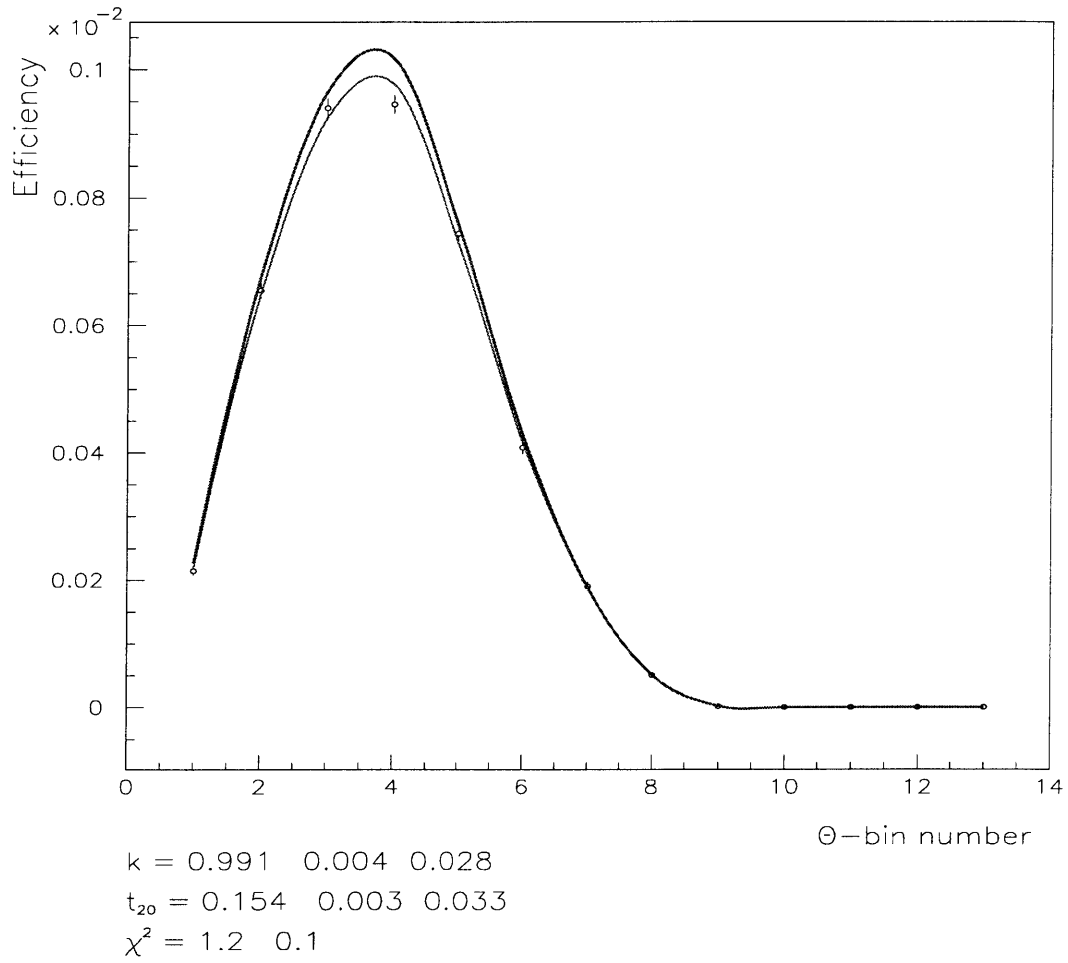
Figure 6-27: Fitting results for t_{20} for Kinematics 3. The same notation as in Figure 6-25.

Asymmetry Fit for Kinematics 4

k = 0.997   0.004   0.029
t_{20} = 0.255   0.005   0.050
χ^2 = 1.1   0.0
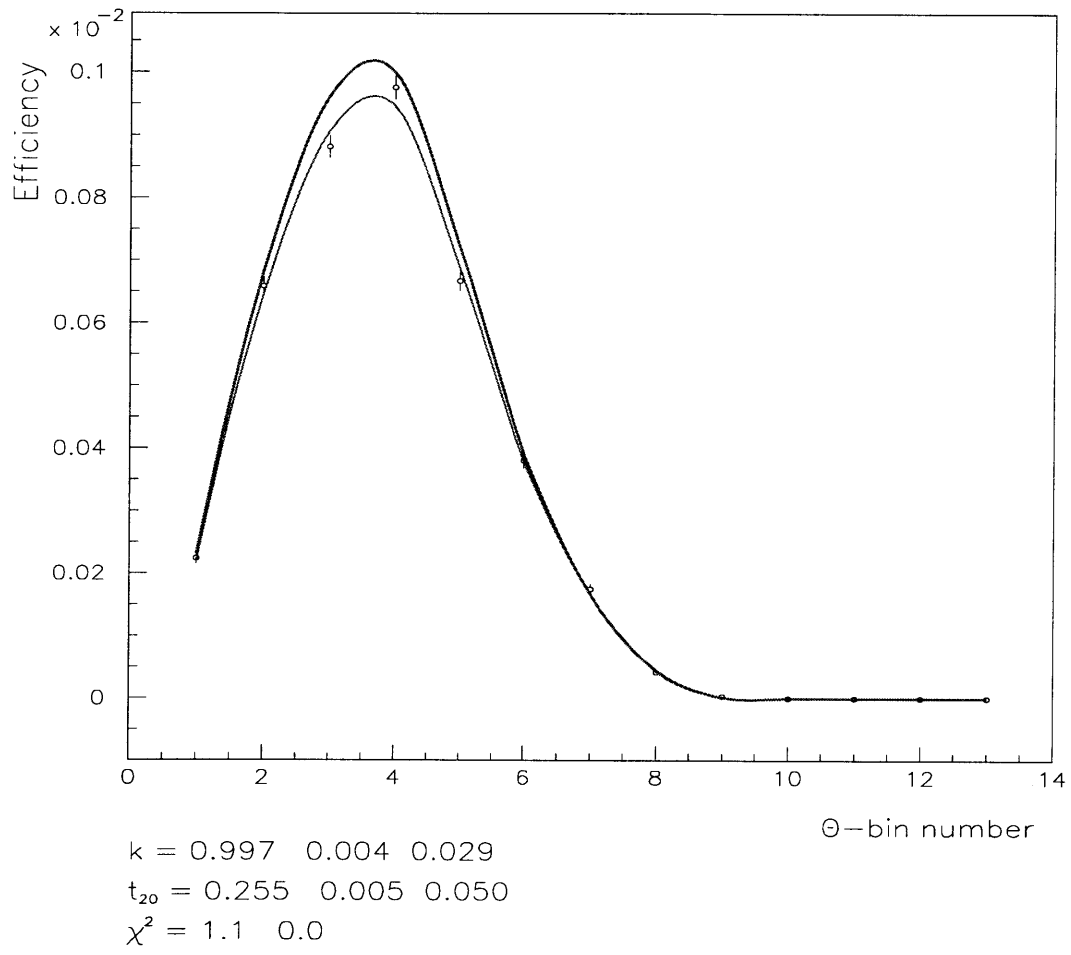
Figure 6-28: Fitting results for t_{20} for Kinematics 4. The same notation as in Figure 6-25.

Asymmetry Fit from ϕ distribution for Kinematics 4

$$t_{20} = 0.255 \quad 0.005 \quad 0.050$$
$$t_{21} = 0.210 \quad 0.005 \quad 0.058$$
$$t_{22} = 0.028 \quad 0.001 \quad 0.036$$
$$\chi^2 = 1.1 \; 0.0$$
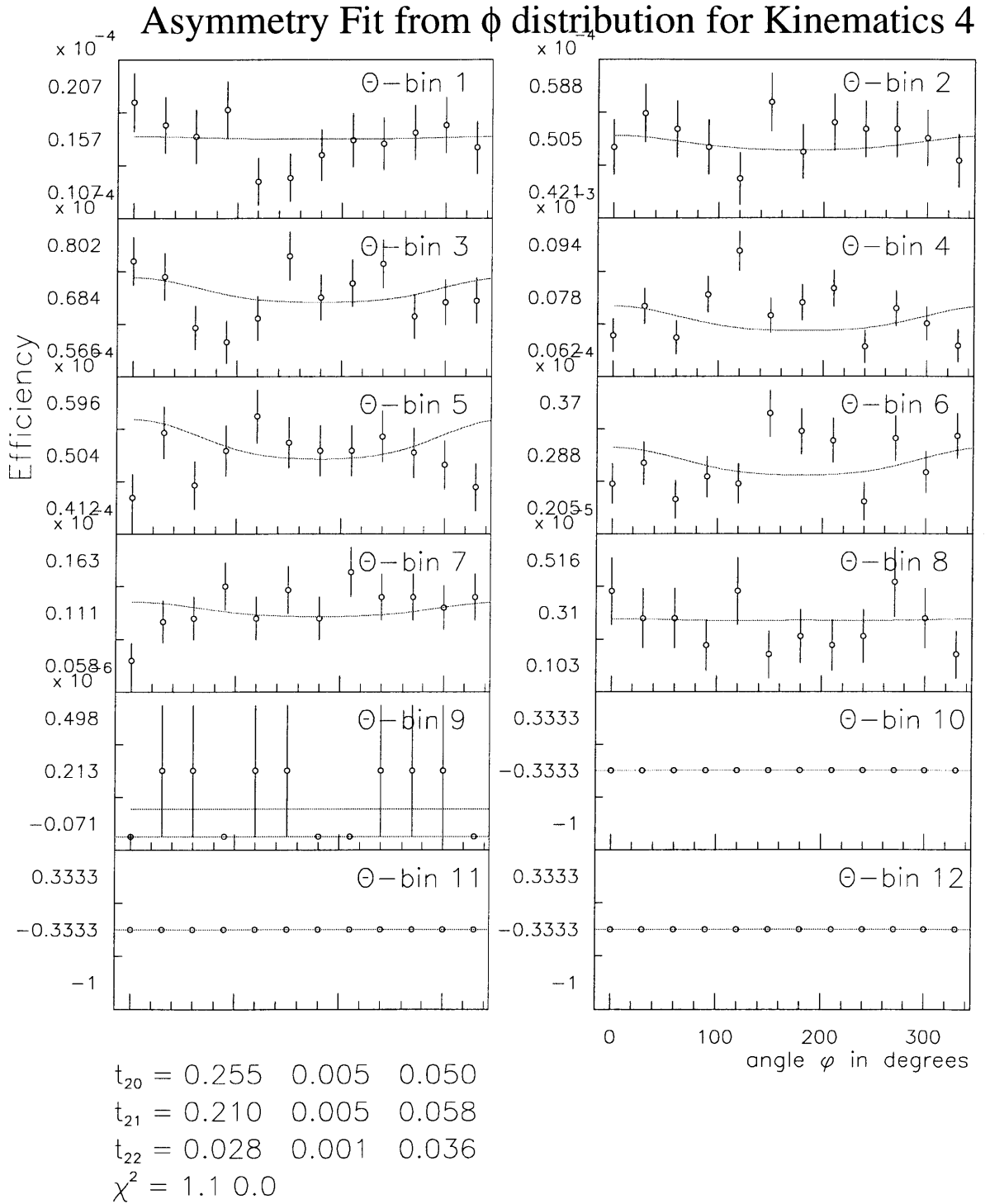
Figure 6-29: ϕ distribution and fitting results for t_{20}, t_{21}, and t_{22} for Kinematics 4.

Q (fm^{-1})	t_{20}	t_{21}	t_{22}
4.10	-0.675±0.038	0.413±0.053	0.115±0.044
4.46	-0.281±0.034	0.315±0.045	-0.028±0.034
5.08	0.154±0.033	0.194±0.043	-0.008±0.029
5.48	0.255±0.049	0.210±0.058	0.028±0.036

Table 6.2: Fitting results of t_{20}, t_{21}, and t_{22} using MINUIT. The uncertainties are statistical uncertainties which represent one standard deviation in the fit.

6.7 Unpolarized Asymmetries in ϕ

Some small instrumental asymmetries in the azimuthal angle ϕ were found both in the Saturne calibration data and the CEBAF experimental data. The asymmetries, intrinsic to the detectors in POLDER or the data analysis, bring bias into the extraction of the tensor polarization moments t_{20}, t_{21}, and t_{22}. The asymmetries were studied in both the calibration and experimental data and their effects on the extraction of the tensor polarization moments were evaluated analytically [98][106].

In general, the instrumental asymmetries in ϕ are expressed by including two terms of A(θ,ϕ) and B(θ,ϕ) in Eq. 6.6 as follows:

$$\epsilon(\theta, \phi) = \epsilon_0(\theta, \phi)[1 + t_{20}T_{20}(\theta) + 2t_{21}T_{21}(\theta)\cos\phi + 2t_{22}T_{22}(\theta)\cos(2\phi)]A(\theta, \phi)$$
$$+ B(\theta, \phi). \tag{6.12}$$

If there be asymmetry from background, the term B(θ,ϕ) will be nonzero. This was found not to be the case in this experiment. When the asymmetries are related to the detectors or generated in the data analysis, term A(θ,ϕ) will not be 1. The possible intrinsic asymmetries could come from a bad alignment of the detectors in POLDER, the assumption that the X and Y planes in a hodoscope have the same z position while they were not, or the geometry cuts used in the data analysis. The asymmetries were

studied by expressing $A(\theta,\phi)$ in the Fourier form of functions $\cos(n\phi)$ and $\sin(n\phi)$,

$$A(\theta, \phi) = \sum_{n=0}^{\infty} [a_n(\theta)\cos(n\phi) + b_n(\theta)\sin(n\phi)], \qquad (6.13)$$

where $\int_0^{2\pi} A(\theta,\phi)d\phi = 1$, $a_n(\theta)$ and $b_n(\theta)$ are the coefficients of asymmetry related to terms $\cos(n\phi)$ and $\sin(n\phi)$ respectively.

The asymmetry coefficients $a_n(\theta)$ and $b_n(\theta)$ were evaluated using the unpolarized calibration data. The quantities $a_n(\theta)$ and $b_n(\theta)$ were calculated as follows:

$$a_n(\theta) = \sum_{\phi} N(\theta, \phi)\cos(n\phi)/[\sum_{\phi} N(\theta, \phi) \sum_{\phi} \cos^2(n\phi)/12] \qquad (6.14)$$

$$b_n(\theta) = \sum_{\phi} N(\theta, \phi)\sin(n\phi)/[\sum_{\phi} N(\theta, \phi) \sum_{\phi} \sin^2(n\phi)/12] \qquad (6.15)$$

where $N(\theta,\phi)$ is the efficiency or yield for the $^1H(\vec{d},2p)n$ reaction. For the calibration data, the unpolarized efficiency which is the sum of yield for spin states 5 to 8, should not exhibit any asymmetries and the coefficients $a_n(\theta)$ and $b_n(\theta)$ should be zero. Non-zero coefficients implies the existence of the asymmetries. The results of the asymmetry coefficients a1, a2, b1, and b2 from the unpolarized calibration data are shown in Figure 6-30 to Figure 6-33. In these figures, the coefficients are shown versus the θ-bin number for the deuteron energies of 170, 200, 260, and 300 MeV, which correspond approximately to the mean deuteron energies for the first four kinematics in the CEBAF experiment. One can see that the ϕ asymmetry exist for the large θ-bin numbers (> 6) and the asymmetry effect is bigger for Kinematics 1 and 2 than Kinematics 3 and 4.
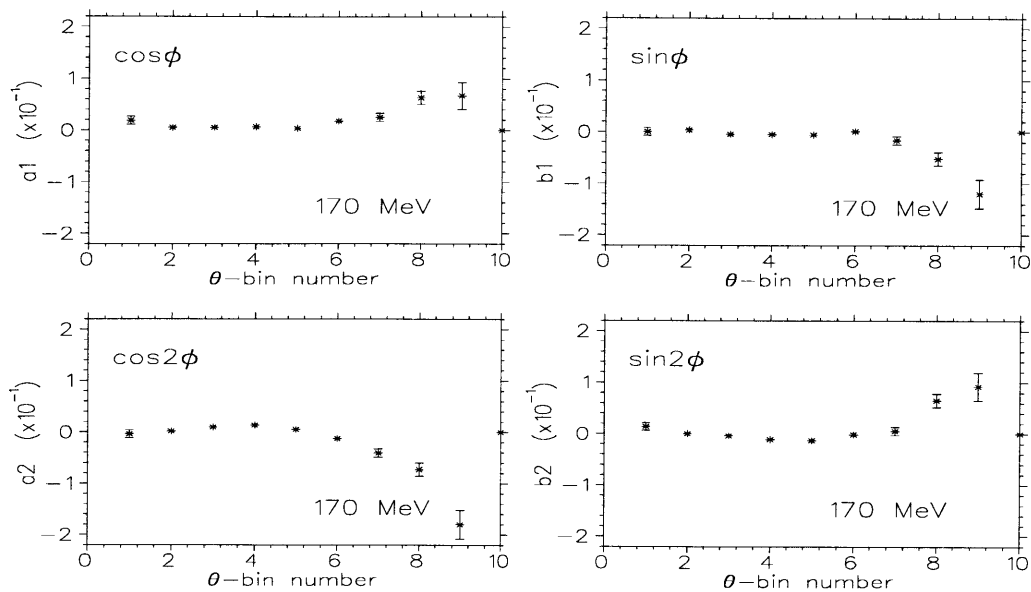
Figure 6-30: Asymmetry coefficients a1, a2, b1, and b2 corresponding to terms $\cos\phi$, $\cos(2\phi)$, $\sin\phi$, and $\sin(2\phi)$ respectively. The results were obtained from the unpolarized calibration data for 170 MeV deuteron beams.
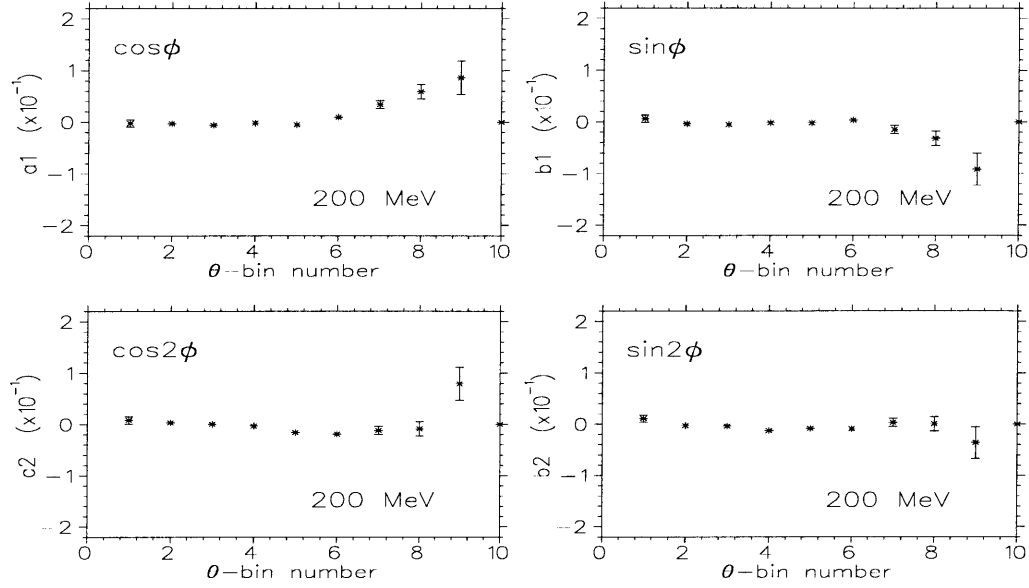
Figure 6-31: The same coefficients as in Figure 6-30, but for 200 MeV deuteron beams.
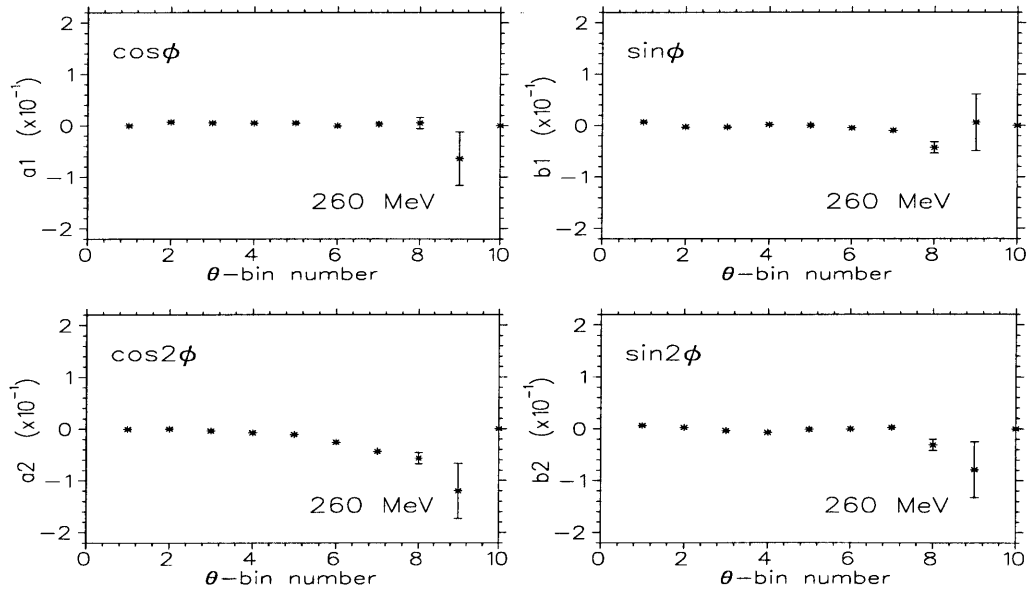
Figure 6-32: The same coefficients as in Figure 6-30, but for 260 MeV deuteron beams.
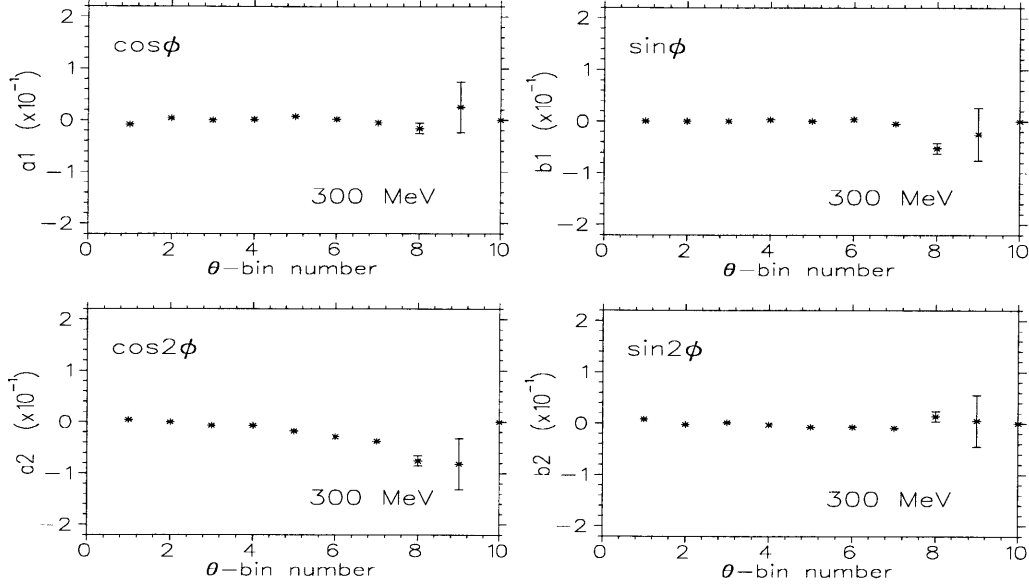
Figure 6-33: The same coefficients as in Figure 6-30, but for 300 MeV deuteron beams.

The effects of the asymmetries on the extraction of the tensor moments t_{ij} were estimated. Considering only the major contributing terms with coefficients a_1, a_2, b_1, and b_2, one has the following equation:

$$\epsilon(\theta, \phi) = \epsilon_0(\theta, \phi)[1 + t_{20}T_{20}(\theta) + 2t_{21}T_{21}(\theta)\cos\phi + 2t_{22}T_{22}(\theta)\cos(2\phi)]$$

$$[1 + a_1\cos\phi + a_2\cos2\phi + b_1\sin\phi + b_2\sin2\phi] \qquad (6.16)$$

An ad hoc simulation was used to estimate the asymmetries effect. A certain number of events were generated with the distribution in Eq. 6.16 Then these events were fit with the standard t_{ij} extraction program. The difference between the tensor moments evaluated in this way and the tensor moments evaluated with no asymmetry is the systematic error due to the instrumental ϕ asymmetries. The errors obtained for t_{20} was negligible while the error for t_{21} and t_{22} could not be neglected and had to be considered. The results are shown in Section 6.9 in the discussion of systematic

uncertainties.

6.8 Precession of the Deuteron Spin in the Dipole

When a deuteron passes through a magnetic field, its spin precesses in the field. The tensor polarizations of the deuteron after exiting the field are changed due to the precession and can be expressed as combinations of various components of the tensor polarization. The relation between unprecessed tensor moments t_{kq} and the precessed tensor components t_{kq}^p has been derived by Schulze [107] and are expressed below:

$$\begin{pmatrix} t_{20}^p \\ t_{21}^p \\ t_{22}^p \end{pmatrix} = \begin{pmatrix} 1 - (3/2)\sin^2(\lambda) & (3/2)^{1/2}\sin(2\lambda) & (3/2)^{1/2}\sin^2(\lambda) \\ -(3/8)^{1/2}\sin(2\lambda) & \cos(2\lambda) & (1/2)\sin(2\lambda) \\ (3/8)^{1/2}\sin^2(\lambda) & -(1/2)\sin(2\lambda) & (1/2)(1+\cos^2(\lambda)) \end{pmatrix} \begin{pmatrix} t_{20} \\ t_{21} \\ t_{22} \end{pmatrix}$$

where $\lambda = \gamma(\mu_d - 1)\theta_B$; γ is the usual relativistic Lorentz factor; μ_d is the deuteron magnetic moment; and θ_B is the bend angle of the dipole magnet.

The dipole magnet in the deuteron channel had a bend angle of 30°. From the above equation, the unprecessed tensor polarizations t_{20}, t_{21}, and t_{22} are expressed in terms of the precessed tensor components t_{20}^p, t_{21}^p, and t_{22}^p as following:

$$t_{20} = c_{00}t_{20}^p + c_{01}t_{21}^p + c_{02}t_{22}^p \tag{6.17}$$

$$t_{21} = c_{10}t_{20}^p + c_{11}t_{21}^p + c_{12}t_{22}^p \tag{6.18}$$

$$t_{22} = c_{20}t_{20}^p + c_{21}t_{21}^p + c_{22}t_{22}^p \tag{6.19}$$

where $c_{ij}, i, j = 0, 1$ are coefficients as listed in Table 6.3. Most of the correction for t_{20} came from the term $c_{01}t_{21}^p$, where c_{01} is roughly a constant of 0.2. The correction for t_{21} mainly come from the term $c_{10}t_{20}^p$, where c_{10} is roughly a constant of -0.1. For t_{22}, the corrections are from both terms of t_{20} and t_{21}. The extracted values of t_{20},

t_{21}, and t_{22} after the precession corrections are listed in Table 6.4.

Q (fm^{-1})	c_{00}	c_{01}	c_{02}	c_{10}	c_{11}	c_{12}	c_{20}	c_{21}	c_{22}
4.10	0.990	0.200	0.008	-0.100	0.987	0.081	0.004	-0.081	0.997
4.46	0.990	0.203	0.008	-0.101	0.986	0.083	0.004	-0.083	0.997
5.08	0.989	0.209	0.009	-0.104	0.985	0.085	0.004	-0.085	0.996
5.48	0.989	0.212	0.009	-0.106	0.985	0.087	0.005	-0.087	0.996

Table 6.3: Coefficients for the correction of t_{20} due to the spin precession of the deuteron in the dipole magnet in the deuteron channel.

Q (fm^{-1})	t_{20}	t_{21}	t_{22}
4.07	-0.585 ± 0.038	0.484 ± 0.053	0.079 ± 0.044
4.47	-0.214 ± 0.034	0.337 ± 0.045	-0.055 ± 0.034
5.09	0.193 ± 0.033	0.174 ± 0.043	-0.024 ± 0.029
5.50	0.297 ± 0.049	0.182 ± 0.058	0.011 ± 0.036

Table 6.4: Results of t_{20}, t_{21}, and t_{22} after corrections due to the precession of the deuteron. The uncertainties are statistical uncertainties only.

6.9 Systematic Uncertainties

The systematic uncertainties of the extracted tensor moments t_{ij} are mainly divided into six groups of sources: the radiative cut, the uncertainty of the incident deuteron energy T_d, calibration, POLDER analysis, instrumental asymmetry, and the precession in the dipole magnet of deuteron channel.

The systematic uncertainties due to the radiative cut were estimated by varying the δ_{cor} in the radiative tail by $\pm 0.5\%$ and rerunning the data. The average difference between the extracted tensor moments with the varied cuts and with the normal cuts are regarded as the uncertainties due to the radiative cut.

The tensor moment t_{20} depends on the energy of the deuteron T_d, especially for

the lower energy kinematics. The values of $\frac{dt_{20}}{dT_d}$ for each kinematics are listed in Table 6.5. They are the average change of t_{20} when T_d is varied by ± 1 MeV manually in the extraction of t_{20}. The error of T_d is summed in quadrature over the individual errors due to the uncertainty of the scattering angle in the HMS (2 mrad), the uncertainty of the electron beam energy (1.5×10^{-3}), and the electron beam offset which was found to be 2mm with an error of ± 1 mm, the error due to the energy interpolation at the mean value of T_d from its asymmetric distribution, and the uncertainty of the energy determination from the deuteron channel measurement.

	point 1	point 2	point 3	point 4
dt_{20}/dT_d	0.07	0.02	0.001	0.002

Table 6.5: Dependence of t_{20} on the deuteron energy T_d.

The systematic uncertainties from the calibration exist in the following sources: the T_{ij} statistical errors, the polarization measurement of the incident deuteron beams, and the stability of the normalization factor k. The error of T_{ij} from the fit contains both the statistical and random systematic errors. There was also an error due to the uncertainty in the absolute measurement of the polarization of the beam [108]. Due to the stability of POLDER during calibration, k was stable at a level of ± 0.006. In the experimental data analysis, k was changed by this amount ± 0.006 and t_{20} was refit. The difference of t_{20} was taken as the uncertainty due the stability of k.

In the analysis of POLDER data, there were errors arising from the α angle cut, the randomization used in the hodoscopes for the position of the protons, the external cone cut, and the uncertainty of the hodoscope z positions. These uncertainties were estimated by varying the α angle by $\pm 1°$, changing random number seeds in the randomization, changing the external cone cut for the two hodoscopes, and changing the z position of the hodoscope by ± 0.1 mm respectively. Each time after changing a cut, the experimental data were reanalyzed to extract tensor moments. The difference

between the new results and the normal results are regarded as the uncertainties of the tensor moments due to that particular source.

The instrumental asymmetries in ϕ and their effect on the tensor moments were discussed in Section 6.7. The systematic uncertainties due to precession correction mainly come from the uncertainty of t_{21} and are roughly the product of the uncertainty of t_{21} and the coefficient 0.2 for each kinematics. The uncertainties due to the proton background are negligible. Table 6.6 lists the values for the systematic uncertainties due to various sources mentioned above. These values are the results of input from the entire t_{20} collaboration. The total systematic uncertainties from different sources were combined in quadrature and are given in the same table.

The main sources for the uncertainties of t_{21} and t_{22} considered here are the uncertainty due to the instrumental ϕ asymmetry, the uncertainty due to different external cone cuts, the T_{ij} statistical error from the fit and the error from the dipole precession correction. Values of these uncertainties for t_{21} and t_{22} are listed in Table 6.7 and Table 6.8 respectively.

sources	point 1	point 2	point 3	point 4
δ_{cor}	0.02	0.01	0.01	0.02
θ	0.06	0.024	0.001	0.003
E_{beam}	0.03	0.012	0.006	0.002
beam offset	0.01	0.003	0.001	*
T_d distribution shape	0.034	0.014	0.004	0.008
DC measurement	0.136	0.04	0.008	0.010
T_{ij} Stat	0.003	0.016	0.003	0.006
beam polarization	0.02	0.01	0.006	0.009
k stability	0.03	0.03	0.04	0.04
α cut	0.02	0.016	0.008	*
ECC	0.012	0.008	0.02	0.03
H1 z pos	0.02	*	*	*
inst. asymmetry	0.01	0.008	0.003	0.004
precession	0.02	*	*	*
total	0.162	0.065	0.048	0.057

Table 6.6: Systematic uncertainties in t_{20}. * denotes the error is negligible.

sources	point 1	point 2	point 3	point 4
ECC	0.09	0.01	0.05	0.04
inst. asymmetry	0.030	0.040	0.014	0.004
T_{ij} Stat	0.013	0.007	0.029	0.037
precession	0.017	0.007	0.007	0.009
total	0.097	0.042	0.060	0.055

Table 6.7: Systematic uncertainties in t_{21}. * denotes the error is negligible.

sources	point 1	point 2	point 3	point 4
ECC	0.02	0.01	0.006	0.003
inst. asymmetry	0.030	0.020	0.020	0.017
T_{ij} Stat	0.003	0.001	0.000	0.001
total	0.036	0.022	0.021	0.017

Table 6.8: Systematic uncertainties in t_{22}. * denotes the error is negligible.

6.10 Separation of Deuteron Form Factors

As described in chapter 1, the charge monopole factor G_C and quadrupole form factor G_Q cannot be separated from the cross-section measurement of elastic e-d scattering. A measurement of another observable which depends on a combination of G_C, G_Q, and G_M different from those for the A(Q) and B(Q) structure functions is necessary to extract the charge monopole and quadrupole form factors individually. The method used to separate the charge monopole and quadrupole form factors for this experiment is described in this section.

In e-d elastic scattering, the tensor polarization t_{20} of the recoil deuterons, together with the structure functions A(Q) and B(Q) from the cross section measurement, allow the separation of the three form factors: G_C, G_Q and G_M. In terms of G_C, G_Q and G_M, $A(Q)$, $B(Q)$ and t_{20} are given below:

$$A(Q) = G_C^2(Q) + \frac{8}{9}\eta^2 G_Q^2(Q) + \frac{2}{3}\eta G_M^2(Q) \tag{6.20}$$

$$B(Q) = \frac{4}{3}\eta(1+\eta)G_M^2(Q) \tag{6.21}$$

$$t_{20} = -\frac{1}{\sqrt{2}I_0}[\frac{8}{3}\eta G_c G_Q + \frac{8}{9}\eta^2 G_Q^2 + \frac{2}{3}\eta(1+\eta)\kappa G_M^2] \tag{6.22}$$

where

$$\eta = Q^2/4M_d^2 \tag{6.23}$$

$$\kappa = \frac{1}{2(\eta + 1)} + \tan^2 \frac{\theta_e}{2} \tag{6.24}$$

$$I_0 = A(Q) + B(Q) \tan^2 \frac{\theta_e}{2}. \tag{6.25}$$

The normalizations of G_C, G_Q and G_M at Q = 0 fm^{-1} are given in Eq. 2.19, 2.20, and 2.21.

The above equations can be solved analytically for G_C, G_Q and G_M. The solutions are functions of $A(Q)$, $B(Q)$ and t_{20}: $G_C(A, B, t_{20})$, $G_Q(A, B, t_{20})$ and $G_M(B)$.

The results for $A(Q)$ [32] and t_{20} from this experiment and the world data of $B(Q)$ were used to extract G_C, G_Q and G_M. The solutions of G_C and G_Q were expressed as functions of I_0, $B(Q)$, and t_{20} instead of $A(Q)$, $B(Q)$, and t_{20}. The measurements for I_0, $B(Q)$ and t_{20} are independent of each other and thus the errors from them are uncorrelated. Only diagonal elements of the error matrix contribute to the errors of G_C and G_Q.

To simplify the notation, the following definitions were made:

$$x = G_C \tag{6.26}$$

$$y = \frac{2}{3}\eta G_Q \tag{6.27}$$

$$F_1 = \frac{1}{2}[t_{20}I_0\sqrt{2} + \frac{1}{2}\kappa B(Q)] \tag{6.28}$$

$$F_2 = I_0 - \kappa B(Q) \tag{6.29}$$

The equations below are derived from Eq. 6.20, 6.21, and 6.22.

$$\frac{x^2}{F_2} + \frac{y^2}{\frac{F_2}{2}} = 1 \tag{6.30}$$

$$x = -\frac{F_1 + y^2}{2y} \tag{6.31}$$

Eq. 6.30 is the equation of an ellipse. Eq. 6.31 is the equation of a hyperbola. The solutions of x and y are the coordinates of the intersections of these two curves.

Figure 6-34 shows the curves and the intersections for the six kinematics data respectively. This set of curves for each kinematics gives four possible pairs of x and y as the solutions: (x_1, y_1), (x_2, y_2), (x_3, y_3), (x_4, y_4). However, $(x_1, y_1) = -(x_3, y_3)$ and $(x_2, y_2) = -(x_4, y_4)$, they differ only by an overall phase change. Since the overall phase is arbitrary, the solution (x_1, y_1) is the same as (x_3, y_3) and the solution (x_2, y_2) is the same as (x_4, y_4).
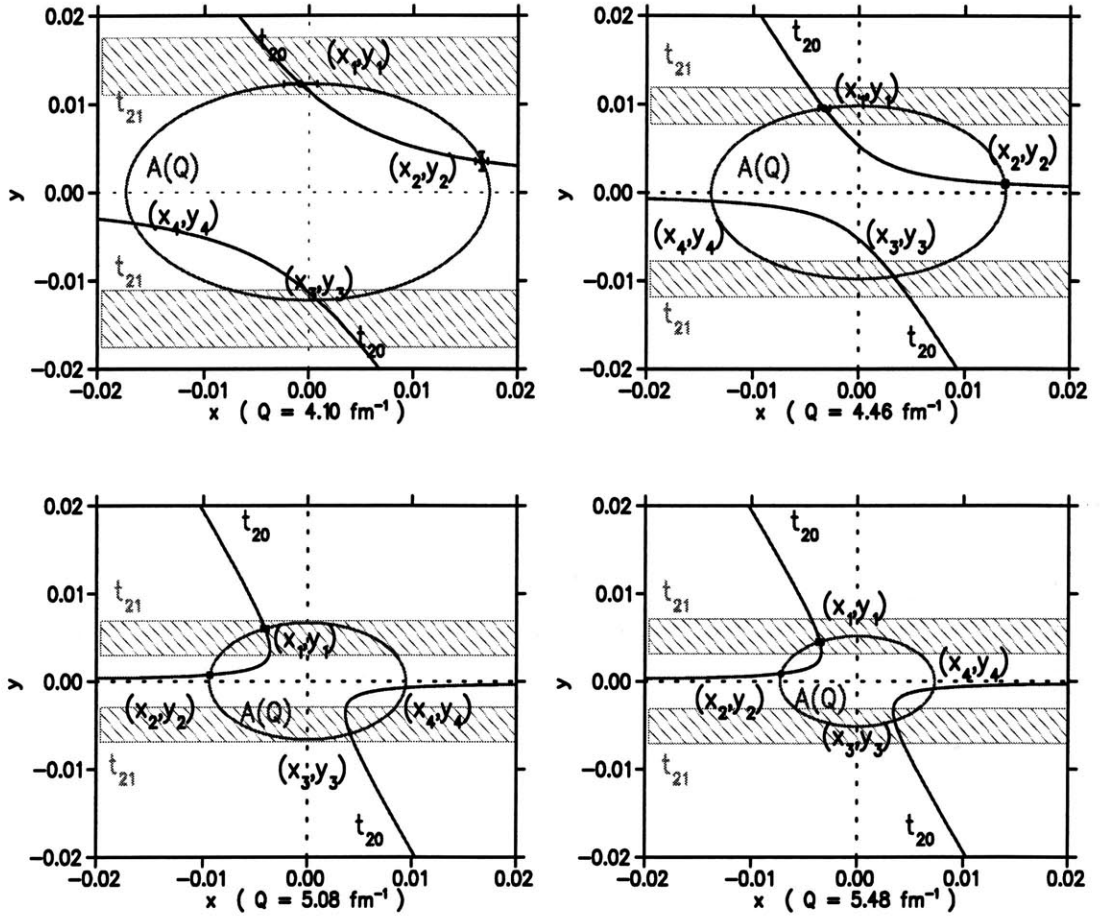
Figure 6-34: Ellipse and hyperbola representing Eq. 6.30 and 6.31 respectively.

The extracted values of t_{21} from this experiment were used as additional information to choose the physics solution from the four possible solutions. In terms of G_C, G_Q and G_M, t_{21} is given by

$$t_{21} \quad = \quad \frac{2}{\sqrt{3}I_0}\eta^{\frac{3}{2}}(1 + \eta \sin^2\frac{\theta_e}{2})^{\frac{1}{2}}G_M G_Q \sec\frac{\theta_e}{2} \tag{6.32}$$

Using previously defined relationships, Eq. 6.33 is derived:

$$y = \pm \frac{2I_0 t_{21}}{3} \sqrt{\frac{1 + \eta}{B(\sec^2 \frac{\theta_e}{2} + \eta \tan^2 \frac{\theta_e}{2})}} \tag{6.33}$$

Equation 6.33 is the functions of two lines which are parallel to the x axis. If the error of t_{21} is considered, two bands are obtained as shown in Figure 6-34. The intersection for the physical solution should be inside the bands. It can be seen from Figure 6-34 that (x_1, y_1) or (x_3, y_3) is the physical solution unambigously for all the four kinematics. The phase of G_Q can be chosen arbitrarily to be positive. Therefore, (x_1, y_1) is selected for all the four kinematics.

The errors of G_C and G_Q were calculated as the quadratic sum of the errors from I_0, t_{20} and $B(Q)$.

$$\sigma_{G_C}^2 = \sum_i (\frac{\partial G_C}{\partial w_i})^2 \sigma_{\omega_i}^2 \tag{6.34}$$

$$\sigma_{F_Q}^2 = \sum_i (\frac{\partial G_Q}{\partial w_i})^2 \sigma_{\omega_i}^2 \tag{6.35}$$

where $\omega_i = I_0, t_{20}, B(Q)$.

The error of G_C is dominated by the error of t_{20}. The error of G_Q is dominated by the error of I_0. The values of $t20$, $A(Q)$, $B(Q)$ and the separated G_C, G_Q for each kinematics are shown in Table 6.9. The node of G_C is determined to be at $Q = 4.03 \pm 0.06$ fm^{-1} by a fourth order polynomial fit to the G_C data. Here the uncertainty was obtained from the uncertainty in the calculation of Q from the deuteron energy.

Q (fm^{-1})	t_{20}	$A(Q)$ $(\times 10^{-2})$	$B(Q)$ $(\times 10^{-5})$	G_C	G_Q
4.10	-.607± .166	326±12	5.28	-.00084 ± .00153	.395 ± .009
4.46	-.229 ± .073	204±8	2.138	-.00331 ± .00050	.261 ± .006
5.08	.186 ± .058	91±4	.461	-.00409 ± .00029	.126 ± .003
5.48	.292 ± .075	54±2	.167	-.00354 ± .00030	.081 ± .003

Table 6.9: Results of G_C and G_Q together with values of t_{20}, $A(Q)$, and $B(Q)$ used in the separation of G_C and G_Q. Values of t_{20} and $A(Q)$ are the measured results from this experiment. Values of $B(Q)$ are from the fit to world data.

6.11   Calculation of t_{21} and t_{22} from G_Q and $B(Q)$

In addition to t_{20}, the tensor moments t_{21} and t_{22} were also extracted from the ϕ distribution of the data in this experiment and the results are shown in Table 6.2. Since t_{21} is related to $G_Q G_M$ in Eq. 2.32 and t_{22} is related to G_M^2 in Eq. 2.33, they can be calculated using the separated results of G_Q and the results of G_M from the world data of $B(Q)$. The calculated results of t_{21} and t_{22} at the six four-momentum transfers are listed in Table 6.10.

In Figure 6-35, the values of t_{21} (circles) extracted from the ϕ distribution in this experiment are compared with the calculated values of t_{21} (squares) using the separated G_Q from this experiment and the world data of $B(Q)$. The results of t_{21} using the two methods are in good agreement with each other within their error bars. The values of t_{22} using these two methods are shown in Figure 6-36 with the same notations as in Figure 6-35. They agree with each other within their error bars for Kinematics 2, 3, and 4. For Kinematics 1, the values of t_{22} are inconsistent. The results of t_{21} and t_{22} will be compared with some typical theoretical calculations in chapter 6.

Q (fm^{-1})	t_{21}	t_{22}
4.10	0.42±0.04	-0.033±0.003
4.46	0.33±0.04	-0.021±0.002
5.08	0.21±0.05	-0.010±0.002
5.48	0.16±0.04	0.006±0.001

Table 6.10: The values of t_{21} are calculated using G_Q extracted from this experiment and the world $B(Q)$ data. The values of t_{22} are calculated using the world $B(Q)$ data.
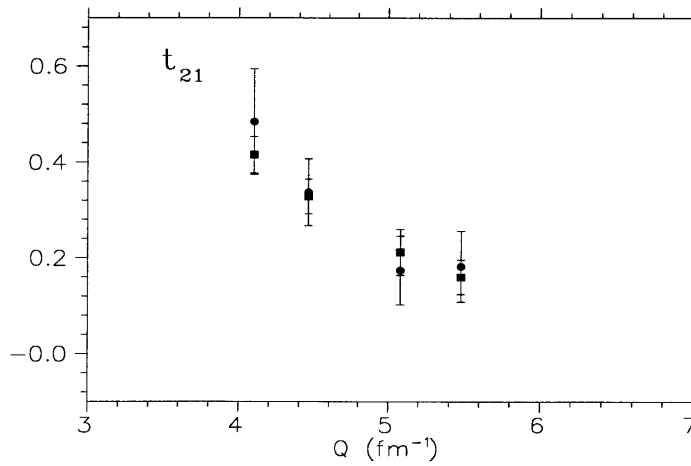

Figure 6-35: Comparison of t_{21} (circles) extracted in this experiment and t_{21} calculated (squares) using the separated G_Q from this experiment and the world $B(Q)$ data. The error bars are the combination of the statistical and systematic errors in quadrature.
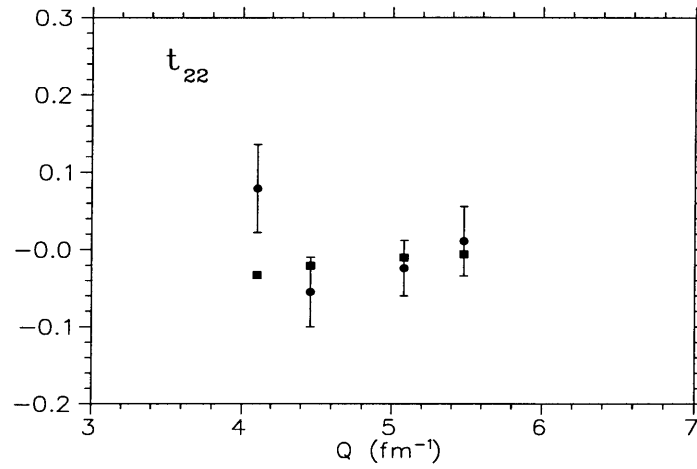
Figure 6-36: Comparison of t_{22} (circles) extracted in this experiment and t_{22} calculated (squares) using the world $B(Q)$ data. The error bars are the combination of the statistical and systematic errors in quadrature.

Chapter 7

Comparison with Theories

7.1 Introduction

As mentioned before, the predictions of the tensor moment t_{20} from different models diverge in the four-momentum transfer range $4.02 \text{ fm}^{-1} < \text{Q} < 6.7 \text{ fm}^{-1}$. The position of the node in G_C is sensitive to various corrections, such as MEC's, relativistic effects, isobar components, and possible quark degrees of freedom. Experimental data with high precision in this four-momentum transfer range are necessary to study these effects and thus probe the short-range behavior of the NN interaction. The experiment [12] performed at MIT-Bates first measured t_{20} of the deuteron in the four-momentum transfer range where t_{20} starts to rise from the minimum. The experiment described in this thesis extended the measurement to higher momentum transfer and provided data with good precision. In this chapter, the results of t_{20}, the charge monopole form factor G_C and charge quadrupole form factor G_Q from this experiment are compared to the predictions from different theoretical models described in Chapter 2. The results of the tensor moments t_{21} and t_{22} from this experiment are also compared with some theoretical predictions. The uncertainties for all the results shown in this chapter are the quadratic sum of the systematic and statistical uncertainties. Since

most of the existing theoretical predictions for t_{20} are given for $\theta_e = 70°$, the results of t_{20} from this experiment were adjusted to $\theta_e = 70°$ and are shown in the figures. The results of the absolute value of G_C are plotted on a log scale for $0 \text{ fm}^{-1} < Q < 8 \text{ fm}^{-1}$ and on a linear scale for $3.6 \text{ fm}^{-1} < Q < 5.1 \text{ fm}^{-1}$ to locate the node of G_C for each calculation. For convenience of comparison, the results from the previous experiments are also displayed in the figures.

7.2 Comparison of Data with Theories

7.2.1 Non-Relativistic Impulse Approximation

The results for t_{20}, G_C, and G_Q calculated by Mosconi and Ricci [1] with the Paris potential are shown and compared with the data in Figures 7-1–7-5. The results for impulse approximation (IA, dotted curve), IA with relativistic corrections (RC, dashed curve), and the full calculations (IA+RC+MEC, solid curve) are illustrated in each figure. For the t_{20} results, the inclusion of both RC and MEC increase the value of t_{20} for $Q > 3.5 \text{ fm}^{-1}$. The full calculation including the relativistic corrections, ρ exchange, and $\rho\pi\gamma$ MEC's gives the best overall agreement with the data. The data for the lowest three kinematics of the present experiment favor the full calculation, while the Bates data, which were in the four-momentum range overlapping with the first two points, are best described by the IA calculation with the relativistic corrections.

The results of G_C and G_Q using Höhler (H) parametrization for the nucleon form factor are shown in Figure 7-2 and 7-3 respectively. Again the full calculation provides the best predictions for the present data, consistent with the comparison of t_{20}. Among the three calculations, the full calculation gives the smallest Q for the position of G_C node which is closest to the G_C node from this experiment. For the results of G_Q, the difference among the three calculations is negligible and the predictions from the three calculations give good agreement with the data. The sensitivity of G_C

and G_Q to different nucleon form factor parametrizations (H, GK, IJL, and IJLG) is shown in Figure 7-4 and 7-5 respectively. All four parametrizations predict almost the same G_C node position. The results of the predicted G_C using GK form factor lies above the predictions with the other three parametrizations, and the IJL form factor gives the lowest prediction of G_C. The predictions using the H and IJLG form factors are indistinguishable. All the predictions reasonably agree with the present data. The comparison of the prediction of G_Q using different nucleon form factor parametrizations with the data is similar to the comparision for G_C.
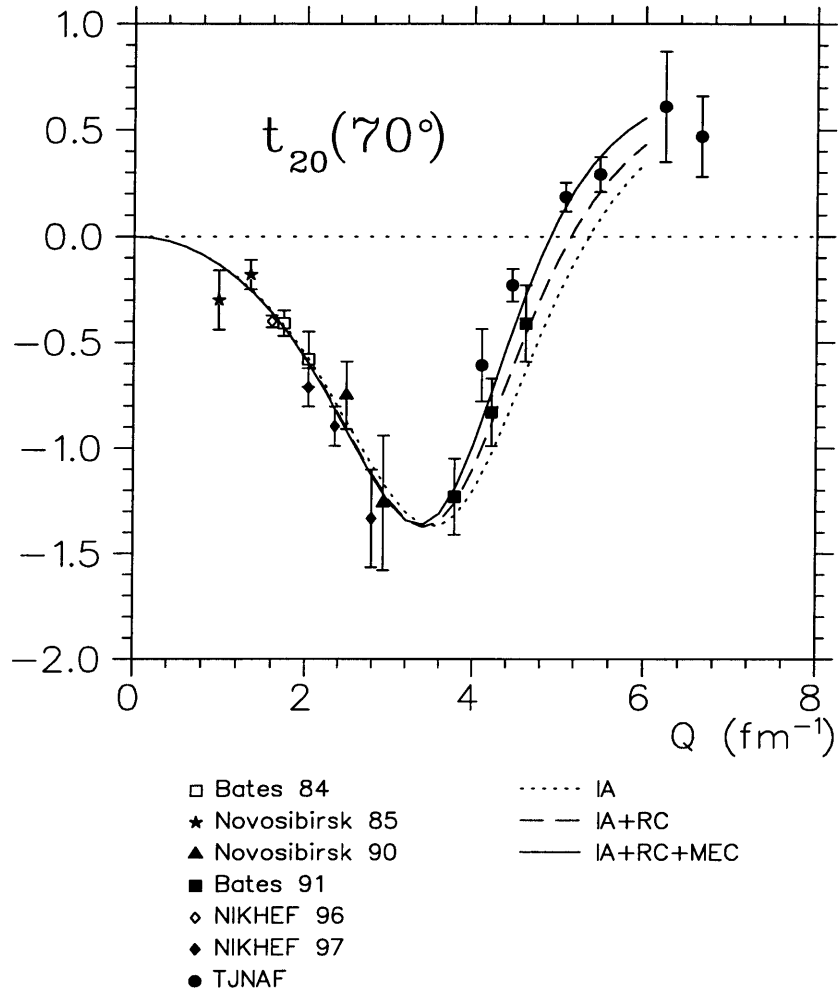
Figure 7-1: Comparison of data with predicted t_{20} from Mosconi and Ricci [1] using H form factor: IA, IA+relativistic corrections (RC), IA+RC+MEC.
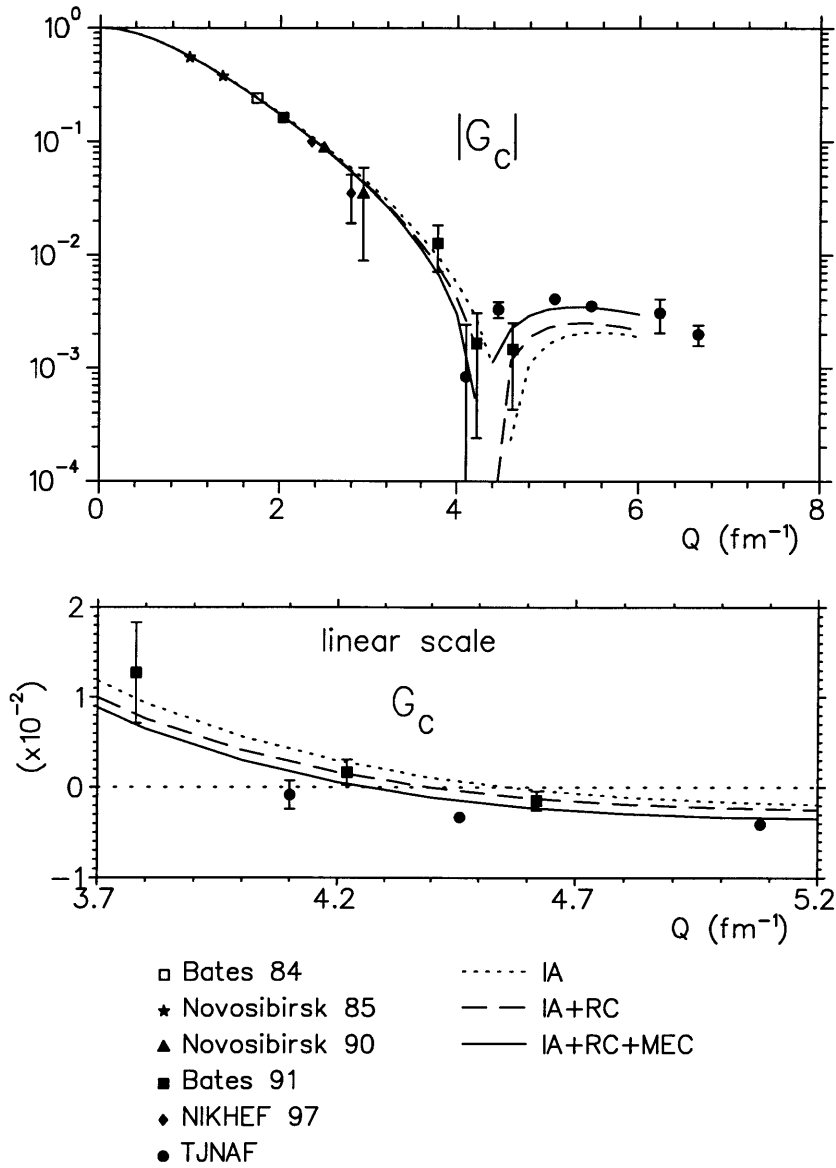
Figure 7-2: Comparison of data with predicted G_C from Mosconi and Ricci [1] using H form factor: IA, IA+relativistic corrections (RC), IA+RC+MEC.
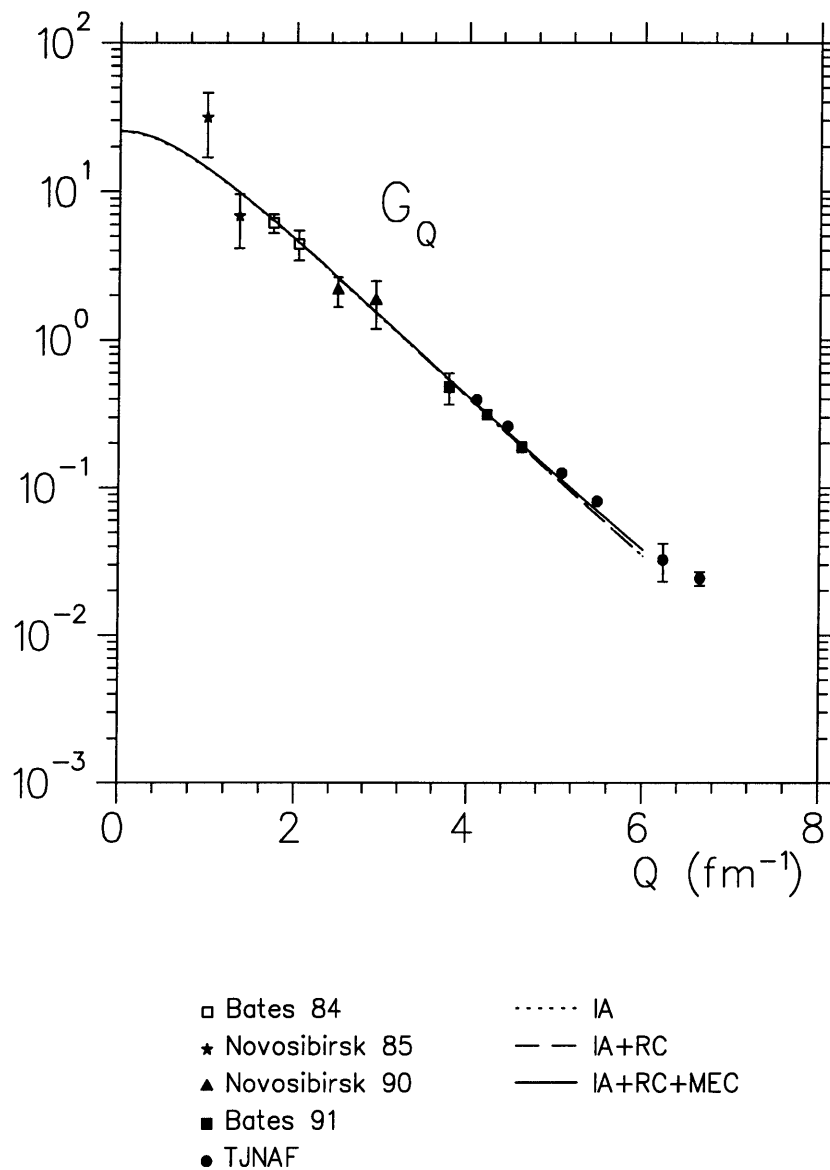
Figure 7-3: Comparison of data with predicted G_Q from Mosconi and Ricci [1] using H form factor: IA, IA+relativistic corrections (RC), IA+RC+MEC.
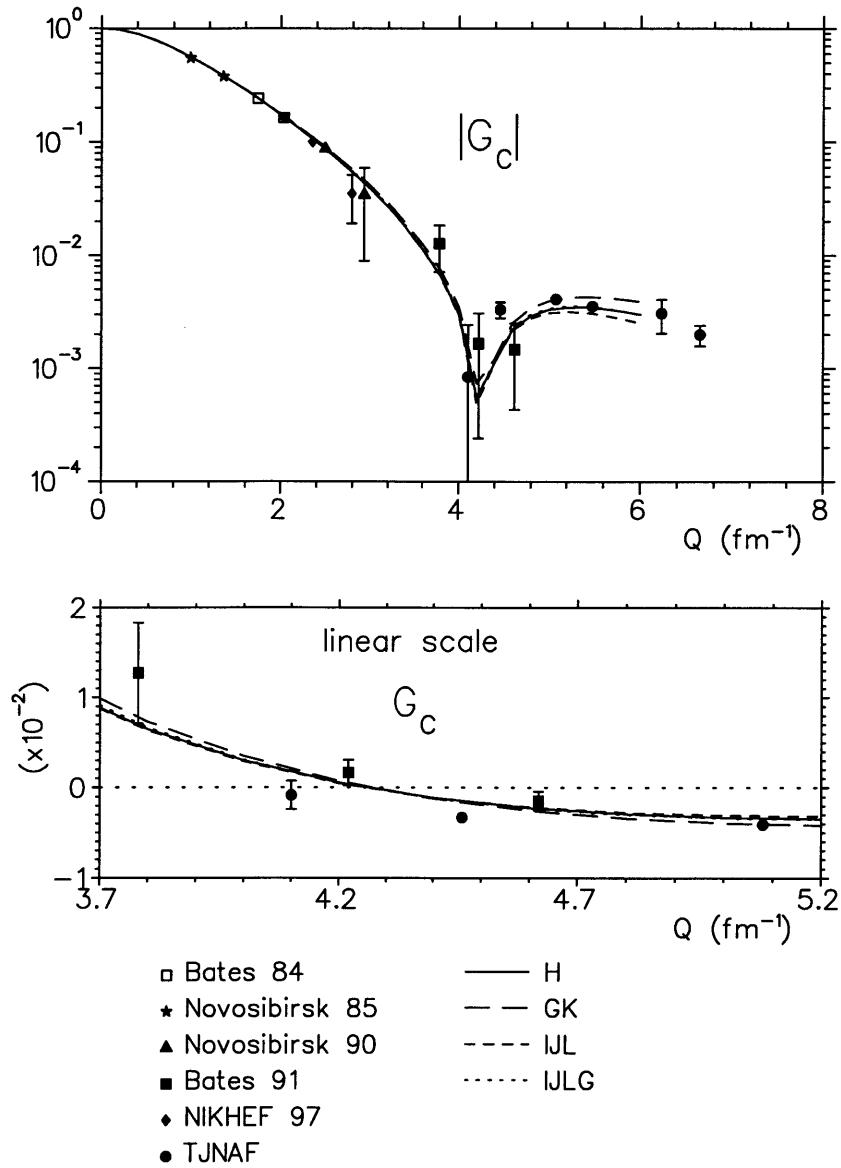
Figure 7-4: Comparison of data with predicted G_C from Mosconi and Ricci [1] using various nucleon form factor parametrizations: H, GK, IJL, and IJLG.
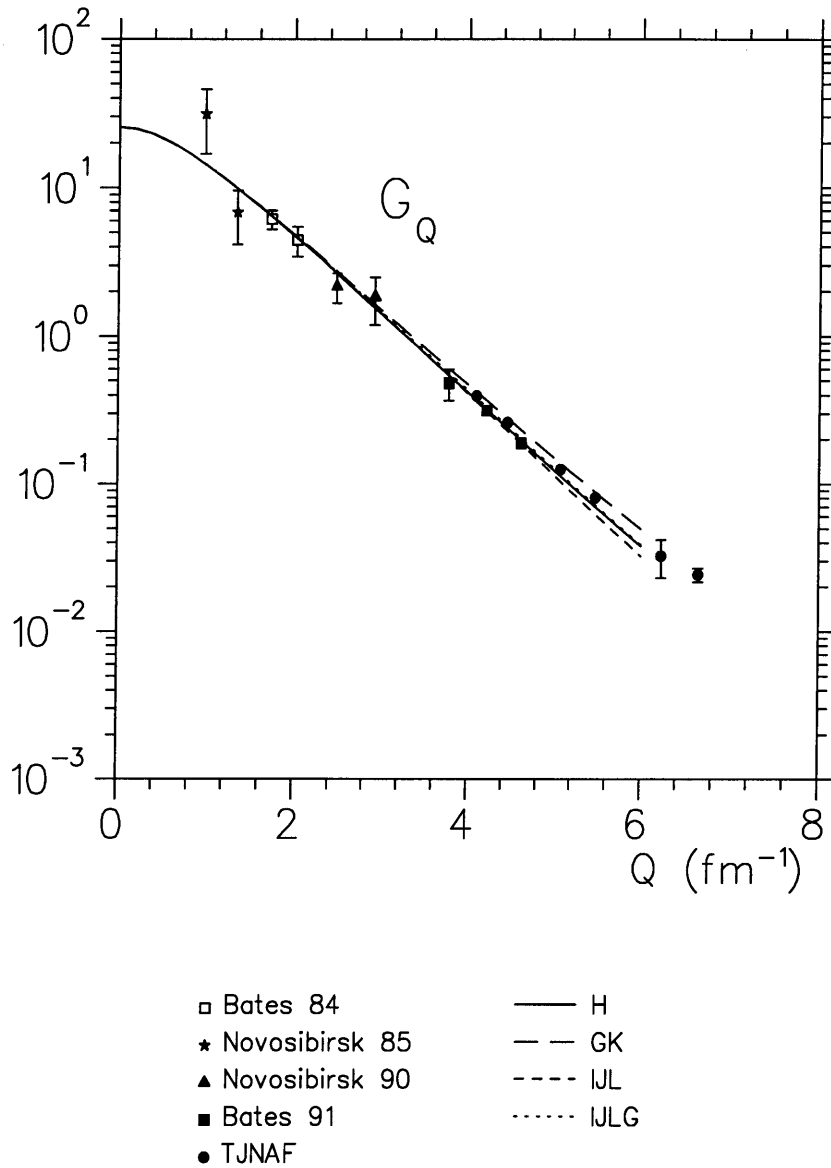
Figure 7-5: Comparison of data with predicted G_Q from Mosconi and Ricci [1] using various nucleon form factor parametrizations: H, GK, IJL, and IJLG.
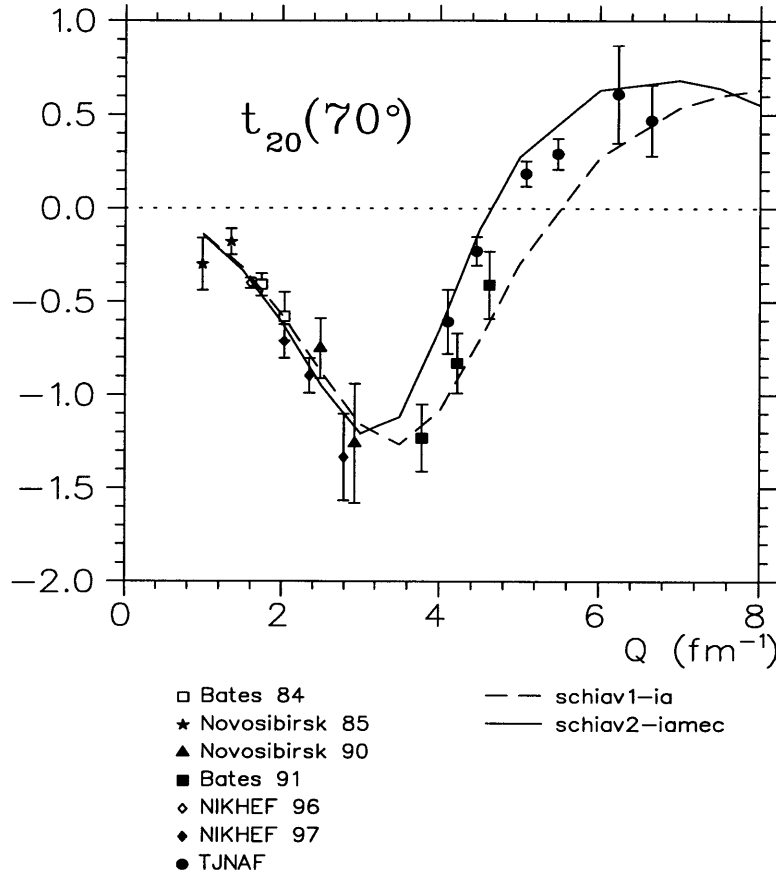
Figure 7-6: Comparison of data with predicted t_{20} from Schiavilla and Riska [42]: IA, IA+RC+MEC.

The results for t_{20} calculated by Schiavilla and Riska [42] using the Argonne v_{14} potential are shown and compared to the data in Figure 7-6. The full calculation (IA+RC+MEC) agrees with the data, while the IA result underestimate the data. The results of G_C are shown in Figure 7-7. The relativistic corrections and the MEC's in the full calculation shift the node of G_C to lower four-momentum transfer. The present data strongly favor the full calculation, while the IA prediction underestimates the data after G_C passes its minimum. For G_Q, although the difference between the IA prediction and the full calculation is small, the present data agree better with the full calculation as shown in Figure 7-8.
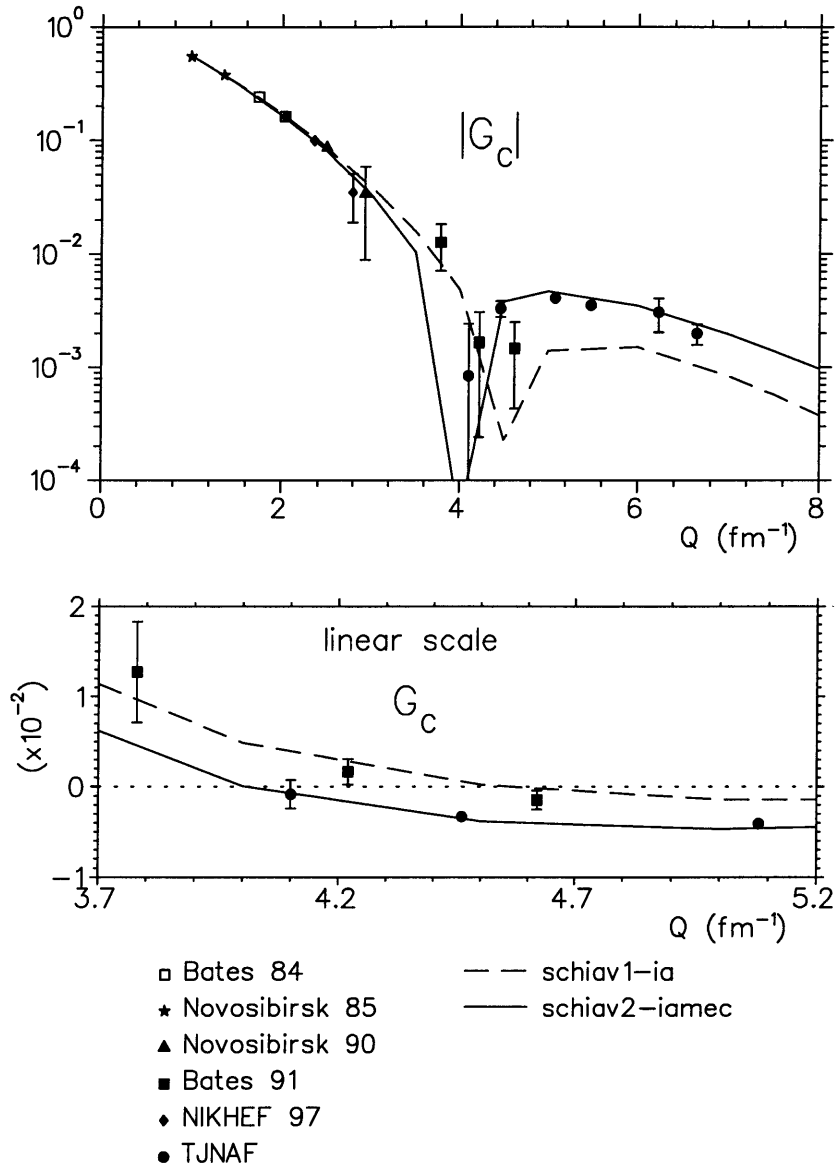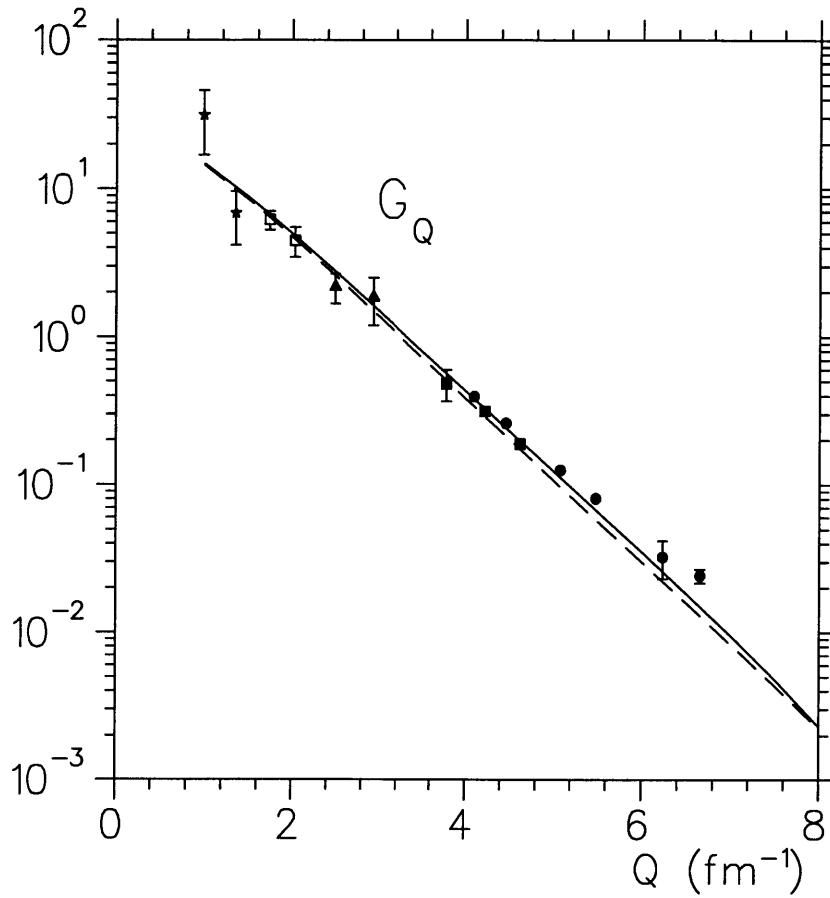
Figure 7-7: Comparison of data with predicted G_C from Schiavilla and Riska [42]: IA, IA+RC+MEC.

Figure 7-8: Comparison of data with predicted G_Q from Schiavilla and Riska [42]: IA, IA+RC+MEC.
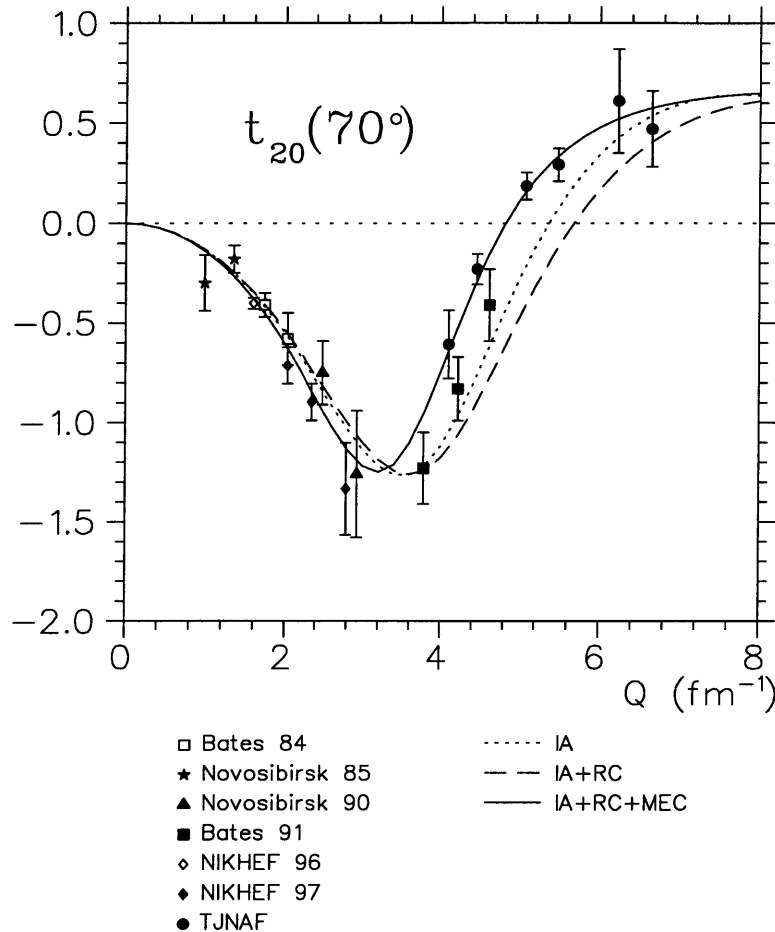
Figure 7-9: Comparison of data with predicted t_{20} from Pauschenwein, Plessas, and Mathelitsch [43] using Paris potential: IA, IA+RC, IA+RC+MEC.

The predictions of t_{20} by Pauschenwein,Plessas, and Mathelitsch (PPM) [43] using the Paris, Bonn OBEPR, Bonn OBEPQ, full Bonn, and folded-diagram full Bonn potentials are shown in Figure 7-9-7-12. In all these calculations, the relativistic corrections shift the IA results down, while the MEC's move the IA result up for 3.5 $\text{fm}^{-1} < Q < 8\ \text{fm}^{-1}$. As shown in Figure 7-9, the full calculation using Paris potential agrees well with the present data while the IA and IA+RC results underestimate the present data, especially the lower kinematics data which have small error bars. The

comparison of the predictions of G_C and G_Q by PPM using Paris potential with the data also indicates that the full calculation is in good agreement with the present data as shown in Figure 7-10 and 7-11. The comparison of the full calculations using different potentials with the data is shown in Figure 7-12. The full calculations using Paris, Bonn OBEPR, and folded-diagram full Bonn potentials give similar predictions of t_{20} and reasonably agree with the present data, while the predictions of t_{20} using Bonn OBEPQ and full Bonn potentials underestimate the data.

Figure 7-10: Comparison of data with predicted G_C from Pauschenwein, Plessas, and Mathelitsch [43] using Paris potential: IA, IA+REL, IA+REL+MEC.

□ Bates 84   ⋯⋯⋯ IA
★ Novosibirsk 85   — — IA+RC
▲ Novosibirsk 90   —— IA+RC+MEC
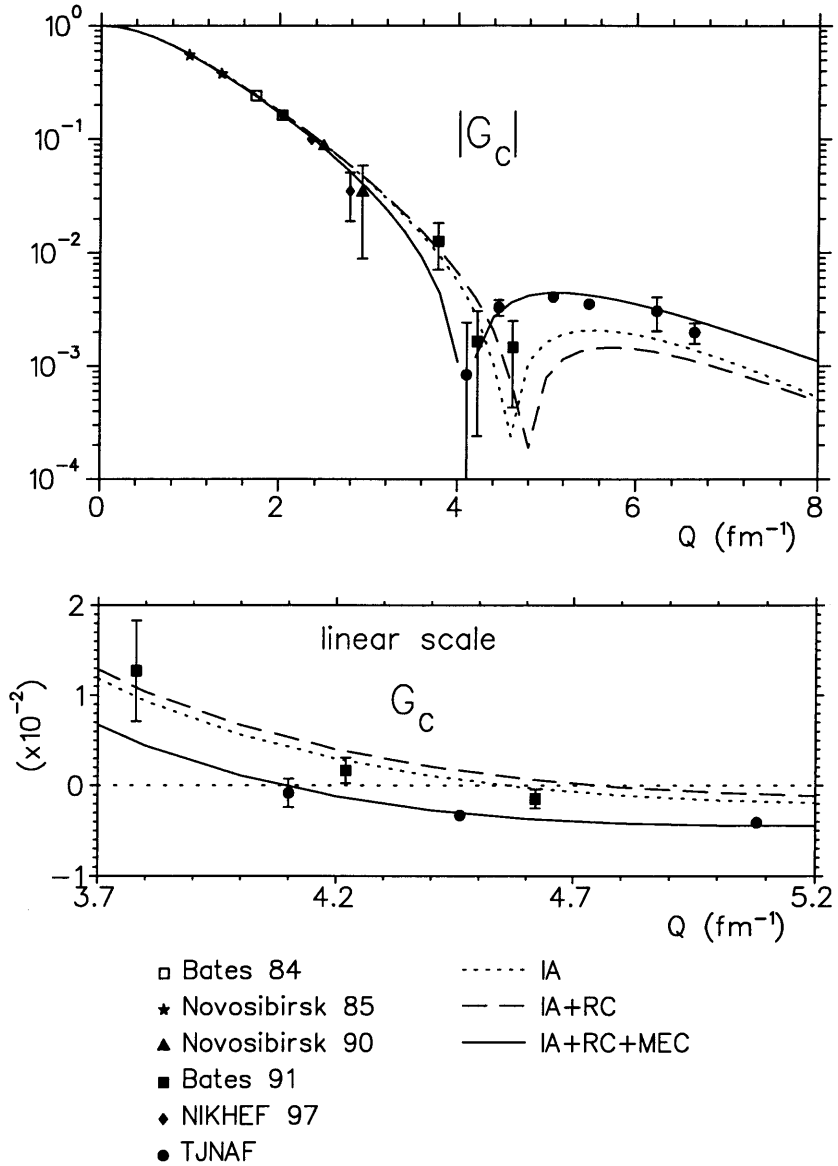■ Bates 91
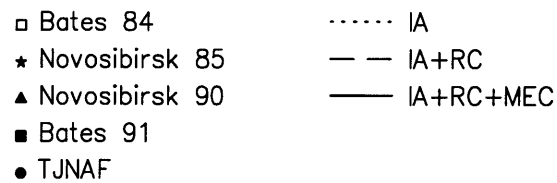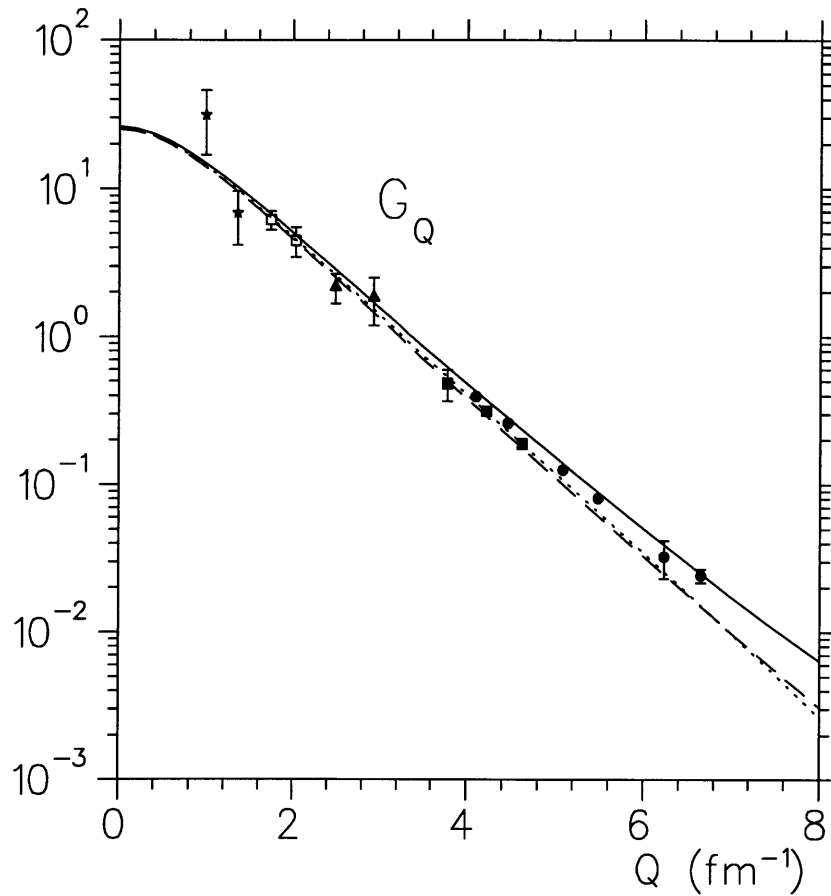● TJNAF

Figure 7-11: Comparison of data with predicted G_Q calculated by Pauschenwein, Plessas, and Mathelitsch [43] using Paris potential: IA, IA+REL, IA+REL+MEC.
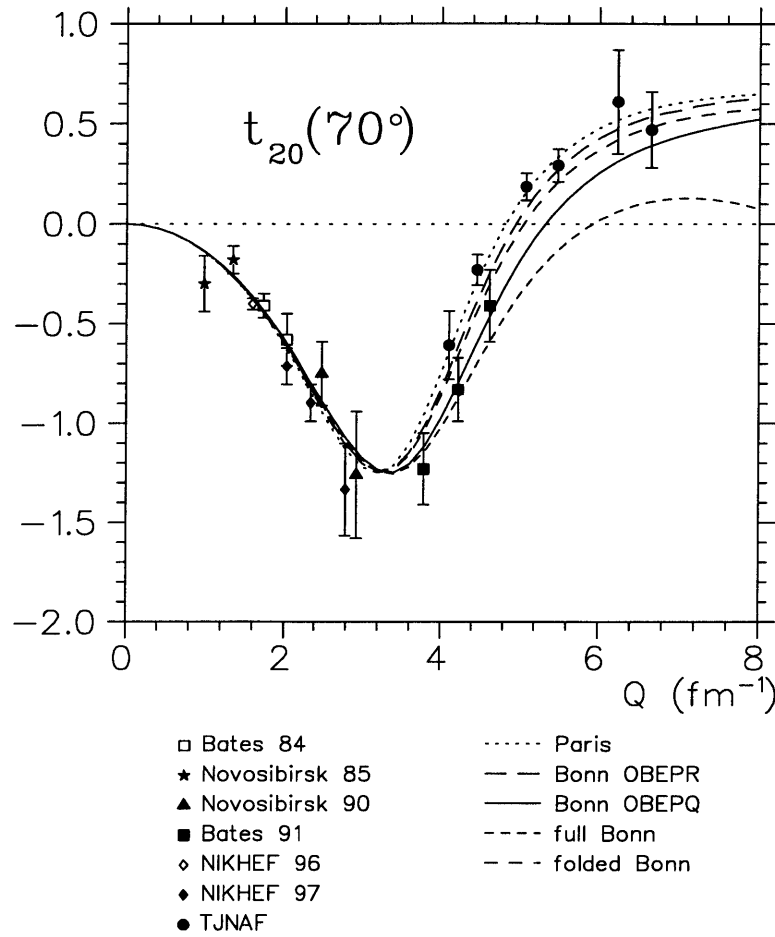
Figure 7-12: Comparison of data with the predicted t_{20} of the full calculation by Pauschenwein, Plessas, and Mathelitsch [43] using various potentials: Paris, Bonn OBEPR, Bonn OBEPQ, full BonnL, folded-diagram full Bonn.

Figure 7-13: Comparison of data with predicted t_{20} from Wiringa, Stoks, and Schiavilla [4] using Argonne v_{18} potential.

The comparison of the results for t_{20}, G_C, and G_Q with calculations using Argonne v_{18} potential by Wiringa, Stoks, and Schiavilla [4] is shown in Figure 7-13-7-15. In Argonne v_{18} potential, three charge-dependent and one charge-asymmetric operators are added to the 14 operator components in the v_{14} potential. The IA prediction for t_{20} in Figure 7-13 underestimates the four lowest Q data points, but agrees with the two highest Q data points within error bars. The full calculation of, which includes the relativistic effects and MEC's, is reasonably consistent with the present data. Comparison of the G_C data with the calculations is shown in Figure 7-14. Again, IA underestimates G_C, while the full calculation agrees with the data. For $G(Q)$, the

difference between these two calculations is small at low Q, but becomes apparent at $Q > 5$ fm^{-1}. The present data favors the full calculation for G_Q.
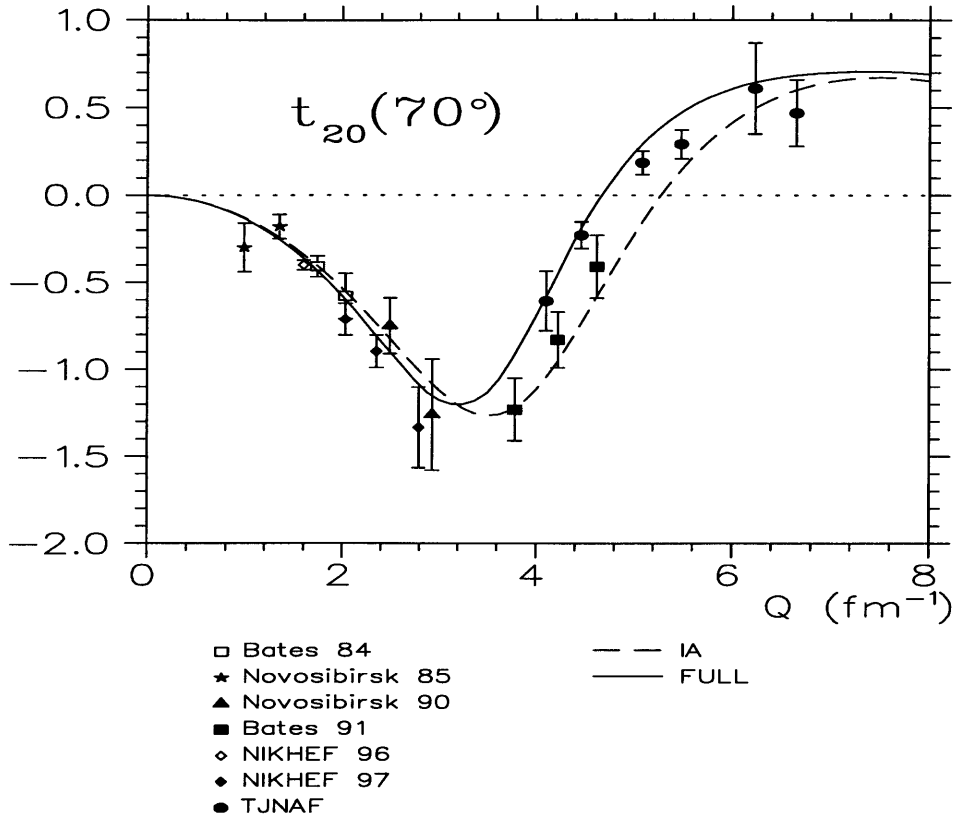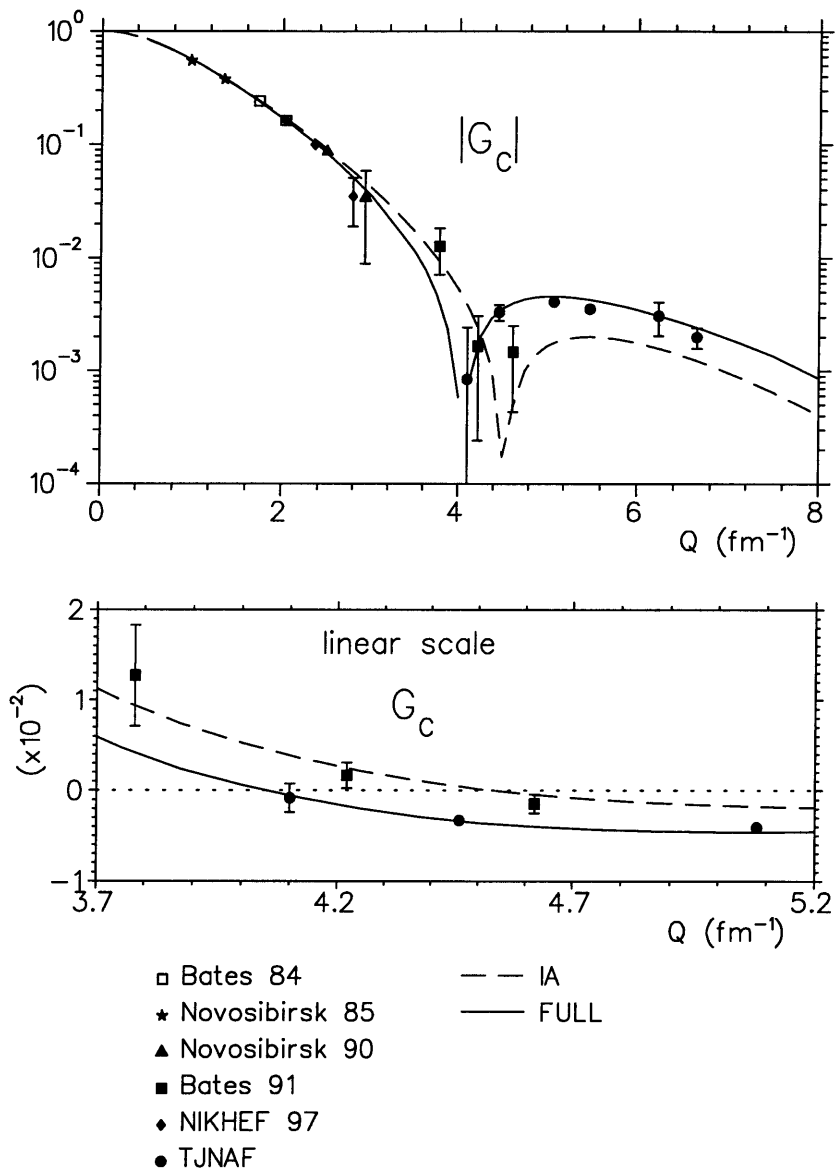

Figure 7-14: Comparison of data with predicted G_C from Wiringa, Stoks, and Schiavilla [4] using Argonne v_{18} potential.
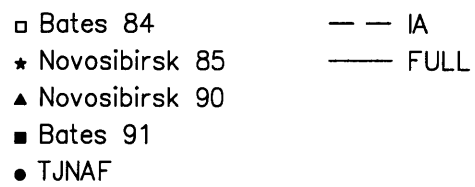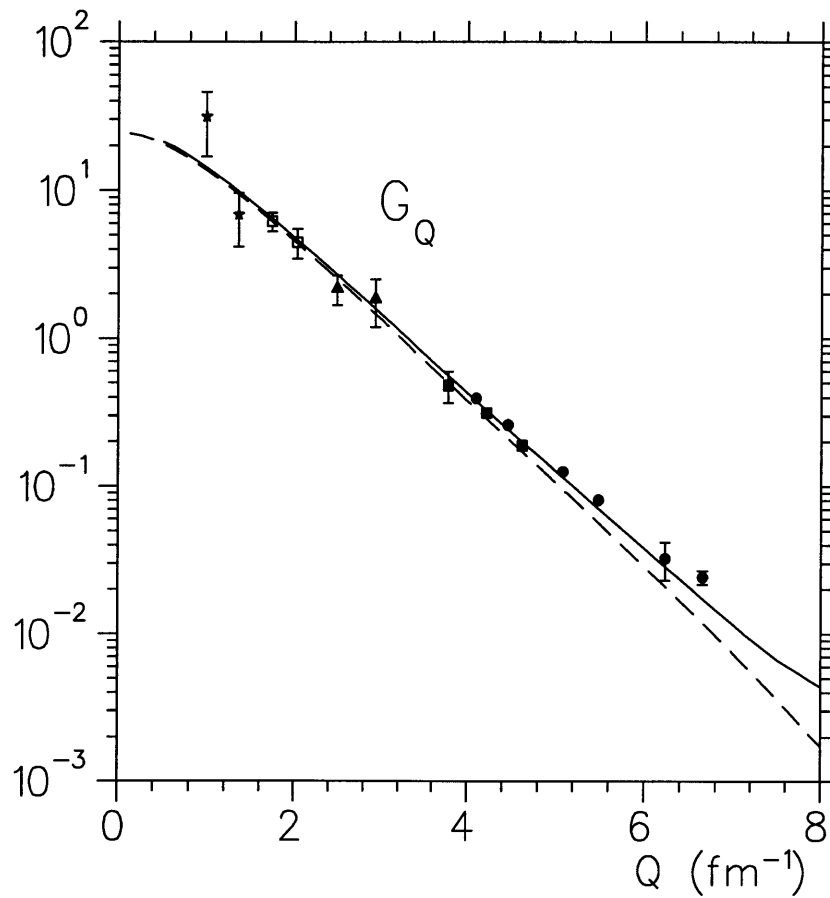
Figure 7-15: Comparison of data with predicted G_Q from Wiringa, Stoks, and Schiavilla [4] using Argonne v_{18} potential.

7.2.2 Relativistic Calculations
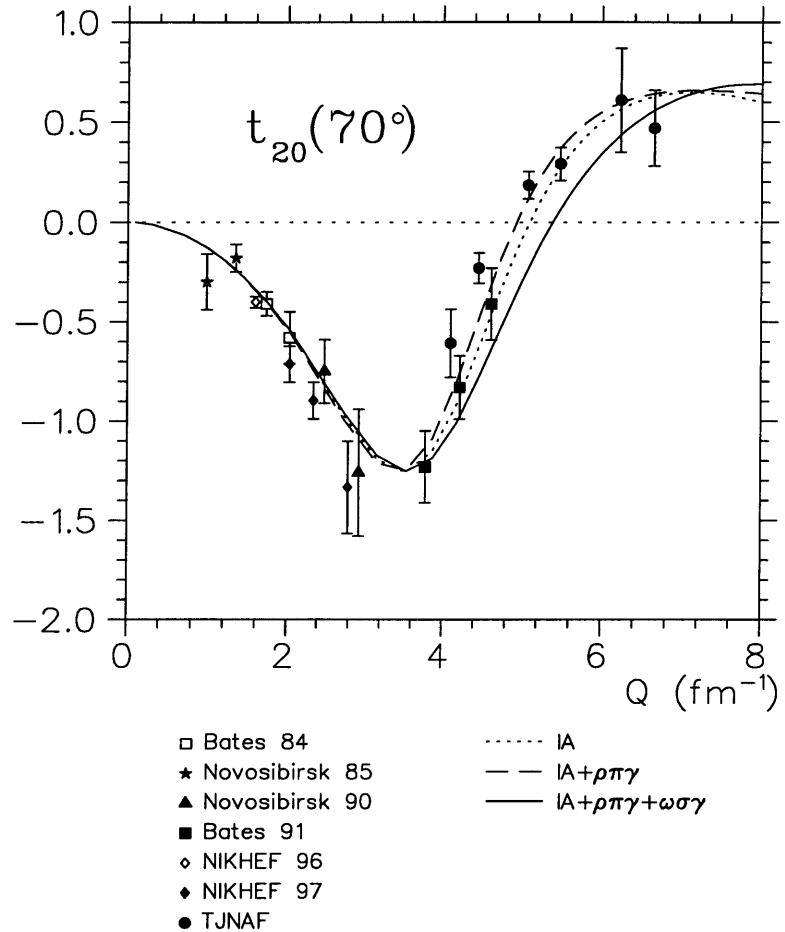
Figure 7-16: Comparison of data with predicted t_{20} calculated by Hummel and Tjon [59, 60] using H form factor: IA, IA+$\rho\pi\gamma$, IA+$\rho\pi\gamma$+$\omega\sigma\gamma$.

Hummel and Tjon [59, 60] performed a relativistically covariant calculation including the contributions from the $\rho\pi\gamma$ and $\omega\sigma\gamma$ MEC's. The data of t_{20}, G_C, and G_Q is compared to their calculations using H nucleon form factor parametrization in Figures 7-16-7-18. As shown in Figure 7-16, $\rho\pi\gamma$ MEC increases the values of t_{20} in the four-momentum transfer range of interest, while $\omega\sigma\gamma$ MEC contributes to t_{20} in the

opposite direction with a bigger effect. As a result, the IA+$\rho\pi\gamma$+$\omega\sigma\gamma$ curve for t_{20} lies below the IA curve, while the IA+$\rho\pi\gamma$ curve is above the IA curve. The IA+$\rho\pi\gamma$ calculation is in fair agreement with the present data. The IA calculation agrees with the last three data points, but underestimates the first three points. The inclusion of the $\omega\sigma\gamma$ MEC makes the prediction underestimate the data. For G_C (see Figure 7-17), the IA+$\rho\pi\gamma$ curve is above the IA curve, while the IA+$\rho\pi\gamma$+$\omega\sigma\gamma$ curve is under the IA curve. None of these calculations predicts the data well, while IA+$\rho\pi\gamma$ calculation is the closest to the data. The sequence (from left to right) of the G_C node positions predicted by these calculations is: IA+$\rho\pi\gamma$, IA, and IA+$\rho\pi\gamma$+$\omega\sigma\gamma$. For G_Q (see Figure 7-18), the $\omega\sigma\gamma$ MEC contribution is in the opposite direction to that of the $\rho\pi\gamma$ MEC, but with roughly the same magnitude. Therefore, IA and IA+$\rho\pi\gamma$+$\omega\sigma\gamma$ curves are almost indistinguishable. All the three calculations underestimate the G_Q data.
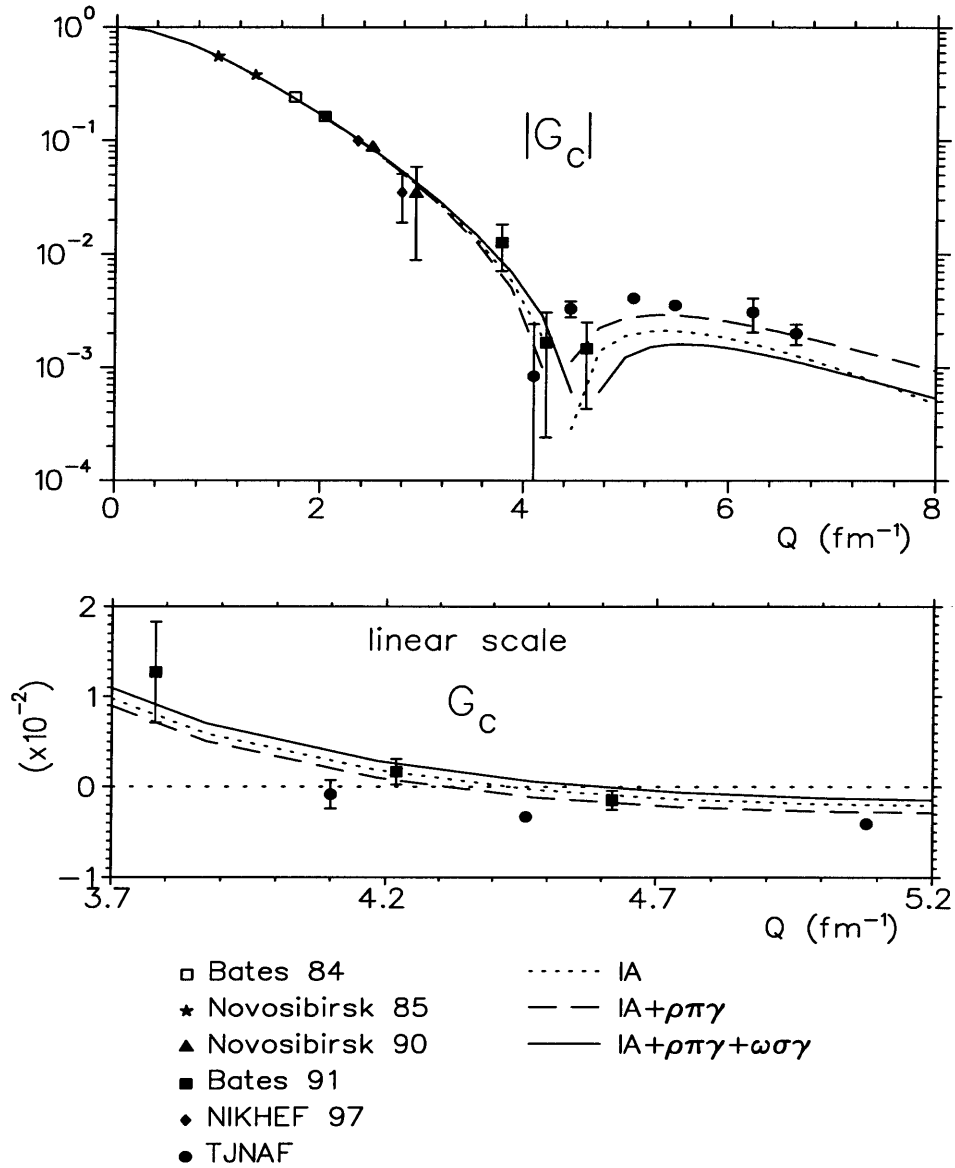
Figure 7-17: Comparison of data with predicted G_C from Hummel and Tjon [59, 60]. Same notations as in Figure 7-16.
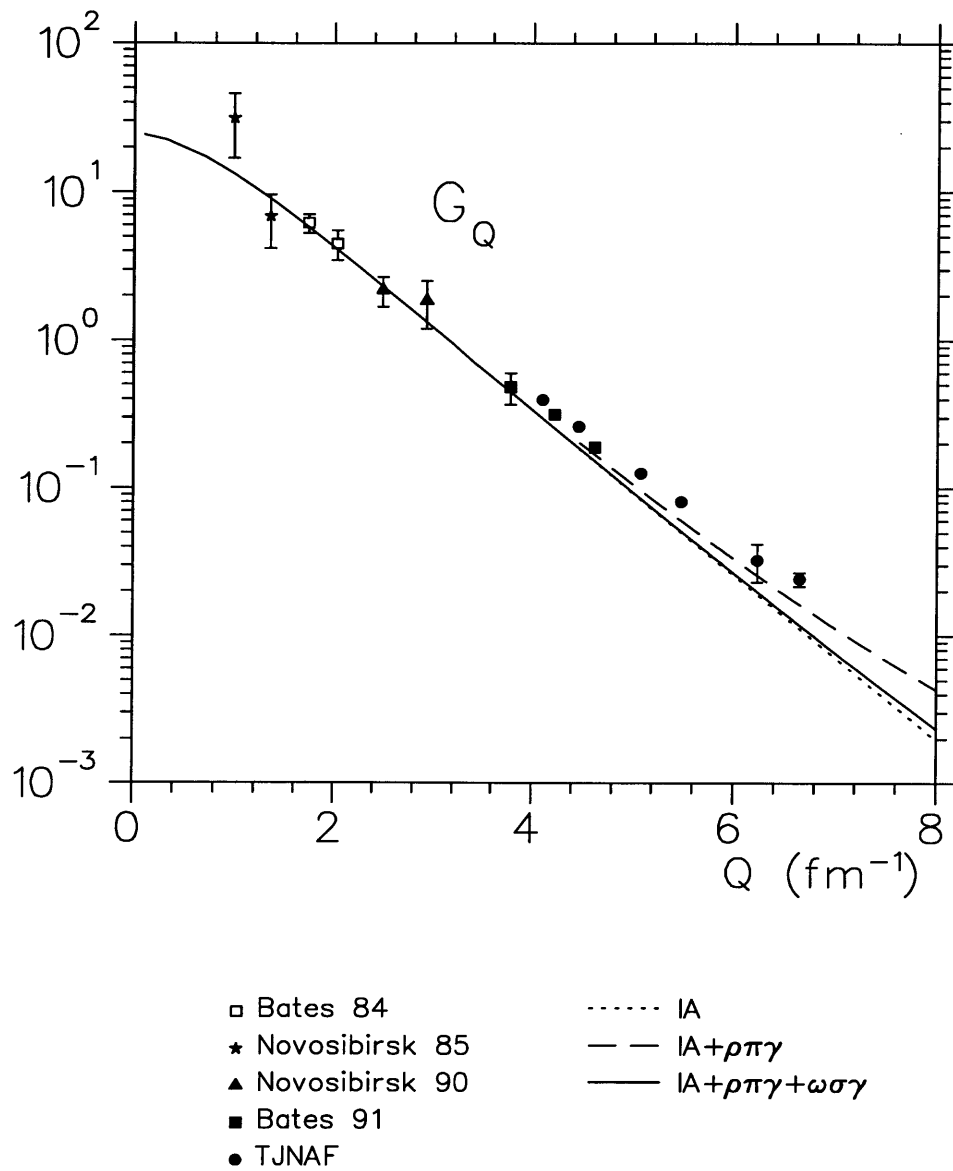
Figure 7-18: Comparison of data with predicted G_Q from Hummel and Tjon [59, 60]. Same notations as in Figure 7-16.

The comparison of the t_{20} data with the calculation from Chung, Coester, Keister, and Polyzou [5] using the Paris potential is shown in Figure 7-19. The calculation is in fair agreement with the data of Bates 91, but underestimates the present data. In Figure 7-20, the G_C data were compared with the calculation using four different nucleon form factor parametrizations (H, GK, L, and D). The four calculations predict roughly the same position of the G_C node. The calculations using H, L, and D parametrizations are almost identical, while the calculation using the GK parametrization is slightly above the other three. All four calculations underestimate the G_C data. As a results of this, the predicted position of G_C node is at larger Q than the data. The data of G_Q is compared with the calculations in Figure 7-21. The calculation using the GK parametrization is above he calculations using the other three parametrizations. The data is in good agreement with the calculation using GK parametrization.

$t_{20}(70°)$

□ Bates 84
★ Novosibirsk 85
▲ Novosibirsk 90
■ Bates 91
◇ NIKHEF 96
◆ NIKHEF 97
● TJNAF
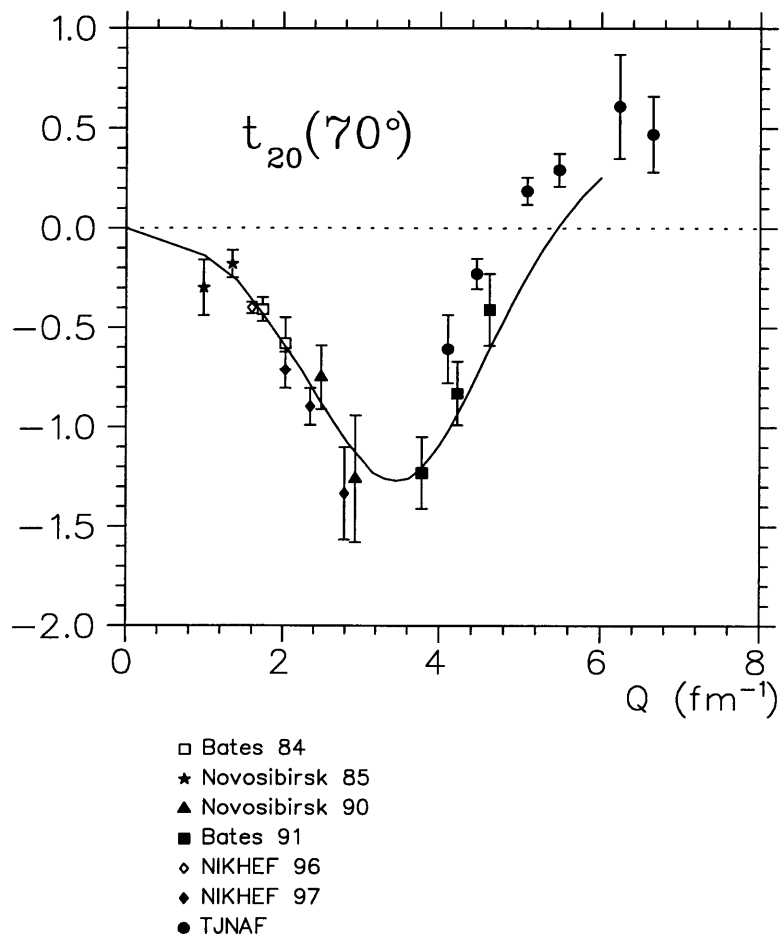
Figure 7-19: Comparison of data with predicted t_{20} from Chung, Coester, Keister, and Polyzou [5] using the Paris potential and H nucleon form factor.
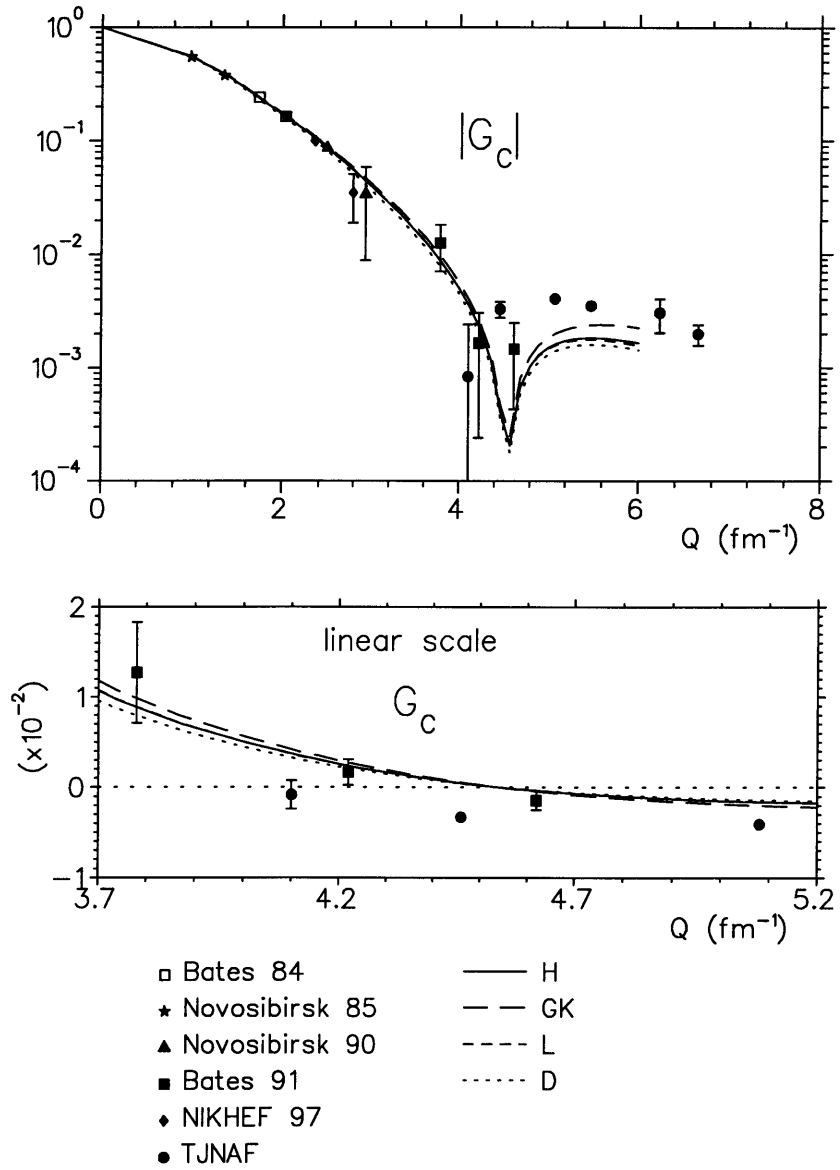
Figure 7-20: Comparison of data with predicted G_C from Chung, Coester, Keister, and Polyzou [5] using the Paris potential and different nucleon form factor parametrizations: H, GK, L, and D.

$$\begin{array}{ll}
\square \text{ Bates 84} & \text{———— H} \\
\star \text{ Novosibirsk 85} & \text{— — GK} \\
\blacktriangle \text{ Novosibirsk 90} & \text{- - - - L} \\
\blacksquare \text{ Bates 91} & \text{······· D} \\
\bullet \text{ TJNAF} &
\end{array}$$
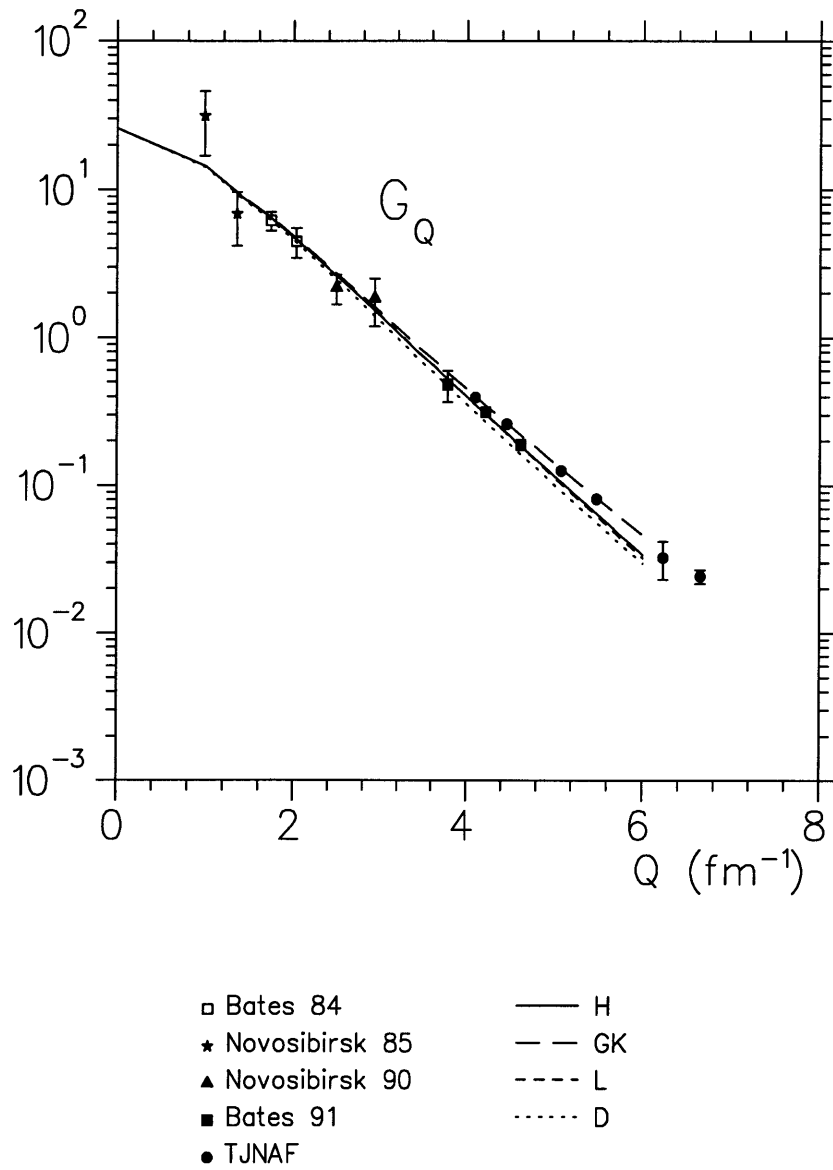
Figure 7-21: Comparison of data with predicted G_Q from Chung, Coester, Keister, and Polyzou [5]. Same notations as in Figure 7-20.

The t_{20}, G_C, and G_Q data are compared with the covariant relativistic CIA calculation from Van Orden, Devine, and Gross [66] in Figure 7-22–7-24. The present data are all in fair agreement with the calculations.
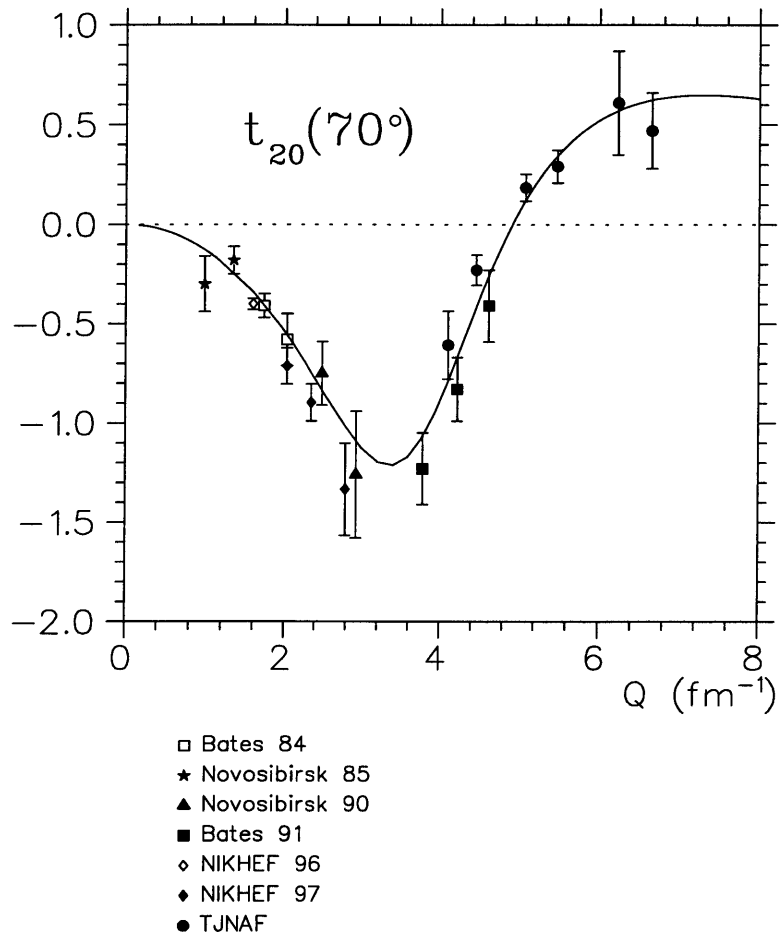
Figure 7-22: Comparison of data with predicted t_{20} from Van Orden, Devine, and Gross [66].
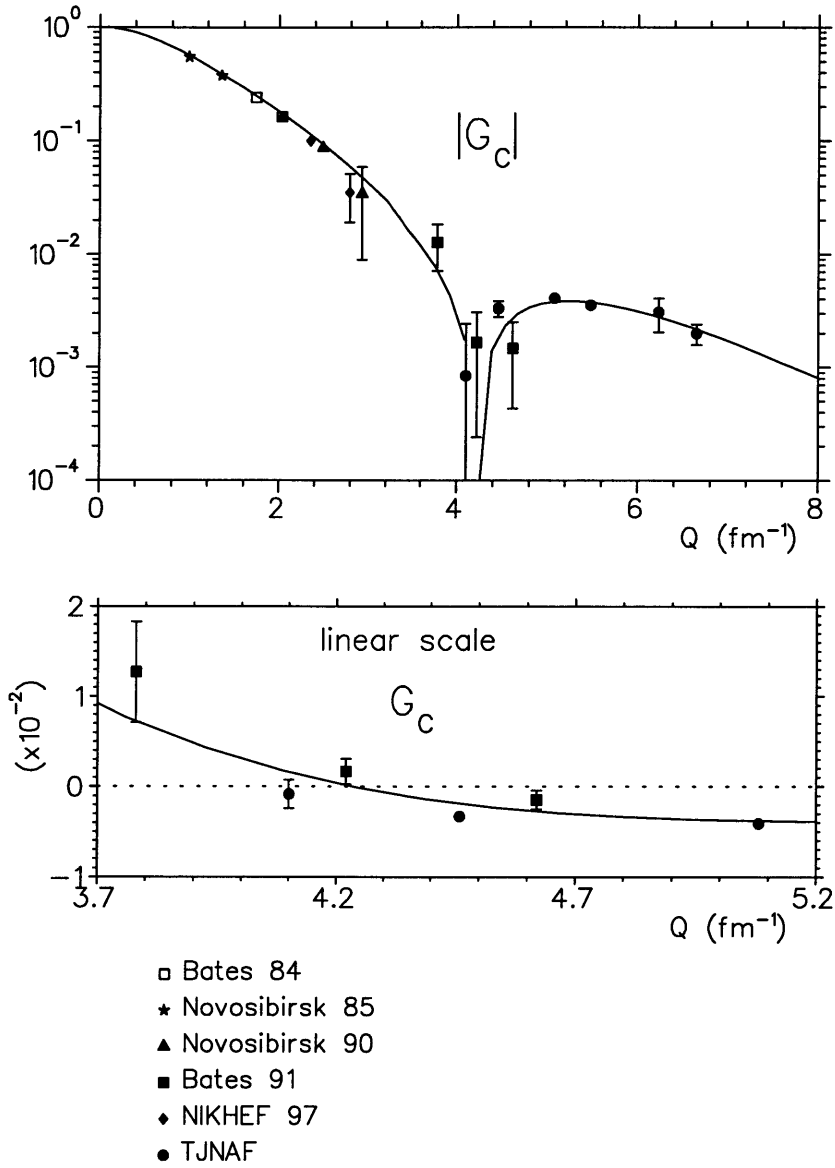
Figure 7-23: Comparison of data with predicted G_C from Van Orden, Devine, and Gross [66].

□ Bates 84
★ Novosibirsk 85
▲ Novosibirsk 90
■ Bates 91
● TJNAF
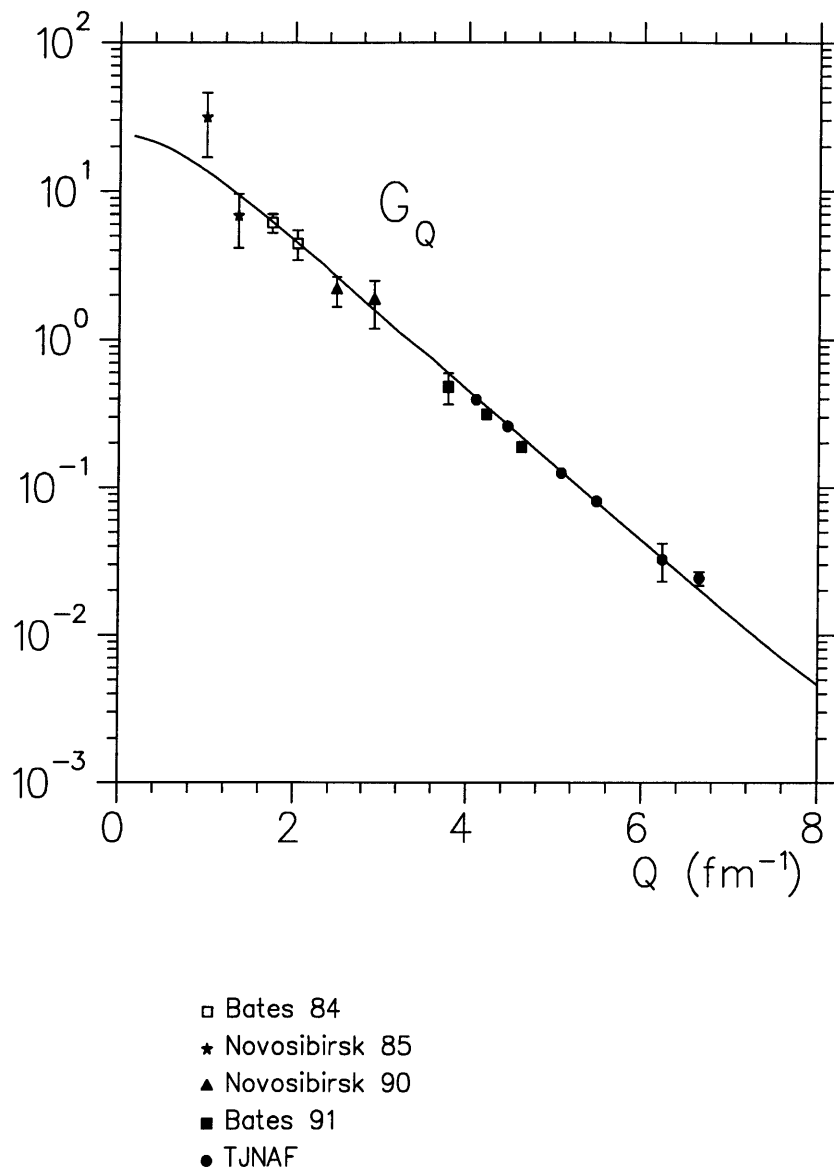
Figure 7-24: Comparison of data with predicted G_Q from Van Orden, Devine, and Gross [66].
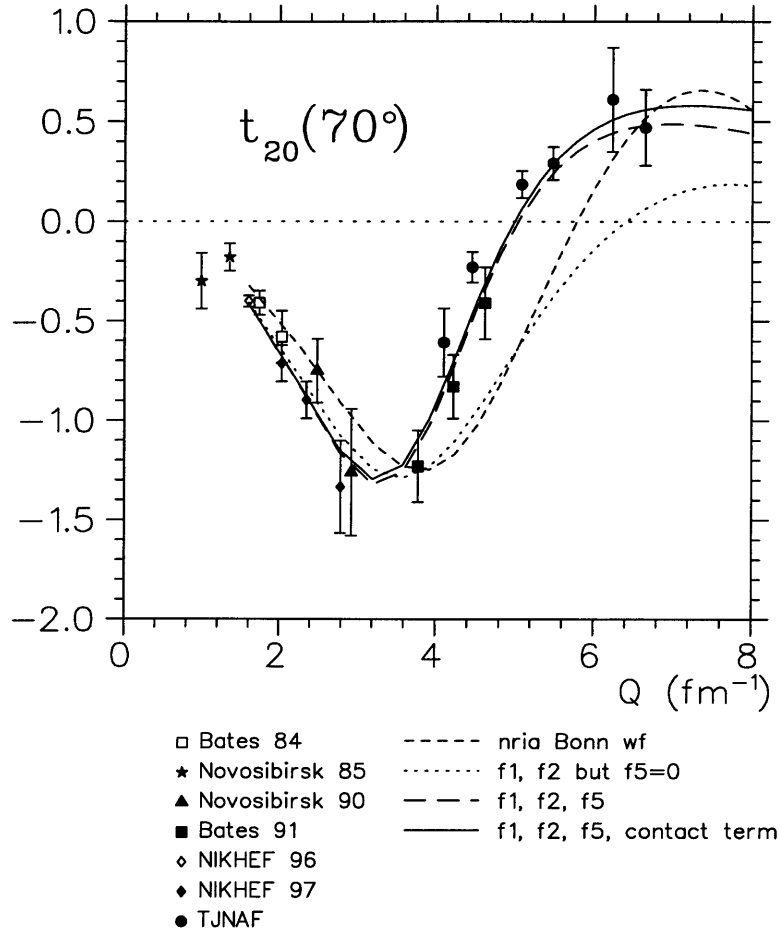
Figure 7-25: Comparison of data with predicted t_{20} from Carbonell, Desplanques, Karmanov, and Mathiot [65].

The comparison of the t_{20}, G_C, and G_Q data with the calculations from Carbonell, Desplanques, Karmanov, and Mathiot [65] using light-front dynamics is shown in Figures 7-25–7-27. For the predictions for t_{20} shown in Figure 7-25, the short-dashed curve is the NRIA calculation with the S- and D- waves of the Bonn-QA wave functions [2], the dotted curve is calculated using the light-front dynamics with components f_1 and f_2 only in the deuteron wave function, the long-dashed curve corresponds to the calculation with component f_5 in addition to f_1 and f_2, and the solid line in-

cludes, in addition to those included in the long dashed curve, the contact term. The incorporation (solid and long-dashed curves) of the component f_5 significantly increases t_{20} for $Q > 3.2$ fm^{-1}. The effect of the contact term is very small. The data favors these two calculations (solid and long-dashed curves). In Figure 7-26 and Figure 7-27, the G_C and G_Q data are compared with the calculations with f_1, f_2, f_5 and the contact term included. The predictions are in fairly good agreement with the present data. The additional contact term only slightly changes the calculations that include the component f_5. These two calculations provide a better fit to the data than the NRIA calculation and the calculation without the f_5 term. In Figure 7-26 and 7-27, only the results of G_C and G_Q with all components of f_1, f_2, f_5, and the contact term are plotted. The predictions are in fairly good agreement with the present data.
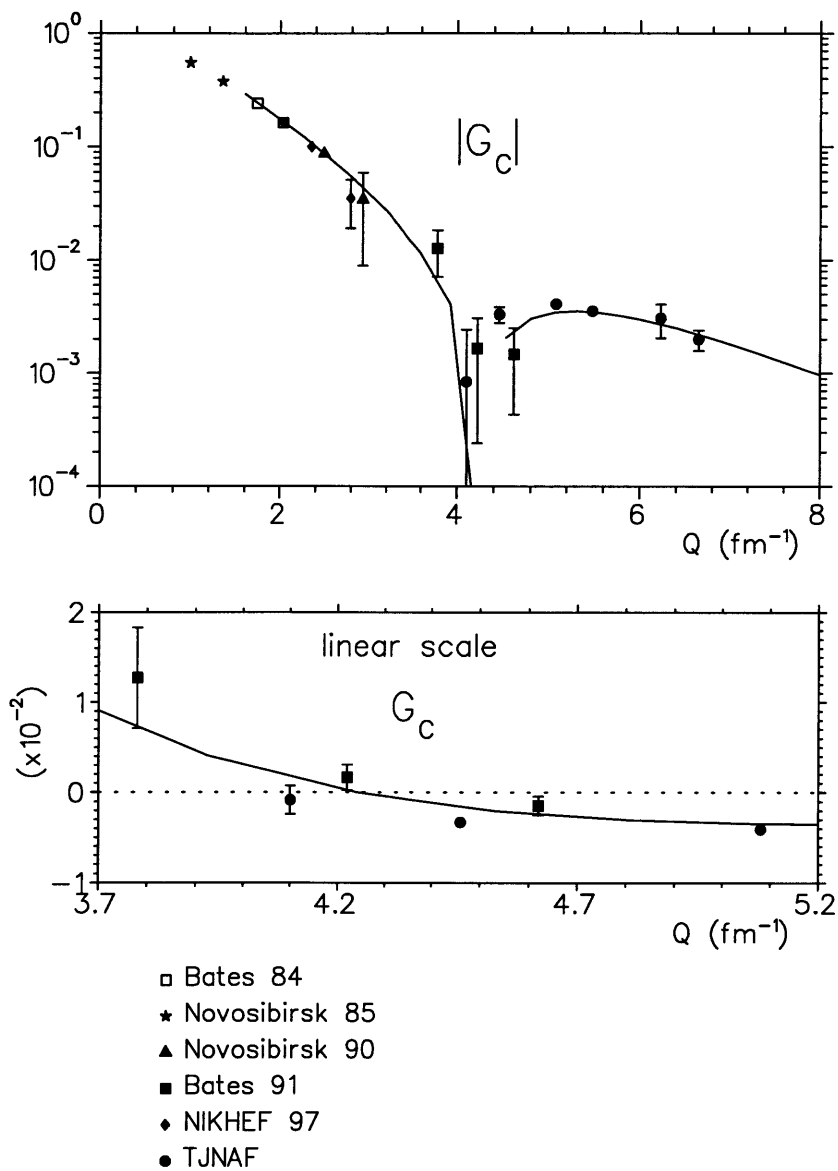
Figure 7-26: Comparison of data with predicted G_C from Carbonell, Desplanques, Karmanov, and Mathiot [65].
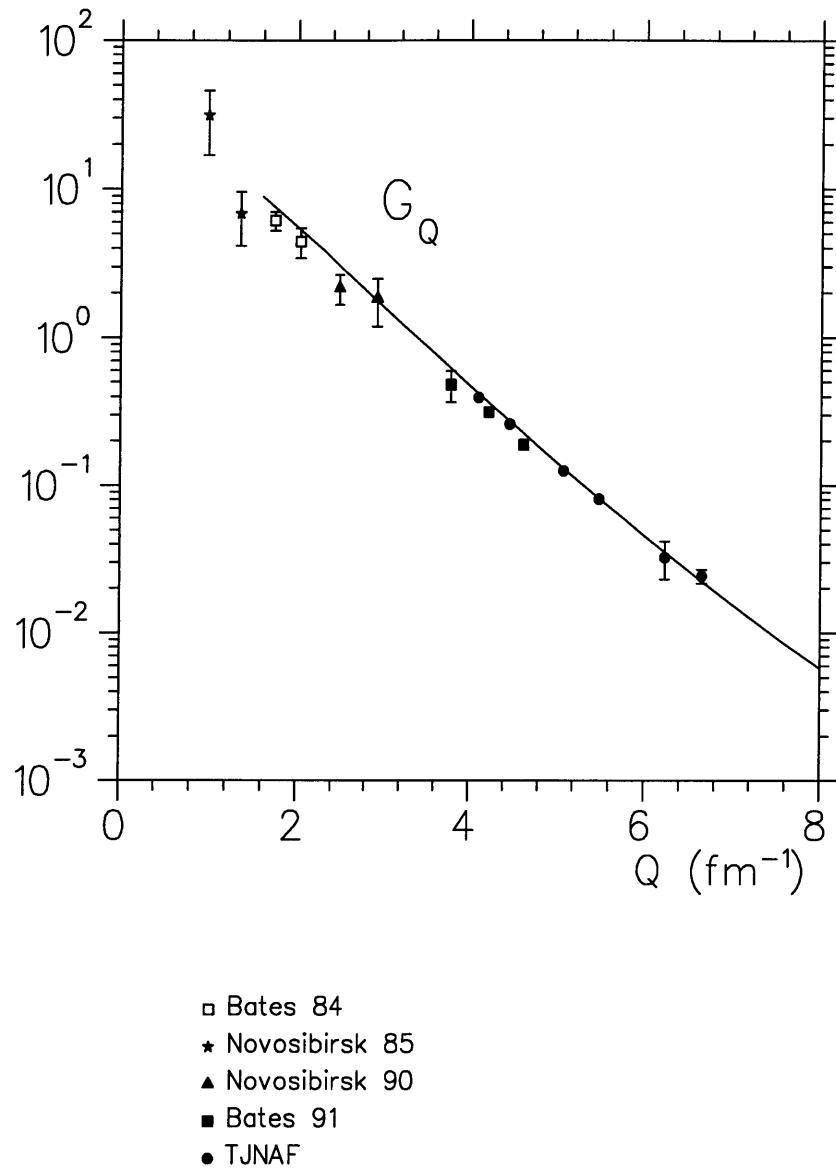
Figure 7-27: Comparison of data with predicted G_Q from Carbonell, Desplanques, Karmanov, and Mathiot [65].

7.2.3 Coupled-Channel Model

Sitarski, Blunden, and Lomon [72] calculated t_{20}, G_C, and G_Q using coupled-channel formalism of nucleons and isobar components. Comparison of the data with these calculations is shown in Figure 7-28–7-30. The predictions of G_C using H nucleon form factor parametrization for models C and D are plotted in Figure 7-28. The calculation of G_C with model D overestimates the present data, while the calculation using model C are in fairly good agreement with the data. Compared to model C, model D predicts a lower Q for the position of the G_C node. In Figure 7-29, the G_C data is compared with the calculation for model C using different nucleoon form factor parametizations H and GK. These two curves differ slightly for $Q < 5$ fm^{-1} which includes the G_C node. As a result, the positions of the G_C node using these two parametrizations are almost identical. For $Q > 5$ fm^{-1}, the difference becomes gradually noticeable. The data appears to favor H parametrization. In Figure 7-30, the G_Q data is compared with model C and D using nucleon form factor parametrizations H and GK. Model D predicts a minimum of G_Q around $6.0 < Q < 7.0$ fm^{-1} it has not been observed in the data. This would seem to rule out model D as a valid description of deuteron structure. The calculation using model C is in good agreement with the data. The difference between the calculations using H and GK parametrization is small. In general, model C with H parametrization provides good agreement with the data.
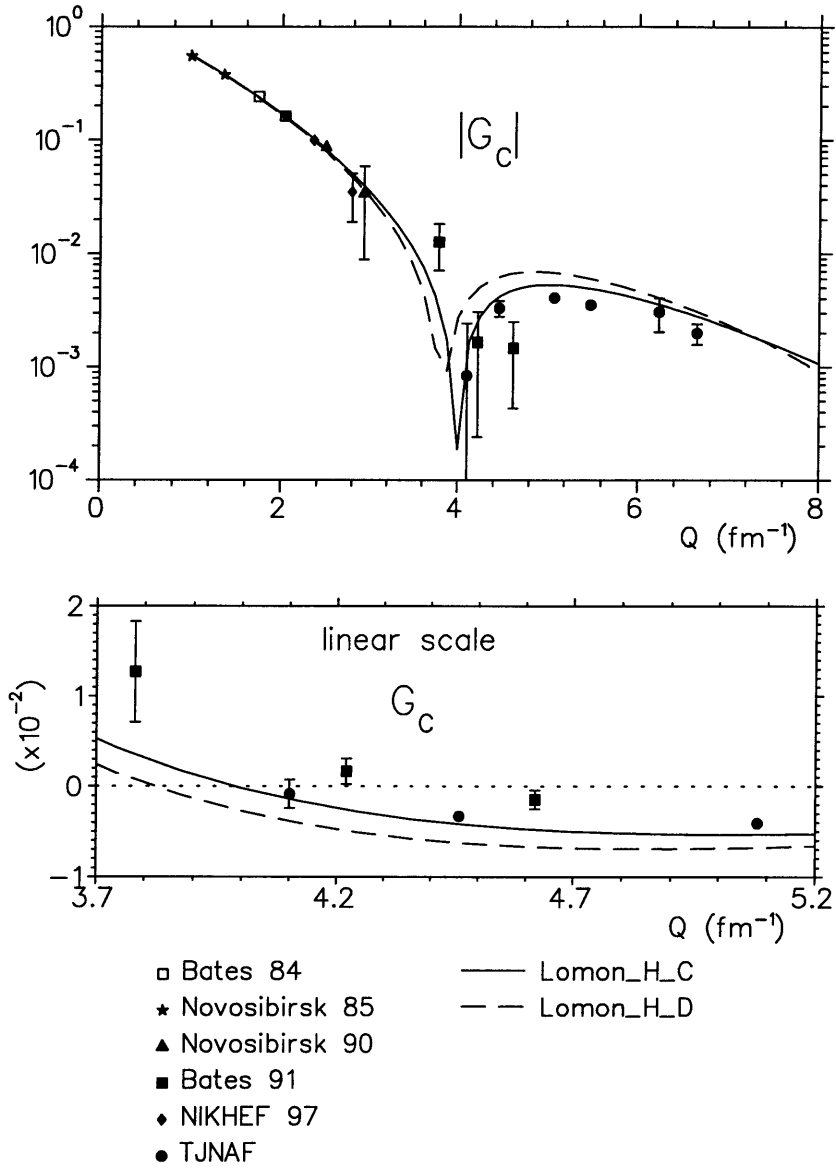
Figure 7-28: Comparison of data with predicted G_C from Sitarski, Blunden, and Lomon [72] using H form factor parametrization and two different models: C and D.
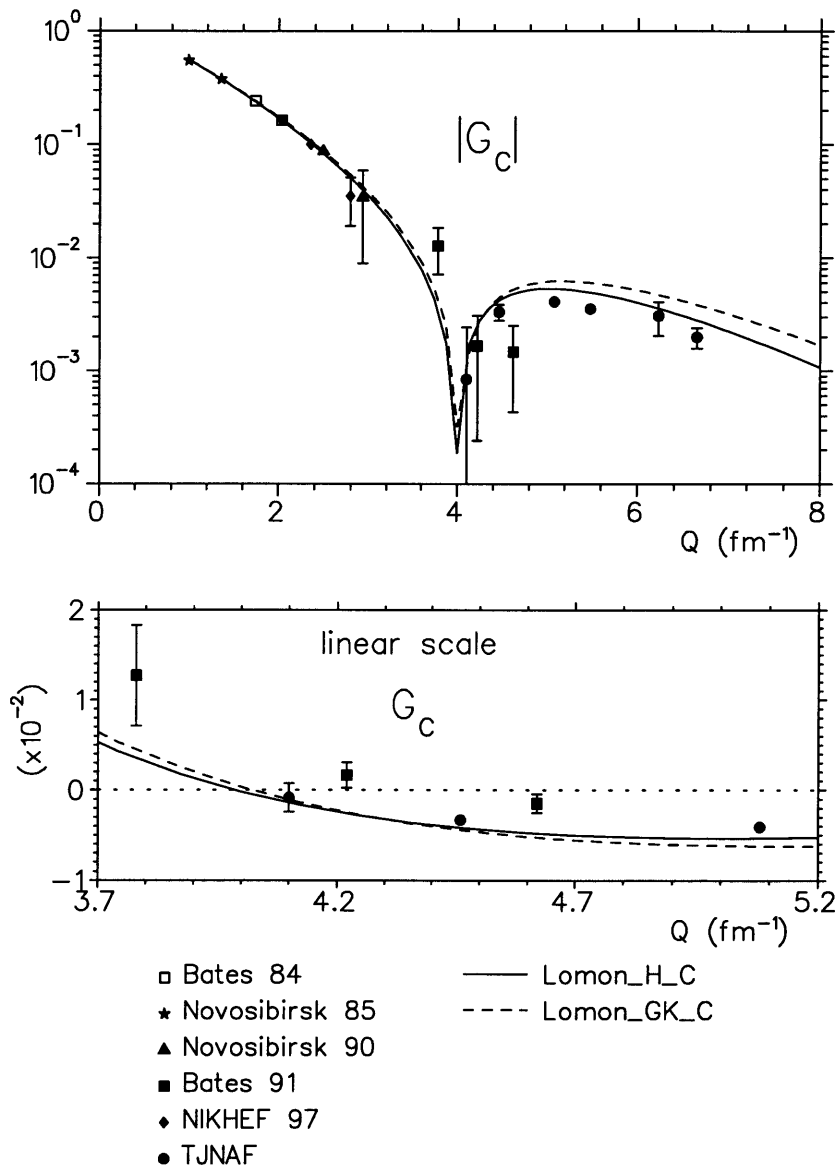
Figure 7-29: Comparison of data with predicted G_C from Sitarski, Blunden, and Lomon [72] using model C and two different nucleon form factor parametrizations: H and GK.

□ Bates 84
★ Novosibirsk 85
▲ Novosibirsk 90
■ Bates 91
● TJNAF

——— Lomon_H_C
— — Lomon_H_D
- - - - Lomon_GK_C
······ Lomon_GK_D
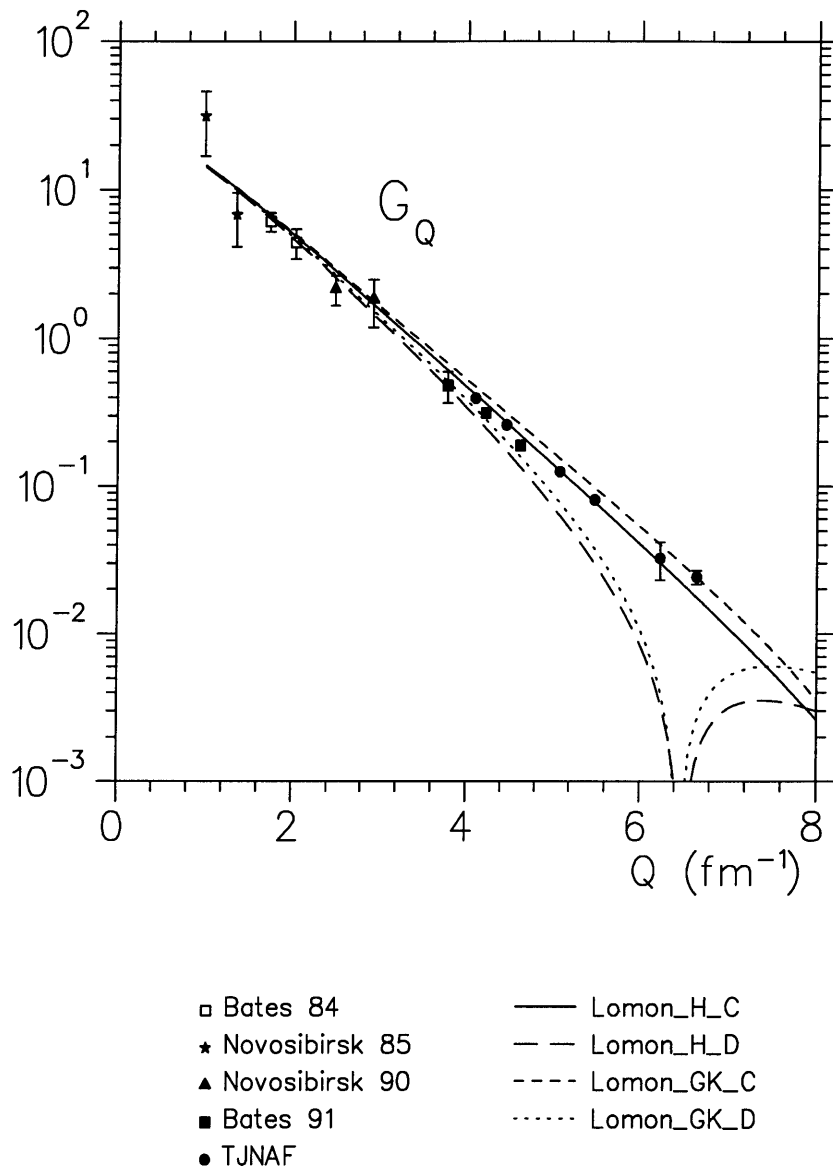
Figure 7-30: Comparison of data with predicted G_Q from Sitarski, Blunden, and Lomon [72] using two different models: C and D; and two different nucleonn form factor parametrizations: H and GK.

7.3 Comparison of t_{21} and t_{22} with Theories

In Figure 7-31 and 7-32, the extracted t_{21} and t_{22} (circles) from the ϕ asymmetry data in this experiment are compared with four typical calculations: non-relativistic impulse approximation (NRIA) by Wiringa, Stoks, and Schiavilla [4] using Argonne v_{18} potential, the same calculation as above but including relativistic corrections and MEC's, the complete impulse approximation (CIA) by Van Orden, Devine, and Gross [66] and the relativistically covariant calculation by Carbonell, Desplanques, Karmanov, and Mathiot [65] using light-front dynamics. t_{21} and t_{22} calculated using G_Q from this experiment and the world $B(Q)$ data are also compared with the theoretical predictions in the figures.

For t_{21}, these four calculations reasonably agree with the data. The extracted t_{21} from this experiment is consistent with the calculated t_{21} within their error bars. For t_{22}, the calculations do not differ too much, give good agreement with the extracted t_{22} for Kinematics 2, 3, and 4, but disagree with the extracted t_{22} for the first kinematics. The calculated t_{22} agrees with the theoretical calculations.
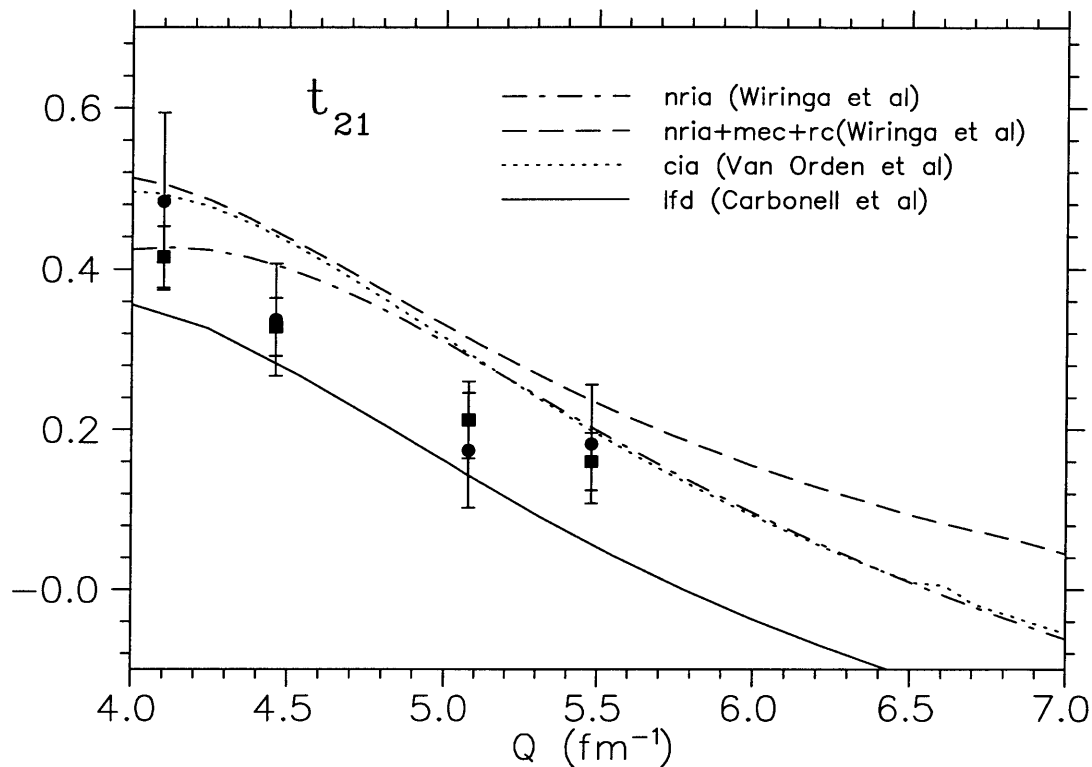
Figure 7-31: Comparison of the extracted t_{21} (circles) with various calculations: nonrelativistic impulse approximation by Wiringa, Stoks, and Schiavilla [4] using Argonne v_{18} potential, the same calculation as above but including relativistic corrections and MEC's, the complete impulse approximation (cia) by Van Orden, Devine, and Gross [66] and the calculation by Carbonell, Desplanques, Karmanov, and Mathiot [65] using Ligh Front dynamics. The square are t_{21} calculated using G_Q from this experiment and the world $B(Q)$ data.
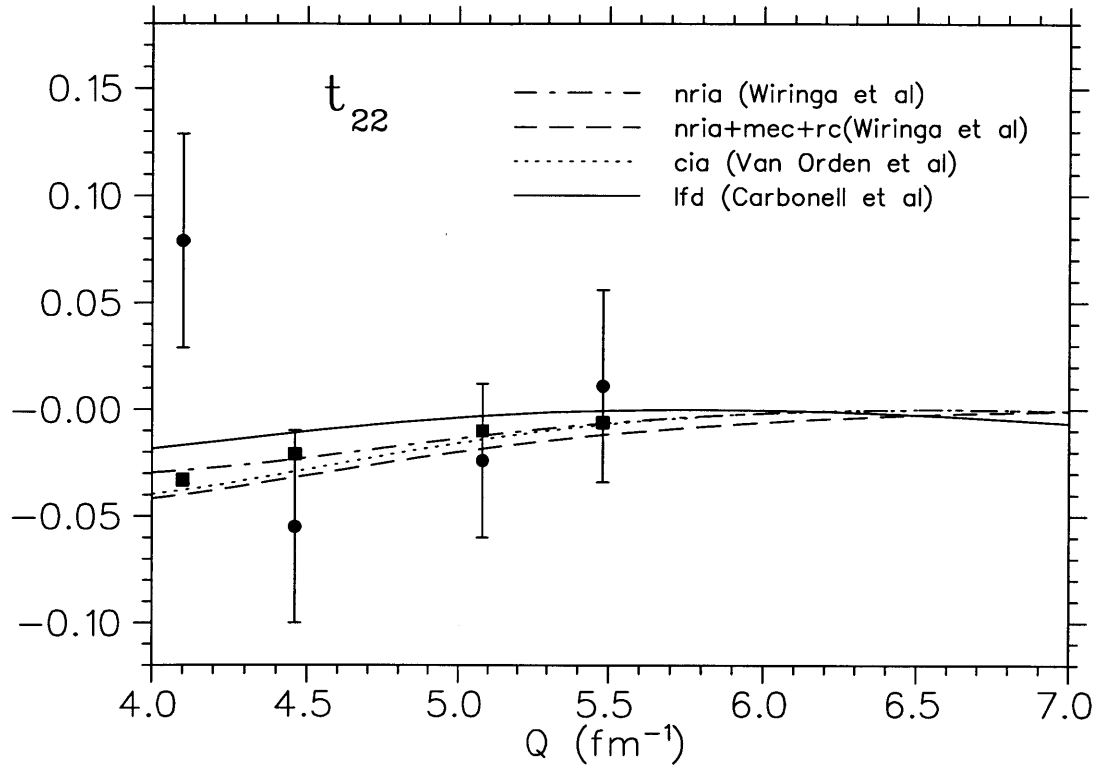
Figure 7-32: Comparison of the extracted t_{22} (circles) with the same calculation as in Figure 7-31. The squares are t_{22} calculated using G_Q from this experiment and the world $B(Q)$ data.

Chapter 8

Conclusions

A summary of the representative sample of theoretical calculations presented here and a somewaht subjective evaluation of their goodness of fit to the present CEBAF data and the previous Bates [12] data are shown in Table 8.1. Although the two data sets agree within their error bars, the present data are systematically more positive than the Bates data in the Q range where they overlap.

This difference results in a significant deviation of the evaluation of goodness of fit of the various calculations to the two data sets. The present data set favor calculations 5, 8, and 14 in Table 8.1, whereas the Bates data favor calculations 2, 10, 13 and 15. In some cases, a calculation that gives a qualitatively good fit to one data set will give a poor fit to the other. It would appear that in general the Bates data prefer potential model calculations that contain no meson exchange currents. The present data, on the other hand, prefer potential model calculations containing meson exchange currents.

The relativistically covariant calculations present a somewhat more confusing picture. These in general either lie between the two data sets or show some preference for the Bates data.

The present data exhibit a node in the monopole charge form factor at $Q = 4.03$ $\pm$ 0.06 fm^{-1}. This is at a somewhat smaller momentum transfer than previously reported [12]. The implications in terms of the analysis of Henning *et al.* [13] (see Chapter 1) is shown in Figure 8-1. The straight line is the best linear fit to calculations based on six different non-relativistic potential models. The longer box to the right is the region allowed by the data of Ref. [12], whereas the smaller box to the left is the region allowed by the present data.
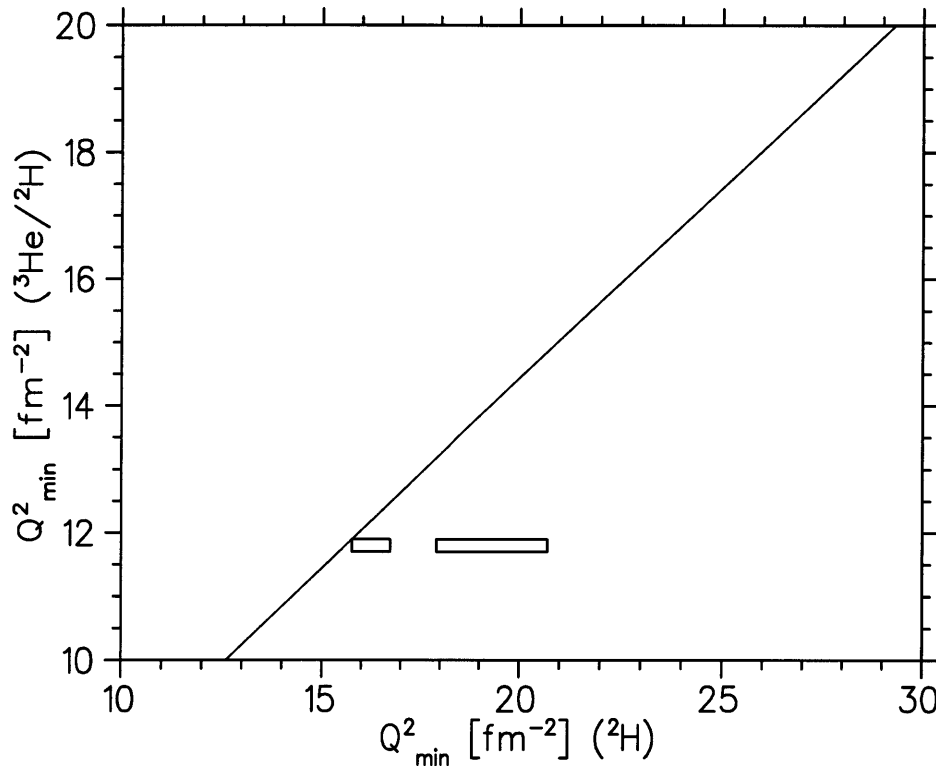
Figure 8-1: Predicted positions of the node for the charge monopole form factors for three-nucleon systems and the deuteron. A linear relationship was obtained from the calculations using six non-relativistic potential models [13]. The longer box indicates the region allowed by the data of Ref. [12], whereas the smaller box indicates the region allowed by the present data.

The present data clearly tend to give a more consistent position of the node for

G_C for the two-nucleon and three-nucleon systems with respect to the theory when compared with the results of Ref. [12]. However, theoretical calculations are not acceptable arbiters of the real world. There is a real experimental discrepancy that must be resolved. Resolving this discrepancy would require an experiment of much higher precision in the momentum transfer range 2 fm^{-1} < Q < 4.7 fm^{-1}. This would also include the minimum in the G_C form factor, which is a strong constraint on the various models. It has been pointed out by Turchinetz, *et al.* [109], that the BLAST facility at the Bates Linear Accelerator Center would be ideal for this experiment. BLAST will be equipped with a polarized internal deuteron target. By taking advantage of its large phase space acceptance and the high intensity stored electron beam of up to 1 GeV in energy in the Bates South Hall Ring, an experiment of about 1000 hours would produce a detailed mapping of the tensor moments in this Q range with statistical accuracy of a few percent. Such an experiment would severly constrain the acceptable choice of theoretical models.

I.D.	Authors	Potential or Model	Included	CEBAF Fit	Bates Fit
1	Mosconi and Ricci [1]	Paris	IA	Poor	Fair
2	Mosconi and Ricci [1]	Paris	IA+RC	Poor	Good
3	Mosconi and Ricci [1]	Paris	IA+RC+MEC	Fair	Fair
4	Schiavilla and Riska [42]	Argonne v_{14}	IA	Poor	Fair
5	Schiavilla and Riska [42]	Argonne v_{14}	IA+RC+MEC	Good	Poor
6	Pauschenwein et al. [43]	Paris	IA	Poor	Fair
7	Pauschenwein et al. [43]	Paris	IA+RC	Poor	Poor
8	Pauschenwein et al. [43]	Paris	IA+RC+MEC	Good	Poor
9	Pauschenwein et al. [43]	Bonn OBEPR	IA+RC+MEC	Fair	Fair
10	Pauschenwein et al. [43]	Bonn OBEPQ	IA+RC+MEC	Poor	Good
11	Pauschenwein et al. [43]	Full Bonn	IA+RC+MEC	Poor	Fair
12	Pauschenwein et al. [43]	Folded Bonn	IA+RC+MEC	Poor	Fair
13	Wiringa et al. [4]	Argonne v_{18}	IA	Poor	Good
14	Wiringa et al. [4]	Argonne v_{18}	IA+RC+MEC	Good	Poor
15	Hummel and Tjon [59, 60]	quasipotential OBE	IA	Poor	Good
16	Hummel and Tjon [59, 60]	quasipotential OBE	IA+$\rho\pi\gamma$	Fair	Fair
17	Hummel and Tjon [59, 60]	quasipotential OBE	IA+$\rho\pi\gamma$+$\omega\sigma\gamma$	Poor	Poor
18	Chung et al. [4]	Paris (LFD)		Poor	Fair
19	Van Orden et al. [66]	CIA	$\rho\pi\gamma$	Fair	Fair
20	Carbonell et al. [65]	Bonn QA	NRIA	Poor	Poor
21	Carbonell et al. [65]	LFD	f_1+f_2	Poor	Poor
22	Carbonell et al. [65]	LFD	$f_1+f_2+f_5$	Fair	Fair
23	Carbonell et al. [65]	LFD	$f_1+f_2+f_5$+contact	Fair	Fair
24	Sitarski et al. [72]	Coupled Channel	Model C	Fair	Poor
25	Sitarski et al. [72]	Coupled Channel	Model D	Poor	Poor

Table 8.1: Summary of the representative theoretical calculations presented here and a subjective evaluation of their goodness of fit to the present CEBAF data and the previous Bates [12] data. Abbriviation used are: IA = Impulse Approximation; RC = Relativistic Corrections; MEC = Meson Exchange Currents; NRIA = Non-relativistic Impulse Approximation; CIA = Complate Impulse Approximation; LFD = Light Front Dynamics.

Appendix A

JLAB E94-018 Collaboration

Measurement of the Deuteron Tensor Polarization at Large Momentum Transfers in D(e,e'd) Scattering

L. Eyraud, C. Furget, <u>S. Kox</u>, F. Merchez, J.-S. Real, R. Tieulent, E. Voutier

Institut des Sciences Nucleaires, IN2P3-UJF, F-38026 Grenoble Cedex, France

J. Ball, J.-E. Ducret, M. Garçon, **K. Hafidi**

DAPNIA/Service de Physique Nucleaire, CEN-Saclay, F-91191 Gif-sur-Yvette, France

L. Bimbot

Institut de Physique Nucleaire, F-91400 Orsay, France

J. Arvieux, E. Tomasi-Gustaffson

Lab National Saturne, IN2P3-CNRS et DSM-CEA, F-911191 Gif sur Yvette, France

A. Honegger, J. Jourdan, J. Zhao

Institut fur Physik, CH-4056 Basel, Switzerland

<u>E. Beise</u>, H.Breuer, N. Chant, G. Collins, F. Duncan, L. Ewell, **K. Gustafsson**,

A. Lung, R. Mohring, **D. Pitz**, P. Roos, D. Spayde

Physics Dept., University of Maryland, College Park, MD 20742 USA

D. Abbott, R. Carlini, J. Dunne, P. Gueye[1], D. Mack, D. Meekins, J. Mitchell,

H. Mrktchyan[2], L. Qin[3], S. Stepanyan[2], K. Vansyoc[3], J. Volmer[4], S. Wood, C. Yan

Jefferson Laboratory, 12000 Jefferson Ave, Newport News, VA 23606

E. Stephenson, W. Schmitt

IUCF, 2401 Milo B. Sampson Lane, Bloomington, IN 47405, USA

A. Ahmidouch, K. Dow, W. Turchinetz, C. Williamson, **W. Zhao**

MIT-Bates Linear Accelerator, PO Box 846, Middleton, MA 01949 USA

R. Gilman, C. Glashausser, G. Kumbartski, J. McIntyre, P. Rutt, R. Ransome

Dept. of Physics & Astronomy, Rutgers University, New Brunswick, NJ 08855 USA

H. Anklin, W. Boeglin, P. Markowitz

Florida International University, Miami, FL USA

S. Beedoe, S. Danagoulian, S. Mtingwa, R. Sawafta

Dept. of Physics, North Carolina A & T, NC USA

1) also Hampton University, Hampton, VA USA

2) also Yerevan Institute of Physics, Yerevan, Armenia

3) also Old Dominion University, Norfolk, VA USA

4) also Vrij Universitat Amsterdam, the Netherlands

* names underlined – spokesperson

* names in bold – thesis students

Bibliography

[1] B. Mosconi and P. Ricci, Few-Body Syst. **6**, 63 (1989); Erratum, *ibid.* **8**, 159 (1990).

[2] R. Machleidt, K. Holinde, and Ch. Elster, Phys. Rep. **149**, 1 (1987).

[3] R. B. Wiringa, R. A. Smith, and T. L. Ainsworth, Phys. Rev. C **29**, 1207 (1984).

[4] R. B. Wiringa, V. G. J. Stoks and R. Schiavilla, Phys. Rev. C **51**, 38 (1995).

[5] P. L. Chung, F. Coester, B. D. Keister, and W. N. Polyzou, Phys. Rev. C **37**, 2000 (1988)

[6] F. Gross, Phys. Rev. **142**, 1025 (1966);Erratum, *ibid.* **152**, 1517 (1966).

[7] V. F. Dmitriev *et al.*, Phys. Lett. **157B**, 143 (1985).

[8] R. Gilman *et al.*, Phys. Rev. Lett. **65**, 1733 (1990).

[9] M. Ferro-Luzzi *et al.*, Phys. Rev. Lett. **77**, 2630 (1996).

[10] M. Bouwhuis *et al.*, Phys. Rev. Lett. **82**, 3755 (1999).

[11] M. E. Schulze *et al.*, Phys. Rev. Lett. **52**, 597 (1984).

[12] I. The *et al.*, Phys. Rev. Lett. **67**, 173 (1991).

[13] H. Henning *et al.*, Phys. Rev. C **52**, 471 (1995).

[14] A. Amroun *et al.*, Phys. Rev. Lett. **69**, 253 (1992).

[15] S. S. M. Wong, *Introductory Nuclear Physics*, (Prentice Hall, Englewood Cliffs, New Jersey, 1990), p. 66.

[16] Particle Data Group, Phys. Lett. **B239**, III.1 (1990).

[17] C. van der Leun and C. Alderliesten, Nucl. Phys. **A380**, 261 (1982).

[18] T. E. O. Ericson and M. Rosa-Clot, Nucl. Phys. **A405**, 497 (1983).

[19] I. Lindgren, in *Alpha-, Beta- and Gamma-Ray Spectroscopy*, edited by K. Siegbahn (North-Holland, Amsterdam, 1965), Vol. 2, pp. 1621-1638.

[20] T. E. O. Ericson and W. Weise, *Pions and Nuclei*, (Oxford University Press, Oxford, 1988).

[21] N. L. Rodning and L. D. Knutson, Phys. Rev. Lett. **57**, 2248 (1986).

[22] T. E. O. Ericson, Nucl. Phys. **A416**, 281c (1984).

[23] R. V. Reid, Annals of Phys. **50**, 411 (1968).

[24] G. E. Brown and A. D. Jackson, *The Nucleon-Nucleon Interaction*, (North Holland Publishing, Amsterdam, 1976).

[25] V. Z. Jankus, Phys. Rev. **102**, 1586 (1956).

[26] V. Glaser and B. Jakšić, Nuovo Cimento **5**, 1197 (1957).

[27] M. Gourdin, Nuovo Cimento **28**, 533 (1963).

[28] E. L. Lomon, Ann. Phys. **125**, 309 (1980).

[29] R. G. Arnold *et al.*, Phys. Rev. Lett. **58**, 1723 (1987).

[30] S. Auffret *et al.*, Phys. Rev. Lett. **54**, 649 (1985).

[31] R. Cramer, Z. Phys. C - Part. and Fields **29**, 513 (1985).

[32] D. Abbott *et al.* (The Jefferson Lab t20 Collaboration), Phys. Rev. Lett. 82 1379 (1999).

[33] L. C. Alexa *et al.* (The Jefferson Lab Hall A Collaboration). Phys. Rev. Lett. 82 1374 (1999).

[34] S. E. Darden, in *Polarization Phenomena in Nuclear Reactions*, edited by H.H. Barschall and W. Haeberli (University of Wisconsin Press, Madison, Wisconsin, 1971), pp. 39-56; see also the summary of the Madison Convention contained in this volume, pp. *xxv-xxix*.

[35] D. Schildknecht, Phys. Lett. **10**, 254 (1964).

[36] D. Schildknecht, Zeit. Phys. **185**, 382 (1965).

[37] R. G. Arnold, C. E. Carlson, and F. Gross, Phys. Rev. C **23**, 363 (1981).

[38] K. Gustafsson, Ph.D. thesis, Univ. of Maryland, in preparation.

[39] D. O. Riska and G. E. Brown, Phys. Lett. **38B**, 193 (1972).

[40] J. Hockert, D. O. Riska, M. Gari and A. Huffman, Nucl. Phys. **A217**, 14 (1973).

[41] I. The, Ph.D. thesis, Massachusetts Institute of Technology, 1992.

[42] R. Schiavilla, D. O. Riska, Phys. Rev. C **43**, 437 (1991).

[43] J. Pauschenwein, W. Plessas, and L. Mathelitsch, Few-Body syst. **6**, 195 (1992).

[44] M. Lacombe *et al.*, Phys. Rev. C **21**, 861 (1980).

[45] F. Iachello, A. D. Jackson, and A. Lande, Phys. Lett. **43B**, 191 (1973).

[46] S. Galster *et al.*, Nucl. Phys. **B32**, 221 (1971).

[47] G. Höhler et al., Nucl. Phys. **B114**, 505 (1976).

[48] M. Gari and W. Krümpelmann, Z. Phys. A - Atoms and Nuclei **322**, 689 (1985).

[49] M. Gari and W. Krümpelmann, Phys. Lett. B **173**, 10 (1986).

[50] Haidenbauer, J., Holinde, K., and Johnson, M. B.: Preprint KFA-IKP(TH)-1991-26

[51] J. L. Friar, Annals of Phys. **81**, 332 (1973).

[52] F. Coester and A. Ostebee, Phys. Rev. C **11**, 1836 (1975).

[53] F. Gross, in *Few Body Systems and Nuclear Forces:* VIII International Conference, Graz, August 24-30, 1978, edited by H. Zingl, M. Haftel, and H. Zankel (Springer- Verlag, Berlin, 1978), Vol. 1, pp.46-49.

[54] R. G. Arnold, C. E. Carlson, and F. Gross, Phys. Rev. Lett. **38**, 1516 (1977).

[55] R. G. Arnold, C. E. Carlson, and F. Gross, Phys. Rev. C **21**, 1426 (1980).

[56] J. A. Tjon and M.J. Zuilhof, Phys. Lett. **84B**, 31 (1979).

[57] M. J. Zuilhof and J. A. Tjon, Phys. Rev. C **22**, 2369 (1980).

[58] M. J. Zuilhof and J. A. Tjon, Phys. Rev. C **24**, 736 (1981).

[59] E. Hummel and J. A. Tjon, Phys. Rev. Lett. **63**, 1788 (1989).

[60] E. Hummel and J. A. Tjon, Phys. Rev. C **42**, 423 (1990).

[61] R. Blankenbecler and R. Sugar, Phys. Rev. **142**, 1051 (1966).

[62] A. A. Logunov and A. N. Tavkhelidze, Nuovo Cimento **29**, 380 (1963).

[63] I. L. Grach and L. A. Kondratyuk, Sov. J. Nucl. Phys. **39**, 198 (1984).

[64] L. L. Frankfurt, I. L. Grach, L. A. Kondratyuk, and M. I. Strikman, Phys. Rev. Lett. **62**, 387 (1989).

[65] J. Carbonell, B. Desplanques, V. A. Karmanov, and J. F. Mathiot, Phys. Rep. **300**, 215 (1998).

[66] J. W. Van Orden, N. Devine and F. Gross, Phys. Rev. Lett. **75**, 4369 (1995).

[67] F. Gross, Phys. Rev. **186**, 1448 (1969); Phys. Rev. D **10**, 223 (1974); Phys. Rev. C **26**, 2203 (1982).

[68] F. Gross, J. W. Van Orden, and K. Holinde, Phys. Rev. C **41**, R1909 (1990); **45**, 2094 (1992).

[69] F. Gross and D. O. Riska, Phys. Rev. C **36**, 1928 (1987).

[70] H. Ito and F. Gross, Phys. Rev. Lett. **71**, 2555 (1993).

[71] K. L. Mitchell, Ph.D. thesis, Kent State University, 1995.

[72] W. P. Sitarski, P. G. Blunden, and E. L. Lomon, Phys. Rev. C **36**, 2479 (1987).

[73] E. L. Lomon and H. Feshbach, Ann. Phys. **48**, 94 (1968).

[74] W. Bartel *et al.*, Nucl. Phys. **B58**, 429 (1973).

[75] R. Dymarz and C. J. Morningstar, R. Gourishankar, and F. C. Khanna, Nucl. Phys. **A507**, 531 (1990).

[76] R. Dymarz and F. C. Khanna, Nucl. Phys. **A507**, 560 (1990).

[77] R. Dymarz and F. C. Khanna, Phys. Rev. C **41**, 2438 (1990).

[78] P. Obersteiner, W. Plessas, and J. Pauschenwein, Few-Body Syst. Suppl. 5, 140 (1992).

[79] L. Mathelitsch, W. Plessas, and W. Schweiger, Phys. Rev. C **26**, 65 (1982).

[80] W. Schweiger, W. Plessas, L.P. Kok, and H. Haeringen, Phys. Rev. C **27**, 515 (1983).

[81] W. Schweiger, W. Plessas, L. P. Kok, and H. Haeringen, Phys. Rev. C **28**, 1414 (1983).

[82] M. Garçon *et al.*, Nucl. Phys. **A458**, 287 (1986); E. J. Stephenson *et al.*, Indiana University Cyclotron Facility Scintific and Technical Report No. 58, 1983.

[83] C. Yan *et al.*, Nucl. Instrum. Meth. **A365**, 261 (1995).

[84] P. Gueye, Status of the Actual Beam Position Monitors in the Hall C Beamline, CEBAF internal Report (unpublished).

[85] J. R. Arrington, Ph.D. thesis, California Institute of Technology, 1998.

[86] *CEBAF Conceptual Design Report* (CEBAF press, Newport News, 1995).

[87] A. Ahmidouch, "HMS Matrix Elements", notes of t_{20} Collaboration meeting, MIT-Bates, 1998.

[88] J. E. Ducret and M. Garçon, "CEBAF t_{20} experiment: Report on the deuteron channel", DAPNIA/SPhN, CEA-Saclay, 1995.

[89] L. Eyraud, Thése de Doctorat, Institut des Sciences Nucléaires de Grenoble, France, Nov. 1998.

[90] D. V. Bugg and C. Wilkin, Phys. Lett. **B152**, 37(1985).

[91] T. Motobayashi *et al.*, Phys. Lett. **B233**, 69 (1989); S. Kox *et al.*, Phys. Lett. **B266**, 264 (1991); S. Kox *et al.*, Nucl. Phys. **A556**, 521 (1993).

[92] J. M. Cameron *et al.*, Nucl. Instrum. Meth. **A305**, 257 (1991).

[93] J. Carbonell, M. Barbaro and C. Wilkin, Nucl. Phys. **A529**, 6531991.

[94] P. Chesny, G. Guillier, P. Marlet, LNS/AIRES report # 92.05 (1992), Saclay, unpublished.

[95] G. Heyes *et al.*, Proc. of TOOLS 8 Conference (Prentice Hall, Santa Barbara, CA, July 1992), pp. 171-183.

[96] Experimental & Physics Industrial Control System (EPICS), Los Alamos National Laboratory, 1984.

[97] S. A. Wood and W. A. W. III, in *Conference Record of the Eight Conference on Real-Time Computer Applications in Nuclear Physics and Plasma Physics*, edited by D.Axen and R.Potissou (TRIUMF, Vancouver B.C. Canada, 1993).

[98] Grenoble team, Calibration analysis report, t_{20} internal report, 1998.

[99] K. Hafidi and M. Garçon, "Proton track reconstruction in POLDER: an alternative approach", t_{20} internal report, 1998.

[100] K. Hafidi and M. Garçon, "Proton track reconstruction in POLDER: Extension of the Saclay method to point 1", t_{20} internal report, 1998.

[101] K. Hafidi, Thése de Doctorat, Universite de Paris XI/Orsay, France, in preparation.

[102] J. Ball, "POLDER LH_2 target geometry", t_{20} internal report, 1998.

[103] M. Garçon and K. Hafidi, "Interpolation of POLDER calibration data and Considerations on deuteron energy distributions", t_{20} internal report.

[104] C. E. Hyde-Wright, Ph.D. thesis, Massachusetts Institute of Technology, 1984.

[105] F. James and M. Roos, Comput. Phys. Commun. **10**, 343 (1975).

[106] M. Garçon, "Experimental asymmetries", notes of t_{20} Collaboration meeting, MIT-Bates, 1998.

[107] M. E. Schulze, Ph.D. thesis, Massachusetts Institute of Technology, 1983.

[108] J. Arvieux *et al.*, "Correction of Beam Depolarization in Calibration", t_{20} internal report, 1998.

[109] W. Turchinetz *et al.*, "Deuteron Elastic Form Factors: Opportunity for Blast?", Proceedings of the Second Workshop on Electronuclear Physics with Internal Targets and the Bates Large Acceptance Toroid (BLAST).

Acknowledgments

The completion of this thesis is the result of the help from many people. It is my pleasure to acknowledge their contributions here.

First, I would like to thank my thesis advisor, Dr. Claude Williamson for his guidance on my graduate study at MIT. Claude is always generous with his time, attention, and patience not only to answer my questions but also to help me through many difficulties during this project. I feel easy and relaxed to work with him, and most of all, I benefit greatly from his remarkable physics insight and expertise.

I would also like to thank Dr. Bill Turchinetz for his suggestions about this thesis, and many useful discussions about the data analysis. Also I would like to thank Prof. Eddy Farhi for serving in my thesis committee.

I would like to thank Drs. Betsy Beise and Serge Kox. This experiment could not have been accomplished so successfully without their great leadership. I have learned a lot from many discusstions with Betsy. Whenever I had a question regarding this experiment, Betsy was always available to answer me. Serge has helped me a lot to understand the calibration experiment and the POLDER detectors. I always felt enthusiastic about this experiment after the discussions with him.

I would also like to thank Dr. Michel Garçon who has had great influence in various phase of this experiment, from the design of the deuteron channel to the data analysis. He is so knowlegeable that I can always expect an answer to my question from him in both theory and experiment. Also I should thank him for sending me many theoretical calculations, which saved me a lot of time and efforts.

I would like to thank Dr. Steve Wood for sharing his expertise in data acquisition, electronics, and data analysis software package. He helped me a lot to set up my PC at CEBAF, to understand the software architecture, and to convert the analysis code from HP platform to Linux system.

I would like to thank Dr. Jean-Sebastien Real for his efforts to develop the analysis

code for POLDER and his patience to answer my questions for the data analysis.

My thanks go to the other five thesis students, Kawtar Hafidi, Kenneth Gustafsson, Laurent Eyraud, David Pitz and Adrian Honeggar. I was impressed with their enthusiasm and hard working in this experiment. Thank Kawtar and Kenneth for sharing ideas and information about data analysis. I should thank Kawtar for her efforts in developing the new proton tracking algorithm. Also I would like to thank Kenneth and Laurent for taking their time to make data tapes, and thank David and Adrian for providing me their beautiful $A(Q)$ data.

I would like to thank Karen Dow for her tremendous efforts in the dipole mapping at MIT. I would like to thank Dr. Abdellah Ahmidouch for his good work on the optics study for this experiment. My thanks also go to Dr. Jean-Eric Ducret for his time to explain to me the simulation code for the deuteron channel and the insteresting stories about his travelling to China. I would also like to thank Drs. Chen Yan and Paul Gueye for measuring the beam energy. My thanks also go to Drs. Christophe Furget and Jack Ball for the discussions about the POLDER electronics and the hydrogen target.

I would like to thank Drs. Joe Mitchel, Fraser Duncan, Jim Dunne, David Meekins and Paul Hood for sharing their expertise and working on the cryotarget. My thanks go to Drs. Dave Mack and Ralph Ent, who explained to me patiently how the HMS detecotors worked.

I would like to thank all the collaborators for either taking shifts or setting up the apparatus. Also I would like to thank the JLAB accelerator crew for delivering stable and high quality beam.

I would like to thank Nilanga Liyanage, Krishni Wijesooriya and Kevin Fissum for their friendship, which made my life more enjoyable in Newport News.

My thanks go to Joanne Gregory for making all the travel arrangements.

I would like to thank my husband Juncai Gao for his love and helping me in almost

every aspect in my life. As a physicist, he gave me many sharp and creative ideas in my data analysis. I should say that I have learned a lot from him in nuclear physics.

I owe a lot to my mother-in-law for helping me taking care of my adorable son Bruce. Without her help, I could not have my thesis finished. I would also like to thank Bruce. My tiredness after a long day would completely disappear when he smiled at me. Finally, I would like to thank my parents and my brothers for their endless love and support.